Investigation of Stability and Catalytic Properties of Atomic Clusters within DFT Framework

Thesis submitted to AcSIR for the award of
the Degree of
DOCTOR OF PHILOSOPHY

in Chemical Sciences

by

Turbasu Sengupta

Registration Number : 10CC12A26007

under the guidance of

Supervisor:
Dr. Nayana Vaval

Co-Supervisor:
Prof. Sourav Pal

Physical and Material Chemistry Division
CSIR National Chemical Laboratory
Pune, India 411008

March 2017

सीएसआयआर–राष्ट्रीय रासायनिक प्रयोगशाला
(वैज्ञानिक तथा औद्योगिक अनुसंधान परिषद)
डॉ. होमी भाभा मार्ग, पुणे - 411 008. भारत
CSIR-NATIONAL CHEMICAL LABORATORY
(Council of Scientific & Industrial Research)
Dr. Homi Bhabha Road, Pune - 411008. India

Certificate

This is to certify that the work incorporated in this Ph.D. thesis entitled **"Investigation of Stability and Catalytic Properties of Atomic Clusters within DFT Framework"** submitted by **Turbasu Sengupta** to Academy of Science and Innovative Research (AcSIR) in fulfillment of the requirements for the award of the degree of **Doctor of Philosophy in Chemical Sciences**, embodies original research work under my supervision. I further certify that this work has not been submitted to any other University or Institution in part or full for the award of any degree or diploma. Research material obtained from other sources has been duly acknowledged in the thesis. Any text, illustration, table, etc., used in the thesis from other sources, have been duly cited and acknowledged.

Turbasu Sengupta
Turbasu Sengupta
(Student)

N. Vaval
Dr. Nayana Vaval
(Supervisor)

Sourav
Prof. Sourav Pal
(Co-supervisor)

Date: **15.03.2017**

Place: CSIR-NCL, Pune

Communications Channels
NCL Level DID : 2590
NCL Board No. : +91-20-25902000
Four PRI Lines : +91-20-25902000
FAX
Director's Office : +91-20-25902601
COA's Office : +91-20-25902660
SPO's Office : +91 20 25902664
WEBSITE
www.ncl-india.org

Declaration of Authorship

I, Turbasu Sengupta, declare that this thesis entitled, **"Investigation of Stability and Catalytic Properties of Atomic Clusters within DFT Framework"** submitted for the degree of Doctor of Philosophy in Chemical Sciences to the Academy of Scientific & Innovative Research (AcSIR), has been carried out by me at the Physical and Material Chemistry Division of CSIR-National Chemical Laboratory, Pune under the supervision of Dr. Nayana Vaval and Prof. Sourav Pal. Such material as has been obtained by other sources has been duly acknowledged in the thesis. The work is original and has not been submitted in part or full by me for any other degree or diploma to any other Institution or University.

Date: March 15, 2017

Place: CSIR–NCL, Pune

Turbasu Sengupta
Turbasu Sengupta

To My Beloved Parents

Acknowledgements

It is my great pleasure to present my thesis before the scientific community, and to express my gratefulness to all who helped me in this endeavor. Foremost, it is a great honor to express my deep sense of gratitude and respect to my guide Dr. Nayana Vaval and co–guide Prof. Sourav Pal. I am grateful for their untiring and prompt help by sparing their valuable time in the supervision of this work by identifying errors and suggesting ways to rectify them. Their caring, persuading and compassionate nature had been bliss during my research work. I am also grateful to both of them for providing me the necessary facilities at the institute. Their guidance helped me in all the time of research and writing of this thesis. I could not have imagined having a better research group to pursue my Ph.D in the field of chemical science. I am deeply indebted to my guide for her gentle guidance, constructive comments and timely intervention which have been vital in shaping the focus of my research and its reporting. Also, I would like to express my sincere gratitude to my research co–guide Prof. Sourav Pal for his continuous support of my Ph.D study, for his patience, motivation, and immense knowledge of quantum and physical chemistry as a whole. Without his precious teaching, tutorials and instructions it would not be possible to conduct this research.

Besides my research advisor, I would also like to thank the members of my DAC committee: Dr. Chinnakonda S. Gopinath, Dr. Kumar Vanka and Dr. Debashree Ghosh not only for their insightful comments and encouragement, but also for the hard questions which have incented me to widen my research from various perspectives. My sincere thanks also goes to Dr. T. G. Ajithkumar, Dr. A. V. Orpe, Dr. Durba Sengupta and Dr. Kavita Joshi for their teaching in the coursework. I would also like to appreciate the continuous support of NCL staff members throughout my research tenure in CSIR–NCL. I duly acknowledge the University Grants Commission (UGC), New Delhi for providing the research fellowship and the Academy of Scientific & Innovative Research (AcSIR) for giving me the opportunity to participate in their exciting Ph.D programme.

I thank my fellow labmates for the stimulating discussions and advice, for their compliments and criticisms, and for all the fun we have had in the last five years in the lab, canteen and shopping complex. All my seniors Achintyada, Anagha, Aryyada, Vidhikadi, Debaratidi, Deeptidi, Guptaji, Himadrida, Kamalikadi, Madhulitadi, Manzoor, Muditji, Sabadi, Sapnadi, Sayalidi, Sumantrada and Susantada certainly deserve my appreciation for their support, guidance and encouragements. Achintyada, Himadrida and Susantada rightfully owed special gratitude due to their direct contribution in the research through the collaborative works. Especially, most of the projects included in the thesis would not be possible without the suggestions and tutorials from Achintyada and Susantada. It is primarily Susantada, whose encouragement influenced me to choose cluster chemistry as the preferred field for my research work. My earnest appreciation also goes to both of my batch–mates Sudip and Deepak. I feel fortunate as well as honored to have work with such talented individuals. Especially, I consider it as a privilege to have the opportunity to work with Sudip for the past five years. It is always a pleasure to have an intellectual, humble and down to earth friend like Sudip, whom I can always trust and approach for help and suggestions. I also like to express my gratitude to Bipasa, Kaushik, Lisa, Majid and Tumpa for their companionship during the course of my Ph.D.

I am grateful to my teachers specially Hironmoy Sinha Roy (Bablada) and Sourendra Majumder in my early school days to give me the confidence and urge to pursue higher education in science. I owed a lot to my tutors Arupda, Durjoyda and Kaushikda for their elite teaching during the graduate level. I'm also extremely grateful to the amazing faculties of Scottish Church

College, Kolkata during my M.Sc days. It was a huge honor for me to be a part of the masters programme in SCC. My gratuitous thanks goes to Dr. Rana Sen, Dr. Utpal Das, Dr. Priyatosh Dutta, Dr. Sanjib Bagchi and all the other gifted faculties for introducing me to the amazing universe of physical chemistry through their erudite classes and practicals. All my students of chemistry and biochemistry department of Asutosh College also owes my heartiest gratitude for their love and appreciation throughout all these years. Without their encouragement it would not be possible to qualify NET examination and continue my Ph.D study.

Among my handful list of friends, I am personally grateful to Suman(Ghosh) to stand beside me in my bad and good times throughout all these years. I don't have enough wisdom to thank him properly. My humble appreciation goes to Arka, Arpan, Arpita, Arundhati, Avishek, Ayan (Mukhopadhyay), Basabendu, Chiranjit, Debgiri, Karuna, Mainak, Monami, Riyadi, Saikat, Sayantani, Soma, Soumya, Soumyada, Soumyajit(Sett), Sucheta, Tithi and Triloke. Among the NCLites, I express my cordial thanks to Amit, Amritadi, Asishda, Atanu, Atrayee, Baljinder, Collins, Diksha, Jaya, Jugal, Manik, Mannada(Arpan), Manoj(Mane), Manojda, Monojit, Monalisa, Mukunda, Nisha, Niveditadi, Paulami, Pranab, Prathitda, Prithvida Rahul, Ruchi, Samik, Santu, Sayantan, Shailja, Shantanu, Sneha, Souvikda, Subarna, Subhrashis, Suman, Sujitda, Swagatadi, Tamal, Tapas, Tiwariji, Ujjwal, Vaibhav, Vipin, Xavier. Lastly, the acknowledgment will be incomplete without thanking two of my roommates and labmates, Shantanuda and Yuvraj. It is due to them who made my stay in Pune homely and comfortable during the tenure of my Ph.D.

It is needless to say that the dissertation would not have been possible without the relentless support from my parents whose selfless sacrifices with pain and tears and unabated prayers has aid me throughout the years to finally reach the present stature. Without their encouragement, assistance and financial supports it will not be feasible to overcome all the hardship and misfortunes I have faced throughout the past years and finally able to accomplish this feat.

Turbasu Sengupta

Contents

List of Figures

List of Tables

CSIR NATIONAL CHEMICAL LABORATORY

Abstract

Electronic Structure Theory Group
Physical and Material Chemistry Division

DOCTOR OF PHILOSOPHY

Investigation of Stability and Catalytic Properties of Atomic Clusters within DFT Framework

by Turbasu Sengupta

Chapter 1: The first chapter contains a concise introduction of the fundamental concepts of cluster chemistry. Brief classification of clusters, prominent historical achievements, method of synthesis and their properties including the fundamental differences with common materials are included. The geometric and electronic shell effect which are the two major contributing factor in cluster stabilization are also discussed in detail. Few important topics regarding the stabilization like Mackay's icosahedra series, spherical and deformed jellium models and odd–even effect are also covered. Other important theoretical models like the spherical cluster approximation or the liquid drop models are added as well. The chapter is intended to cover all the essential topics which are of importance for the later chapters included in this thesis.

Chapter 2: The present chapter provides a brief introduction to the fundamental concepts of the density functional theory (DFT) which is used for majority of the calculations included in the thesis. Starting from the basics of quantum chemistry, crucial components of the density functional theory (DFT) are covered. Significant works from antiquity, like the Thomas–Fermi model are included as well. The fundamentals of modern DFT including the Hohenberg–Kohn theorem and the Kohn–Sham model are discussed. A separate section is included in order to discuss conceptual density functional theory and few additional topics.

Chapter 3: In this chapter, energetics and the in-depth reaction mechanism of the oxidative addition step of the cross-coupling reaction are studied in the framework of density functional theory (DFT) on aluminum nanoclusters. Aluminum metal in its bulk state is totally inactive towards carbon-halogen bond dissociation but selected Al nanoclusters (size ranging from 3 to 20 atoms) have shown a significantly lower activation barrier towards the oxidative addition reaction. The calculated energy barriers are lower than the gold clusters and within a comparable range with the conventional and most versatile Pd catalyst. Further investigations reveal that the activation energies and other reaction parameters are highly sensitive to the geometrical shapes and electronic structures of the clusters rather than their size, imposing the fact that comprehensive studies on aluminum clusters can be beneficial for nanoscience and nanotechnology. To understand the possible reaction mechanism in detail, the reaction pathway is investigated with the *ab initio* Born Oppenheimer Molecular Dynamics (BOMD) simulation and the Natural Bond Orbital (NBO) analysis. In short, the present chapter highlights the thermodynamic and kinetic details of C-I bond dissociation on aluminum clusters for future endeavors in cluster chemistry.

Chapter 4: The influence of spin on the properties of small sized transition metal doped aluminum clusters are investigated in the framework of density functional theory (DFT). Detailed analysis on minimum spin doped aluminum clusters has shown prominent indication of odd–even oscillation in various calculated properties, supporting the presence of jellium shell structures within them. However, optimized high spin ground state counterparts, on the other hand, show rather smooth trends consistent with the properties of bulk materials. Resemblance to the bulk transition metals is further reflected in the gradual declining trends of heat of adsorption of CO_2 molecule on cluster surface by sequentially changing the dopant atom from scandium to zinc. All the observations are also compared and found to be consistent with the earlier theoretical and experimental findings as obtained in the current literature. The similarities in the properties between atomic clusters and the bulk material is of utter importance and indeed precious considering the promising influence of the acquired information in understanding the process of evolution of nanoparticles from constituent atoms.

Chapter 5: The stability and electronic structure of radical attached aluminum nanoclusters are investigated using density functional theory (DFT). A detailed investigation shows good correlation between the thermodynamic stability of radical attached clusters and the stability of the attached radical anions. All other calculated parameters like HOMO–LUMO gap and charge transfer are also found to be consistent with the observed thermodynamic stabilities of the complexes. Investigation of the electronic structure of radical attached complexes further shows the presence of jellium structures within the core similar to the ligated clusters. Comparison with available experimental and theoretical data also proves the validity of superatomic complex theory for the radical attached clusters as well. Based on the evaluated thermodynamic parameters, selected radical attached clusters are observed to be more thermodynamically stable in comparison with experimentally synthesized ligated clusters. Stabilization of small metal clusters is one of the greatest challenges in current cluster science and the present investigation confirms the fact that radical attached clusters can provide a viable alternative to ligated clusters in the future.

Chapter 6: The activation process of carbon–iodine bond on neutral and cationic niobium metcar its cation is investigated using density functional theory and related computational techniques. Metalcarbohedrenes or metcars are a class of stable metal–carbide clusters of fixed stoichiometry and of great interest to cluster chemists since their first discovery. The detail reaction mechanism along with the overall energy profile of the C–I dissociation reaction on niobium metcar and its cation is presented. The tunneling corrected rate constants and the related reaction parameters like the pre–exponential factor are also included alongside. The major differences between the reaction mechanism of the neutral and cationic metcar is also highlighted. Despite the available experimental results, the carbon–iodine bond dissociation on metcars has mostly remained an unexplored problem in the theoretical and computational domain. Thus, the present investigation can fill in the gap and may also able to provide new insight provoking further developments in cluster chemistry in future.

Chapter 7: A short summary of all the works included within the thesis is presented in this chapter. The possible future prospects of the included works are also discussed.

List of Abbreviations

AIM	**A**toms in **M**olecules
BCC	**B**ody **C**entered **C**ubic
BE	**B**inding **E**nergy
BOMD	**B**orn **O**ppenheimer **M**olecular **D**ynamics
BSSE	**B**asis **S**et **S**uperposition **E**rror
CDA	**C**harge **D**ecomposition **A**nalysis
CFT	**C**rystal **F**ield **T**heory
COM	**C**enter of **M**ass
CSE	**C**luster **S**ize **E**ffects
DFT	**D**ensity **F**unctional **T**heory
DOS	**D**ensity **O**f **S**tates
EA	**E**lectron **A**ffinity
FC	**F**ace **C**entered
FCC	**F**ace **C**entered **C**ubic
GGA	**G**eneralized **G**radient **A**pproximation
GIAO	**G**auge **I**ndependent **A**tomic **O**rbital
HCP	**H**exagonal **C**lose **P**acking
HEG	**H**omogeneous **E**lectron **G**as
HPA	**H**irshfeld **P**opulation **A**nalysis
IE	**I**onization **E**nergy
IP	**I**onization **P**otential
IRC	**I**ntrinsic **R**eaction **C**oordinate
LDA	**L**iquid **D**rop **A**pproximation
LDF	**L**ondon **D**ispersion **F**orce
LDM	**L**iquid **D**rop **M**odel
LJ	**L**ennerd **J**ones
MEP	**M**inimum **E**nergy **P**ath
MIC	**M**ultilayered **I**cosahedral
MO	**M**olecular **O**rbitals
NBO	**N**atural **B**ond **O**rbitals
NICS	**N**ucleus **I**ndependent **C**hemical **S**hift
NMST	**N**uclear **M**agnetic **S**hielding **T**ensor
NPFM	**N**o **P**air **F**erromagnetic **B**onding
PDOS	**P**artial **D**ensity of **S**tates
QSE	**Q**uantum **S**ize **E**ffects
RDG	**R**educed **D**ensity **G**radient
SCA	**S**pherical **C**luster **A**pproximation
SSCM	**S**imple **S**pherical **C**luster **M**odel
STM	**S**canning **T**unneling **M**icroscopy
vdW	**v**an **d**er **W**aals
VTZ	**v**alence **T**riple **Z**eta

Physical Constants

Speed of Light	$c = 2.997\,924\,58 \times 10^{8}\,\mathrm{m\,s^{-1}}$ (exact)
Elementary charge	$e = 1.602\,176\,565 \times 10^{-19}\,\mathrm{C}$
Planck's constant	$h = 6.626\,069\,57 \times 10^{-34}\,\mathrm{J\,s}$
Reduced Planck's constant	$\hbar = 1.054\,571\,726 \times 10^{-34}\,\mathrm{J\,s}$
Boltzmann's constant	$k = 1.380\,648\,8 \times 10^{-23}\,\mathrm{J\,K^{-1}}$
Avogadro's constant	$N_A = 6.022\,141\,29 \times 10^{23}\,\mathrm{mol^{-1}}$
Gas constant	$R = 8.314\,462\,1\,\mathrm{J\,K^{-1}\,mol^{-1}}$
Faraday's constant	$F = 9.648\,533\,65 \times 10^{4}\,\mathrm{C\,mol^{-1}}$
Mass of electron	$m_e = 9.109\,382\,91 \times 10^{-31}\,\mathrm{kg}$
Mass of proton	$m_p = 1.672\,621\,777 \times 10^{-27}\,\mathrm{kg}$
Mass of neutron	$m_n = 1.674\,927\,351 \times 10^{-27}\,\mathrm{kg}$
Atomic mass constant	$m_u = 1.660\,538\,921 \times 10^{-27}\,\mathrm{kg}$
Bohr magneton	$\mu_B = 9.274\,009\,68 \times 10^{-24}\,\mathrm{J\,T^{-1}}$
Bohr radius	$a_0 = 5.291\,772\,109 \times 10^{-11}\,\mathrm{m}$
Rydberg constant	$R_\infty = 1.097\,373\,157 \times 10^{5}\,\mathrm{cm^{-1}}$
Fine structure constant	$\alpha = 7.297\,352\,569\,8 \times 10^{-3}$
Second radiation constant	$c_2 = 11.438\,777\,0 \times 10^{-2}\,\mathrm{m\,K}$
Stefan–Boltzmann constant	$\sigma = 5.670\,373 \times 10^{-8}\,\mathrm{W\,m^{-2}\,K^{-4}}$
Standard acceleration of free fall	$g = 9.806\,65\,\mathrm{m\,s^{-2}}$
Gravitational constant	$G = 6.673\,84 \times 10^{-11}\,\mathrm{N\,m^{2}\,kg^{-2}}$

"*One of the greatest features of science is that it doesn't matter where you were born, and it doesn't matter what the belief systems of your parents might have been: If you perform the same experiment that someone else did, at a different time and place, you'll get the same result. When different experiments give you the same result, it is no longer subject to your opinion. That's the good thing about science: It's true whether or not you believe in it. That's why it works.*"

Neil deGrasse Tyson

Chapter 1

A Preface to Cluster Chemistry

1.1 Introduction

On the trail of evolution, intelligence is a rare commodity seldom achieved by individual species as a result of unpredictable genetic modifications. Among the extensive biodiversity found in our home planet, the humans are among the few, fortunate enough to possess this trait in order to not only comprehend the universe around them but also capable to reshape it in accordance to their necessities. In this eternal quest of mankind versus nature, the humans have been successfully utilized the available natural resources to their benefits since the first representative of extant human walked on the surface of the earth. Considering this aspect it can be argued, if not straight–away discarded, that the voyage of material science has began few billion years ago from the unknown corner of a dimly lit cave. However, despite the obscure origin, there is certainly no denial about the impact and influence of modern material science in shaping our day to day lifestyle of the 21^{st} century. Especially, the present time can be considered as the absolute pinnacle of material science, an achievement which would seem to be a far cry even just five decades ago. The major credit to this accomplishment is certainly be attributed to the recent innovation of new state–of–the–art experimental technique with better precision and control over the test subject. The rapid progress in the high performance computing systems and advanced electronics in the past years also have aided adequately in this revolution. Due to the widespread variation of material science, choosing a particular field of preference is surely no easy task. However, it can be said with enough assurance that to a novice scout, few topic that can be more intriguing than that of cluster chemistry. In the common language of chemistry, a *'Cluster'* is defined as a collection of atoms or molecules which are intermediate in size between atoms or molecules and the bulk solids. As clusters represents very small fraction of the total number of atoms which can be considered negligible for a bulk solid, their properties usually widely differ than that of a bulk material. From an alternative perspective, a cluster can also be viewed as a collection of atoms where the electrons are confined in a shallow potential well, resulting in discrete energy levels rather than the continuous band structure. It is needless to say that both this viewpoints are interrelated and collectively define the properties of a cluster. The unique characteristics of the cluster is the sole reason of their worth and allure to material chemists. By investigating the properties of clusters, an actuated scientific mind can scavenge crucial information about the growth of bulk matter from the unit of atom. Moreover, quantitative studies on cluster may guide us to design new materials with unique properties which may eventually aid in the real life problems. Let us clarify this statement by citing few fascinating examples from popular literature. As we all know that the all the material known to mankind are composed of atoms as assigned in the periodic table. A lesser known fact is that not all element can be mixed with another element in the bulk phase. A prominent example of this kind is that the miscibility of alkali metal with aluminum. Even in molten state the miscibility of potassium metal with molten aluminum is $10^{-4}\%$.[1] Thus, the property as well as the possible potential of a binary metal composed of aluminum and potassium is totally unknown to

us. However, in cluster state, a single potassium or more can easily be doped into an aluminum cluster resulting in new moieties with indefinite possibilities. As a second example, the *'f'* block element gold is infamous for its inertness in bulk state and a honored member of the class of noble metals. However, in cluster state, gold is observed to be exceptionally reactive and can even catalyze complex reaction like cross–coupling[2,3] which in bulk state is only possible on specific transition metals. Due to the presence of discrete electronic shells, specific clusters also known to have striking resemblance with the properties of atoms.[4–8] Thus, clusters can provide an alternative basis of artificially tailored materials with innovative applications.

Up to this point, it is expected that we have convinced ourselves about the importance and impact of cluster chemistry in modern material world. Before exploring further, it will be wise to clarify few arguments which often baffle newcomers in this particular research field. Based on the definition cited earlier, one of the most popular question which can be raised is about the fundamental difference of atomic clusters with molecules or nanoparticles.[1] The question is a legitimate one because both molecules and nanoparticles are also just aggregates of atoms similar to the atomic clusters. The differences with molecules are obvious and is summarized in Table 1.1. However, citing the differences with nanoparticles is certainly tricky, if not downright

TABLE 1.1: Major difference between molecules and clusters

Topic	Molecules	Clusters
Origin	Naturally available and abundant.	Majority are synthesized artificially.
Stability	Usually stable in ambient condition.	Highly reactive, stable in inert of near vacuum condition.
Interaction	Weakly interact with each other.	Weak or strong interaction depending the nature of the cluster.
Size and Composition	Composition and size are fixed	Variable composition and size.
Isomers	Number of isomers are limited.	Large number of possible isomer.
Coalescence	No tendency to coalesce.	Metastable, therefore have high tendency to coalesce.
Nature of Bonding	Bonding is either covalent or ionic.	Variable bonding types: vdW, metallic, ionic or covalent.

impossible. The major reason is that in the early stage of development, both research fields of cluster and small particles (the term 'nanoscience' was still not a fashionable scientific term) were widely different. Clusters were usually smaller than 1 nm, whereas, nanoparticles were much larger in size($>$ 10 nm). However, with the technological progress this difference has now been reduced, nanoparticles with size lower than few nanometers or atomic cluster containing few thousand atoms can now easily be synthesized. Hence, considering the present scenario, a more convenient way to define an atomic cluster is,

" An aggregates of atoms whose size and composition is exactly known and whose change of properties can be studied (by experimental or theoretical methods) one atom at a time"

In simpler terms, if an atomic aggregates is composed of countable number of atoms and the change of the properties is significant upon addition or reduction of a single atom, it is called a cluster. Beyond a particular size scale it becomes difficult to determine the exact composition also the change in the properties becomes less drastic upon addition or subtraction of a single atom. From this size range onward, the aggregates are addressed as nanoparticle. So, the definition is a variable one, with the advancement in the experimental precision and measurement techniques, larger sized nanoparticles may eventually be considered as clusters. Thus, in modern literature clusters are often refereed as 'nanoclusters' irrespective of their sizes, just to recollect this firm connection between the two research fields.

1.2 A Link to the Past

Like the enticing properties and potential of atomic clusters, the antiquity of the research field is not less exciting. Although the major development in the field may have started just 30-40 years ago, the term 'Cluster' was often used in scientific contents. The oldest reference to clusters probably have been made by the famous Robert W. Boyle (FRS) in 1661. In the proposition II of his famous book 'The Sceptical Chymist: or Chymico-Physical Doubts & Paradoxes' he has mentioned,[9]

"Neither is it impossible that of these minute particles divers of the smallest and neighbouring ones were here and there associated into minute masses or clusters, and did by their coalitions constitute great store of such little primary concretions or masses as were not easily dissipable into such particles as composed them."

In simple words, that it is not impossible to combine atoms to forms clusters which will be stabler than the atoms itself and will not easily dissociate into constituent atoms. However, first experimental investigation of clusters in modern science was never began before Eduard Zintl's studies on Zintl phases[10] within the period 1930–1940's. Zintl phases (A term first coined by Fritz Laves in 1941) are a variation of stable inter metallic clusters usually diamagnetic or have temperature independent paramagnetism. However, The term 'Cluster' was probably first used in modern context by the eminent American inorganic chemist Frank A. Cotton in the 1960's to describe compounds containing intermetallic bonds.[11] The existence of geometric magic numbers due to icosahedral close packing in inert gas clusters was first reported by Recknagel et al. at the end of 1981.[12] Despite these noteworthy mentions, two discoveries, occurred almost simultaneously in two consecutive years is considered as the foundation of current cluster chemistry. The first one is the observation of the abundance spectra in alkali metal clusters by W.D. Knight and coworkers in the year 1984.[13] In that paper, for the first time it was observed that closed shell metal clusters are more stable than the open shell ones, resulting in variable abundance in the mass spectra. The relative stabilities and related properties were also explained by invoking the jellium model, which is still considered as one of the fundamental models for predicting the properties of metal clusters. The second innovation is the discovery and the prediction of the weird structure of the well known C_{60} molecule by Kroto , Heath, O'Brien, Curl, and Smalley at Rice University in 1985.[14] Although, it must be mentioned that the structure of C_{60} was already been predicted theoretically by Japanese computational chemists Eiji Osawa in 1970, during his search for an possible superaromatic molecule.[15,16] However, during the experimental discovery it was still unknown as the paper by Osawa was published in Japanese journal (Kagaku) rather than a international peer reviewed one. Despite the innovation of C_{60} in 1984, the first conformation of the structure was achieved five years later (1990) when W. Krätschmer and his coworkers first discovered a bulk synthesis method of C_{60} from carbon soot.[17] The natural occurrence of fullerenes in 'Shungite' ore was discovered two years later in 1992.[18] In 1994, fullerences were found in the fragment of 'Allende' meteorite (Mexico, 1969).[19,20] As of latest, in 2010, C_{60} and higher fullerenes were proven to exists in planetary nebula.[21] The year 1992, is also famous for the innovation of dual tetrahedral cluster Ti_8C_{12} by Castleman and coworkers.[22] The Ti_8C_{12} cluster is an honorable member of a new class of stable clusters of same stochiometry, commonly abbreviated as metcars.[23,24] Beside fullerenes, metcars are the only carbon containing network clusters which are relatively stable, although the process to synthesize them in bulk amount is still unknown. In the first decade of the present 21^{st} century, Castleman, Khanna and coworkers had discovered that specific clusters can behave like atoms based on their jellium shell structure.[4–8] Thus, clusters can be considered as an alternative building blocks of materials aside from atoms and hence, they constitutes a new dimension of the periodic table of elements.

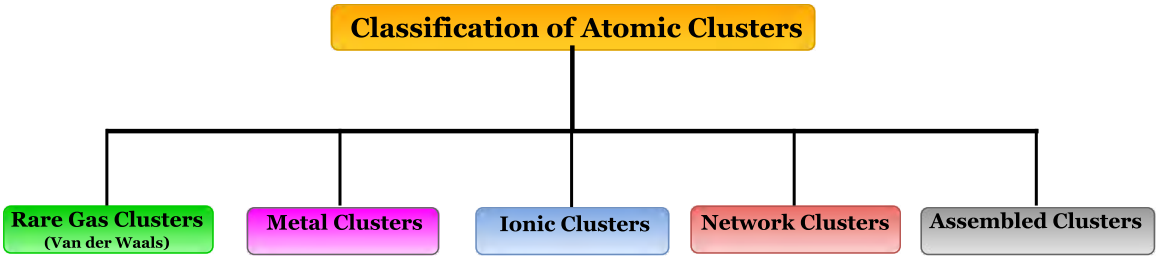

FIGURE 1.1: A schematic of five common classes of atomic clusters.

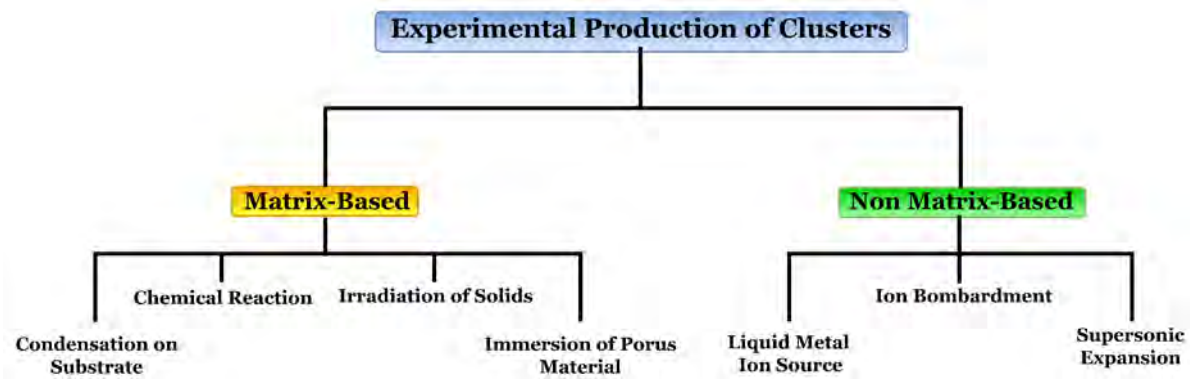

FIGURE 1.2: A list of Matrix and Non–Matrix based cluster synthesis methods.

1.3 Classification of Atomic Clusters

Due to the wide variation in the properties of atomic clusters it is often difficult to properly classify the clusters into separate categories. Moreover, the classifications available in the current literature are often biased by the research interest and the personal preferences of the author(s). Therefore, In this thesis, we have decided to include a classification (Figure 1.1) solely based on our personal choice and which are relevant for this thesis. Although the classification are based on our personal liking, we have ensured that the listed classes are general enough to provide the readers a flavor of overall variations in the cluster chemistry. The examples cited here are mostly taken from abundant literature and can be considered as simplest examples available for the specific kind.

a. Rare Gas Clusters: If rare gases like He, Ne, Ar etc are cooled enough to very low temperatures, they can combine with each other and forms clusters. Due the filled octet structure, the dominant attractive forces in rare gas clusters are mainly weak short range dispersion force (van der Waals) countered by short range quantum mechanical repulsive force due to the atomic cores. The binding energies are certainly low ($\sim$ 0.3-0.5 eV/atom). The stability of these clusters solely depends on geometrical close packing rather that of electronic origin. As a common observation it has been found that clusters with close packed icosahedral structure is stabler than the others. As the interacting force within the clusters can easily be modeled by two particle forces, van der Waals clusters are of interest for classical dynamics simulations or in the phase transition problems. Few rare research fields includes superfluidity and quantum effects. Most common examples are He_N, Ne_N, Rn_N etc. Closed shell molecular clusters like $(I_2)_N$, $(SF_6)_N$, $(N_2)_N$ also belongs to this category.

b. Metal Clusters: The family of metal clusters are probably the most extensive classes of atomic clusters known to chemists till date. A major portion of the present thesis is also focused on these type of clusters. The metal clusters can further be subdivided in subcategories based on the type of metals by which they are composed of. Thus, cluster consists of alkali metals(Group 1), alkaline earth(Group 2),coinage metals(Group 11) and transition metal atoms each forms separate subcategories with variable properties. In addition to that, bimetallic clusters(composed with two different type of metal atoms) and other 's' and 'p' block metals (like Al) are also part of this category. The properties and stabilities of simple metal clusters can be explained by the famous jellium model, however, the situation is far more complicated for more complex clusters and new models fro reproducing their behavior is still under development. Although modeling metallic bonding is a difficult task as they can not be simplified by two body potential. Hence, modeling this type of clusters is extremely difficult considering the classical picture. In the quantum reign, although advanced algorithm for optimization and dynamics are available, due to higher computational cost they cannot be utilized to investigate the properties of larger clusters. Related investigations like the phase transition of different type of metal clusters, catalysis and magnetic properties of 'd' block clusters are still popular among the material chemists.

c. Ionic Clusters: Ionic clusters are usually formed when two type of elements with large electronegativity differences are combined to form a cluster. Ionic cluster can be synthesized combining an electropositive element from the left side of the periodic table with an electronegative element of the right hand side. The overall stability of the cluster is due to the attractive electrostatic interaction between the counter–ions. The presence of a short range repulsion in between the ionic core is also observed. The strong Coulombic attraction is the sole reason

for high binding energy of these type of clusters($\sim$ 3–4 eV/atom). The shape of these clusters shows high resemblance with bulk materials or alloys. The clusters can be considered as small cubic or rectangular units of the bulk solids. Common examples of this kinds are $[Na_mCl_n]^{(m-n)+}$,$[Mg_mO_n]^{2(m-n)+}$.

d. Network Clusters: Elements with predominant covalent character like C,Si and Ge forms this type of clusters. The bonding within the atoms in this clusters are predominantly covalent and directional. The binding energies are also strong within $\sim$ 1–4 eV/atom. The elements like Si and Ge are semiconductors in bulk state. Hence, some variation of network clusters are also often addressed as semiconductor clusters. The most prominent example of network cluster is the family of fullerenes where each carbon is 'sp^2' hybridized. The cluster of Si are also well studied. However, unlike fullerenes, they do not form cage like structures and hence the ground state structure of Si clusters usually widely differ than of carbon clusters. Another interesting example of this kind is the family of metcar which are formed by combining carbon with early 'd' block transition elements.

e. Assembled Clusters: Composing new stable materials by combining atomic clusters is one of the recent research topic to cluster chemists. The last category is solely devoted to this type of materials which are composed of clusters. As the field is of recent interest and due to the technical difficulties of assembling clusters by keeping its identity intact, such examples are extremely rare as by now. One of the most prominent example of this kind is the fullerite solid ($[C_{60}]_N$, which is composed of C_{60} units.[25] Other possible candidates to synthesize cluster assembled solids are Al_{13}^- or $Al_{12}X$, where 'X' is a group 14 element which were studied extensively. Although, no stable bulk solids is still reported experimentally.

1.4 Experimental Production of Atomic Clusters

Throughout the past three–four decades, there has been an enormous progress in the field of synthetic chemistry. As an obvious consequence, artificial synthesis methods of atomic clusters have now grown quite a vast almost beyond comprehension. Therefore, it is nearly impossible(also beyond the scope of the present thesis) to include all of the latest developments and their associated details in this present thesis. However, for the sake of the readers, we have included few important methods along with examples taken from the abundant literature. In a broader sense, the methods to synthesize cluster can be classified into two sub–categories, matrix and non–matrix based methods. In matrix based methods clusters are synthesized in solvents or inert materials, which often prevent embedded clusters from coalescence and protect from reacting with impurities and active substances present in the vicinity. The non–matrix methods consist of synthesize clusters in the gas phase. Due to the high reactivity, gas phase synthesis of clusters are usually done in inert or near vacuum atmosphere using high purity source material.

1.4.1 Matrix Based Methods

a. Condensation on Substrate: If the metal vapor generated by extreme heating either by laser source or by oven is condensed on a inert substrate like metallic oxide or salt like solid materials, clusters of nano–meter size range is synthesized via aggregation. Use of a scanning tunneling microscope (STM) provides further control over the cluster arrangement on the substrate and well organized array of nano–clusters can be synthesized by this way. Thin films decorated

with cluster nano–fabrication has also been synthesized. Further complex micro–structures can also be synthesized by direct condensation of cluster beams on the substrate instead of atoms. The resulting materials may have important application in nano–electronics and semiconductor industries.

b. Chemical Reaction: Synthesizing clusters by chemical reactions is probably the oldest method available to cluster chemists. Stable clusters with size ranging from 1–50 nm can be synthesized by chemical reaction. The process may vary from simple precipitation,hydrolysis, reduction even thermal decomposition. As for example, mono–dispersed cobalt clusters can be synthesized by the thermal decomposition of $Co_2(CO)_8$ as the following,

$$Co_2(CO)_8 \longrightarrow 2\,Co + 8\,CO \tag{1.1}$$

Using surfactants and stabilizing materials one can control the growth of cluster and also can protect the clusters against oxidation. Gold clusters can be synthesized by reducing solution of gold salts with dispersed reducing agent like sodium,

$$Na + AuSR \longrightarrow NaSR + Au \tag{1.2}$$

where 'S' is sulfur atom and 'R' is alkyl group. Ligated gold clusters can be synthesized from AuSR using excess RSSR as the following,

$$N(AuSR) \longrightarrow Au_N(SR)_M \tag{1.3}$$

where usually $N \geq M$. Similarly, ligated aluminum clusters like $Al_4(Cp^*)_4$ [Cp^* = C_5Me_5] is prepared reacting $MgCp^*{}_2$ with dissolved AlCl solution resulting in very high yield of the complex ~ 90 %,

$$4\,AlCl + 4\,[MgCp^*{}_2] \xrightarrow[Et_2O]{\text{toluene}} [Al_4Cp^*{}_4] + 2\,[mgClCp^*(OEt_2)]_2 \tag{1.4}$$

Another alternative method for synthesizing the same complex via reductive dehalogenation is given below,

$$2\,Al_2Cl_6 \xrightarrow[-ClSiMe_3]{Cp^*SiMe_3} 2\,[AlCl_2Cp^*{}_2] \xrightarrow{K} [Al_4Cp^*{}_4] \tag{1.5}$$

c. Irradiation of Solids: Aggregation of atoms can also be generated if beam of high energy particles being bombarded on well ordered crystal lattices. As for example, lithium clusters of variable size can be formed if crystal lattices of LiF or Li_2O being bombarded with high energy neutron particle. Impure or mixed clusters can also be synthesized via the same way by using lattice of metal alloys or by mixing two separate metals in an inert substrate followed by irradiation. Tweaking the strength and irradiation time, the size and concentration of the generated clusters can be controlled.

d. Immersion of Porous Materials: In this methods aggregates of atoms are synthesized by immersing a specially tailored porous material into the liquid or molten metal followed by the application of very high pressure. Small droplets composed of atoms are formed within the pores of the material which can further be utilized for practical application like catalysis. Some specific glass like materials or zeolites with well defined pore sizes are usually used for this purpose. By controlling the pore sizes and the applied pressure, cluster of various size ranges can be synthesized.

1.4.2 Non–Matrix Based Methods

a. Liquid Metal Ion Source: The Liquid Metal Ion Source method is suitable for synthesizing clusters of metals with very low melting point. In this methodology first the metal is distilled out from the source via differential heating and passed into a preheated tungsten capillary tube within which the metal remains in liquid form. Using a very high potential difference ($\sim$ 2 kV) between the capillary tube and an extraction electrode, metal cluster ions with different size ranges are synthesized. Few electrostatic lenses were used around the direction of flow to collimate the cluster ions. Single as well as multiple charged clusters can be synthesized via this method.

b. Ion Bombardment: When a steady stream of inert gas ions (e.g Xe^+) is bombarded on a solid surface with very high kinetic energy (e.g $\geq$ 11 eV), Sputtering of clusters ions is observed by the impact. The ion beam is focused onto a very small spot of the solid surface which is of 1–2 mm by diameter. The method is relatively cheap and clusters of noble gases, transition elements and ionic materials can be synthesized by this way. The method is also suitable for the generation of clusters of solids with high melting point. Detailed studies have proven that the generation of clusters stream is due to the spontaneous collision chain initiated by a single bombarded ions. Although argument exists whether the formation of cluster is the result of the fragmentation of lattice sites or an outcome of the statistical reorganization of independently ejected free atoms due to ion bombardment.

c. Supersonic Expansion: The supersonic expansion methods is one of the mode widely used non–matrix based methods for cluster synthesis in gas phase. In the procedure the metal source is vaporized via heating in an oven or by laser irradiation. The resulting vapor with a pressure ranging from 10^3 to 10^5 Pa is mixed with a stream of inert carrier gas (e.g He, Ne, Ar) which is kept in an stagnant high pressure (P_0) of 10^5 to 10^6 Pa and high temperature (T_0) of 100-1500 K. The metal and inert carrier gas mixture then suddenly expanded through a very small orifice(nozzle) of radius (r) 0.015–0.5 mm into vacuum (10^{-1}–10^{-3} Pa). The resulting adiabatic supersonic expansion cools the gas mixture and clusters are formed with variable sizes as the expanded gas become supersaturated with the atoms. The production of clusters usually terminated within few nozzle diameter from the orifice as the vapor gets less dense. It is observed that the formation of clusters occurs within the nozzle as well as at the outside region. However, the factor can be controlled via the parameter P_0r. For a low value of P_0r , more numbers of clusters will form in the inner region of the nozzle and beyond a particular threshold value, each increment of P_0r will result increase in the formation rate of the clusters in the outer region of the expansion nozzle. In a similar fashion the average size range of the produced clusters can also be controlled by regulating P_0, T_0 and A, the cross section of the nozzle aperture. The average size of cluster increases with increasing P_0 and A, whereas high temperature favors small sized clusters. The use of carrier gases is not essential. Synthesis of molecular and inert gas clusters including cluster composed of metals with very low melting point has been achieved without the aid of any carrier gases. For van der Waals clusters low temperature (below room temperature) is needed for cluster condensation.

1.5 The Rules of Stabilization

Up to this point of the discussion, it is apparent that atomic clusters are a separate class of material much different from either atoms, molecules or even bulk solids. However, the dissimilarities of the properties of atomic clusters with these well known materials do not end there.

One of the fundamental differences lies within is the stability of individual clusters when compared with the rest of the series. Due to their metastable nature, atomic cluster obeys some stabilization rules which is uncommon in molecules or bulk metals.The stabilization principle depending on various factor like the composition, bonding, electron density distribution of the cluster, which of course differs from one cluster series to another. If carefully observed, it can be seen that each series of cluster types have their unique way of stabilization. However, despite the variation, two major factors which plays dominant role in the stabilization process, is primarily of two different origin, geometric and electronic. In this section we will take a brief look on this two stabilization factors and their influences on the stabilities and other related properties of relevant clusters.

1.5.1 The Geometric Shell Effect

Among the wide variation within the cluster family, the geometric stabilization is predominantly important for clusters composed of noble(rare) gases. Due to the filled octet, nobel gas clusters cannot achieve electronic stabilization via molecular orbital (MO) formation. The situation can easily be illustrated by only considering the situation for the simplest noble element,i.e. the Helium(He) gas. The 'He' atom has a closed shell $1s^2$ configuration. Hence in the diatomic species, He_2, two electrons will occupy the bonding σ_g MO and the rest two will be placed in the antibonding σ_u^* orbital resulting no net gain in the overall stabilization of the cluster. Thus, the only binding interaction present in rare gas clusters are non covalent van der Waals(vdW) interactions, the primary contribution in which is the long range attractive London dispersion forces (LDF). The London attractive interaction arises from the random fluctuation of the electron density within the atom resulting in instantaneous dipolar and multipolar interactions among the local neighbors. The LDF is the weakest attractive interactions when compared with other two attractive vdW forces namely, Keesom (dipole–dipole) and Debye (dipole–induced dipole) interactions. All this three contributing forces varies with the inverse sixth power of the distance. In a summarized way the vdW interaction energy between an asymmetric pair A and B can be represented as,

$$V_{vdW} = -\frac{A_{vdW}}{r^6} = -\frac{A_L + A_D + A_K}{r^6} \tag{1.6}$$

Upon expanding the terms,

$$V_{vdW} = -\left[\frac{1}{(4\pi\varepsilon_0)^2 r^6}\right]\left[\frac{3}{2}\frac{I_A I_B \alpha_A \alpha_B}{I_A + I_B} + \frac{\mu_A^2 \mu_B^2}{3k_b T} + (\mu_A^2 \alpha_B + \mu_B^2 \alpha_A)\right] \tag{1.7}$$

where, α ,μ are respectively the polarizabilities and dipole moment of the two species, I is the ionization potential and ε_0 is the permittivity of the vacuum. Other terms have their usual significance. If we also consider the higher order contribution, the overall dispersion energy can be expressed as a series,

$$V_{disp} = -\left[\frac{A_{vdW}}{r^6} + \frac{A_2}{r^8} + \frac{A_3}{r^{10}} + ...\right] \tag{1.8}$$

However, as the higher order terms are usually very low in magnitude in comparison with the vdW term, usually the series is truncated after the first term for the sake of simplicity. Therefore, the V_{disp} term essentially reduces to,

$$V_{disp} = V_{vdW} = -\frac{A_{vdW}}{r^6} \tag{1.9}$$

Apart from the long range dispersion attraction there exists short range repulsive interaction between two atoms. The repulsion arises from two major factors, first is the electrostatic repulsion between two closely placed nuclei, second is the Coulombic repulsion in between the electron density of two atoms. In addition to that there is also Pauli repulsion in between the electron with same spins. All these repulsive interactions can be modeled by a $\frac{1}{r^n}$ dependent repulsive potential, where n is generally set to 12. (It is important to mention that later improvements has proven that an exponential dependence $exp^{-\alpha r}$, known as the Buckingham potential represents the repulsive interaction more accurately). Combination of the attractive dispersion term deduced earlier and this short range repulsion term generates the popular 6–12 model potential or Lennard–Jones (LJ) pair potential,[26]

$$V_{LJ} = 4\varepsilon\left[\left(\frac{\sigma}{r}\right)^{12} - \left(\frac{\sigma}{r}\right)^{6}\right] = \varepsilon\left[\left(\frac{r_0}{r}\right)^{12} - 2\left(\frac{r_0}{r}\right)^{6}\right] \tag{1.10}$$

where ε is the depth of the potential well, σ is the distance where inter–particle potential is zero, r is the distance between the two species and $r_0(=2^{\frac{1}{6}}\sigma)$ is the equilibrium inter–nuclear distance. Although for bigger clusters simple two body potential is not sufficient, since many body interactions within the neighbors becomes more significant with cluster growth, however, it is observed that even for a large cluster the many body contribution is found to be less significant ($\leq$ 8–10% of total lattice energy). For this reason, two body pair potential is still widely used for the determination of the global minimum structure of inert gas clusters.

As the major interaction forces in noble gas clusters is primarily two body interactions, therefore noble gas clusters are essentially stabilized by maximizing their near neighbor contacts resulting in closely packed structures with high cluster binding energy (B.E). Thus ground state structure of pristine inert gas clusters with 3 atoms (n=3) is found to be equilateral triangle, n=4 is tetrahedral and so on. The larger structures are formed by combining tetrahedral units in a compact manner, a pattern which is commonly known as the polytetrahedral growth. Thus for n=7, the global minimum is pentagonal bipyramind (five tetrahedral unit) and the structure for n=13 is the famous icosahedra, where 20 tetrahedral units share a common vertex at the very center of the cluster. It is crucial to mention that, the icosahedral structure is one of the member of the platonic solids family, a collection of structures which are known to be naturally abundant and favored. According to the scientific definition, ***'a platonic solid is a regular, convex polyhedron constructed by congruent regular polygons such a way that the number of faces converged to each vertex remains the same.'*** The platonic solids are known since antiquity due to their highly symmetric structure and mathematical interpretations. The curved stone balls of Scotland which made by Neolithic people (2000 B.C) shows high resemblance with the five platonic solids. Ancient Greek philosopher Plato, in his dialogue Timaeus(360 B.C), had postulated the platonic solids as the shape of five fundamental elements of nature namely, earth, air, water, fire and ether. Figure 1.3 depicts the five platonic solids with associated details included in Table 1.2. Although the platonic solids are observed to be structurally different, all five can be related via a simple mathematical equation known as the Euler's rule for convex polyhedra,

$$V - E + F = 2 \tag{1.11}$$

where V,E and F are respectively the number of vertices, edges and faces of the associated platonic solids (Table 1.2). Each solids is observed to obey further two common relations which can be verified from Table 1.2 ,

$$\begin{aligned} pF &= 2E \\ qV &= 2E \end{aligned} \tag{1.12}$$

where p is the number of sides of each face, and q is the number of edges meeting at each

TABLE 1.2: The Geometrical Details of the Five Platonic Solids

Platonic Solids	Schläfli symbol {p,q}	V	E	F	Point Group
Tetrahedron	{3,3}	4	6	4	T_d
Octahedron	{3,4}	6	12	8	O_h
Hexahedron	{4,3}	8	12	6	O_h
Icosahedron	{3,5}	12	30	20	I_h
Dodecahedron	{5,3}	20	30	12	I_h

vertex. These two parameters is cumulatively represented by Schläfli symbol({p,q}) presented in the second column of Table 1.2. If we now substitute the value of F = $\frac{2E}{p}$ and V = $\frac{2E}{q}$ obtained from equation 1.6 in equation 1.7 , resulting,

$$\frac{1}{p}+\frac{1}{q}=\frac{1}{E}+\frac{1}{2} \tag{1.13}$$

From this equation it is evident that the only possibilities for the {p,q} are (3,3),(3,4),(4,3),(3,5) and (5,3), signifying that only the five platonic solids is physically possible and no others. As mentioned earlier, that all of these five structures are very common in nature and the molecular universe is no different. The tetrahedral arrangement of directional orbitals, cubic crystal (lattice) structures, octahedral organometallic complexes, and dodecahedral shaped C_{20} are among a few common examples. Hence, the icosahedral structure of vdW clusters are no surprise and can be considered as a natural preference just as the others.

The Mackay Icosahedra Series

The unusual stabilities of icosahedral structures compared to others is reflected in the mass spectrum of the clusters. The mass spectrum of xenon clusters (n$\leq$150) studied by Echt and coworkers[12] shows the abundance peaks are not smoothly varied with the size of the clusters. Specific sized clusters show higher abundance peaks than the others, signifying that they are stabler than the rest and denoted as 'magic', an analogy rented from the nuclear chemistry. The primary stability peaks is observed for n=13, 55 and 147. The secondary stability peaks which are somewhat less prominent is also noticed in several other sizes e.g. at n=19, 23, 26, 81, 101 and 135. The primary magic numbers can easily be explained as they corresponds to the number of atoms needed to form icosahedral closed packed structured and can be fitted in a numerical series, commonly called Mackay icosahedra sequence,[27]

$$n_g = 1+\sum_{k=1}^{N}(10k^2+2) \tag{1.14}$$

which can be expanded into,

$$n_g = \frac{1}{3}\left(10N^3+15N^2+11N+3\right) \tag{1.15}$$

First five geometric magic numbers are 13, 55, 147, 309 and 561 for N = 1, 2, 3, 4 and 5 respectively. Each of these numbers signifies the completion of a stable icaosahedric geometrical shell resulting in their high abundance in the mass spectrum. The structures of first five Mackay's

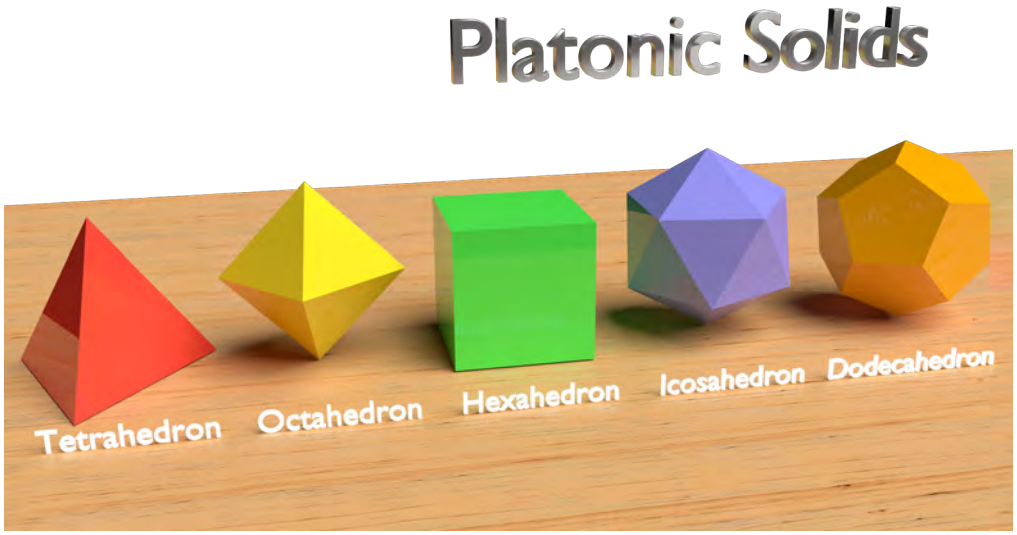

FIGURE 1.3: A simple illustration of the five platonic solids

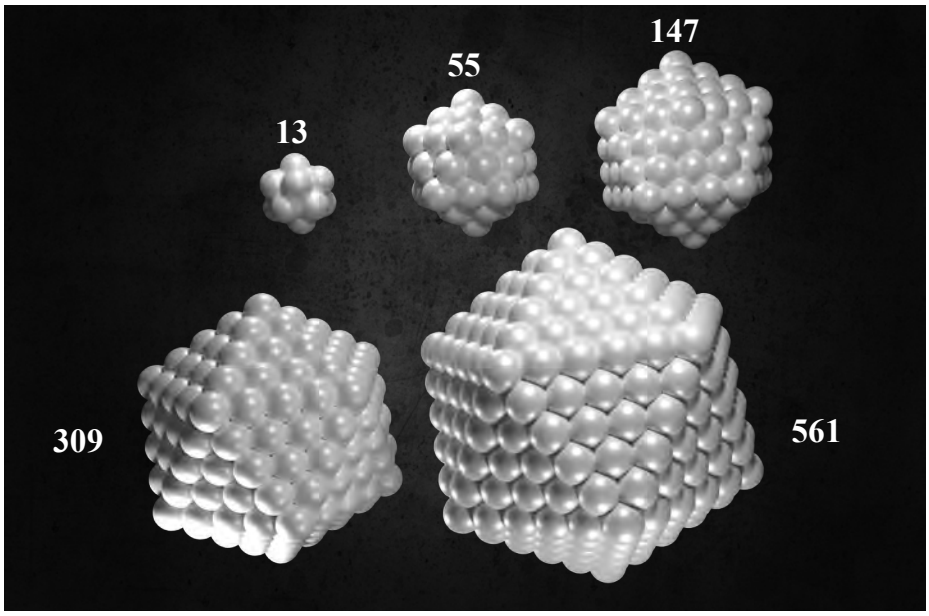

FIGURE 1.4: The first five geometrical shells in accordance to the Mackay icosahedra series.

icosahedra shell is shown in Fig 1.4. The major abundance peaks of bigger inert gas clusters can also be explained in a similar fashion using the same mathematical series.

Explaining the occurrence of secondary stability peaks is not as straight forward as the primary ones. In order to explain the full set of secondary magic numbers it is necessary to understand the growth of inert gas clusters starting from the smaller ones. As depicted in Figure 1.5, the smallest icosahedral cluster n=13 (Ic_{13}) can be decorated in either two possible ways. In the first case, The new atoms are arranged onto the faces(F) and vertices (V) of Ic_{13} skeleton. As Ic13 is composed of 20 triangular faces, 30 edges and 12 vertices (Table 1.2), this type of decoration results in a new cluster containing a subtotal of 45 (13+20+12)atoms. The common nomenclature of this arrangement is called as the anti–Mackay or face centered (FC) packing. In the second type of decoration, the new atoms occupies the vertices (V) and the edges (E) of underlying cluster, generating the next cluster with 55 (13+12+30) atoms, which is nothing but the next icosahedra in accordance to the Mackay series. Therefore, this second type of decoration is known to be multilayered icosahedral (MIC) packing. In the overall growth process of the clusters both of this decoration patterns are always in competition with each other and depending on the size scale and type of the constituent atoms one is usually favored over the other. In the very initial stages of growth, i.e. from Ic_{13} the FC decoration gets more favored than the MIC. The prime reason of that is at this size range, arranging atoms in the FC mode results in the generation of larger number of shorter bonds than in MIC arrangement increasing the stability of the cluster. Considering the FC mode as the preferred way of decoration in the initial stage, the occurrence of the secondary stability peaks can be attributed to a sub–shell closure of the respective cluster. As for example, the Ic_{13} cluster gets slight stability boost when a pentagonal cap consisting six atoms is completed on top of Ic_{13} skeleton resulting a double icosahedra structure (Fig 1.6) with total atom count of 19 (13+6). Adding another four atoms on the adjacent side results in the completion of a second sub–shell with a total atom count 23 (19+4). A third sub–shell is completed at N=26 which is also corresponds to a secondary stability peaks. However, with the increment in the number of completed sub–shell, the internal strain of the cluster predominates and soon at the range of N $\sim$ 27–30, MIC decoration gets favored over the FC. The transition from FC to MIC can be achieve by a reordering of the atoms in the outer shell since both decorations are mutually exclusive. The next set of secondary magic numbers e.g 32, 36, 39, 43, 46 and 49 can similarly be explained considering the sub–shell closure of MIC covering. Thus, considering either FC or MIC as the favored way of decorations for a particular size region, most of the secondary magic numbers can be explained and also theoretically validated.

Although at small size scale the FC and MIC decoration are observed to be competitive in nature, the situation changes for bigger clusters composed of thousands of atoms where FC decoration gets favored over the MIC one. This observation is expected, because although in small scale the icosahedral structure is more stable due to higher number of near neighbor contact, its five fold symmetric structure is totally incompatible to form a close packed periodic bulk crystal lattice. Thus, as the cluster grows larger, it is expected that there must be some critical size, beyond which the atomic arrangement would mimic the bulk lattice arrangement which is incidentally FCC for rare gases. The transition from MIC to FC in the critical size range can also alternatively be viewed from the perspective of simple geometry. The edge or side length (s_{Ic}) of a regular icosahedron is $\sim$5% longer than the radius (r_{Ic}) of the enclosing sphere,

$$s_{Ic} = 1.0514 r_{Ic} \tag{1.16}$$

Therefore, if a perfect icosahedral structure is attempted to be constructed using 13 rigid sphere, although all the spheres on the surface will be in direct contact with the central one but they will not be in contact with each other. Such scenario is certainly destabilizing for the cluster, as we

have already seen that the vdW clusters essentially get stabilized by increasing the number of near neighbor contacts as the principle interaction is two body in nature. In order to achieve the stabilization, the surface atoms usually reduced their contact distances in expense of the radial distance from the center of the icosahedron. This reduction of the radial distances generate a repulsive elastic strain within the core of the icosahedral cluster. For smaller clusters, the gain in the stability due to the lowering of surface energy outweighs the effect of the strain. However, as the cluster grows bigger initially via MIC pathway, after a particular size limit the elastic strain eventually destabilizes the MIC structure compared to the FCC geometries. From that point onward the FC growth pattern is continues till the bulk limit is reached.

1.5.2 The Electronic Shell Effect

Aside from the geometric stabilization, another important contributing factor which controls the stability of an atomic cluster is of electronic in origin. In the early 1980's Knight and coworkers[13,28] observed that in the mass spectrum of alkali metal clusters generated by supersonic expansion, there is some non–monotonic variation of abundance with cluster size. Some specific even numbered clusters e.g. N = 8, 20, 40, 58 and 92, shows higher abundance than the rest of them. The observed stability trend can either results from the occurrence of unknown stable geometries at those specific sizes or may be of electronic origin. However, in depth studies have shown, that those specific 'magic' clusters also have very high ionization energy and low electron affinity compared to the two adjacent clusters (with atom count of N-1 and N+1 respectively) which are 'non–magic' in nature. This observation proves that the primary contributing factor responsible for the unusual stability of these 'magic' alkali metal clusters are certainly electronic in nature, and in order to explain the stability and related phenomena, requirement of a new theoretical model has soon emerged as an absolute priority. In order to explain the anomalous abundance and related properties Knight and coworkers proposed a theoretical model known as the 'jellium shell model'. It is important to mention though, that the jellium shell model was originally developed earlier in order to explain the unusual stability of some specific atomic nuclei as observed during radioactive decay. The scientific term 'magic' which is often used to emphasize unusually stable clusters, is also coined from nuclear chemistry due to its similar analogy. The jellium model including its later modifications are probably the finest theory available to cluster chemists till date and is able to explain the properties and trends of atomic clusters with quantitative prediction upto a respectable level of complexity in the cluster size and composition.

In the spherical jeliium shell model a 'N' atomic metal cluster is considered as an uniform, positively charged ionic sphere surrounded by the free electron gas composed of valence electrons of each metal atoms. In such a picture, the finer structure of the ionic core i.e. the exact location of each atom is totally ignored and the valence electrons are considered as completely free. The core potential is usually replaced by a theoretically modeled weak pseudo–potential, whose lowest eigenstates must corresponds to the valence states of the atomic clusters. The assumption is widely similar with the common picture of an atom (Figure 1.7) and therefore must be compared. In an atom the positively charged nucleus is considered to be stationary at a particular point, hence, the resulting positive charge is zero elsewhere. In a simple mathematical fashion,

$$n_+(r) = n_+^0 \delta(r) \tag{1.17}$$

where, $n_+^0 = Z_A$, i.e. the atomic number and $\delta(r)$ is the delta function which has a value of 1 at the position of nuclei and zero elsewhere. In a similar fashion,the positive charge distribution of the central ionic core can be presented as,

$$n_+(r) = n_+^0 \Theta(R-r) \tag{1.18}$$

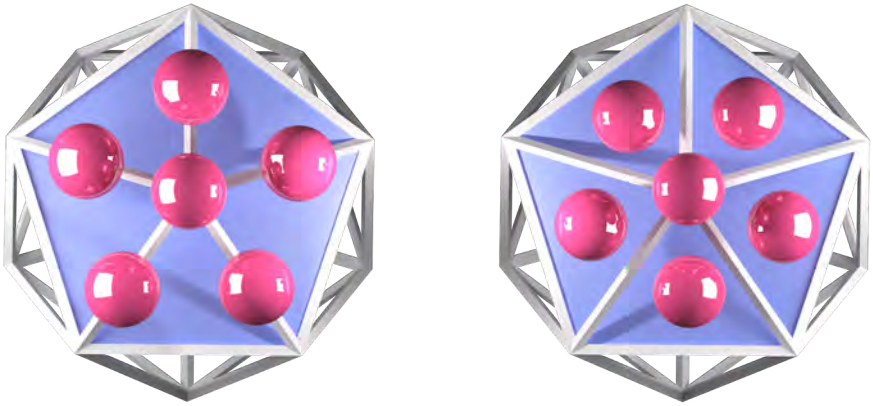

FIGURE 1.5: A depiction of MIC and FC covering of Ic13 skeleton.

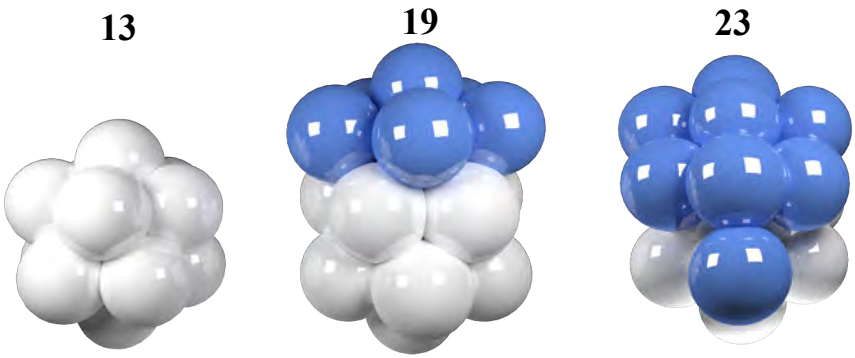

FIGURE 1.6: A simple illustration of the secondary geometric shell closure for n = 19 and n = 23

R is the radius of the ionic sphere, the parameter $\Theta(R-r)$ is essentially a step function, whose value is 1 when r<R and 0 when r>R. The constant n_+^0 is related with the valence number(Z) by the following equation,

$$n_+^0 = \frac{Z}{\Omega} \tag{1.19}$$

where Ω is the mean volume per atom in the bulk metal, .i.e.,

$$\Omega = \frac{4\pi R^3}{3N} = \frac{4\pi r_{ws}^3}{3} \tag{1.20}$$

where r is the Wigner–Seitz radius which is radius of a sphere whose volume is equal to the volume per atom in the bulk solid. The jellium potential can be empirical or effective potential can be generated by *ab initio* methods like Density Functional Theory (DFT) of simple Hatree Fock (HF) method. At this point it is important to mention that the validity of spherical jellium model strictly based on some pre–determined assumptions. Firstly, the model is only valid if the valence electron of a metal cluster is very weakly bound and hence can be considered as free. The central ionic core also must be sensitive to external perturbation. Lastly, but most importantly the spherical approximation of the ionic core and the negligence of the finer structure works well if the cluster is in molten state i.e. there is no well defined three dimensional structure within the core. All of these approximation are found to be well valid for alkali metal clusters and also noble metal (e.g. Cu, Ag and Au) clusters.

Considering the jellium picture, the Schrödinger equation for a single electron which is constrained within the sphere under the influence of the effective potential from the ionic core can be solved. Due to the spherical nature of the jellium potential, the solution of the Schrödinger equation can be separated into radial and angular parts,

$$\psi_{nlm_l}(r,\theta,\phi) = R_{nl}(r).Y_{lm_l}(\theta,\phi) \tag{1.21}$$

Thus, similar to an atom the energy levels of the electrons constrained within a spherically symmetric potential can be characterized by four different quantum numbers,

a. The principle or radial quantum number n, with values 1,2,3 ...

b. The angular moment quantum number l, allowed values of l are 0,1,2,3 ... with no restriction.

c. The magnetic quantum number m_l, from +l to -l including 0, a subtotal of 2l+1 values.

d. The spin quantum number m_s with only two values $+\frac{1}{2}$ and $-\frac{1}{2}$.

It is important to mention that the principle quantum number 'n' in jellium model differs from the principle quantum number (n_a) used in the atomic picture due to its origin from nuclear physics. The two quantum numbers is mutually related as,

$$n = n_a - l \tag{1.22}$$

where l is the angular momentum quantum number. Thus the number of radial nodes in a jellium orbital is also equal to n-l, rather than n_a-l-1 for atomic orbitals.

Solving the Schrödinger equation yields different jellium orbitals similar to the atomic orbitals and also denoted like the same. Thus the n = 1, l = 0, m_l = 0 corresponds to the 1S orbital (use of Uppercase is just to emphasize the difference between jellium and atomic orbitals), n = 2, l = 1, m_l = 0, $\pm$ 1 is the threefold degenerate 2P orbitals. Similarly the energy also increases

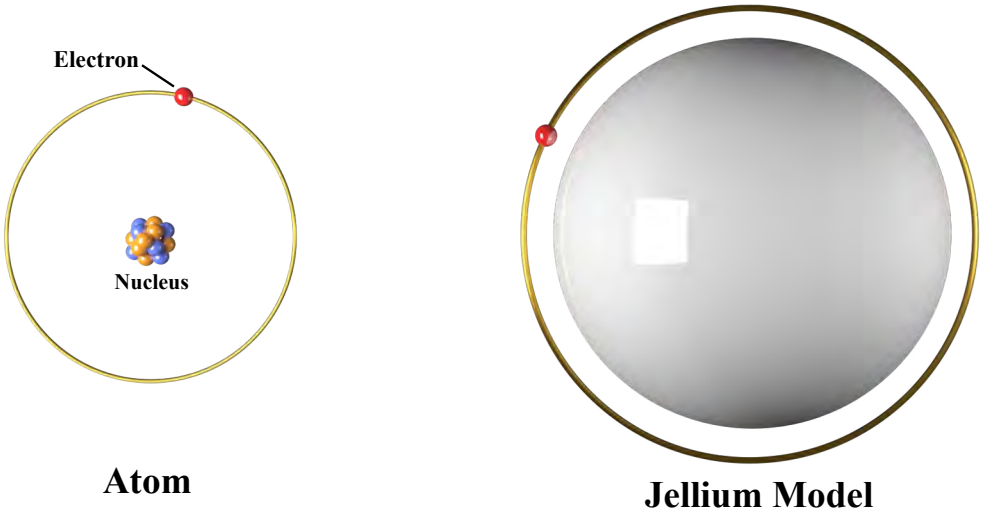

FIGURE 1.7: A pictorial comparison of the classical model of an atom with the jellium picture of clusters.

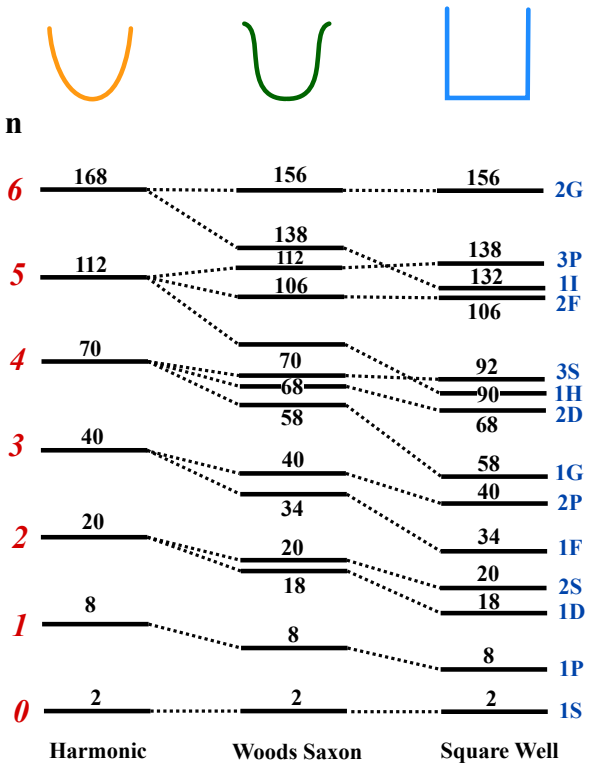

FIGURE 1.8: The relative order of jellium orbitals in three different potential.

with the increment of the principle quantum number n and angular momentum quantum number l, and the orbital degeneracy is also equal to $(2l + 1)$. However, the exact energy ordering of the jellium orbitals are dependent on the radial form of the effective potential. Figure 1.8 includes such an orbital ordering with degeneracy for three commonly used potentials, harmonic, Woods–Saxon and the square well potential. Among all three of them, the most accurate one is the Woods–Saxon potential which is expressed as,

$$V_{WS} = -\frac{V_0}{exp\left[\left(R - R_0\right)/\sigma\right] + 1} \tag{1.23}$$

where R_0 is the radius of the cluster, and σ is a scaling constant with unit of distance (usually 1.5 Bohr. V_0 is the sum of Fermi energy(E_F) and the work function(W_s) of the bulk solid,

$$V_0 = E_F + W_s \tag{1.24}$$

From Fig 1.8, it is evident that the shape of the W.S potential is just the intermediate between harmonic and square well potentials. The orbital energy ordering is also intermediate of the two extremities. Both the W–S and the square well potential shows similar orbital ordering upto 2D jellium orbital. The discrepancy between the two models starts to be pronounced after 68 jellium electrons.

The Prediction of the Jellium Model

Until now, we were discussing the fundamental concepts and theoretical development of the spherical jellium shell model. In this subsection we will attempt to demystify the abundance spectrum and stability trend of the metal clusters in the light of the spherical jellium model. Explanation of the experimentally observed trend of few other associated properties will also be discussed. Before continuing the discussion regarding the metal cluster and the jellium model, as both atomic and jellium model are nearly similar by principle, let us first focus on the atomic picture and the stability trend observed therein. In the atomic world, it is well known the atoms with filled shell (octet) such as noble gases are the most stable ones compared to the rest in the periodic table. The unusual stabilization of these atoms are due to the pairing of electrons which lowers the energy of the highest filled shell resulting in large energy gaps between the filled shell and the lowest unoccupied atomic orbital. Due to the enhanced stabilization, the noble gases also have very high ionization energy and low electron affinity due to the filled octet. In a similar manner the stability trend of metal cluster can be explained with the help of jellium model. The metal clusters with filled shell are more stable and therefore show high abundance in the mass spectra. Considering the orbital ordering via Woods–Saxon potential as implemented in Figure 1.8, such shell closing occurs at valence electron count of 2, 8, 18, 20, 34, 40, 58... and so on. The set essentially covers all the magic numbers obtained by Knight and coworkers[13,28] for alkali metal clusters. As alkali metals are mono–valent in nature, the shell closing numbers also corresponds to the number of atoms present in the cluster as well. Thus, the high abundance of those specific clusters are primarily due the occurrence of the filled jellium shell at those specific sizes. The observation of the high I.E and low E.A of these specific clusters are also due to the same reason. In case of the anionic alkali metal clusters, the shell closing will happen at specific nuclearities which are one less than the neutral ones (N = 7, 17, 19, 33, 39, 57 etc). Likewise, the magic numbers for cationic alkali metal will be observed at N = 3, 9, 19, 21, 35, 41, 59 etc. For a neutral clusters composed of divalent metal the respective magic numbers will occur at nuclearities which are half than the monovalent metal. Thus, for neutral magnesium the magic numbers corresponds to 4, 9, 10, 17, 20, 29, etc. The situation of a trivalent metal is also similar. Thus, for aluminum first few magic clusters are Al_7^+, Al_{13}^-, Al_{23}^+. All of these predictions

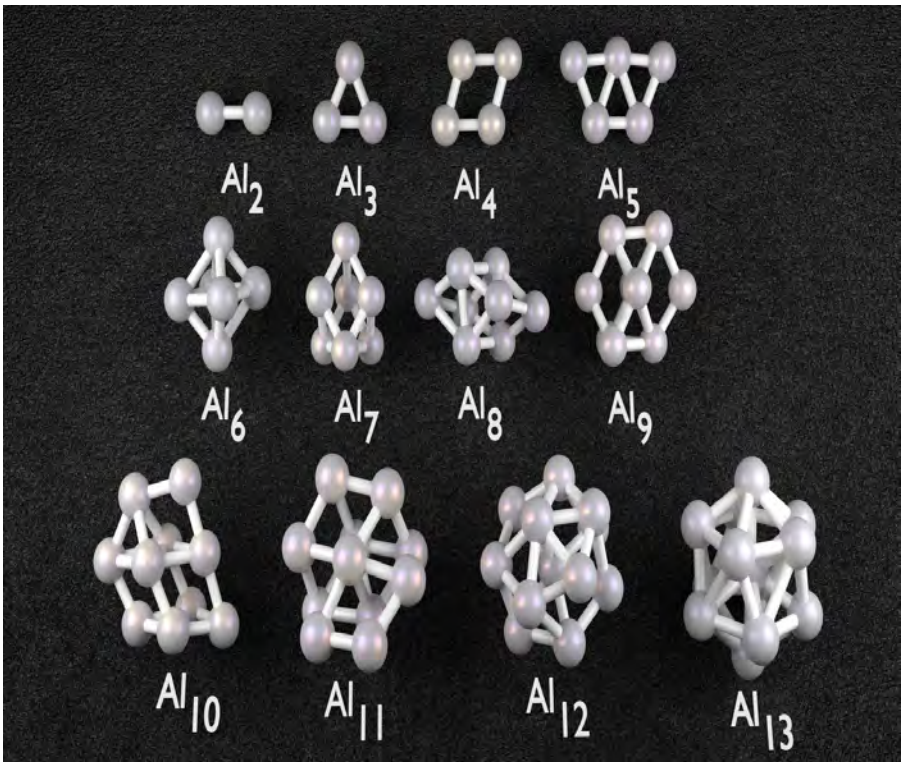

FIGURE 1.9: The ground state optimized structures of first few (N = 2–13) aluminum clusters.

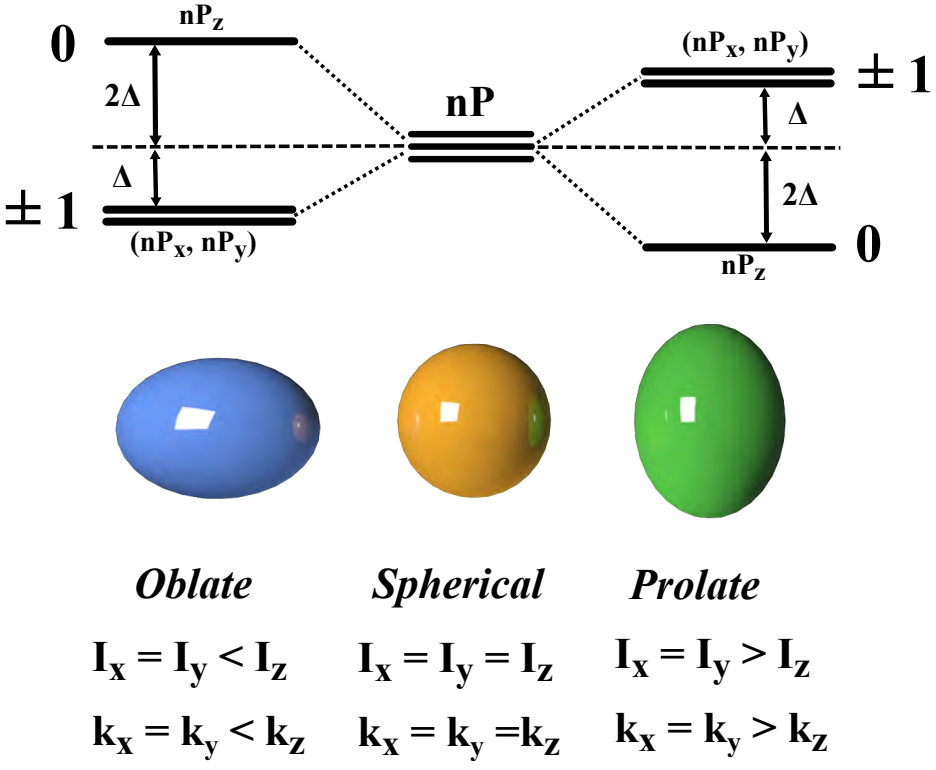

FIGURE 1.10: The ellipsoidal shell model and the splitting of spherical jellium 'np' orbitals upon ellipsoidal distortion.

have been proven correct via numerous experimental investigations throughout the years and henceforth, the jellium model is considered as one of the most reliable tool for explaining the properties of simple metal clusters available to cluster chemists till date.

However, to our surprise, the resemblance of metal clusters with the atoms does not end there. Since the past few decades it has been observed that specific metal clusters not only shows resemblance with that of specific atoms in terms of jellium shell configuration, but also able to mimic there properties to a considerable extent. Such type of metal clusters is nicknamed as the 'Superatoms'. Few prominent example of this kind can be cited from the family of aluminum clusters. The ground state optimized structures of first few aluminum clusters with size range N = 2–13 are shown in Figure 1.9. In the free state the '3s' and '3p' state of aluminum atom are separated by an energy gap of $\sim$ 5 eV. Thus, in low coordination i.e. in smaller clusters aluminum atom behaves as a monovalent element.[29] As a consequence smaller clusters upto N = 5 is observed to be planar similar to that of alkali metals. However, as the clusters start to grow bigger the 's' and 'p' hybridization become more pronounced and from Al_6 the aluminum cluster becomes three dimensional. Starting from $\sim$ Al_7–Al_8 the s–p hybridization becomes pronounces and in Al_{13} and beyond the s–p hybridization can be considered as complete. Considering three valence electrons per atom the jellium configuration of Al_{13} cluster (39 e) becomes, $1S^2\ 1P^6\ 1D^{10}\ 2S^2\ 1F^{14}\ 2P^5$, i.e just one electron less to achieve a filled magic shell configuration of 40 jellium electrons. Thus, the electron configuration of Al_{13} cluster is very similar to that of halogens in which there also exists a similar vacancy in the '2p' shell just one electron shorter to achieve a filled octet. Theoretical investigation have shown that Al_{13} has a high electron affinity $\sim$ 3.57 eV which is just intermediate between Cl (3.62 eV) and Br (3.36 eV).[1] Experimental investigation supported by theory also have shown like halogens, Al_{13} forms covalent bond with iodine,[30] produce polyhalide like compounds,[6] generates salt like material with superalkai countercations like K_3O^+.[8,31] All of these observations proves the 'superatomic' behavior of Al_{13} moiety. In a similar way, the anionic form $Al_{13}{}^-$ which has a magic shell configuration of 40e is observed to be inert like nobel gases with high HOMO–LUMO gap of $\sim$ 1.9 eV. Although the bulk aluminum is susceptible to oxygen etching, $Al_{13}{}^-$ is observed to be resistant to oxygen and other reactive reagents.[32–34] On the other hand, $Al_7{}^-$ (22e) is known for its variable oxidation state like Germanium,[35] $Al_7{}^+$ with closed shell 20e configuration is observed to be inert and stable like $Al_{13}{}^-$.

The jellium shell effect has also been successfully utilized to artificially stabilized suitable non–magic clusters via ligand attachment. A detailed account of which can be found at chapter 5. In short, if a cluster has jellium electron count higher than a magic configuration, suitable numbers of electron withdrawing ligand can be attached such that the jellium configuration of the core reduced to the nearby close shell magic configuration. The principle is commonly known as the 'Super–Atomic Complex Theory (SACT)'. Successful implementation of SACT is observed for numerous clusters of Au and Ag and also for small and medium sized aluminum clusters.[36–39] It is needless to say that with the innovation of the 'Superatoms', the material chemists now have access to an entire new dimension of periodic table with infinite possibility to synthesize novel materials using clusters as the building units instead of atoms. With the discovery of each new superatoms such a possibility is certainly not very far ahead.

The Clemenger–Nilsson Jellium Model and the Odd–Even Effect

Although the spherical jellium model (SJM) is able to explain the relative stability and related properties of simple metal clusters, detailed investigation have shown there exists some finer anomalies within the experimental results, which can not be explained by the SJM. The primary reason behind these discrepancies are due to the non–spherical shape of the atomic clusters which reduces the degeneracy of the jellium orbitals. Such loss to the orbital degeneracy

generates some unusual systematic periodic oscillation in the properties of the metal clusters commonly known as the odd–even effect. Few instances of the odd–even effect for specific cluster series can be summarized as the following,

a. The measured ionization energy of alkali metal clusters with even number of atoms is observed to be systematically higher than their odd neighbors. An opposite trend is noticed for the electron affinities of alkali metal clusters.

b. For cationic and anionic noble metal clusters systematic alteration in their abundances is noticed upto $N \leq 40$. Clusters composed of odd number of atoms is observed to be more abundant than their even neighbors.

c. The odd–even effect is also observed in the dissociation energy trend of small alkali as well as noble metal clusters. The dissociation energy of a cluster is the minimum amount of energy needed to dissociate a cluster into two separate fragments amount of energy needed to evaporate one single atom from the cluster. For a cluster with 'N' number of atoms, the dissociation energy can be represented as,

$$\Delta E_{diss} = E^{N-1}_{cluster} + E_{atom} - E^{N}_{cluster} \tag{1.25}$$

As for example in Cu^{+}_{N} cluster series, the dissociation energies of odd numbered clusters are larger than their even size neighbors.

In order to rectify such limitations of SJM and also to explain the odd–even effect Clemenger has developed a modified jellium model in 1985 which is applicable for ellipsoidal metal clusters. The Clemenger model was originally based on a similar method invented by Nilsson (1955)to describe the properties of ellipsoidally distorted atomic nucleus. The so called odd–even effect is the consequence of the interplay between cluster deformation and electron multiplicity. When a jellium orbital like 'P' shell remains partially filled, the electron density become spherically asymmetric, resulting a distortion of the perfect spherical shape which in turn leads to the splitting of the 'P' subshells. In the ellipsoidal jellium model a perturbed harmonic potential is used with three distinct force constants, k_x, k_y and k_z oriented along three Cartesian axis. The axial symmetry is always maintained such a way that a minimum of two force constants always remains equal. The deviation from the spherical symmetry results in the loss of $(2l + 1)$ degeneracy of jellium orbitals as obtained in the SJM. As the axial symmetry is conserved, the splitting generates a set of $\pm m_l$ shells and $m_l = 0$ remains separate. As depicted in Figure 1.10, two different types of ellipsoidal distortions are possible which are named as oblate and prolate.

In the oblate deformation the ordering of the respective force constant is $k_x = k_y < k_z$. The moment of inertial also follows a similar order (Figure 1.10). As the motion of the electron along 'z' axis is restricted compared to their motion in the 'xy' plane, which results the increment of the energy of those orbitals whose greatest amplitude are directed along the 'z' axis (For a simple analogy, it is well known from the simple particle in a box model that the energy increase with the reduction of the box length). Thus the 'P' jellium shell in a oblate shaped cluster will split such a way that the P_x and P_y will remain degenerate and will be lower in energy whereas the energy of P_z will be elevated. A similar but opposite scenario will be noticed for prolate shape. In this case the set of $| m_l | = 1$ will be energetically higher than the P_z shell. The observed odd–even effect can easily be explained with the splitting of jellium orbitals in combination with the spin pairing effect. Similar splitting of the 'd' shell can explain the odd–even effects observed for clusters made with heavier atoms.

1.6 Additional Theoretical Models

Aside from the most popular theoretical models of atomic clusters described in the previous section, there exists a few different ones which were specifically developed for theoretical predictions of selected properties and their variation with the size of clusters. These proposed models are usually very straightforward in nature however, the oversimplifications implemented in these models often provide inaccuracy for quantitative estimation, especially for clusters with complex electronic and geometric influences. Nevertheless, for specific scenarios, these simplistic models can still be used for quick qualitative determination of selected properties or may aid in the explanation of experimental trends. The present section include such few standard models of atomic clusters. However, for the sake of convenience we have only introduced a brief account of each, further details can be obtained from the cited references.

1.6.1 The Simple Spherical Cluster Model

The simple spherical cluster model (SSCM) or spherical cluster approximation (SCA) is one of the most elementary theoretical model exist for atomic clusters. According to this model any cluster is approximated as a perfect sphere composed of N number of atoms. It is needless to say which is definitely not true for smaller clusters, however as clusters get quite larger with enough number of surface atoms and a finite surface to volume ratio, the SCA becomes a better approximation and the derived equations works well in this large cluster limit. The primary assumption of SCA is that for a finite size spherical cluster composed of N atoms, the radius of the cluster (r_c), surface area (S_c), and volume (V_c) can be related to the respective parameters, namely, radius (r_a), surface area (S_a) and volume (V_a) of the constituent atoms by some simple mathematical equations. Firstly, the cluster volume is approximated as the volume of an atom multiplied by the total number of atoms within the cluster,

$$V_c = N.V_a \tag{1.26}$$

Again, as mentioned earlier , the equation represents a rigorous oversimplification, since it does not include the fact that any number of hard spheres cannot be closely pack to fill the entire space as there must exists some vacant interstitial spaces. However, as the model is specifically focused on deriving parameters for qualitative agreement or for obtaining scaling relationships, we assume that neglecting the packing fraction will not cause much deficit here. Now, equating the volume of the clusters with the total volume of 'N' number of atoms,

$$\frac{4}{3}\pi r_c^3 = N\frac{4}{3}\pi r_a^3 \tag{1.27}$$

Rearranging the equation we obtain the relation between cluster radius ((r_c) with that of constituent atomic radii (r_a),

$$r_c = N^{\frac{1}{3}} r_a \tag{1.28}$$

By a similar fashion the relation between the surface area of the cluster can be related to that of an atom,

$$S_c = 4\pi r_c^2 = 4\pi \left(N^{\frac{1}{3}} r_a\right)^2 = N^{\frac{2}{3}} S_a \tag{1.29}$$

The equations can further be utilized to determine the total number of surface atoms (N_s) in a finite sized cluster, which is simply the ratio of the surface area of the cluster to the cross-sectional area of an atom (A_a),

$$N_s = \frac{S_c}{A_a} = \frac{4\pi N^{\frac{2}{3}} r_a^2}{\pi r_a^2} = 4N^{\frac{2}{3}} \tag{1.30}$$

Many important properties of atomic clusters are dependent on the fraction of total number of atoms (f_s) resides on the surface of the cluster. For a spherical clusters the quantity can be defined as,

$$f_s = \frac{N_s}{N} = 4N^{-\frac{1}{3}} \tag{1.31}$$

Again, the relationship is observed to deviate for smaller clusters, however, as the cluster grows bigger the value of f_s slowly converges to the limiting value i.e. $N^{-\frac{1}{3}}$ as predicted by the equation. For practical purposes, the atomic radii (r_a) is often substituted by the so called Wigner–Seitz radii (r_{ws}), which is the radius of a sphere whose volume is equal to the average volume per atom. Common way to estimate r_{ws} is to define it in terms of molar mass (M) and density (ρ) of the material,

$$r_{ws} = \left(\frac{3M}{4\pi\rho N_A}\right)^{\frac{1}{3}} \tag{1.32}$$

The Empirical Laws of Scaling

The SSCM model can effectively be utilized to determine many generic cluster properties , such as ionization energy (I.E) or ionization potential(I.P), electron affinity (E.A), melting temperature (T_m) and cohesive or binding energy (E_b) for large clusters as they show a regular variation with cluster size in this size regime. By this approximation the smooth cluster size effect (CSE) behavior can be described by simple scaling equations, which can be expressed either in powers of the cluster radius(r_c),

$$\chi(r_c) = \chi(\infty) + ar_c^{-\alpha} \tag{1.33}$$

or, dependent on the number of atoms in the cluster,

$$\phi(N) = \phi(\infty) + br^{-\beta} \tag{1.34}$$

where ∞ in the parenthesis signifies the value of the respective properties (χ or ϕ) in the bulk size limit. a,b, α and β are empirically fitted constants. According to the experimental observations, for large sized clusters with significant surface to volume ratio most important properties usually depend on the fraction of total number of atoms resides on the surface (f_s), and as we have already seen that $f_s \propto N^{-\frac{1}{3}} \propto r_c^{-1}$, hence most usual choice of α is 1 and of β is $\frac{1}{3}$. As for common example, we can cite[26] the fitted equation for the I.P. of potassium clusters with $N \gtrsim 100$,

$$\begin{aligned} I^K(r_c)/eV &= 2.3 + 5.35(r_c/\text{Å})^{-1} \\ I^K(N)/eV &= 2.3 + 2.04N^{-\frac{1}{3}} \end{aligned} \tag{1.35}$$

The interpolation is proven to be highly accurate for the given size range of potassium clusters. Similarly, the melting temperature of large gold structure can be expressed as,

$$T_m^{Au}(r_c)/K = 1336.15 - 5543.65(r_c/\text{Å})^{-1} \tag{1.36}$$

This equation also works as expected for large Au clusters, however, major deviation can be seen for medium and smaller cluster with dominant presence of CSE.

1.6.2 The Liquid Drop Model

The liquid drop model (LDM) is a classical treatment of metal clusters utilizing the principle of fundamental electrostatics. The model is solely developed for obtaining the scaling laws of various properties of metal clusters with incremental size. In this model a metal cluster of finite size is assumed to be an uniform conducting sphere, and similar to the SCA, the scaling laws are represented in the form of an equation relating the respective property of the cluster with the bulk property of the same. As for example, the amount of energy needed to eject an electron from bulk metal surface is called the 'work function(W_s)'. According to the mathematical treatments of LDM, parameters the ionization energy (I.E) must decrease with cluster growth,.i.e, ejecting an electron from a larger cluster requires less energy than in smaller ones. Therefore, the I.E of any metal clusters can be written in terms of the work function (W_s) of bulk metal and the reciprocal of the cluster radius (r_c),

$$I(r_c) = W_s + \frac{3}{32\pi\varepsilon_0 r_c} \tag{1.37}$$

If we represent I.E in the unit of eV and the radius of the cluster (r_c) in terms of , the equation reduces to,

$$I(r_c)/eV = (W_s/eV) + 5.4(r_c/\text{Å})^{-1} \tag{1.38}$$

The equation is very similar with the equation obtained in SCA (e.g. for potassium cluster). In both the cases the ionization energy has inverse dependence on the cluster radius (r_c). In a similar manner the electron affinity can also be presented,

$$\zeta(r_c) = W_s - \frac{5}{32\pi\varepsilon_0 r_c} \tag{1.39}$$

or,

$$\zeta(r_c)/eV = (W_s/eV) - 9.0(r_c/\text{Å})^{-1} \tag{1.40}$$

Thus, according to the prediction of LDA the E.A of a cluster increases with the growth of the cluster. From both the equation it is evident that as the size of the cluster grows towards the bulk limit, $N \to \infty$ and hence $r_c^{-1} \to 0$. Therefore, in bulk limit both the values of I.E and E.A, eventually converges to the work function of the bulk metal.

The predicted I.E and E.A by the LDM can further be utilized to calculate other important properties like HOMO–LUMO gap of metal clusters. According to Koopman's theorem, the HOMO and LUMO energy is approximated by I.E and E.A of the cluster respectively. Since, both I.E and E.A shows a r_c^{-1} or $N^{-\frac{1}{3}}$ dependence, it is expected that the HOMO–LUMO gap will also follows the same. Also according to the LDM equations, as at the bulk limit both I.E and E.A monotonically converges to the work function, the HOMO–LUMO gap would then definitely be reduced to zero. This result is indeed valid, since it is well known that any metal is characterized by a zero band gap. The liquid drop model can also be utilized to predict other associated properties of larger clusters. As for example, the electronic spectrum of a small sized metal cluster is consists of discrete peaks due the presence of discrete electronic shell. However in large size cluster the discrete spectrum are replaced by a single broader peak due to the collective valence electronic excitation against the positive charged core. This phenomenon is commonly called as the Mie resonance. The frequency (ω_M) and the linewidth

(Γ_M) of Mie resonance can similarly be expressed in an equation for like I.E or E.A. Thus, for silver nanoparticle with diameter $2 \geq \mathrm{d}_c$ *leq* 10 nm,[26]

$$\hbar\omega_M(d_c)/eV = 3.21 + \frac{0.58}{d_c/nm} \tag{1.41}$$

$$\Gamma_M(d_c)/eV = 0.04 + \frac{0.59}{d_c/nm} \tag{1.42}$$

In both the expression, the dependence of inverse power of the diameter, i.e. on the inverse power of cluster radius must be noticed.

Similar to the SSCM/SCA model the liquid drop model seems to work well with large size cluster. The linear equations seem to deviate from the experimental points due to the random oscillation in the calculated properties for small range clusters. The oscillation is primarily due to the the predominant presence of electronic shell effect (or, quantum size effect (QSE)) in smaller cluster as already mentioned in the context of jellium model. Also, based on the complexity of real system it is certainly not expected that all the properties of every type of clusters would show r_c^{-1} ($N^{-\frac{1}{3}}$) dependence. As a matter of fact, in several experiments on bigger clusters such type of deviations are recorded. The HOMO–LUMO gap of small copper cluster anions shows and $N^{-1.8}$ dependence instead of $N^{-\frac{1}{3}}$.

References

(1) Jena, P.; Castleman, J.; Welford, A, *Nanoclusters: A Bridge Across Disciplines*; Elsevier, Oxford: 2010, pp 1–589.

(2) González-Arellano, C.; Abad, A.; Corma, A.; García, H.; Iglesias, M.; Sanchez, F. *Angewandte Chemie* **2007**, *119*, 1558–1560.

(3) Corma, A.; Juárez, R.; Boronat, M.; Sánchez, F.; Iglesias, M.; García, H. *Chemical Communications* **2011**, *47*, 1446–1448.

(4) Bergeron, D. E.; Castleman, A. W.; Morisato, T.; Khanna, S. N. *Science* **2004**, *304*, 84–87.

(5) Castleman Jr, A.; Khanna, S. *J. Phys. Chem. C* **2009**, *113*, 2664–2675.

(6) Bergeron, D.; Roach, P.; Castleman, A.; Jones, N.; Khanna, S. *Science* **2005**, *307*, 231–235.

(7) Bergeron, D. E.; Roach, P. J.; Castleman Jr, A. W.; Jones, N. O.; Reveles, J. U.; Khanna, S. N. *J. Am. Chem. Soc.* **2005**, *127*, 16048–16053.

(8) Reber, A. C.; Khanna, S. N.; Castleman, A. W. *J. Am. Chem. Soc.* **2007**, *129*, 10189–10194.

(9) Boyle, R., *The Sceptical Chymist: Or, Chymico-physical Doubts & Paradoxes, Touching the Spagyrist's Principles Commonly Call'd Hypostatical, as They are Wont to be Propos'd and Defended by the Generality of Alchymists. Whereunto is Praemis'd Part of Another Discourse Relating to the Same Subject. London, Printed by F. Cadwell for F. Crooke, 1661*; F. Cadwell: 1965.

(10) Fässler, T. F., *Zintl phases: principles and recent developments*; Springer Science & Business Media: 2011; Vol. 139.

(11) Mingos, D. M. P.; Wales, D. J., *Introduction to cluster chemistry*; Prentice Hall: 1990.

(12) Echt, O; Sattler, K; Recknagel, E *Phys. Rev. Lett.* **1981**, *47*, 1121–1124.

(13) Knight, W. D.; Clemenger, K.; de Heer, W. A.; Saunders, W. A.; Chou, M.; Cohen, M. L. *Phys. Rev. Lett.* **1984**, *52*, 2141–2143.

(14) Kroto, H. W.; Heath, J. R.; O'Brien, S. C.; Curl, R. F.; Smalley, R. E., et al. *Nature* **1985**, *318*, 162–163.

(15) Osawa, E. *Kagaku* **1970**, *25*, 101.

(16) Kroto, H. *Fullerenes, Nanotubes, and Carbon Nanostructures* **1994**, *2*, 333–342.

(17) Krätschmer, W; Lamb, L. D.; Fostiropoulos, K; Huffman, D. R. *Nature* **1990**, *347*, 27.

(18) Buseck, P. R. *Earth and Planetary Science Letters* **2002**, *203*, 781–792.

(19) Becker, L.; Bunch, T. *Meteoritics & planetary science* **1997**, *32*, 479–487.

(20) Becker, L.; Bunch, T. E.; Allamandola, L. J. *Nature* **1999**, *400*, 227–228.

(21) Cami, J.; Bernard-Salas, J.; Peeters, E.; Malek, S. E. *Science* **2010**, *329*, 1180–1182.

(22) Guo, B.; Kerns, K.; Castleman Jr, A. *Science* **1992**, *255*, 1411.

(23) Deng, H.; Guo, B.; Kerns, K.; Castleman, A. *International Journal of Mass Spectrometry and Ion Processes* **1994**, *138*, 275–281.

(24) Cartier, S.; May, B.; Castleman Jr, A. *The Journal of chemical physics* **1994**, *100*, 5384–5386.

(25) Yamanaka, S.; Kini, N. S.; Kubo, A.; Jida, S.; Kuramoto, H. *Journal of the American Chemical Society* **2008**, *130*, 4303–4309.

(26) Johnston, R. L., *Atomic and Molecular Clusters*; CRC Press, London and New York: 2002, pp 1–250.

(27) Mackay, A. *Acta Crystallogr.* **1962**, *15*, 916–918.

(28) Knight, W. D.; de Heer, W. A.; Clemenger, K.; Saunders, W. A. *Solid State Commun.* **1985**, *53*, 445–446.

(29) Alonso, J., *Structure and Properties of Atomic Nanoclusters*; World Scientific, London: 2005, pp 1–427.

(30) Bergeron, D. E.; Castleman, A. W.; Morisato, T.; Khanna, S. N. *Science* **2004**, *304*, 84–87.

(31) Clayborne, P; Jones, N. O.; Reber, A. C.; Reveles, J. U.; Qian, M.; Khanna, S. N. *Journal of Computational Methods in Science and Engineering* **2007**, *7*, 417–430.

(32) Reber, A. C.; Khanna, S. N.; Roach, P. J.; Woodward, W. H.; Castleman, A. W. *J. Am. Chem. Soc.* **2007**, *129*, 16098–16101.

(33) Leuchtner, R.; Harms, A.; Castleman Jr, A. *J. Chem. Phys.* **1989**, *91*, 2753–2754.

(34) Burgert, R.; Stokes, S. T.; Bowen, K. H.; Schnöckel, H. *Journal of the American Chemical Society* **2006**, *128*, 7904–7908.

(35) Reveles, J. U.; Khanna, S.; Roach, P.; Castleman, A. *Proceedings of the National Academy of Sciences* **2006**, *103*, 18405–18410.

(36) Clayborne, P. A.; Lopez-Acevedo, O.; Whetten, R. L.; Grönbeck, H.; Häkkinen, H. *J. Chem. Phys.* **2011**, *135*, 094701.

(37) Walter, M.; Akola, J.; Lopez-Acevedo, O.; Jadzinsky, P. D.; Calero, G.; Ackerson, C. J.; Whetten, R. L.; Grönbeck, H.; Häkkinen, H. *Proc. Natl. Acad. Sci. U. S. A.* **2008**, *105*, 9157–9162.

(38) Jung, J.; Kang, S.; Han, Y.-K. *Nanoscale* **2012**, *4*, 4206–4210.

(39) Huber, M.; Henke, P.; Schnöckel, H. *Chem.Eur.J.* **2009**, *15*, 12180–12183.

Chapter 2

The Fundamentals of Density Functional Theory

2.1 Introduction

In the course of the past few decades, the density functional theory or DFT has become the pivotal computational tool used by the theoretical and experimental chemists around the world. However, to many physicists as well as chemists the journey of DFT from just a theoretical concept to the present state of glory is often considered as fortuitous if not outright unjustified. This disfavor is due the easy achievement of the accuracy of DFT which is often considered as a difficult task in the *ab initio* wave function based methods. A majority of theoretical chemists also found the fundamental theories are somewhat dubious and the simplistic single deterministic approach provokes further skepticism. However, considering the accuracy in addition to the computational cost, the widespread preference to DFT seems a rational choice rather than a prejudice. As of recent developments, DFT is able to provide all sorts of computational tools essential to calculate complete set of properties of materials with the additional benefit of economical computing and variable implementations, suitable for all type of systems. Due to the consent to modern DFT, performing accurate complex calculations for a vast number of systems within a limited time has become possible. Supporting experimental results by theoretical calculations has now been reduced to a days job rather than months with the aid of DFT. Therefore, the extensive availability of DFT software packages and the ever–growing community must be viewed as a natural progress rather than a miracle. It goes without saying, all the calculations presented in this thesis are also evaluated via the implementation of DFT using standard computational packages. Therefore, the present chapter is solely dedicated to provide a very brief introduction to the fundamentals of density functional theory. Few other relevant topics including the fundamental concepts of quantum chemistry are also discussed in short.

2.2 The Schrödinger Equation

The central notion of modern quantum mechanics is the time dependent non–relativistic Schrödinger equation proposed by Erwin Rudolf Josef Alexander Schrödinger in 1926. In most of the problems regarding atoms and molecules, the time dependent interactions are often not important, hence the time–independent variation of the Schrödinger equation is generally considered as the pivotal equation in the modern quantum chemistry. For a system consisting of M nuclei and N electrons, the time independent non–relativistic Schrödinger equation is written as,

$$\hat{H}\Psi\left(\vec{x}_1,\vec{x}_2,...,\vec{x}_N,\vec{R}_1,\vec{R}_2,...,\vec{R}_M\right) = E\Psi\left(\vec{x}_1,\vec{x}_2,...,\vec{x}_N,\vec{R}_1,\vec{R}_2,...,\vec{R}_M\right) \tag{2.1}$$

where $\hat{H}$ is the Hamiltonian operator, $\vec{x}$ and $\vec{R}$ are the coordinates of the respective electrons and nuclei. ψ_i is a many–particle wave function, E is the energy of the system. The Hamiltonian

operator in atomic units is represented as,

$$\hat{H} = -\frac{1}{2}\sum_{i=1}^{N}\nabla_i^2 - \frac{1}{2}\sum_{A=1}^{M}\frac{\nabla_A^2}{M_A} - \sum_{i=1}^{N}\sum_{A=1}^{M}\frac{Z_A}{r_{iA}} + \sum_{i=1}^{N}\sum_{j>i}^{N}\frac{1}{r_{ij}} + \sum_{A=1}^{M}\sum_{B>A}^{M}\frac{Z_A Z_B}{R_{AB}} \tag{2.2}$$

A and B indicates a total of the M nuclei while i and j denote the N number of electrons in the system. The first two terms in equation 2.2 describe the kinetic energy of the electrons and nuclei respectively. The rest of the three terms respectively represent the attractive electrostatic interaction between the nuclei and the electrons, the repulsive potential of the electron-electron and the nucleus-nucleus interactions. Other associated terms have their usual significance.

Now as nuclei are much heavier than the electrons, hence, they move much slower. Therefore according to the **Born–Oppenheimer approximation** we can consider that all of the electrons are existing in the field of fixed nuclei and the nuclear kinetic energy is zero and their potential energy is merely a constant. Thus, the Hamiltonian can be reduces to only containing the electronic part,

$$\hat{H}_e = -\frac{1}{2}\sum_{i=1}^{N}\nabla_i^2 - \sum_{i=1}^{N}\sum_{A=1}^{M}\frac{Z_A}{r_{iA}} + \sum_{i=1}^{N}\sum_{j>i}^{N}\frac{1}{r_{ij}} = \hat{T} + \hat{V}_{Ne} + \hat{V}_{ee} \tag{2.3}$$

Therefore, the solution of the Schrödinger Equation with electronic Hamiltonian yields the electronic energy (E_e) of the system when operated on the electronic wave function(ψ_e),

$$\hat{H}_e \psi_e = E_e \psi_e \tag{2.4}$$

and the total energy of the system becomes the sum of electronic energy (E_e) and the nuclear repulsion term E_{nuc}.

$$E_{tot} = E_e + E_{nuc} \tag{2.5}$$

where,

$$E_{nuc} = \sum_{A=1}^{M}\sum_{B>A}^{M}\frac{Z_A Z_B}{R_{AB}} \tag{2.6}$$

If a system is in the state ψ, the expectation value of energy for the particular system is given by

$$E[\psi] = \frac{\langle\psi|\hat{H}|\psi\rangle}{\langle\psi|\psi\rangle} \tag{2.7}$$

where $\langle\psi|\hat{H}|\psi\rangle = \int \psi^* \hat{H}\psi d\tau$. Now according to the **Variational Principle** the energy calculated using an guessed ψ is always an upper bound to the original ground state energy (E_0) of the system of interest,

$$E[\psi] = \frac{\langle\psi|\hat{H}|\psi\rangle}{\langle\psi|\psi\rangle} \quge E_0 = \frac{\langle\psi_0|\hat{H}|\psi_0\rangle}{\langle\psi_0|\psi_0\rangle} \tag{2.8}$$

Thus, Full minimization of the given functional E[ψ] with respect to all of the allowed N-electronic wave functions will provide the true ground state ψ_0 and the corresponding energy E[ψ] = E_0. The ground state N electronic wave function is usually represented by an antisymmetrized product of N numbers of orthonormal spin orbitals $\phi_i(\vec{x})$, each of which is a product of spatial orbital $\chi_k(\vec{r})$ and the spin function $\sigma(s) = \alpha(s) or \beta(s)$. The resulting formulation is

called as the **Slater Determinant**,

$$\psi(\vec{x}_1,\vec{x}_2,\cdots\vec{x}_N) = \frac{1}{\sqrt{N!}} \begin{vmatrix} \phi_1(\vec{x}_1) & \phi_2(\vec{x}_1) & \cdots & \phi_N(\vec{x}_1) \\ \phi_1(\vec{x}_2) & \phi_2(\vec{x}_2) & \cdots & \phi_N(\vec{x}_2) \\ \phi_1(\vec{x}_3) & \phi_2(\vec{x}_3) & \cdots & \phi_N(\vec{x}_3) \\ . & . & . & . \\ . & . & . & . \\ . & . & . & . \\ \phi_1(\vec{x}_N) & \phi_2(\vec{x}_N) & \cdots & \phi_N(\vec{x}_N) \end{vmatrix} \tag{2.9}$$

2.3 Function, Operator and Functional

In this section we will introduce a few important definitions.

2.3.1 Function

A function is a mathematical recipe to map one variable into another. Thus if x and y be two variable so related that for each and every value of x (defined within a given domain), there are values of y, then y is a function of x. In the present scenario, x is called a *independent variable* or an argument and y is referred as *dependent variable*. According to the common convention a function of a dependent variable 'x' is denoted by symbols such as $f(x), F(x), G(x), \psi(x), \phi(x)$ etc. It may be possible that for a particular value of the independent variable two or more values of the function is generated. In such cases the function is defined as a **multiple–valued** function, otherwise the function is **single–valued**. However, using proper limitation a multiple valued function can be separated into several single valued functions. Thus $y^2 = x$ can be broken into $y = +\sqrt{x}$ and $y = -\sqrt{x}$ and so on. A function can also be undefined for some particular value(s) of the independent variable. thus $f(x) = \frac{1}{x}$ is undefined for $x = 0$.

2.3.2 Operator

In common mathematics, an operator is a description of mathematical operation which is operated on a function in order to generate a new function. According to common convention an operator is symbolically presented like $\hat{F}$ or via calligraphy e.g. $\mathscr{F}$. Some common examples of common operators are multiplication by a constant, square root, $\frac{d}{dx}$ and $\frac{d^2}{dx^2}$. Few common example with simple operations can be included here. Thus, operating the square operator i.e, $\hat{F} = {}^2$ on a function like $\cos(x)$ we get, $\hat{F}cos(x) = cos^2(x)$. Similarly second derivative of a function w.r.t x can be calculated by the operator, $\hat{F} = \frac{\partial^2}{\partial x^2}$, and the result is $\hat{F}f(x) = \frac{\partial^2}{\partial x^2}f(x) = \frac{\partial^2 f(x)}{\partial x^2}$. In quantum mechanics 'Nabla' (∇) is the popular differenial operator in three dimensional coordinate. In Cartesian coordinate it is represented as,

$$\nabla = \left(\vec{\mathbf{i}}\frac{\partial}{\partial x} + \vec{\mathbf{j}}\frac{\partial}{\partial y} + \vec{\mathbf{k}}\frac{\partial}{\partial z}\right)$$

Important parameter like forces (which are vectors) which is the gradients of potential energy can be calculated by operating ∇ on the potential, $Force = -\nabla V$. The square of ∇ is called the Laplacian operator,

$$\Delta = \nabla^2 = \left(\frac{\partial^2}{\partial x^2} + \frac{\partial^2}{\partial y^2} + \frac{\partial^2}{\partial z^2}\right)$$

The ∇^2 or Δ is another important operator in quantum chemistry since it is related with the kinetic energy operator. An operator is called linear if the following relation holds,

$$\hat{F}(C\psi) = C\hat{F}\psi \tag{2.10}$$

where 'C' is a constant. As for example the first order differentiation ($\frac{d}{dx}$) operator is linear. However, operator like square root is not a linear operator, since,

$$\sqrt{(C\psi)} \neq C(\sqrt{\psi}) \tag{2.11}$$

2.3.3 Functional

A functional is defined as a function of another function. A Functional takes a function as the input in order to provide the output. In common convenience, a functional is symbolically presented with the function in square brackets as $F[f] = b$. As for example we can consider the integration of a function from $-\infty$ to $+\infty$ as a functional,

$$F[f] = \int_{-\infty}^{+\infty} f(x)dx \tag{2.12}$$

The mathematical formulation of the expectation value given in (2.8) can also be considered as the total energy functional($E[\psi]$) of the function ψ as it takes the function ψ as input and provide the value of energy for that particular state (ψ).

The properties of the functionals are also similar to the functions. Like the function, a functional can also have derivatives, the formulation is much similar to the derivatives of functions as well. The differentiation of a functional $F[f]$ is defined as,

$$\partial F[f] = F[f+\partial f] - F[f] = \int \frac{\partial F}{\partial f(x)} \partial f(x)dx \tag{2.13}$$

The rule of differentiation are also similar to the functions,

$$\frac{\partial}{\partial f(x)}(C_1F_1 + C_2F_2) = C_1\frac{\partial F_1}{\partial f(x)} + C_2\frac{\partial F_2}{\partial f(x)} \tag{2.14}$$

$$\frac{\partial}{\partial f(x)}(F_1F_2)\frac{\partial F_1}{\partial f(x)}F_2 + \frac{\partial F_2}{\partial f(x)}F_1 \tag{2.15}$$

2.4 The Electron Density

The wave function ψ introduced earlier has no physical significance as it is not an observable. However, the square of a wavefunction is directly associated with the probability density of electrons. The electron density is definitely an observable and can be measured by suitable experiments like X–ray diffraction. The total electron density of a N electronic system can be defined as N–times (since electrons are indistinguishable) of the integral of the modulus square of wavefunction over all the spin coordinates of all electrons and over all but one of the spatial coordinates ($\vec{x} \equiv \vec{r}.s$),

$$\rho(\vec{r}) = N \int\int \cdots \int |\psi(\vec{x}_1, \vec{x}_2, \cdots \vec{x}_N,)|^2 ds_1 d\vec{x}_2 d\vec{x}_3 \cdots d\vec{x}_N \tag{2.16}$$

Here $\rho(\vec{r})$ represents the probability of finding any of the N–electrons within a volume element of d$\vec{r}$ with arbitrary spin. Other (N-1) electrons have arbitrary positions and spin as represented by the state defined by ψ . Although ρ(r) represents the probability density, it is commonly known as the electronic density. ρ(r) obeys some specific properties mentioned below,

a. $\rho(r)$ is a non-negative function of the three spatial variables which integrates to the total number of electrons and vanishes at infinity,

$$\begin{aligned} \rho(\vec{r} \longrightarrow \infty) &= 0 \\ \int \rho(\vec{r}) d\vec{r} &= N \end{aligned} \tag{2.17}$$

b. At the specific position of an atom $\rho(\vec{r})$ shows a discontinuity resulting a cusp.

$$\lim_{r_{iA} \to 0} \left[\frac{\partial}{\partial r} + 2Z_A \right] \overline{\rho}(\vec{r}) = 0 \tag{2.18}$$

where $\overline{\rho}(\vec{r})$ is the spherical average of $\rho(\vec{r})$

c. $\rho(\vec{r})$ shows a asymptotic exponential decay for large distances from all nuclei within the system,

$$\rho(\vec{r}) \propto exp\Big[-2\sqrt{2I}|\vec{r}|\Big] \tag{2.19}$$

where 'I' is the ionization energy.

In a similar fashion the pair density which is the probability of finding two electrons with spins σ_1 and σ_2 simultaneously within respectively two different volume elements dr_1 and dr_2 is given as,

$$\rho_2(\vec{x}_1, \vec{x}_2) = N(N-1) \int \int \cdots \int |\psi(\vec{x}_1, \vec{x}_2, \cdots \vec{x}_N,)|^2 d\vec{x}_3 \cdots d\vec{x}_N \tag{2.20}$$

The remaining N-2 number of electrons is considered have arbitrary positions and spins. The pair density is also a positive number and normalized to the total number of non–distinct pairs of electrons .i.e, N(N-1)[1]

2.5 The Thomas–Fermi Model

Although the journey of the modern density functional theory began just few decades ago, the first attempt to use electron density in place of wave function is dated back to the early days of quantum mechanics. Using electron density as the fundamental parameter of a quantum mechanical system has always been a tempting topic to theoretical chemists. The prime reason of that is twofold. Firstly, unlike the wave function, the electron density of a quantum mechanical system is a experimentally measurable quantity. Secondly, it depends on three Cartesian coordinates, whereas, the wave function of a system composed of 'N' number of particles has a dependency on 4N number of variables (3N for coordinates and N for spin). Thus using density is far more economical than using the wavefunction if one considered the computational time and resources. The first simplest approximation of such kind is proposed by Thomas (1927) and Fermi (1928) and is known as the Thomas–Fermi(TM) model in short.[1,2]

[1] A different normalization factor $\frac{N(N-1)}{2}$ is also used commonly which corresponds to the distinct number of pairs of electrons.

In this model Thomas and Fermi has derived the expression of kinetic energy of a quantum mechanical system based on the electron density alone by utilizing the concept of uniform electron gas. In this quantum statistical model except the kinetic energy, all other contributions due to nuclear–electron attraction and electron-electron repulsion are treated in a completely classical manner. Thus, according to the model the kinetic energy of a quantum mechanical system can be expressed by the following functional,

$$T_{TF}[\rho(\vec{r})] = \frac{3}{10}(3\pi^2)^{\frac{2}{3}} \int \rho(\vec{r})^{\frac{5}{3}} d\vec{r} \tag{2.21}$$

Using the classical contribution the total energy of the system becomes,

$$E_{TF}[\rho(\vec{r})] = \frac{3}{10}(3\pi^2)^{\frac{2}{3}} \int \rho(\vec{r})^{\frac{5}{3}} d\vec{r} - Z\int \frac{\rho(\vec{r})}{r} d\vec{r} + \frac{1}{2}\int\int \frac{\rho(\vec{r_1})\rho(\vec{r_2})}{r_{12}} d\vec{r_1} d\vec{r_2} \tag{2.22}$$

As the expression of the kinetic energy expression is a very rough estimate of the actual kinetic energy of the system and as the exchange and correlation effects are completely ignored, the TF model shows very poor performance in describing real systems. Thus upon implementing the TF model for molecular system it is observed that the model is unable to describe the existence of chemical bond. Thus, the model is hardly of any use for practical purposes. However, the real importance of Thomas Fermi model is not due to the accuracy of the method but due to that it is the first instance where the energy of a system is represented as a whole using only the electron density. However, for that time being no immediate solution was found to rectify the limitation of the model and hence the wave function based methods remained as the only way to approach and analyze the real systems. In order to find out the correct density which to be inserted in the above equation, Thomas and Fermi have utilized the variational principle. They assumed that the ground state of the system is related to the density for which the expression of total energy is minimized under the constraint $\int \rho(\vec{r}) d\vec{r} = N$. At this point it is important to mention that at that time it was still unknown that whether expressing the total energy of a system in terms of density is theoretically justified or using variational principle in the said context is even valid. Despite the fact, Thomas and Fermi proceeded with the assumption as for that time it was the only solution that seemed logical and reasonable.

2.6 The Hohenberg and Kohn Theorem

The field of modern density functional theory we know and use today was born when in 1964 Hohenberg and Kohn[3] proposed and proved two fundamental postulates regarding the electron density of the system. These two postulates not only solve the queries regarding the justification of the approximations used in the Thomas Fermi model but also provide the theoretical foundation needed to construct the rigorous density functional theory and related developments. The two postulates can be summarized as,[1,2]

I. Every observable of a stationary quantum mechanical system (including energy), can be calculated, in principle exactly, from the ground-state density alone, i.e., every observable can be written as a functional of the ground-state density.

II. The ground state density can be calculated, in principle exactly, using the variational method involving only density,

The original theorems was intended for the time independent stationary ground states, but was later extended to excited states and time dependent systems as well.[4,5]

In order to prove the validity of first theorem, Hohenberg and Kohn utilized some valid assumptions based on the fundamental principles of quantum chemistry. If one considers the Born-Oppenheimer approximation, the ground state of a electronic system is a direct result of the potential exerted by the nuclei (called 'external potential', $\hat{V}_{ext}$). This assumption can further be clarified by looking into the expression of the electronic Hamiltonian ($\hat{H}_e$) of Equation 2.3. In that equation the kinetic energy of electrons ($\hat{T}$) and the electron-electron repulsion term ($\hat{V}_{ee}$) simply 'adjust' themselves to the external potential. Thus for a specific value of $\hat{V}_{ext}$, every other variables of the system including the electron density, adjusts themselves to provide the lowest possible ground state energy of the electronic system. Thus $\hat{V}_{ext}$ can be considered as the only variable term in the electronic Hamiltonian, and every other parameters indirectly depends on it.

Entrusting the aforesaid assumption, Hohenberg and Kohn asked a common question, "Is the parameter $\hat{V}_{ext}$ can be uniquely determined just from the knowledge of electron density $\rho(\vec{r})$ alone? Is it possible (at least by principle, not necessarily to be easy) to get the information about the position and the type of the nuclei are, if we accurately know the density $\rho(\vec{r})$ of the ground state? Is there exists a precise path of mapping from the density ($\rho(\vec{r})$) to the external potential ($\hat{V}_{ext}$)?" The answer to all of these questions were found to be affirmative. In reality, the mapping from $\rho(\vec{r})$ to $\hat{V}_{ext}$ is observed to be accurate within a constant, which is not a big concern since it is well known Schrödinger equations with $\hat{H}_e$ and $\hat{H}_e + const$ provides exactly the same eigen–states. Only thing that will change in that case is that the energy levels will be shifted by the value of this *const*. Now, all measured energies are known only within some constants which is the reason of the foundation of the frame of reference. Thus, if this is true the knowledge of only the density is enough to get the complete information about the system. As $\rho(\vec{r})$ can be utilized to yield the total number of electrons N:

$$N = \int \rho(\vec{r}) d\vec{r} \tag{2.23}$$

and $\rho(\vec{r})$ also determines the $\hat{V}_{ext}$, the knowledge of $\rho(\vec{r})$ is equivalent to the knowledge of ψ, i.e., the wave function of the system.

They've also provided the mathematical proof of the theorem which is based on *reductio ad absurdum* which is as follows,

Let us assume $\rho(\vec{r})$ represents an exact ground state density of a non–degenerate system[2] and ψ is the wave function of the ground state. We may further assume that for that specific density $\rho(\vec{r})$, there can be two possible external potentials which are $\hat{V}_{ext}$ and $\hat{V}'_{ext}$ respectively. Now these two different external potential will certainly corresponds to two separate electronic Hamiltonian operators ($\hat{H}_e$ and $\hat{H}'_e$) both of them will yield two different wave functions for the same ground state, ψ and ψ' respectively.

Therefore, the energies corresponds to each wave function are $E_0 = \langle \psi | H | \psi \rangle$ and $E'_0 = \langle \psi' | H' | \psi' \rangle$ respectively. If we now calculate the expectation value of energy for the ψ' with the Hamiltonian $\hat{H}$ and utilize the variational principle we get,

$$E_0 < \langle \psi' | H | \psi' \rangle = \overbrace{\langle \psi' | H' | \psi' \rangle}^{E'_0} + \langle \psi' | H - H' | \psi' \rangle = E'_0 + \int \rho(\vec{r}) [\hat{V}_{ext} - \hat{V}'_{ext}] d\vec{r} \tag{2.24}$$

[2]It is important to note that later investigations has proven that HK theorems can easily be extended for degenerate ground states as well.[6]

Similarly, the expectation value of energy for the ψ with the Hamiltonian $\hat{H}'$ yields,

$$E_0' < \langle \psi | H' | \psi \rangle = \underbrace{\langle \psi | H | \psi \rangle}_{E_0} + \langle \psi | H' - H | \psi \rangle = E_0 - \int \rho(\vec{r})[\hat{V}_{ext} - \hat{V}_{ext}']d\vec{r} \tag{2.25}$$

Adding equations (2.24) and (2.25) by each sides leads to a contradictory solution,

$$E_0 + E_0' < E_0' + E_0 \tag{2.26}$$

Thus, it is now proven that there cannot be two different V_{ext} that give the same $\rho(\vec{r})$ for the ground state. Thus, $\rho(\vec{r})$ uniquely determines N and $\hat{V}_{ext}$, and also all the properties of the ground state, including the kinetic energy of electrons ($T(\rho)$) and energy of electron interactions E_{ee}. Thus, the total ground state energy of the system can be represented as simply a functional of density alone,

$$E[\rho] = \underbrace{E_{Ne}[\rho]}_{system\ dependent} + \underbrace{T[\rho] + E_{ee}[\rho]}_{universal} \tag{2.27}$$

where we have retained the subscript 'Ne' to emphasize the type of external potential in our case, which is just the electron and nucleus attraction. We can further grouped together the functionals which are just responses and can be considered as secondary compared to the $E_{Ne}[\rho]$,

$$E[\rho] = E_{Ne}[\rho] + F_{HK}[\rho] = \int \rho(\vec{r})\hat{V}_{Ne}(\vec{r})d\vec{r} + F_{HK}[\rho] \tag{2.28}$$

The newly defined F_{HK} functional depends only on density and is universal, i.e., its mathematical form does not depend on the type of system under consideration. The simple looking F_{HK} functional is the most important term used in DFT. If we know the explicit form of both the terms in it, we would have able to solve the Schödinger equation exactly. However, the exact forms of both the terms are still unknown and is considered the major challenges in DFT. Although, the Second term $E_{ee}[\rho]$ can further be separated into two terms, the classical Coulombic part ($J(\rho)$) and the non-classical contribution ($E_{ncl}[\rho]$) to the $E_{ee}[\rho]$, which contains self–interaction correction and the exchange and Coulomb part,

$$E_{ee}[\rho] = \frac{1}{2}\int\int \frac{\rho(\vec{r}_1)\rho(\vec{r}_2)}{r_{12}} d\vec{r}_1 d\vec{r}_2 + E_{ncl}[\rho] = J[\rho] + E_{ncl}[\rho] \tag{2.29}$$

Until now, the proof of first HK theorem shows that the ground state density alone is sufficient to evaluate all the properties of a system. However, the first theorem does not tell us how to be sure that the density of our choice is the correct density for the system. The second HK theorem offers a possible solution to that problem in terms of variational principle introduced in the earlier section of this present chapter. In a simplified manner, the second theorem tells that the energy functional $E[\rho]$ is an upper bound to the exact ground state energy, i.e., E_0. Thus, for any chosen trial density $\tilde{\rho}(\vec{r})$ which satisfies the necessary boundary conditions like, $\tilde{\rho}(\vec{r}) \geq 0$ and $\int \tilde{\rho}(\vec{r})d\vec{r} = N$ and which corresponds to some external potential $\tilde{V}_{ext}$, the calculated energy $E[\tilde{\rho}]$ will be either higher or equal to the exact ground state energy $E_0[\rho_0]$,

$$E_0[\rho_0] \leq E[\tilde{\rho}] = E_{Ne}[\tilde{\rho}] + T[\tilde{\rho}] + E_{ee}[\tilde{\rho}] \tag{2.30}$$

$E[\tilde{\rho}]$ will only be equal to E_0 if and only if the trial density $\tilde{\rho}$ equals to the exact ground state density(ρ_0) of the system. The mathematical proof of equation 2.30 is really simple. Since it is known any trial density must $\tilde{\rho}$ corresponds to a Hamiltonian ($\tilde{H}$) and to a wave function ($\tilde{\psi}$). The corresponding wave function can now be utilized as the trial wave function for the

Hamiltonian originated from the true external potential namely V_{ext}. Therefore,

$$\left\langle \tilde{\psi}|\hat{H}|\tilde{\psi}\right\rangle = T[\tilde{\rho}] + E_{ee}[\tilde{\rho}] + \int \tilde{\rho}(\vec{r})d\vec{r} = E[\tilde{\rho}] \geq E_0[\rho_0] = \left\langle \psi_0|\hat{H}|\psi_0\right\rangle \tag{2.31}$$

which is the expected proof.

Before we proceed further, let us focus on few theoretical complexities which are essential in this present context. As we have already mentioned, in order to the theorem to be valid, the trial density $\tilde{\rho}$ must obey few predetermined rules. These conditions are abbreviated as the **representability of density**. The first one is called the N–representability which is the $\tilde{\rho}$ must sum up to the total electron number 'N' upon integration.[1,7–9] This condition is easy to achieve and automatically ensured if $\tilde{\rho}$ originates from a antisymmetrized wave function. The second condition which was just mentioned in the previous para, is that the trial density must be associated with some external potential (V_{ext}). This condition is known as the V_{ext} representability (or simply as 'v' reprentability) problem[10] and which is not as trivial as the case of N–representability. In a simpler language, among the many trial densities available, not all are suitable in accordance of the Hohenberg-Kohn theorem. Among many only those those densities are valid which are mapped with an antisymmetric wave function and therefore with a Hamilton operator with some type of V_{ext}. This is still an open problem in DFT since till date it is not known what condition must a trial density satisfy in order to be V_{ext} representable. By taking some reasonable trial densities Levy (1982) and Lieb (1983) has shown that they cannot be mapped to any V_{ext}.[11,12] Thus, if one chose any of those specific densities it would be impossible to converge to any physically relevant ground state via variational optimization. If we restrict ourselves to only N as well as v representable trial densities, the second HK theorem is considered to be valid in all the cases.

2.7 The Kohn and Sham Method

From the Hohenberg–Kohn theorem we have shown that the ground state energy of a system of interest can be written as,[3]

$$E_0 = min_{\rho\to N}\left(F[\rho] + \int \rho(\vec{r})\hat{V}_{Ne}(\vec{r})d\vec{r}\right) \tag{2.32}$$

where, $F[\rho]$ is the pre–mentioned universal functional which contains kinetic energy the classical Coulomb interaction term and the non–classical interactions,

$$F[\rho] = T[\rho] + J[\rho] + E_{ncl}[\rho] \tag{2.33}$$

Among these three only $J[\rho]$ is known. Unfortunately, the expression of the kinetic energy ($T[\rho]$) is not known with adequate accuracy. Even with the modified Thomas–Fermi, the final expression is still underdeveloped and not work very well with molecular systems. In 1965, Kohn and Sham[13] proposed an alternative to bypass this limitation and provide an alternative way to reach the ultimate goal sought by many. Since the kinetic energy of a system can easily calculated from a known wave function, Kohn and Sham proposed to calculate the exact kinetic energy of a reference non–interacting system whose electron density is the same with the real interacting system of interest. Thus,

$$T_S = -\frac{1}{2}\sum_i^N \left\langle \psi_i|\nabla^2|\psi_i\right\rangle \tag{2.34}$$

[3] from now on we will use the notation F instead of F_{HK} for convenience

and

$$\rho_S(\vec{r}) = \sum_i^N \sum_s |\psi_i(\vec{r},s)|^2 = \rho(\vec{r}) \tag{2.35}$$

where, ψ_i is the wave function of the reference system. It is evident that $T_S \neq T$ even if both the systems (interacting and non–interacting) have same electron density. however it is expected a major portion of $T[\rho]$ is recovered via T_S. In order to correct this error, Kohn and Sum suggested the following partition of the universal functional $F[\rho]$,

$$F[\rho] = T_S[\rho] + J[\rho] + E_{XC}[\rho] \tag{2.36}$$

where, $E_{XC}[\rho]$ is defined as the **Exchange–Correlation Energy** and expressed as,

$$E_{XC}[\rho] = (T[\rho] - T_S[\rho]) + (E_{ee}[\rho] - J[\rho]) \tag{2.37}$$

Thus $E_{XC}[\rho]$ contains all the contributions to energy which are unknown and not accounted for, i.e.:

- The contribution of electron exchange.
- The contribution of electron correlation which is a crucial part of energy for systems containing interacting electrons.
- The residual portion of the kinetic energy which is not included in the term T_S and hence essential to get the true kinetic energy of the real system of interest i.e, $T[\rho]$.
- A correction for the self-interaction which is originated from the by the classical coulomb potential.

As a matter of fact, all the components of the total energy whose exact forms are unknown and difficult to obtain via theoretical means are *'swept under the carpet'* within this functional. As of recent time, highly accurate, superior approximations for this functional are easily available.

At this point an important question which can be asked is how do we be able to find the potential V_S for the non–interacting reference system, so that that leads to a antisymmetrized wave function (Slater determinant) which is associated with the exact same density as our system of interest. To answer this we will rewrite the energy of our system in terms of the newly separated $F[\rho]$ as written in (2.36),

$$E[\rho] = T_S[\rho] + J[\rho] + E_{XC}[\rho] + E_{Ne}[\rho] \tag{2.38}$$

Expanding the respective terms we obtain,

$$E[\rho] = T_S[\rho] + \frac{1}{2}\int\int \frac{\rho(\vec{r}_1)\rho(\vec{r}_2)}{r_{12}} d\vec{r}_1 d\vec{r}_2 + E_{XC}[\rho] + \int V_{Ne}\rho(\vec{r}) d\vec{r} \tag{2.39}$$

$$\begin{aligned} = -\frac{1}{2}\sum_i^N \langle \psi_i|\nabla^2|\psi_i\rangle + \frac{1}{2}\sum_i^N\sum_j^N \int\int |\psi_i(\vec{r}_1)|^2 \frac{1}{r_{12}} |\psi_j(\vec{r}_2)|^2 d\vec{r}_1 d\vec{r}_2 \\ + E_{XC}[\rho] - \sum_i^N \int \sum_A^M \frac{Z_A}{r_{1A}} |\psi_i(\vec{r}_1)|^2 d\vec{r}_1 \end{aligned} \tag{2.40}$$

The only unknown term in the equation (2.40) is $E_{XC}[\rho]$. If we now apply variational principle on (2.40) to minimize the energy under the constraint $\langle \psi_i|\psi_j\rangle = \delta_{ij}$, we obtain the famous

Kohn–Sham equation,

$$\left(-\frac{1}{2}\nabla^2 + \underbrace{\left[\int \frac{\rho(\vec{r}_2)}{r_{12}} d\vec{r}_2 + \hat{V}_{XC}(\vec{r}_1) - \sum_A^M \frac{Z_A}{r_{1A}} \right]}_{V_{eff}(\vec{r}_1)} \right) \psi_i = \varepsilon_i \psi_i \tag{2.41}$$

where, $\hat{V}_{XC}$is defined as the functional derivative of E_{XC} with respect to ρ,

$$\hat{V}_{XC}(\vec{r}) = \frac{\partial E_{XC}[\rho(\vec{r})]}{\partial \rho(\vec{r})} \tag{2.42}$$

The resulting equation is very similar to the eigen–equation of the Hartree-Fock method. However, equation (2.41) it is much simpler as in the HF case the Fock operator contains the non–local potential which is different for each electron. In the Kohn-Sham operator the V_{eff} potential depends only on $\vec{r}$, and not on the index of the electrons and hence it is same for all electrons. The Kohn-Sham orbitals, ψ_i, which can be easily derived from equation (2.41)and can be used to calculate compute the total density,

$$\rho(\vec{r}) = \sum_{i=1}^{N} |\psi_i(\vec{r})|^2 \tag{2.43}$$

which can further be utilized to calculate a new improved potential $\hat{V}_{eff}(\vec{r})$ which will eventually lead to a new self-consistent cycle. It is crucial to mention that $\psi_i(\vec{r})$'s are not equivalent to the the real orbitals of the system, and hence they do not associated to any real physical meaningful system. Their sole purpose is to provide a theoretical mapping in between between the kinetic energy and the density. Also to mention that the total KS wave function is a single determinant approach and fails where multiple determinant are needed in order to describe the system e.g. during dissociation process of a molecule. An example scheme of KS iteration during single point or optimization cycle is depicted in Figure 2.1.

2.8 Conceptual DFT

2.8.1 Global Reactivity Descriptors

As we have already mentioned, in order locate the minima of the energy functional i.e, $\partial E[\rho(\vec{r})] = 0$, it must be constrained by the N–representability condition[1,7–9] of the density which is already optimized.[4] For the present case the N–representability constraint can be represented as,

$$\int \rho(\vec{r}) d\vec{r} - N = 0 \tag{2.44}$$

Now, using the Lagrange's method of undetermined multipliers we get,

$$\partial \left\{ E[\rho(\vec{r})] - \mu \left[\int \rho(\vec{r}) d\vec{r} - N \right] \right\} = 0 \tag{2.45}$$

[4] the equation must also be constrained by v-representability[10] as well, however, as of now we still not have any clue how to mathematically express v–representability. Some mathematical formulation like Levy's constrained search (1982) and Petkov's local–scaling approximation (1986) are available in the literature which automatically ensure v–representability during density optimization.[11,14]

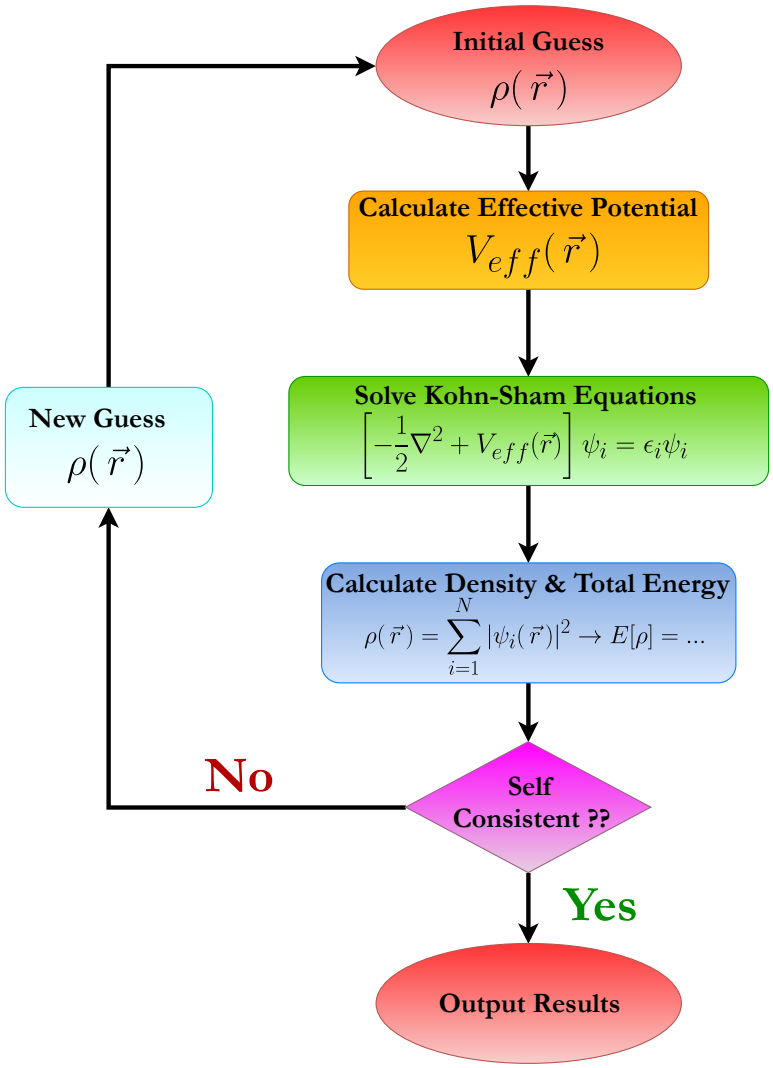

FIGURE 2.1: A common flowchart of the Kohn–Sham iteration scheme.

where, μ is the undetermined multiplier. Solving the differential equation leads to,

$$\partial E[\rho(\vec{r})] - \mu\partial\left\{\int \rho(\vec{r})d\vec{r}\right\} = 0 \tag{2.46}$$

Now we know that the definition of differential of the functional can be presented as,

$$F[f+\partial f] - F[f] = F = \int \frac{\partial F}{\partial f(x)}\partial f(x)dx \tag{2.47}$$

Using the aforementioned formula also considering the fact that the differential and integral signs can be mutually interchanged we get

$$\int \frac{\partial E[\rho(\vec{r})]}{\partial \rho(\vec{r})}\partial\rho(\vec{r})d\vec{r} - \mu\int \partial\rho(\vec{r})d\vec{r} = 0 \tag{2.48}$$

As both the integration have the same limit and runs over the same variable, we can combine the whole expression under a single integral,

$$\int\left\{\frac{\partial E[\rho(\vec{r})]}{\partial \rho(\vec{r})} - \mu\right\}\partial\rho(\vec{r})d\vec{r} = 0 \tag{2.49}$$

which is the condition for constrained minimization and also defines the value of the Lagrange multiplier μ at minimum. using equation (2.28) we can represent μ in terms of the external potential($\hat{V}_{ext}$),

$$\mu = \frac{\partial E[\rho(\vec{r})]}{\partial \rho(\vec{r})} = \hat{V}_{ext}(\vec{r}) + \frac{\partial F_{HK}[\rho(\vec{r})]}{\partial \rho(\vec{r})} \tag{2.50}$$

This equation is commonly known as the Euler–Lagrange equation.

In 1978, Parr and coworkers[15] provided a interpretation of the Lagrangian multiplier μ. They have shown that showed that under *N*–representability and *v*–representability condition and if the density is associated with some anti–symmetric wavefunctions, the Lagrangian multiplier μ obtained from Eqn.2.50 can be represented as the the derivative w.r.t. the value of constraint, N, of the minimum of the functional E$[\rho(\vec{r})]$

$$\mu = \left(\frac{\partial E}{\partial N}\right)_{\hat{V}_{ext}(\vec{r})} \tag{2.51}$$

If we consider an analogy to thermodynamic chemical potential which is defined as,

$$\mu_{therm} = \left(\frac{\partial G}{\partial N}\right)_{P,T} \tag{2.52}$$

where, G is the Gibbs free energy and N is the number of moles, the undetermined multiplier μ can be termed as electronic chemical potential. In a similar way like the chemical potential, μ estimates the escaping tendency of the electrons from the system. Iczkowski and Margrave[16] have given further clarification of the Lagrange multiplier by providing the electronegativity formula which is $\mathscr{X} = -(\frac{\partial E}{\partial N})_{n=0}$, where n=N–Z, Z is the atomic number of the nucleus. Thus the electronegativity can be related with μ with the following formula,

$$\mathscr{X} = -\mu = -\left(\frac{\partial E}{\partial N}\right)_{\hat{V}_{ext}(\vec{r})} \tag{2.53}$$

It is important to note that the Mulliken's definition of electronegativity,

$$\mathscr{X}_M = \frac{I+A}{2} \tag{2.54}$$

where, I and A are the ionization energy and electron affinity respectively, are actually the finite difference approximation of equation 2.53

In a similar manner, the second derivative of the energy with respect to number of electrons is termed as absolute hardness (η) by Parr and Pearson[17],

$$\eta = \frac{1}{2}\left(\frac{\partial^2 E}{\partial N^2}\right)_{\hat{V}_{ext}(\vec{r})} = \frac{1}{2}\left(\frac{\partial \mu}{\partial N}\right)_{\hat{V}_{ext}(\vec{r})} \tag{2.55}$$

Therefore from 2.55, chemical hardness or η can be interpreted as the resistance of chemical potential to the change in the number of electrons of the system. The definition of η can further be related with the conventional definition,

$$\eta = \frac{I-A}{2} \tag{2.56}$$

via the finite difference approximation of equation2.55. Similar to the chemical hardness another important parameter is the softness (S), which is defined as,

$$S = \frac{1}{2\eta} = \left(\frac{\partial N}{\partial \mu}\right)_{\hat{V}_{ext}(\vec{r})} \tag{2.57}$$

The concept of η was later utilized for the theoretical deduction of HSAB principle by the same author. However, detail discussion regarding HSAB principle is out of the scope of the present thesis.

Another very important reactivity descriptor namely the electrophilicity index was introduced by Parr, Von Szentpaly and Liu by combining the concept of hardness and electronegativity introduced earlier. In their proposed model, the electrophile is assumed to be exist within a sea of free electrons which is at zero temperature and at zero chemical potential[18]. The energy change due to electron transfer from the free electron sea to the electrophile is represented in a power series expansion upto second order at constant external potential,

$$\Delta E = \mu \Delta N + \frac{1}{2}\eta \Delta N^2 \tag{2.58}$$

the saturation point of electron inflow was considered as,

$$\frac{\Delta E}{\Delta N} = 0 \tag{2.59}$$

Combining Eqs.2.58 and 2.59, we get the amount of electron transfer,

$$\Delta N = -\frac{\mu}{\eta} \tag{2.60}$$

and the stabilization energy due to electron transfer,

$$\Delta E = -\frac{\mu^2}{2\eta} \tag{2.61}$$

The term $\frac{\mu^2}{\eta}$, is denoted as electrophilicity index (W) in an analogy to the equation of power

($W = \frac{V^2}{R}$) from classical electricity and considered as a measurement of electrophilicity of the chemical species. (W) is also considered as a measure of the "electrophilic power" of the electrophile. Using the finite difference approximation, (W) can be written as,

$$W = \frac{\mu^2}{2\eta} = \frac{(I+A)^2}{8(I-A)} \tag{2.62}$$

Equation 2.62 can be related to frontier orbital energies by using the Koopman's approximation from the molecular orbital theory. According to Koopman's approximation ionization energy (I) and electron affinity (A) can be expressed in terms of HOMO and LUMO energies[19–21].

$$I = -\varepsilon_{HOMO} \tag{2.63}$$

$$A = -\varepsilon_{LUMO} \tag{2.64}$$

Although, all these parameters like chemical potential, electrophilicity index, softness and hardness are capable to describe the overall reactivity of the system (hence the name, global reactivity descriptor) , they do not contain any information about the type of active atoms or functional groups within the molecule.

2.8.2 Local Reactivity Descriptors

In all chemical process the reactivity of individual atoms or functional groups matters most rather than the reactivity of the molecule as a whole. Thus, despite the global reactivity descriptors are theoretically profound and interesting concept, in real practice, it is not that useful as GRD's are unable to provide the important local information mostly sought by the chemists. Thus, since the early days of conceptual DFT, all these demands from the chemistry community have facilitated the development of some descriptors which are local in nature and commonly abbreviated as the local reactivity descriptors or LRDs.

The concept of utilizing electron density as a tool of describing the reactivity of molecules was first initiated by Kenchi Fukui when he proposed three fundamental principles regarding the frontier molecular orbitals orbitals of aromatic compounds in 1952.[22,23]. The proposal considered that the attacking site is influenced by the electron density of the electrons in the frontier–orbitals. Thus, for electrophilic attack, the frontier orbitals should be the highest occupied molecular orbitals or HOMO, for nucleophilic attack, the frontier orbitals are of lowest unoccupied molecular orbital or LUMO. Similarly, for radical attack, one electron is assumed to be in HOMO and another one is in LUMO.

Parr and his collaborators was among the first who was able to provide a connection in between the Fukui's frontier molecular orbitals theory and the density functional theory[1,17,24,25]. Using the ensemble formulation of DFT, they have defined the frontier function as,

$$f(r) = \left(\frac{\partial \mu}{\partial \hat{V}_{ext}(\vec{r})}\right)_N = \left(\frac{\partial \rho(\vec{r})}{\partial N}\right)_{\hat{V}_{ext}(\vec{r})} \tag{2.65}$$

The equations for change in energy is considered as,

$$dE = \mu dN + \int \rho(\vec{r}) dV_{ext}(\vec{r}) dr \tag{2.66}$$

$$d\mu = 2\eta dN + \int f(\vec{r}) dV_{ext}(\vec{r}) dr \tag{2.67}$$

In the equation 2.67 the quantity $d\mu$ estimates the extent of the reaction. The preferred direction is considered as the one in which the initial value of $|d\mu|$ for the species is found to be a maximum. The first term on the right hand side of 2.67 consists only global quantities and is generally less direction sensitive than the second term on the r.h.s at larger distance. The preferred direction is associated with maximum $f(r)$ at the respective reaction site.
Similar to E(N), $\rho(r)$ also has discontinuity at integral N. The equation 2.65 shows two reaction indices as left and right– hand side derivatives which are needed to include under consideration for a given number of electrons, N=N_0.

$$f^{-}(\vec{r}) = \left(\frac{\partial \rho(\vec{r})}{\partial N}\right)^{-}_{V_{ext}(\vec{r})} \tag{2.68}$$

which is for for an electrophilic attack associated an electron density increase in the system, and

$$f^{+}(\vec{r}) = \left(\frac{\partial \rho(\vec{r})}{\partial N}\right)^{+}_{V_{ext}(\vec{r})} \tag{2.69}$$

which is for a nucleophilic attack associated an electron density decrease in the system.
If we consider the frozen core approximation $d\rho = d\rho_{valence}$ in each case and hence for the electrophilic attack

$$f(\vec{r})^{-} = \rho_{HOMO} \tag{2.70}$$

and the nucleophilic attack can be approximated as

$$f(\vec{r})^{+} = \rho_{LUMO} \tag{2.71}$$

and the third function which governs a radical attack, is a average of the above two,

$$f(\vec{r})^{0} = \frac{1}{2}(\rho_{HOMO} + \rho_{LUMO}) \tag{2.72}$$

Frontier function is normalized to unity,

$$\int f^{a}(\vec{r})dr = 1 \qquad \forall a = +,-,0 \tag{2.73}$$

Thus, although FF can provide the relative information about different reactive regions of a given molecule, it is, however, does not able to describe the local intensity of the response. Another parameter namely the local softness $s(r)$, introduced by Parr and Yang can be used for such purpose,[26]

$$s(r) = \left(\frac{\partial \rho(\vec{r})}{\partial \mu}\right)_{V_{ext}(\vec{r})} \tag{2.74}$$

$s(r)$ is considered as a local analogue to the global softness S (2.57). Using the chain rule, the local softness can be rewritten as the product of total softness and the FF,

$$s(r) = \left(\frac{\partial \rho(\vec{r})}{\partial \mu}\right)_{V_{ext}(\vec{r})} = \left(\frac{\partial \rho(\vec{r})}{\partial N}\right)_{V_{ext}(\vec{r})} \left(\frac{\partial N}{\partial \mu}\right)_{V_{ext}(\vec{r})} = f(r).S \tag{2.75}$$

In order to describe all three type of attack namely, electrophilicity, nucleophilicity or radical, The above equation can also be written as,

$$\int s^{a}(\vec{r})dr = f^{a}(\vec{r})S \qquad \forall a = +,-,0 \tag{2.76}$$

$$S = \int s^a(\vec{r})dr \qquad \forall a = +,-,0 \tag{2.77}$$

2.8.3 Atom Condensed Local Descriptors

As the Fukui function ($f(r)$) is a function of r, one can identify the reactive centers within a molecule only from the plot of $f(r)$ with respect to r. However, such implementation is not so trivial and in order to obtain a quantitative description of reactivity of each atom, it is soon found to be essential to get a new descriptor which would provide a single valued numerical contribution of each atoms or sites towards the overall reactivity of the molecule. Yang and Mortimer first defined such Fukui functions via following a similar procedure like the population analysis technique[18] and commonly called as '*Atom condensed Fukui functions*.'

$$f_A^+ = q_{A,N_0+1} - q_{A,N_0} \tag{2.78}$$

$$f_A^- = q_{A,N_0} - q_{A,N_0-1} \tag{2.79}$$

$$f_A^0 = \frac{1}{2}(q_{A,N_0+1} - q_{A,N_0-1}) \tag{2.80}$$

where, $q_{A,N}$ signifies the electronic population of atom A of a system with N number of electrons. In the original article Mulliken's population scheme[27] was used to describe the reactivity of each atoms within the molecule. However, in common practice other population analysis like Löwdin population[28] analysis, Hirshfeld population, natural population analysis[29], Bader's atoms–in–molecules (AIM) method[30], charges derived from molecular electrostatic potential[31,32] and electronegativity equalization methods[33,34], are also commonly used in order to calculate the atom condensed FFs.
Using Equations 2.76, 2.77 and 2.78 – 2.80 it is also possible to define various condensed local softness of any specific atoms,

$$s_A^a = f_A^a S \qquad \forall a = +,-,0 \tag{2.81}$$

where, +, – and 0 indicate the electrophilicity, nucleophilicity and susceptibility for radical attack respectively.
Pal and co–workers have introduced the concepts of '*Relative Electrophilicity*' (R.E) and '*Relative nucleophilicity*' (R.N)[35]. These descriptors were proven to be highly accurate and reliable descriptors for determining the intramolecular reactivity since they can provide information about both the electrophilic and nucleophilic character. The description of these descriptors were given as,

$$R.E = \frac{s_A^+}{s_A^-} \tag{2.82}$$

$$R.N = \frac{s_A^-}{s_A^+} \tag{2.83}$$

The local electrophilicity (w_A^+) was introduced considering the additive rule, $S = \sum s_A^+$ and Eq. 2.62,

$$W = \frac{\mu^2}{2\eta} = \frac{\mu^2}{2}S = \frac{\mu^2}{2}\sum s_A^+ = \sum w_A^+ \tag{2.84}$$

From equation 2.84, Perez *et al.* have proposed a regional electrophilicity power values, condensed on atom A[36].

$$w_A = \frac{\mu^2}{2} s_A^+ \tag{2.85}$$

Assuming the existence of some possible function $w(r)$ which integrates to the global philicity (W), Chattaraj and co–authors[37] have presented a generalized version of aforementioned equation using the resolution of the identity associated with Fukui functions,

$$W = W \int f(r) = \int W f(r) = \int w(r) \tag{2.86}$$

They have proclaimed that the $w(r)$ has the information about both $f(r)$ and W which can successively also provide information of softness and the chemical potential. Therefore, it can be considered as the most powerful concept of reactivity and selectivity if compared to other descriptors. However, by observing the numerical performance, this concept was further criticized by Roy and coworkers[38,39]. They have argued that the philicity index does not contribute any additional reliability over other descriptors as in all of the the original contribution is coming from the Fukui functions. Atom condensed philicity can be represented as,

$$w_A^a = W f_A^a \qquad \forall a = +, -, 0 \tag{2.87}$$

References

(1) Parr, R. G.; Yang, W., *Density functional theory of atoms and molecules*; Oxford University Press, New York: 1989, pp 1–352.

(2) Koch, W.; Holthausen, M. C., *A chemist's guide to density functional theory*; John Wiley & Sons: 2015.

(3) Hohenberg, P.; Kohn, W. *Physical review* **1964**, *136*, B864.

(4) Gross, E.; Kurth, S., *Density Functional Theory: The Modern Treatment of Electron Correlations*; Springer US: 1994, pp 367–409.

(5) Gross, E.; Kohn, W *Advances in quantum chemistry* **1990**, *21*, 255–291.

(6) Dreizler, R. M.; Gross, E., *Density Functional Theory: An Approach to the Quantum Many-Body Problem Springer*; Berlin: 1990.

(7) Gilbert, T. *Physical Review B* **1975**, *12*, 2111.

(8) Lieb, E. *A. Shimony and H. Feshbach (MIT, Cambridge, MA)* **1982**, 111.

(9) Harriman, J. E. *Physical Review A* **1981**, *24*, 680.

(10) Kohn, W *Physical review letters* **1983**, *51*, 1596.

(11) Levy, M. *Physical Review A* **1982**, *26*, 1200.

(12) Lieb, E. H. *International Journal of Quantum Chemistry* **1983**, *24*, 243–277.

(13) Kohn, W.; Sham, L. J. *Physical review* **1965**, *140*, A1133.

(14) Petkov, I. Z.; Stoitsov, M. V.; Kryachko, E. S. *International Journal of Quantum Chemistry* **1986**, *29*, 149–161.

(15) Parr, R. G.; Donnelly, R. A.; Levy, M.; Palke, W. E. *The Journal of Chemical Physics* **1978**, *68*, 3801–3807.

(16) Iczkowski, R. P.; Margrave, J. L. *Journal of the American Chemical Society* **1961**, *83*, 3547–3551.

(17) Parr, R. G.; Pearson, R. G. *Journal of the American Chemical Society* **1983**, *105*, 7512–7516.

(18) Parr, R. G.; Szentpaly, L. v.; Liu, S. *Journal of the American Chemical Society* **1999**, *121*, 1922–1924.

(19) Pearson, R. G. *J. chem. Educ* **1987**, *64*, 561.

(20) Koopmans, T *Physica* **1933**, *1*, 104–113.

(21) Pearson, R. G. *Proceedings of the National Academy of Sciences* **1986**, *83*, 8440–8441.

(22) Fukui, K; Yonezawa, T; Shingu, H; Yonezawa, T *J. chem. Phys* **1952**, *20*, 722.

(23) Fukui, K.; Yonezawa, T.; Nagata, C.; Shingu, H. *The Journal of Chemical Physics* **1954**, *22*, 1433–1442.

(24) Parr, R. G.; Yang, W. *Journal of the American Chemical Society* **1984**, *106*, 4049–4050.

(25) Yang, W.; Parr, R. G. *Proceedings of the National Academy of Sciences* **1985**, *82*, 6723–6726.

(26) Geerlings, P.; De Proft, F.; Langenaeker, W. *Chemical reviews* **2003**, *103*, 1793–1874.

(27) Mulliken, R. S. *The Journal of Chemical Physics* **1955**, *23*, 1833–1840.

(28) Löwdin, P.-O. *Physical Review* **1955**, *97*, 1474.

(29) Reed, A. E.; Weinstock, R. B.; Weinhold, F. *The Journal of Chemical Physics* **1985**, *83*, 735–746.

(30) Bader, R. F. *Chemical Reviews* **1991**, *91*, 893–928.

(31) Singh, U. C.; Kollman, P. A. *Journal of Computational Chemistry* **1984**, *5*, 129–145.

(32) Bayly, C. I.; Cieplak, P.; Cornell, W.; Kollman, P. A. *The Journal of Physical Chemistry* **1993**, *97*, 10269–10280.

(33) Gasteiger, J.; Marsili, M. *Tetrahedron* **1980**, *36*, 3219–3228.

(34) De Proft, F; Langenaeker, W; Geerlings, P *Journal of Molecular Structure: THEOCHEM* **1995**, *339*, 45–55.

(35) Roy, R.; Krishnamurti, S; Geerlings, P; Pal, S *The Journal of Physical Chemistry A* **1998**, *102*, 3746–3755.

(36) Pérez, P.; Toro-Labbé, A.; Aizman, A.; Contreras, R. *The Journal of organic chemistry* **2002**, *67*, 4747–4752.

(37) Chattaraj, P. K.; Maiti, B.; Sarkar, U. *The Journal of Physical Chemistry A* **2003**, *107*, 4973–4975.

(38) Roy, R. K. *The Journal of Physical Chemistry A* **2004**, *108*, 4934–4939.

(39) Roy, R. K.; Usha, V; Paulovic, J.; Hirao, K. *The Journal of Physical Chemistry A* **2005**, *109*, 4601–4606.

Chapter 3

The Effect of Electronic Shell Structure of Aluminum Nanoclusters on the Oxidative addition of C−I bond

3.1 Introduction

The C–C cross coupling reaction with transition metals as catalyst is the most promising tool of organic and material synthesis since the last four decades[1,2]. Bond formation process between two carbon atoms is highly energy demanding and hence a slow process[3,4]. Therefore C–C coupling reaction requires suitable catalyst to bring down the energy barrier and make the reaction practically viable with reasonably good chemical yield. Most extensively used catalysts are Cu, Ni and Pd complex[5–7]. Recent development in both experimental and theoretical contexts have shown Fe[8–10] and Au[11–13] perform moderately well in C–C cross coupling reaction. Among all these popular methodologies, most versatile and efficient catalyst for cross coupling reaction is the heterogeneous Pd(0) catalyst[14–16], commonly used via the different reaction schemes primarily developed by Kumada[17], Heck[18], Sonogashira[19], Negishi[20], Stille[21] and Suzuki[14,22] in the early 70-80's. Heterogeneous Pd(0) catalyst not only gives good chemical yield with better product quality, but it is also reusable and most of the reaction schemes are less demanding[23]. Furthermore, most of the organo–palladium complexes are less sensitive towards moisture or air and also have high functional group tolerance. However, despite the above, Pd catalyst suffers from some well known disadvantages. Heterogeneous Pd catalyst is prone to catalyst poisoning and leaching[24,25]. Both Pd and Ni which are widely used catalyst for cross–coupling are highly expensive and poisonous, having low LD_{50} values[26,27]. Fine powder of Pd used as heterogeneous catalyst is pyrophoric as well[28].Therefore, finding an alternatives catalyst of Ni and Pd is the prime field of research to both theoreticians and experimentalists in recent years[16]. Among the newly developed alternative catalysts, both experimental[13,29] and theoretical investigations[30] have shown that Au nanoparticles can be used as an effective catalyst for C–C cross–coupling reaction. However, similar to Pd catalyst Au is also a rare element and highly expensive, which restricts its use for large scale industrial synthesis.

Al nanoclusters are well known for its reactivity[31–33]. Specifically, small sized aluminum clusters of 2–50 atoms are extremely reactive and show strong affinities to adsorb gaseous species such as H_2, D_2, O_2, N_2 and H_2O[34–38].The reactivity trends of open and closed shell aluminum clusters with oxygen are of great interest lately and experimental implementation[39–41] of the same is proven to be extremely influential in elucidating the role of spin conservation on the reactivity of aluminum clusters. Recent work by Castleman and Bergeron has shown that small sized aluminum cluster anions can dissociate the C–I bond of methy iodide with relative ease[42]. Scientists have also observed that CH_3II can be dissociated on Al(111) surface, confirmed by both scanning tunneling microscopy (STM) and DFT investigation[43]. Further analysis based on Jellium model reveals that specific Al clusters have some unique features. For example, Al_{13}

cluster shows similarity with halogens, forms stable complexes with iodine[44], produces ionic assemblies with superalkali countercations[45,46], and even forms similar family of compounds comparable with polyhalides[47]. On the other hand, Al_7 shows both divalent and tetravalent valencies[48] similar to that of carbon. All of these observations, stability and reactivity can neatly be explained by homogeneous electron gas (HEG) model or most commonly mentioned as *'Jellium model'* first used by Knight and co–workers[49] for similar context. These potent studies on Al clusters provoke further interest to judge their stabilities and reactivities for different chemical reactions and to observe and explain the effects of electronic structures, size and shape upon the energetics and mechanism. Detailed analysis can be useful and will have promising impacts in the field of nanoscience and technologies in the upcoming days.[50]Alongside these wide possibilities within the nano–regime, experiment and theoretical studies on atomic clusters can also be proven convenient in disclosing the long lasting queries about the bulk matter itself. Recently, Schnöckel and coworkers[41,51,52] have shown that oxidation reactions of Al_{13}^- cluster in HCl and Cl_2 environment can be treated as a precise micro analogue of the oxidation reaction of the bulk counterpart. Based on the state-of-the-art FT–ICR mass spectrometry they have evaluated each possible sub reaction steps of the oxidation process in both environment with absolute accuracy. Aside from the kinetic similarities regarding the products and intermediates, DFT investigation have shown astonishing thermodynamic resemblance in terms of exothermicity with the bulk metal for the same reactions. It is needless to say that in depth studies like these are of utter importance and definitely prospective in understanding the growth and form of bulk matter with atomic precision.

Figure 3.1 shows most common schematics[14] of cross–coupling reaction using Pd as catalyst. Other catalysts e.g Ni, Fe or Au follow similar mechanistic steps. The reaction proceeds via the oxidative addition of Pd(0) complex to organo–halide to form a Pd(II) complex. Next step is the transmetallation with another organometallic reagent where the nucleophile R′ is transferred from the metal to the Pd(II), which is the slowest step in the whole cycle and hence the rate determining step. The final process is the reductive elimination to give the coupled product (R–R′) and regeneration of the Pd(0) complex, to be ready for the next catalytic cycle. The overall catalytic reaction can be summarized as,

$$\mathrm{R-X+R'-M} \xrightarrow{\mathrm{M'(0)}} \mathrm{R-R'+M-X} \tag{3.1}$$

where M′=Pd,Ni,Au,Fe etc.

Oxidative addition is the process by which C–I bond dissociates and two separate bonds with the metal are created[3]. The opposite reaction is commonly known as reductive elimination. The process is reversible, but depending on overall thermodynamics, basicity of the metal and nature of the reactants, one particular direction is generally favored over the other one. Oxidative addition to a mononuclear complex increases the oxidation state of the metal center by 2, whereas for a binuclear metal catalyst, oxidation state of each metal center increases by one unit. One of the most amazing feature of oxidative addition is the wide range of reactants which can be involved in the dissociation process. Starting from highly polar molecule like organo halides or acids to totally non–polar molecule(H_2) can be dissociated with equivalent ease. The oxidative process can proceed via any of the four mechanistic pathways depicted in Figure 3.2. The first one is commonly know as the concerted mechanism, where breaking of C–I bond and formation of the bonds with the metals occurs simultaneously via a three member transition state. This process is common for non–polar molecules or aryl halides and followed by retention of configuration of corresponding stereogenic center. Unlike the concerted one, the S_N2 mechanism proceeds via the nuclophillic attack of the metal to less electronegative counterpart of the substrate leading to the cleavage of R–X bond in a organometallic cation, followed by coordination of X^- anion. This mechanism is mostly common for polar molecules and resulting retention of configuration

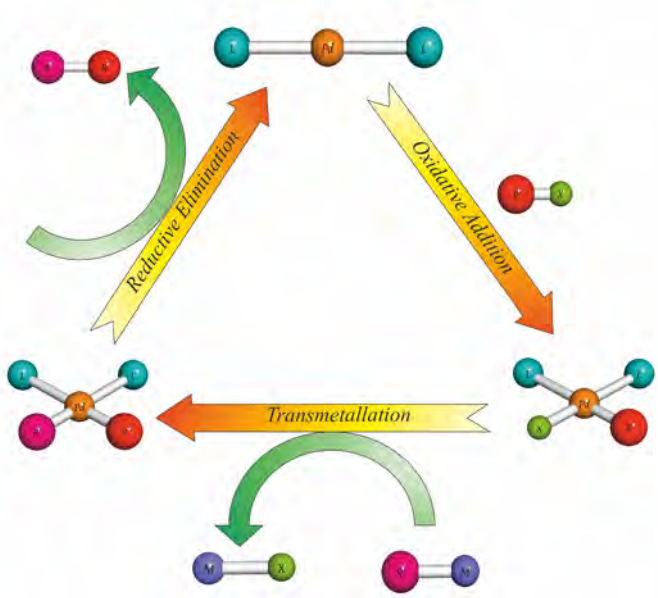

FIGURE 3.1: A common scheme for cross coupling reaction cycle using Pd as catalyst. The transmetallation step is the slowest step and hence the rate determining step.

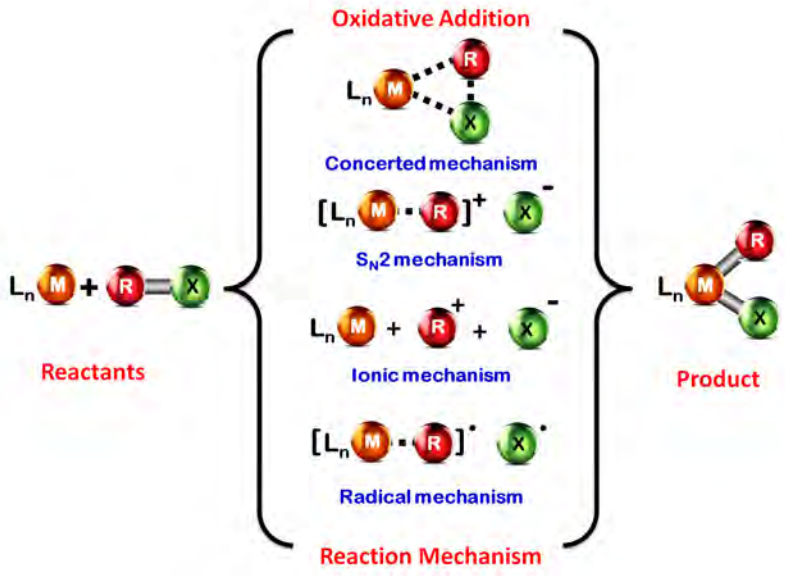

FIGURE 3.2: All the possible reaction mechanisms for the oxidative addition of organohalides with metal catalyst.

of the stereogenic center. Third possibility of oxidative addition is through the ionic mechanism. This pathway is possible if the substrate (R–X) gets completely dissociated into two ionic fragments prior to the reaction. The overall mechanism can proceed via two following ways. First one is the attachment of R^+ fragment to the metal center, followed by subsequent coordination of X^- with the cationic complex. The alternative one is just the opposite where halide anion first coordinates with the metal center resulting an anionic complex with a rapid coordination of R^+ yielding the final product. The final one among the listed mechanism is non chain radical pathway[53]. The overall process in this mechanism is similar to S_N2 mechanism, only difference being that the fragmentation process generates radical species rather than ions, with the halide radical attaches itself with the organometallic radical. Rate of the reaction depends on the basicity of the metal, bond strength of R–X fragment and nature of substrate and solvent. The default rate of the reaction can further be influenced by modifying substrates, solvents or by adding foreign substances like radical scavengers[3], which in fact can even introduce radical pathway in a reaction which otherwise would have followed non–radical pathway. In some rare situations, two or more mechanistic pathway can participate in a competitive manner and the final outcome depends on the thermodynamics and the kinetics of each pathway and also on the imposed reaction conditions. Oxidative addition reactions of organo–halides are extensively studied and their mechanism is well established because of their importance in cross coupling reaction. The choice of halogens is usually in the order I > Br > Cl as C–X bond dissociation energy follows an opposite order[54] C–Cl($\sim$ 83 kcal mol^{-1}) > C–Br($\sim$72 kcal mol^{-1})> C–I($\sim$57 kcal mol^{-1}). Hence, iodine is the best leaving group among all the halides.

In this current chapter we have presented the thermodynamic and kinetic details for the dissociation of C–I moiety on Al nanoclusters. Accurate DFT calculations shows that the Al nano clusters can participate in C–I bond dissociation, effective in both aliphatic and aromatic C–I bond cleavage. In addition with that in–depth reaction mechanism,detailed structural analysis and effect of shell structures of the clusters on the reaction controlling parameters are also properly accounted with BOMD simulation and NBO analysis.

The chapter is organized as follows, in section 2 we have described in details the computational technique used. Section 3 deals with our results and elaborate discussion. Important conclusions are drawn in section 4.

3.2 Computational Details

All the clusters, Al_3, Al_5, Al_6, Al_7, Al_8, Al_{13} and Al_{20} in different possible conformations are optimized in the frame work of DFT using Gaussian 09 software package[55] with the TZVP basis set and B3PW91 functional. Only the lowest energy optimized structure in each case is chosen as one of the reactants in the C–I dissociation. All the organo–iodides (iodoethane, iodoethene and iodobenzene) are also optimized using same TZVP basis and B3PW91 functional for C and H similar to the prior case. However, for iodine, an ECP basis set such as LANL2DZ is used. Optimization of reactants and transition state are performed using Berny's algorithm implemented in Gaussian 09 package. Normal modes of vibration of the optimized structures are carefully observed and it is made sure that all the energetically minimized structure (reactants) have no imaginary frequency whereas the transition states must and only have one single imaginary frequency of appropriate magnitude and which corresponds to the C–I bond itself. Intrinsic reaction coordinate (IRC) calculations are performed to confirm that the transition structures are connected with proper reactants and products along positive and negative direction of chemical reaction coordinate. Same calculations are further repeated using Minnesota functional M06–2X and also in BHandHLYP functional in an attempt to properly bracket the activation barrier for C–I dissociation on Al clusters. Thermodynamically controlled product of the reaction for

each metal cluster was determined by calculating the energies of all possible products and choosing the energetically lowest conformer. Basis set superposition error (BSSE) are corrected using Boys and Bernardi's counterpoise correction scheme[56] within the Gaussian 09 software. Rate constants of C–I dissociation are calculated by using the Eyring–Polanyi equation[57–59]

$$k = \frac{k_B T}{h} e^{-\frac{\Delta G^{\ddagger}}{RT}} \quad where \quad \Delta G^{\ddagger} = G^{\ddagger}_{TS} - G_{Reactant} \tag{3.2}$$

of transition state theory at 298 K and 1 atm pressure.
For a brief analysis of underlying reaction mechanism Natural Bond Orbital (NBO) analysis are performed on selected pre and post reaction complexes using NBO 3.0 suite implemented in Gaussian 09. NBO analysis are further used for each clusters separately to get the insight about stabilization of cluster during aromatic and aliphatic C–I bond cleavage on Al nanoclusters. The second order perturbative estimation of donor–acceptor stabilization energy(E_s) within the NBO basis are computed by

$$E_s = \Delta E_{ij} = q_i \frac{F_{ij}^2}{\Delta \varepsilon_{ji}} \tag{3.3}$$

where q_i is donor orbital occupancy number. F_{ij} is off–diagonal elements of Fock matrix in NBO basis. $\Delta\varepsilon_{ji}$=ε_j-ε_i is the orbital energy difference between acceptor(j) and donor(i) NBO.

Three dimensional potential energy surface scan is performed in B3PW91 functional and with the basis set described earlier in this section.The surface consists of a total 3111 grid points. 51 markers are assigned for C–I bond stretching along x axis and 61 are for increment of Al–I–C angle along y axis. Relaxed optimization are performed at each point without imposing any additional constraints. Energies(in a.u) obtained through the DFT calculation in each optimized points are plotted along the z axis. The surface is constructed by connecting all the plotted points in three dimensional Cartesian coordinate and a colormap is assigned based on the DFT calculated data range.

To gain further insight into the reaction mechanism we have carried out *ab initio* molecular dynamics simulation(BOMD) at room temperature (300K) using deMon.2.2.6[60] package. A total simulation time of 40 pico–second (ps) is introduced to assure that R–I molecule can have sufficient time to interact properly with the Al cluster. The temperature of the complex is maintained using the Berendsens thermostat (I = 0.5 ps) in an NVT ensemble[61]. The nuclear positions are updated using velocity Verlet algorithm with a time step of 1 fs. Throughout the whole simulation, we have fixed the total angular momentum of the cluster to zero, thereby suppressing the cluster rotation. Auxiliary density functional theory is employed for the BOMD simulations[62].

3.3 Results and Discussion

To investigate the dissociation process of C-I bond on Al atomic clusters , we have chosen seven different atomic clusters of aluminum viz. Al_3, Al_5, Al_6, Al_7, Al_8, Al_{13} and Al_{20} keeping in mind that properties of atomic cluster are size and shape sensitive. Among them lowest energy conformers of Al_3 and Al_5 are planner and two–dimensional reflecting the monovalent character of aluminum alike alkali metals in low coordination[63]. However, starting from Al_6 cluster becomes three dimensional as overlapping effect between s and p orbital becomes pronounced. As the second reactant we have selected three organo–iodides which are ethyl, ethylene and benzyl iodide respectively i.e. a combination of one alkyl, one alkene and one aryl halide of choice. Although calculations are performed in three different DFT functionals B3PW91, BHandHLYP and M06–2X, during structural and binding energy comparison and also for Natural Bond Orbital (NBO) analysis we have followed the results obtained by M06–2X functional

as family of Minnesota functionals are well known for good structural prediction as well as bonding interactions[64]. Binding energies of the R–I molecule with Al clusters in all cases are calculated by the following formula $\Delta E = E(Al_n...IR) - E(R\text{-}I) - E(Al_n)$ All the thermodynamic parameters are calculated at 298 K and in 1 atm pressure.

The results and discussion section is divided into three parts. In the first part we have discussed structural and thermo–chemical aspects of C–I dissociation on selected Al clusters based on DFT investigation. Second part of the discussion includes the mechanistic aspects of oxidative addition over Al cluster based on the DFT calculation and the natural bond orbital(NBO) analysis. The findings of Born Oppenheimer Molecular Dynamics simulation of C–I bond activation upon Al cluster are further included in this section. One of the important features of atomic clusters is that each cluster can behave drastically different from each other. The major reason lies behind is the electronic and geometric shell effect of the cluster itself, commonly known as the cluster size effects(CSE)[65]. CSE of a cluster can uniquely change the reactivity of each member of same cluster family, and as a result all the parameters including thermochemistry, reaction mechanism and structure of reactants and products can be abruptly different for each member, even for the same reaction. Due to above fact, we have tried to emphasize on each cluster while discussing in details. Specific observations which may be caused by CSE are also duly noted and attempted to explain accordingly. Third part provide the comparison of our result with experimental and theoretical results available in modern literature. Fourth section comprises remarks and final conclusions.

3.3.1 Structural and Thermochemical aspects

We begin our discussion with the two smallest clusters of our study which are Al_3 and Al_5. As mentioned earlier, both these clusters are two dimensional having very high surface to volume ratio. Hence, it is expected that both of these cluster should be more reactive and hence will show low activation barrier. Table 3.1–3.6 compiles all the thermodynamic data including rate constants and binding energy for all three organo–iodides. It is evident from the table that for all three cases both Al_3 and Al_5 indeed have shown low activation barrier and very high rate constants in all three functionals. Results obtained in B3PW91 functional is usually less than other two functionals, in some cases estimated barrier in B3PW91 functional is lower by factor of two or three when compared with the results obtained in other two functionals. An activation energy($\Delta G^{\ddagger}$) of 1.8 kcal mol^{-1} in B3PW91 functional is also observed for ethyl iodide on Al_3 cluster, which is the lowest activation barrier reported within the study (therefore highest rate constant of magnitude $\sim 10^{11}$ unit) ,whereas same parameter predicted by other two functionals is much higher. This trend is also observed in other clusters which seems to raise a suspicion that results obtained in B3PW91 functional seem to underestimate the activation barrier. Underestimation of activation barrier is not uncommon for B3PW91 functional and DFT investigations have shown that other functional like BHandHLYP performs better in such cases[66]. Although it must also be mentioned, that this underestimation seems to be less pronounced for bigger clusters and in some rare cases activation barrier obtained in B3PW91 function is closer with M06–2X result (e.g. dissociation of iodoethene on Al_8 cluster) than BHandHLYP functional.

Comparison of the reactivity of Al_3 cluster with Al_5 cluster is not as straight forward as comparing its reactivity with other members within our study. According to the jellium model, considering the monovalent character of aluminum in this size scale, Al_3 cluster has a total of 3 valence electrons ,one electron higher than the magic number 2 due to 'S' Jellium shell closing. Hence a low activation barrier for oxidative addition is expected as the cluster achieves the stable filled shell magic cluster configuration upon one electron loosing. So, based on the argument Al_3 cluster should be more reducing than Al_5 cluster as this stability driven electronic shell effect is absent in later case. This prediction is proven correct for ethyl iodide(Table 3.1

TABLE 3.1: Thermodynamic data of C–I bond dissociation of ethyl iodide on Al nanoclusters in B3PW91, BHandHLYP and M06–2X functional.

	Activation Barrier (kcal mol^{-1})						Exothermicity (kcal mol^{-1})					
Al	$\Delta H^{\ddagger}$			$\Delta G^{\ddagger}$			ΔH			ΔG		
nanoclusters	B3PW91	BHandHLYP	M06–2X	B3PW91	BHandHLYP	M06–2X	B3PW91	BHandHLYP	M06–2X	B3PW91	BHandHLYP	M06–2X
Al_3	0.705	7.292	6.202	1.832	11.192	7.295	-68.081	-71.553	-64.846	-67.456	-68.444	-63.575
Al_5	5.164	11.060	9.479	7.316	14.918	10.846	-58.403	-61.849	-60.713	-56.262	-57.428	-59.827
Al_6	4.439	12.144	8.857	6.541	15.625	11.379	-47.158	-56.626	-40.552	-46.537	-54.080	-39.978
Al_7	2.841	9.640	7.709	4.036	12.238	5.483	-53.555	-57.093	-50.184	-51.612	-54.186	-48.669
Al_8	9.413	16.282	13.711	10.632	18.397	14.737	-65.354	-69.868	-67.631	-61.816	-66.651	-66.661
Al_{13}	8.597	7.258	16.695	9.178	8.838	16.560	-45.236	-50.683	-42.455	-42.414	-46.067	-39.977
Al_{20}	11.469	16.544	18.805	13.644	18.306	20.031	-48.776	-55.676	-47.731	-48.232	-54.399	-46.490

TABLE 3.2: Thermodynamic data of C–I bond dissociation of ethylene iodide on Al nanoclusters in B3PW91, BHandHLYP and M06–2X functional.

	Activation Barrier(in kcal mol^{-1})						Exothermicity(kcal mol^{-1})					
Al	$\Delta H^{\ddagger}$			$\Delta G^{\ddagger}$			ΔH			ΔG		
nanoclusters	B3PW91	BHandHLYP	M06–2X	B3PW91	BHandHLYP	M06–2X	B3PW91	BHandHLYP	M06–2X	B3PW91	BHandHLYP	M062X
Al_3	4.006	6.826	8.791	3.863	8.654	9.586	-73.791	-77.766	-69.935	-72.377	-74.146	-68.929
Al_5	3.41	6.946	7.87	5.87	10.094	9.37	-60.89	-65.742	-63.84	-56.65	-60.636	-61.94
Al_6	19.389	27.248	25.621	21.205	30.240	26.141	-51.935	-61.309	-49.841	-50.561	-58.799	-48.487
Al_7	0.0119	4.095	3.465	2.792	6.332	3.4142	-49.237	-51.670	-48.396	-43.689	-47.857	-46.610
Al_8	13.181	22.654	16.330	16.192	27.652	19.013	-70.875	-76.372	-74.621	-68.449	-71.590	-70.903
Al_{13}	15.575	6.025	13.344	14.765	9.963	14.297	-48.890	-55.785	-45.624	-46.921	-50.573	-45.218
Al_{20}	18.830	27.634	23.864	22.645	29.934	24.625	-54.431	-62.086	-53.145	-51.850	-59.805	-54.103

TABLE 3.3: Thermodynamic data of C–I bond dissociation of benzyl iodide on Al nanoclusters in B3PW91, BHandHLYP and M06–2X functional.

	Activation Barrier (kcal mol^{-1})						Exothermicity (kcal mol^{-1})					
Al	$\Delta H^{\ddagger}$			$\Delta G^{\ddagger}$			ΔH			ΔG		
nanoclusters	B3PW91	BHandHLYP	M06–2X	B3PW91	BHandHLYP	M06–2X	B3PW91	BHandHLYP	M06–2X	B3PW91	BHandHLYP	M06–2X
Al_3	3.481	8.143	11.948	4.950	10.796	12.721	-74.692	-78.099	-67.672	-69.841	-72.341	-67.209
Al_5	3.492	6.963	8.603	5.200	11.071	8.205	-64.80	-65.956	-67.480	-61.30	-60.477	-63.855
Al_6	16.798	24.783	20.505	18.232	26.438	21.321	-49.720	-56.960	-46.863	-47.156	-53.253	-46.011
Al_7	5.029	4.237	6.803	8.708	6.666	9.926	-58.275	-61.880	-51.150	-53.974	-60.206	-49.409
Al_8	19.184	28.822	15.942	19.294	33.059	18.710	-70.119	-76.144	-71.593	-69.550	-72.259	-68.978
Al_{13}	16.404	11.172	17.034	14.805	13.099	16.182	-47.936	-54.385	-42.701	-47.047	-53.240	-43.065
Al_{20}	22.309	29.801	26.408	21.067	31.146	29.952	-52.173	-61.441	-51.088	-54.767	-60.064	-48.499

TABLE 3.4: Rate constants and binding energies for C–I bond dissociation of ethyl iodide on Al nanoclusters in B3PW91, BHandHLYP and M06–2X functional.

Al nanoclusters	E.P Rate constant			Binding Energy(kcal mol^{-1})	
	B3PW91	BHandHLYP	M062X	ΔE(M06–2X)	ΔE_{BSSE}(M06–2X)
Al_3	$2.815x10^{11}$	$3.845x10^{4}$	$2.772x10^{7}$	-5.005	-4.348
Al_5	$2.677x10^{7}$	$7.124x10^{1}$	$6.901x10^{4}$	-4.338	-3.786
Al_6	$9.909x10^{7}$	$2.155x10^{1}$	$2.804x10^{4}$	-9.805	-8.923
Al_7	$6.809x10^{9}$	$6.573x10^{3}$	$5.907x10^{8}$	-1.856	-0.838
Al_8	$9.904x10^{4}$	$1.999x10^{-1}$	$9.656x10^{1}$	-6.987	-5.938
Al_{13}	$1.154x10^{6}$	$2.047x10^{6}$	$4.445x10^{0}$	-4.781	-3.919
Al_{20}	$6.122x10^{2}$	$2.331x10^{-1}$	$1.267x10^{-2}$	-9.491	-8.393

TABLE 3.5: Rate constants and binding energies for C–I bond dissociation of ethylene iodide on Al nanoclusters in B3PW91, BHandHLYP and M06–2X functional.

Al nanoclusters	E.P Rate constant			Binding Energy(kcal mol^{-1})	
	B3PW91	BHandHLYP	M06–2X	ΔE(M06–2X)	ΔE_{BSSE}(M06–2X)
Al_3	$9.121x10^{9}$	$2.792x10^{6}$	$5.788x10^{5}$	-4.414	-3.927
Al_5	$3.077x10^{8}$	$2.456x10^{5}$	$8.343x10^{5}$	-3.351	-2.976
Al_6	$1.744x10^{-3}$	$4.131x10^{-10}$	$4.188x10^{-7}$	-8.389	-7.607
Al_7	$5.567x10^{10}$	$1.410x10^{8}$	$1.946x10^{10}$	-2.146	-1.904
Al_8	$8.280x10^{0}$	$3.265x10^{-8}$	$7.070x10^{-2}$	-4.400	-3.642
Al_{13}	$9.221x10^{1}$	$3.065x10^{5}$	$2.031x10^{2}$	-3.599	-2.976
Al_{20}	$1.534x10^{-4}$	$6.913x10^{-10}$	$5.418x10^{-6}$	-6.503	-5.579

TABLE 3.6: Rate constants and binding energies for C–I bond dissociation of benzyl iodide on Al nanoclusters in B3PW91, BHandHLYP and M06–2X functional.

Al nanoclusters	E.P Rate constant			Binding Energy (kcal mol^{-1})	
	B3PW91	BHandHLYP	M06–2X	ΔE(M06–2X)	ΔE_{BSSE}(M06–2X)
Al_3	$1.454x10^{9}$	$7.504x10^{4}$	$2.910x10^{3}$	-6.312	-5.851
Al_5	$9.539x10^{8}$	$4.719x10^{4}$	$5.966x10^{6}$	-3.811	-3.406
Al_6	$2.642x10^{-1}$	$2.532x^{-7}$	$1.433x10^{-3}$	-8.980	-8.129
Al_7	$2.549x10^{6}$	$8.023x10^{7}$	$3.262x10^{5}$	-6.784	-6.109
Al_8	$4.398x10^{-2}$	$3.534x10^{-12}$	$1.178x10^{-1}$	-7.122	-6.394
Al_{13}	$8.612x10^{1}$	$1.536x10^{3}$	$8.425x10^{0}$	-6.907	-6.068
Al_{20}	$2.203x10^{-3}$	$8.943x10^{-11}$	$6.711x10^{-10}$	-8.800	-7.768

and Figure 3.6 (a)). Both $\Delta G^{\ddagger}$ and $\Delta H^{\ddagger}$ values for Al_3 cluster are lower than Al_5 cluster for all three functionals. However, the same cannot be said for other two iodides. Results obtained for iodoethene and iodobenzene in all three functionals are too close to comment about their exact reactivity order towards oxidative addition of C–I bond. As a matter of fact, inclusion of other factors like nature of the reactants(iodides), geometrical stability of clusters and structure of transition states are necessary to conclude their relative reactivity. It is evident that all of these factors cumulatively determine the magnitude of the activation barrier rather than the electronic shell effect alone.

All the other clusters within our study are three dimensional with relatively lower surface to volume ratio than Al_3 or Al_5. Most of them have shown comparatively higher activation barrier than the planner ones as expected(Table 3.1–3.6). Only exception is the Al_7 cluster which have shown exceptionally low activation barrier for all three iodides in all three functional. Computed activation energies of Al_7 cluster is comparable with planer clusters or even lower than that of Al_3 and Al_5 clusters. Explanation of this unusual behavior can again be given from jellium picture. According to the jellium model, electronic structures of Al_7 and Al_3 cluster are similar. Al_7 cluster has 21 valence electrons, one electron more than closed shell configuration(20). Hence, similar to that of Al_3 cluster, it is expected that Al_7 cluster should show low activation barrier towards oxidative addition. This conclusion further proves the fact that unlike the case of Al_3, electronic shell effect is the dominant factor for the reactivity of Al_7 cluster. Among all the clusters Al_7 has shown the second lowest activation barrier($\Delta G^{\ddagger}$ of 2.8 kcal mol^{-1}) and second highest E.P rate constant of order $\sim 10^{10}$ unit for iodoethene in B3PW91 functional. In spite of these exceptional behavior of Al_3 and Al_7 due to electronic shell effect(ESE), the activation barrier seems to increase with increase in the size of the cluster, as expected, which after a particular size scale would eventually render the cluster completely ineffective towards the oxidative addition, as observed in bulk phase. Thus, based on all three functionals Al_{20} cluster on average shows highest activation barrier and hence lowest rate constants among all the clusters listed. Figure 3.6(a) collects activation free energies for ethyl iodide in all three DFT functionals. It is prominent from the oscillatory nature from the plot that 'Shell effect' is indeed the key factor which determines the chemical reactivity of aluminum clusters towards oxidative addition. As mentioned earlier all the clusters having number of valence electron higher by one unit than the closed jellium shell configuration shows lower activation barrier and higher rate constant than the rest of the members. This observation is indeed consistent with the experimental findings obtained by Castleman and Bergeron[42], where the reactivity of the cluster anion is found to be inversely proportional with the electron affinity of them and Al_{13}^- is found to be least reactive.The chemical inertness of Al_{13}^- is also observed in the acid dissolution experiment performed by Bowen, Schnöckel and coauthors[41,51]. Even with strong acid like hydrochloric, Al_{13} cluster anion is found to be resistant towards oxidation due to the presence of highly endothermic intermediate reaction steps.Hence, in order to initiate the cascade of acid leaching reactions, additional energy input via radio–frequency (RF) pulse is observed to be essential. Similar behavior is again reflected in experiment with Cl_2[41,52],O_2[39–41]as well as NH_3[67] environment. The chemical inertness of Al_{13}^- can again be attributed to its filled shell magic number(40) configuration alike to the present study.

Moving to the exothermicity values, first thing to observe from Table 3.1–3.6 is both the ΔG and ΔH values for all clusters are highly negative. When compared by magnitude, the exothermicity values are nearly double or triple than the ΔG and ΔH values obtained for gold clusters in the same functionals[30]. Highly negative ΔG values indeed indicate enhanced spontaneity of the reaction in accordance to thermodynamic principles and high exothermicity(ΔH) proves higher thermodynamic stability of the post reaction complexes. One important observation in all the cases of our study is that the change in Gibbs free energy of the reaction (ΔG) values are always

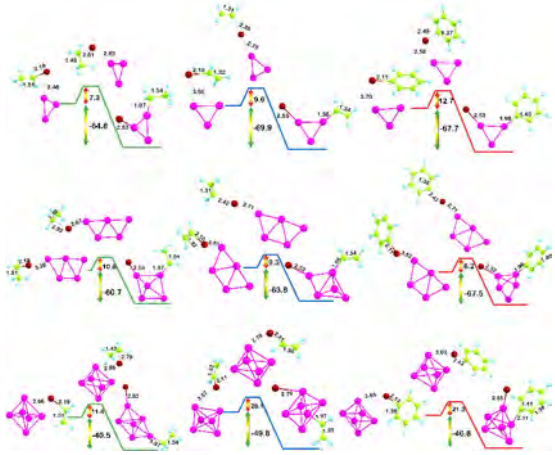

FIGURE 3.3: Energy profile diagrams for Al_3-Al_6 clusters for all three iodides.Orange arrow highlights the activation barrier ($\Delta G^{\ddagger}$) and green arrow highlights corresponding exothermicity(ΔH) in M06–2X functional

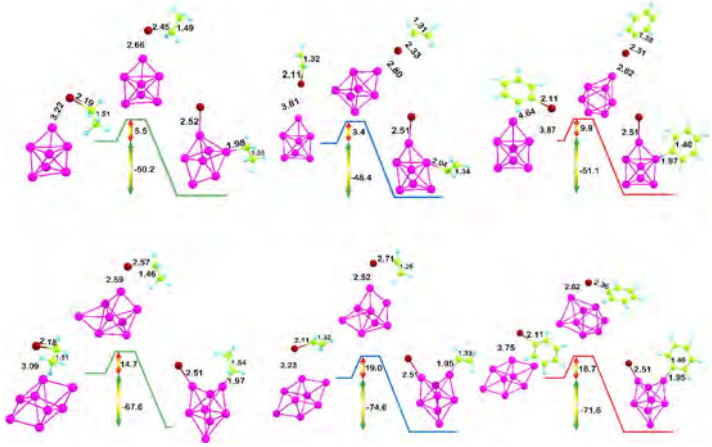

FIGURE 3.4: Energy profile diagrams for Al_7 and Al_8 clusters for all three iodides.Orange arrow highlights the activation barrier ($\Delta G^{\ddagger}$) and green arrow highlights corresponding exothermicity(ΔH) in M06–2X functional

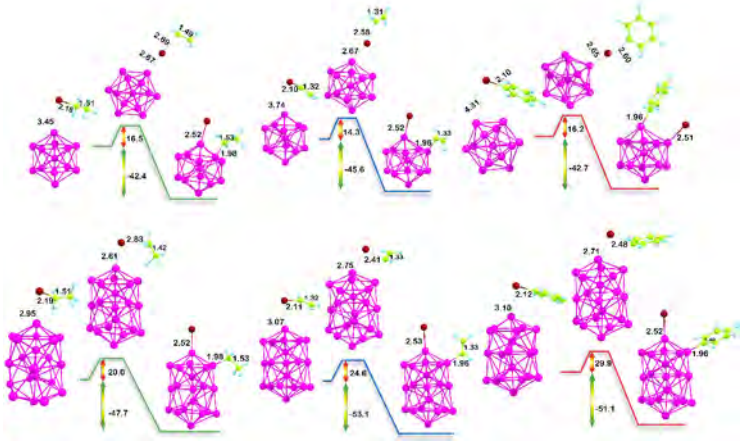

FIGURE 3.5: Energy profile diagrams for Al_{13} and Al_{20} clusters for all three iodides.Orange arrow highlights the activation barrier ($\Delta G^{\ddagger}$) and green arrow highlights corresponding exothermicity(ΔH) in M06–2X functional.

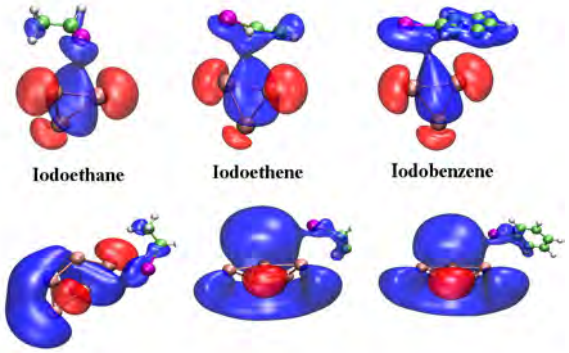

FIGURE 3.6: Frontier molecular orbitals of pre–reaction complexes of Al_3 and Al_5 cluster with all three iodides. In all cases iodine binds with Al cluster utilizing its lone pair. In specific cases minor contribution from π electrons (for ethylene and benzyl group) are also observed.

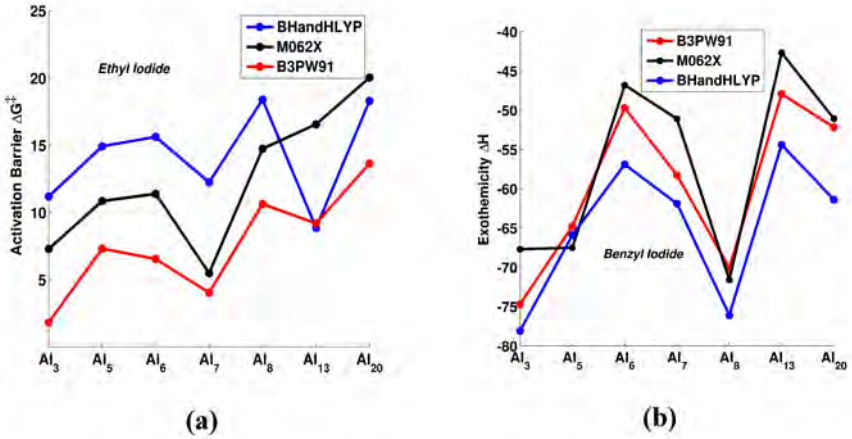

FIGURE 3.7: Plot of activation energies (a) for ethyl iodide and exothermicities (b) for benzyl iodide in all three functionals.The random trend shows strong influence of *'Shell effect'* on both the parameters. Low activation barriers (a) for Al_3 and Al_7 can be explained by invoking the concept of spherical *Jellium shells*.

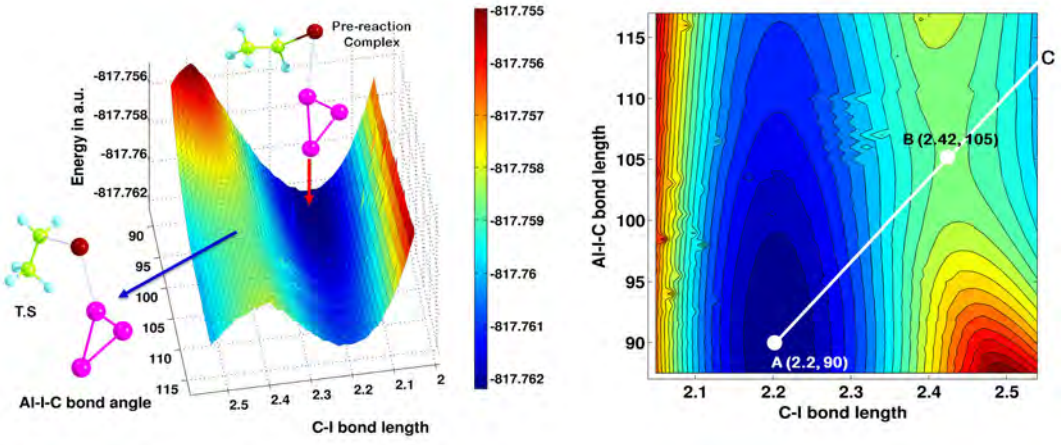

FIGURE 3.8: A segment of three dimensional potential energy surface (calculated in B3PW91 functional) for the reaction between Al_3 cluster and ethyl iodide. Contour plot for the same is given in the right hand side. The plot clearly indicates position of pre–reaction complex, transition state and the minimum energy path (MEP) towards the post–reaction complex.

greater than change in enthalpy of reaction(ΔH) values. Hence, the reaction is entropically unfavorable, which is expected in case of oxidative addition. Brief investigation using NBO analysis reveals that principle reason of this high exothermicity is intra–cluster stabilization in the post reaction complexes. NBO calculation indicates that all the post–reaction complexes are highly stabilized by multiple newly introduced donor acceptor(Al–Al) interactions which were either absent or have negligible contribution in the pre–reaction complexes. For example, for the reaction of iodoethane on Al_3 cluster we have found two newly introduced Al(LP)–Al(LP*) donor acceptor interactions of magnitude 72.6 and 122.1 kcal mol^{-1} respectively in the post–reaction complex, whereas no Al(LP)–Al(LP*) interaction with stabilization energy contribution higher than 32 kcal mol^{-1} is found in the pre–reaction complex for the same. Similar intra–cluster interactions are also observed for other clusters within the list as well. This signifies that the cluster gets more stabilized via intra–cluster donor acceptor interaction upon attachment of the fragmented R–I moieties after the dissociation process. This is the prime reason of high exothermicity and high spontaneity of the dissociation process. Figure 3.9 shows pictorial representation of some of these intra–cluster interactions with their respective stabilization energies for different clusters. Plotting the exothermicity values with cluster size(Figure 3.6 (b)) shows similar oscillatory pattern as obtained in case of activation energies in all functional and for all three organo iodides. The exothermicity pattern again reflects the importance of electronic shell effect on determining their chemical behavior.

In this context it is interesting to look upon the geometrical or structural stability of the aluminum clusters. All the structures of pre and post– reaction complexes are included Figure 3.3, 3.4 and 3.5. It is evident that upon attachment of R and I group, all of the small sized (Al_3–Al_8) clusters get structurally distorted. Only exception is the Al_3 cluster which due to having a planer three membered ring, is unable to release the strain (Baeyer's strain) via out–of–plane bending. Hence, only distortions which are observed for Al_3 cluster are mostly consists of bond length or angle distortions. Except Al_3 cluster, all the other clusters upto Al_8 show significant distortions in the post–reaction complexes upon R–I attachment. Most notable among them is the dramatic structural change of Al_5 cluster which, in its lowest energy conformer, is planer but changes to a distorted pyramidal shape in the post reaction complex as evident from Figure 3.3. On the contrary bigger clusters Al_{13} and Al_{20} are mostly found resistant to structural changes (Figure 3.5). Al_{13} is a 13 atom icosahedral cluster, icosahedral shape is well known for its high stability and the key factor to control the geometrical stability in cluster chemistry. On the other hand structure of Al_{20} cluster can easily be constructed by combining two Al_{13} clusters on top of each other and removing the pentagonal pyramidal cap of the lower cluster. These unique shapes of both Al_{13} and Al_{20} are the key reasons of their structural integrity. Except some minor distortions,the icosahedral cores of both the Al_{13} and Al_{20} clusters are found to be totally intact in the post–reaction complexes.That proves that unlike the case of HCl and Cl_2[41,51,52]icosahedric Al clusters are structurally resistant towards leaching by the organo–iodides, which is, as a matter of fact is also proven by related experiment[42].

Tables 3.2, 3.4 and 3.6 collect binding energy values calculated in M06–2X functional for all three iodides calculated using the formula mentioned earlier. Binding energy values represents the strength of Al–I bond in the pre–reaction complexes. Binding energy values are significantly lower than that of gold clusters, which can be explained improvising the fact that position of aluminum in the periodic table is in period 3, whereas gold (Au) an element of period 6 lies much closer with iodine (period 5). Hence, binding of iodine will be more stronger with iodine than aluminum due to better orbital matching. In our case, binding energy values on aluminum clusters for all thee iodides lies within the range $\sim$ 1 kcal mol^{-1} to $\sim$ 10 kcal mol^{-1}. Highest BSSE corrected binding energy value is obtained in case of Al_6 for iodoethane which is 8.9 kcal mol^{-1}. Based on our DFT calculations on all three reactants and in M06–2X functional, Al_6 cluster shows better binding energy(ΔE_{BSSE} 7.6–8.9 kcal mol^{-1}) than rest of the clusters. Trends

in binding energies also follow the same random pattern like activation energy and exothermicity values signifying that CSE is the dominant factor in this case as well.

3.3.2 Reaction mechanism

To understand the details of the reaction mechanism of C–I bond dissociation on aluminum cluster, we have performed natural bond orbital (NBO) analysis and Born Oppenheimer Molecular Dynamics(BOMD) simulation along with the DFT calculation. Second order perturbation treatment of Fock matrix in the NBO basis usually provides information about most stabilizing donor–acceptor interaction between Lewis acid–base pairs which are present within the chemical species. On the other hand, BOMD calculation can simulate and interpret the dissociation process of C–I bond on aluminum cluster in real time. Observation based on frontier molecular orbital shows that in each case organo–iodides bind with aluminum cluster utilizing its lone pair electron density. Figure 3.7 shows the frontier molecular orbitals for the pre reaction complexes of both Al_3 and Al_5 cluster. Minor contribution from π electron density of iodoethene and iodobenzene can be observed from the figure. NBO analysis indicates a stabilization energy contribution of about 13.48 kcal mol^{-1} due to donor–acceptor interaction between nonbonding orbital(LP) of iodine in iodoethane to antibonding orbital (LP*) of Al_3 cluster. In case of iodoethene and iodobenzene on Al_3 stabilization energy values due to I(LP)–Al(LP*) interaction are found to be 10.86 kcal mol^{-1} and 7.31 kcal mol^{-1} respectively. The I(LP)–Al(LP*) stabilization energy for Al_5 cluster with ethyl iodide is 16.8 kcal mol^{-1}, for ethylene iodide it is 8.2 kcal mol^{-1} and in case of benzyl iodide which is 9.5 kcal mol^{-1} intermediate of the previous two values. Despite the fact that the frontier orbital picture indeed shows participation of π electron density in the bonding process with the cluster, NBO analysis shows no significant stabilization due to this interaction. In fact, no donor acceptor stabilization energy value more than 2 kcal mol^{-1} is obtained due to π electron participation to aluminum cluster. This result confirms that the dominant contribution to the stabilization of the pre–reaction complexes is due to the interaction between lone pair of iodine and with the cluster itself. The π electron density induces negligible effect in the binding energies.

The stabilizing interactions of iodine with the cluster are slightly different in post–reaction complexes of C–I dissociation. As observed from Figure 3.8, that in the pre–reaction complex of Al_3 and iodoethane the donor acceptor interaction are of σ type i.e. the orientation of non–bonding orbital of iodine and antibonding orbital of aluminum are along a common axis. However, this interaction changes to a parallel or π interaction in the post–reaction complexes can be seen from Figure 3.8. Although it seems that interchanging the orbital orientation barely affects the stabilization energy contributions. In all three post–reaction complexes of Al_3 cluster the I(LP)–Al(LP*) stabilization energies are in the range 11.3–11.4 kcal mol^{-1}, whereas for Al_5 cluster these values are within 8.5–12.0 kcal mol^{-1} for all three iodides. Binding of Carbon fragment in the post–reaction complex differs with that of iodine by two ways. Firstly,donor–acceptor stabilization energies are manyfold higher than that of iodine with aluminum. As for example C(LP)–Al(LP*) stabilization energies for ethyl, ethylene and benzyl iodide with Al_3 cluster are 71.6,83.1 and 66.1 kcal mol^{-1} respectively. The principle reason lies in the fact that both carbon and aluminum lies much closer in the periodic table, hence orbitals are well matched energetically as well as coefficient wise. Therefore the overlap between the NBO orbitals of carbon and aluminum is more effective resulting in higher stabilization energy contributions. Second major difference is that unlike the case of iodine which can only be stabilized by only one type of donor acceptor interaction(I(LP)–Al(LP*)), NBO calculation shows carbon can produce multiple types of donor acceptor interactions varied in stabilization energy, for

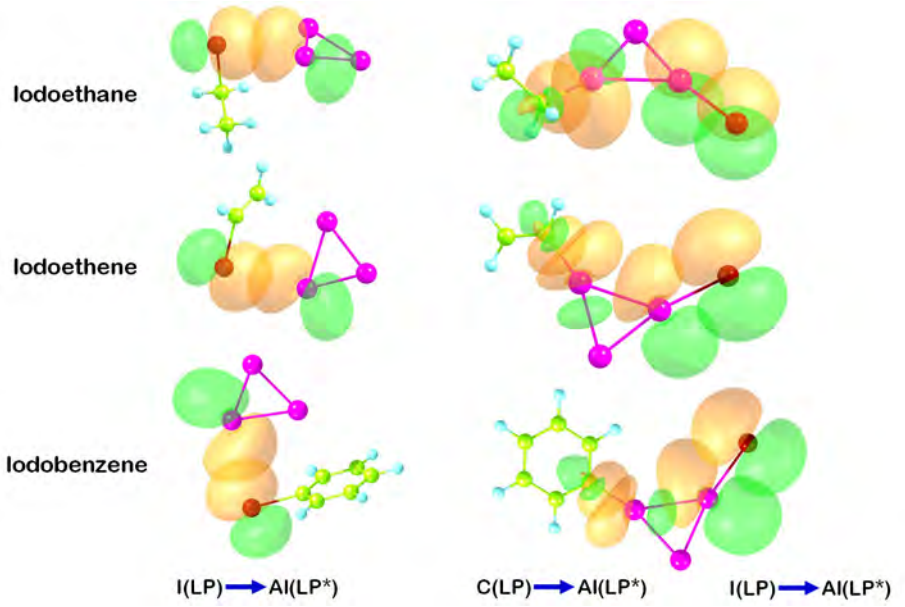

FIGURE 3.9: Most stabilizing donor–acceptor interactions for pre and post reaction complexes of Al_3 cluster as indicated by NBO analysis.

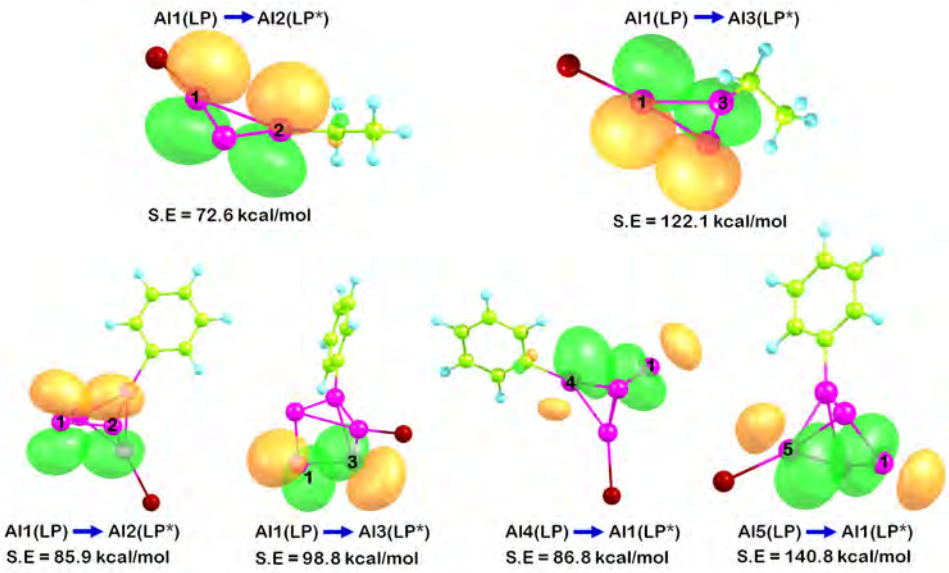

FIGURE 3.10: Most stabilizing intracluster donor–acceptor interactions in the post–reaction complexes for Al_3(iodoethane) and Al_5(iodobenzene) are shown as indicated by NBO analysis. These intracluster stabilization are the reason for the high exothermicity as indicated by DFT calculation.

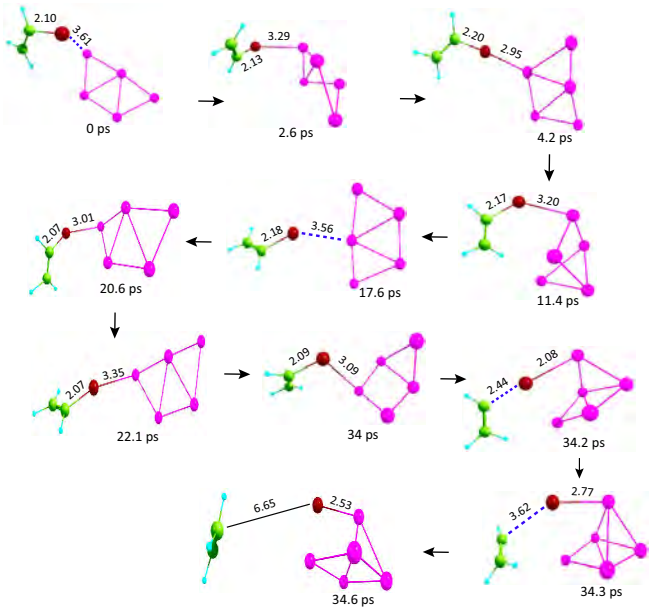

FIGURE 3.11: Molecular dynamics (BOMD) simulation steps of C–I dissociation(iodoethene) over Al_5 cluster. Bond lengths are in and simulation time in picosecond(ps).

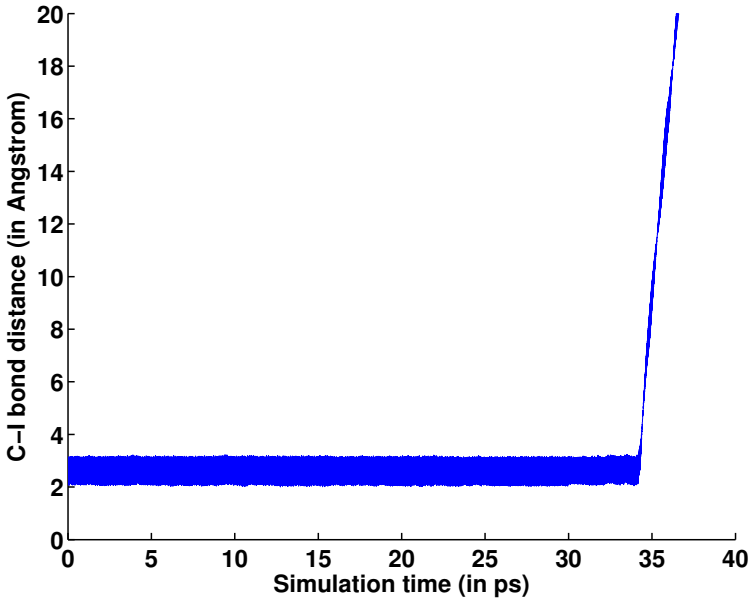

FIGURE 3.12: C–I bond length fluctuation during BOMD simulation of Al_5–C_2H_3I complex.

example Al_7 cluster The Al...C bond is stabilized by an amount of 21.5 kcal mol^{-1} due the interaction between non–bonding orbital of Al(n) and sigma antibonding interaction (Σ^*) of Al–C bond. This interaction is unique and not observed in any previous cases.

To further investigate the reaction in details, part of the potential energy surface is constructed for the reaction between Al_3 cluster and iodoethane in B3PW91 functional and in the given basis. Due to computational constraint and high exothermicity of the reaction (the post–reaction complex lies far below in the potential energy surface) only most significant portions of the surface is evaluated. Position of both pre–reaction and the transition states are evident from Figure 3.10. The right hand contour plot clearly shows that point C, which is the path towards the post–reaction complex is connected with the pre–reaction complex (point A) by a first order saddle point B.The geometry of the system at point A and B, evaluated from the potential surface calculation are indeed matches exactly with the optimized structures of pre–reaction complex and the transition state obtained by B3PW91 calculation as mentioned before. As shown in the right hand contour plot that point A, B and C can be connected via a possible minimum energy path (MEP) directing towards the post–reaction complex of the reaction. Figure 3.11 and 3.12 concludes the result obtained by Born–Oppenheimer Molecular Dynamics (BOMD) simulation of iodoethene on Al_5 cluster. The BOMD simulation demonstrates that after absorbing on Al surface R–I molecule undergoes several orientations until dissociates as shown in Figure 3.11. The starting geometry for MD simulation at 0 picosecond(ps) is the M06–2X optimized geometry of the reactant of iodoethene on Al_5 cluster. In the initial sturture at 0 ps the Al–I and I–C bond lengths are found to be 3.61 and 2.10 respectively. The C–I bond oscillate between 2.2 to 3.1 during the initial simulation steps upto 34 ps then it rapidly increases and finally dissociates at 34.6 ps as clearly observed from the plot of C-I bond length (in) versus time (ps) in Figure 3.12 .

3.3.3 Comparison with reported values

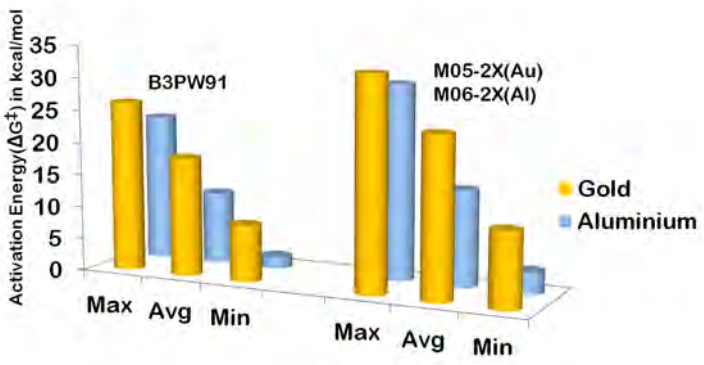

FIGURE 3.13: Qualitative comparison of activation free energies ($\Delta G^{\ddagger}$) of aluminum with gold cluster for C–I bond dissociation . In all aspects aluminum cluster shows better activation barrier than gold nano–clusters.

Comparison of the results obtained within the present study with other results available in literature is essential in order properly understand the reactivity of small sized aluminum

cluster towards C–I bond dissociation. Based on recent literatures, it is nearly impossible to quantitatively compare the results due to two prime reasons. Firstly, theoretical results obtained are often calculated in different theoretical levels with variable accuracy. As a second reason, it must be said that, there is certainly some limitation in terms of experimental context. As atomic clusters are extremely small particles ranging even within sub–nano level and also metastable in nature, there is difficulty associated to properly predict the structure and nature of reactants and products by experimental means. Hence, data obtained by experimental methods are rare and suffer from uncertainties due to the unstable nature of nano–clusters and there discrete size.

In spite of all these, it is still possible to compare and conclude qualitatively based on the data available in the literature. As mentioned in the introduction section, Corma and coworkers[13,29] have studied extensively the sonogashira cross–coupling on gold nanoparticles supported on cerium oxide(CeO_2) nanocrystals. Their study also includes the DFT calculated activation barrier for iodobenzene on Au_{38} cluster in PW91 functional which is 11.3 kcal mol^{-1}. Further study using B3PW91/6–31G(d,p) level of theory indicated that this activation barrier is much higher (31.6 kcal mol^{-1}) in Au^I complexes(Me_3PAuI) when compared to Au_{38} cluster. A more detailed DFT investigation is performed by Datta *et al.*[30] for the dissociation of ethyl, ethylene and benzyl iodide on neutral and positive charged clusters ranging from Au_3 to Au_{20}, much similar to our calculation. Their overall investigation is comprises of two types of DFT calculation in B3PW91/TZVP, LANL08(Au,I) and M05–2X/6-31+G(d), LANL2DZ(Au,I) level of theory. The maximum activation barriers obtained for neutral Au cluster in their calculation are 26.2 and 32.6 kcal mol^{-1} with an average of 18.2 and 24.5 kcal mol^{-1} at two levels of theory respectively. In both levels, the lowest free energy barrier(8.7 and 11.5 kcal mol^{-1} respectively) is calculated for iodobenzene on Au_3 cluster improvising the fact that small Au clusters are more reactive than the larger ones. Inclusion of results obtained for charged cluster within this data only barely affects the average activation barrier and maximum and minimum free energy barriers are not altered at all. Figure 3.13 shows a qualitative comparison column plot between the free energy barrier($\Delta G^{\ddagger}$) obtained for Au clusters with the results obtained for Al clusters in this current study. Qualitative comparison between two different set of DFT functional proves the superiority of the results obtained for aluminum cluster than gold cluster. In both set of data, aluminum cluster shows lower activation energy in all three categories which are maximum, minimum and average energy of activation. In B3PW91 functional aluminum clusters show an average free energy of activation of 11.1 kcal mol^{-1} with 22.6 kcal mol^{-1} and 1.8 kcal mol^{-1} being the maximum and minimum activation energy respectively. Similarly The maximum, average and minimum $\Delta G^{\ddagger}$ for Al clusters in M06–2X functional are found to be 29.9, 3.4 and 14.7 kcal mol^{-1}, much better than the results obtained for gold cluster mentioned earlier.

Comparison of our results with Pd cluster is more difficult because of the wider range of Pd contained complexes used in cross coupling reaction. Pd complexes usually shows a range of activation barrier starting from very low to medium activation free energy depending on the type of ligands attached with them and the reactants which are used. The different dissociative pathway can also differ in activation barrier in significant manner. Based on these facts activation barrier calculated for Pd catalyst also consists of broad range rather than a slender one. Available literature shows that concerted dissociation of C–I bond on Pd catalyst via a three member transition state shows an activation energy of 17 kcal mol^{-1}[3]. On the other hand, Bickelhaupt and de Jong, based on their gas phase relativistic DFT calculation, have shown that the activation barrier calculated by activation strain model for C–I bond dissociation via a S_N2 pathway with rearrangement on Pd catalyst is as low as 10 kcal mol^{-1}[68]. Calculated average activation barrier by two different functional for Al cluster(11.1 and 14.7 kcal mol^{-1}) lies closer within this range as mentioned above.

3.4 Conclusion

Present study includes a theoretical investigation of oxidative addition of C–I bond over Al clusters combining both Density functional theory and molecular dynamics methods. C–I bond dissociation is indeed a crucial reaction and provides a key step in various important organic reactions like cross–coupling. Most commonly used catalyst are d and f block elements like Pd, Ni, Cu, Fe and Au. Our investigation shows that although Al, which is a p block element is ineffective to dissociate the carbon–halogen bond in bulk phase, nano–clusters are found to be highly effective for the same. Calculated activation barriers reveal that Al nano–clusters are remarkably efficient towards C–I bond activation and dissociation. In terms of activation barriers and exothermicity, aluminum clusters have shown better results as compared to Au clusters. The calculated activation barriers are also within the range shown by the most versatile and efficient Pd catalyst. Further observation reveals that the reactivity of aluminum clusters in terms of activation barriers and other reaction parameters are highly dependent on the electronic (Jellium) shell configuration of the clusters, an observation consistent with the experimental findings.[39–42,51,52,67] This indeed concludes that effective reactivity can also be obtained in selected bigger clusters or even in solid supported clusters. Our study highlights a brief analysis including structures and stabilities of the reacting species along with the thermochemistry and mechanistic pathway of the reaction which may be proved highly useful for future experimental implementation for similar purposes. Al clusters have long been known for their high reactivity, as proven numerous times by both experiments and theory, our investigation also suggests that in cluster state aluminum can be equivalently reactive even as the transition metals. With the technological and experimental progress in nano–cluster synthesis, separation and stabilization, such fundamental studies based on the reactivity and stabilities of aluminum clusters may be proven rewarding and will no doubt be highly beneficial in disclosing the deepest secrets within the nano-regime.

References

(1) Kohei, T.; Miyaura, N. In *Cross-Coupling Reactions*; Springer: 2002, pp 1–9.

(2) Miyaura, N.; Buchwald, S. L., *Cross-coupling reactions: a practical guide*; Springer: 2002; Vol. 219.

(3) Melchor, M. G., *A Theoretical Study of Pd-Catalyzed CC Cross-Coupling Reactions*; Springer Science & Business Media,Springer International Publishing Switzerland: 2013.

(4) Colacot, T., *New Trends in Cross-Coupling: Theory and Applications*; Royal Society of Chemistry: 2014; Vol. 21.

(5) Diederich, F.; Stang, P. J., *Metal-catalyzed cross-coupling reactions*; John Wiley & Sons: 2008.

(6) Beletskaya, I. P.; Cheprakov, A. V. *Coordination chemistry reviews* **2004**, *248*, 2337–2364.

(7) Negishi, E. *Accounts of Chemical Research* **1982**, *15*, 340–348.

(8) Fürstner, A.; Leitner, A.; Méndez, M.; Krause, H. *Journal of the American Chemical Society* **2002**, *124*, 13856–13863.

(9) Fürstner, A.; Martin, R. *Chemistry Letters* **2005**, *34*, 624–629.

(10) Sherry, B. D.; Fürstner, A. *Accounts of chemical research* **2008**, *41*, 1500–1511.

(11) Zhang, G.; Peng, Y.; Cui, L.; Zhang, L. *Angewandte Chemie International Edition* **2009**, *48*, 3112–3115.

(12) Han, J.; Liu, Y.; Guo, R. *Journal of the American Chemical Society* **2009**, *131*, 2060–2061.

(13) González-Arellano, C.; Abad, A.; Corma, A.; García, H.; Iglesias, M.; Sanchez, F. *Angewandte Chemie* **2007**, *119*, 1558–1560.

(14) Miyaura, N.; Suzuki, A. *Chemical reviews* **1995**, *95*, 2457–2483.

(15) Bellina, F.; Carpita, A.; Rossi, R. *Synthesis* **2004**, *2004*, 2419–2440.

(16) Johansson Seechurn, C. C.; Kitching, M. O.; Colacot, T. J.; Snieckus, V. *Angewandte Chemie International Edition* **2012**, *51*, 5062–5085.

(17) Tamao, K.; Sumitani, K.; Kumada, M. *Journal of the American Chemical Society* **1972**, *94*, 4374–4376.

(18) Heck, R. F., *Palladium reagents in organic syntheses*; Academic Press London: 1985; Vol. 6.

(19) Sonogashira, K. *Journal of organometallic chemistry* **2002**, *653*, 46–49.

(20) King, A.; Okukado, N.; Negishi, E. *Journal of the Chemical Society, Chemical Communications* **1977**, 683–684.

(21) Stille, J. K. *Angewandte Chemie International Edition in English* **1986**, *25*, 508–524.

(22) Suzuki, A. *Journal of Organometallic Chemistry* **1999**, *576*, 147–168.

(23) Molnar, A. *Chemical reviews* **2011**, *111*, 2251–2320.

(24) Albers, P.; Pietsch, J.; Parker, S. F. *Journal of Molecular Catalysis A: Chemical* **2001**, *173*, 275–286.

(25) Webb, J. D.; MacQuarrie, S.; McEleney, K.; Crudden, C. M. *Journal of Catalysis* **2007**, *252*, 97–109.

(26) Rosen, B. M.; Quasdorf, K. W.; Wilson, D. A.; Zhang, N.; Resmerita, A.-M.; Garg, N. K.; Percec, V. *Chemical reviews* **2010**, *111*, 1346–1416.

(27) Kielhorn, J.; Melber, C.; Keller, D.; Mangelsdorf, I. *International Journal of Hygiene and Environmental Health* **2002**, *205*, 417–432.

(28) Bodnar, J.; Lugosi, G.; Nagy, G. Process for the preparation of non-pyrophoric palladium catalysts., US Patent 4,239,653, 1980.

(29) Corma, A.; Juárez, R.; Boronat, M.; Sánchez, F.; Iglesias, M.; García, H. *Chemical Communications* **2011**, *47*, 1446–1448.

(30) Nijamudheen, A; Datta, A. *The Journal of Physical Chemistry C* **2013**, *117*, 21433–21440.

(31) Khanna, S.; Jena, P *Phys. Rev. Lett.* **1992**, *69*, 1664.

(32) Khanna, S.; Jena, P *Phys. Rev. B* **1995**, *51*, 13705.

(33) Jones, N.; Reveles, J. U.; Khanna, S.; Bergeron, D.; Roach, P.; Castleman Jr, A. *The Journal of chemical physics* **2006**, *124*, 154311.

(34) Cox, D.; Trevor, D.; Whetten, R.; Kaldor, A *The Journal of Physical Chemistry* **1988**, *92*, 421–429.

(35) Jarrold, M. F.; Bower, J. E. *Journal of the American Chemical Society* **1988**, *110*, 70–78.

(36) Woodward, W. H.; Eyet, N.; Shuman, N. S.; Smith, J. C.; Viggiano, A. A.; Castleman Jr, A. *The Journal of Physical Chemistry C* **2011**, *115*, 9903–9908.

(37) Kulkarni, B. S.; Krishnamurty, S.; Pal, S. *J. Phys. Chem. C* **2011**, *115*, 14615–14623.

(38) Das, S.; Pal, S.; Krishnamurty, S. *The Journal of Physical Chemistry C* **2014**, *118*, 19869–19878.

(39) Burgert, R.; Schnöckel, H.; Grubisic, A.; Li, X.; Stokes, S. T.; Bowen, K. H.; Ganteför, G.; Kiran, B.; Jena, P. *Science* **2008**, *319*, 438–442.

(40) Neumaier, M.; Olzmann, M.; Kiran, B.; Bowen, K. H.; Eichhorn, B.; Stokes, S. T.; Buonaugurio, A.; Burgert, R.; Schnokel, H. *Journal of the American Chemical Society* **2014**, *136*, 3607–3616.

(41) Burgert, R.; Schnöckel, H. *Chemical Communications* **2008**, 2075–2089.

(42) Bergeron, D.; Castleman, A. *Chemical physics letters* **2003**, *371*, 189–193.

(43) Mezhenny, S.; Sorescu, D. C.; Maksymovych, P.; Yates, J. T. *Journal of the American Chemical Society* **2002**, *124*, 14202–14209.

(44) Bergeron, D. E.; Castleman, A. W.; Morisato, T.; Khanna, S. N. *Science* **2004**, *304*, 84–87.

(45) Clayborne, P; Jones, N. O.; Reber, A. C.; Reveles, J. U.; Qian, M.; Khanna, S. N. *Journal of Computational Methods in Science and Engineering* **2007**, *7*, 417–430.

(46) Reber, A. C.; Khanna, S. N.; Castleman, A. W. *J. Am. Chem. Soc.* **2007**, *129*, 10189–10194.

(47) Bergeron, D.; Roach, P.; Castleman, A.; Jones, N.; Khanna, S. *Science* **2005**, *307*, 231–235.

(48) Reveles, J. U.; Khanna, S.; Roach, P.; Castleman, A. *Proceedings of the National Academy of Sciences* **2006**, *103*, 18405–18410.

(49) Knight, W. D.; Clemenger, K.; de Heer, W. A.; Saunders, W. A.; Chou, M.; Cohen, M. L. *Phys. Rev. Lett.* **1984**, *52*, 2141–2143.

(50) Jena, P. *The Journal of Physical Chemistry Letters* **2015**, *6*, 1549–1552.

(51) Burgert, R.; Stokes, S. T.; Bowen, K. H.; Schnöckel, H. *Journal of the American Chemical Society* **2006**, *128*, 7904–7908.

(52) Burgert, R.; Schnöckel, H.; Olzmann, M.; Bowen, K. H. *Angewandte Chemie International Edition* **2006**, *45*, 1476–1479.

(53) Kozuch, S.; Shaik, S. *Journal of the American Chemical Society* **2006**, *128*, 3355–3365.

(54) Blanksby, S. J.; Ellison, G. B. *Accounts of Chemical Research* **2003**, *36*, 255–263.

(55) Frisch, M. J. et al. Gaussian09 Revision D.01., Gaussian Inc. Wallingford CT 2009.

(56) Boys, S. F.; Bernardi, F. d. *Molecular Physics* **1970**, *19*, 553–566.

(57) Eyring, H. *The Journal of Chemical Physics* **1935**, *3*, 107–115.

(58) Eyring, H. *Chemical Reviews* **1935**, *17*, 65–77.

(59) Evans, M. G.; Polanyi, M. *Trans. Faraday Soc.* **1935**, *31*, 875–894.

(60) Koster, A.; Geudtner, G; Calaminici, P; Casida, M.; Dominguez, V.; Flores-Moreno, R; Gamboa, G.; Goursot, A; Heine, T; Ipatov, A, et al. DeMon2k, Version 3., 2011.

(61) Neumaier, H. J.; Postma, J. P. M.; van Gunsteren, W. F.; DiNola, A.; Haak, J. *The Journal of chemical physics* **1984**, *81*, 3684–3690.

(62) Köster, A. M.; Reveles, J. U.; del Campo, J. M. *The Journal of chemical physics* **2004**, *121*, 3417–3424.

(63) Alonso, J., *Structure and Properties of Atomic Nanoclusters*; World Scientific, London: 2005, pp 1–427.

(64) Hohenstein, E. G.; Chill, S. T.; Sherrill, C. D. *Journal of Chemical Theory and Computation* **2008**, *4*, 1996–2000.

(65) Johnston, R. L., *Atomic and Molecular Clusters*; CRC Press, London and New York: 2002, pp 1–250.

(66) Durant, J. L. *Chemical physics letters* **1996**, *256*, 595–602.

(67) Grubisic, A.; Li, X.; Gantefoer, G.; Bowen, K. H.; Schnöckel, H.; Tenorio, F. J.; Martinez, A. *The Journal of chemical physics* **2009**, *131*, 184305.

(68) De Jong, G. T.; Bickelhaupt, F. M. *Journal of Chemical Theory and Computation* **2007**, *3*, 514–529.

Chapter 4

The Breakdown of Electronic Shell Effect: Transition Metal Doped Aluminum Clusters–A Case Study

4.1 Introduction

In the universe of matter and materials, atomic clusters hold a unique place by its own right. In the process of investigation of the evolution of nanoparticles from atomic units, small sized atomic clusters have provided much insight and much more promises in recent years. Starting from the concept of electronic and geometric stability,[1–4] unique magnetic and catalytic properties and as alternate building blocks of materials in the form of superatoms,[5–9] it is not a surprise that atomic clusters has prevailed as the prime motif of material investigation since the early 80's. Among the widespread variation within the cluster family, bimetallic clusters are probably one of the major categories of supreme interest. To the experimental and material chemists, impure clusters are the source of synthesize new materials with wide possibilities. In bulk state, it is practically impossible to alloy all kind of elements because of their substantial immiscibility towards alloy formation. However, in cluster state, formation of heteroatomic cluster is possible in arbitrary composition and with varied properties. One classic example of this kind is the mixing of aluminum and potassium metal[10]. In bulk molten state potassium is barely miscible with aluminum but one unit of potassium atom can be doped within an Al_{13} icosahedral cluster reaching the effective potassium atom concentration of about 7.7%. Thus, heteroatomic clusters can provide the key to the synthesis of new materials with phenomenal properties never seen before. In theoretical perspective, however, the interest to bimetallic clusters is of different origins. The stability of most of the pristine atomic clusters and all the related phenomenon such as the occurrence of magic numbers, odd-even effect, chemical reactivity can be explained by the so called jellium model first used for the present context by knight et al[1,11]. In jellium model, the existence of loosely bound valence electrons are considered against an uniformly positively charged background and properties of the clusters are explained based on the resulting electronic shell configurations much similar to an atom. Inclusion of additional impurities can be sufficed to perturb the order of jellium shells resulting in different sets of magic numbers and thereby alternating the reactivity trends, ionization energies and other related properties for the whole set of clusters.[12,13] All these phenomena provide new challenges and excellent opportunity to develop new models and also modify existing one which will eventually be able to predict and explain such observations.[14–16] Aside from these, clusters with impurities can further be considered as micro analogue of bulk metals, hence, they can provide substantial amount of information about the bulk state of corresponding material. As for example, immiscibility in bulk state may also be reflected within the intermolecular distances of heteroatomic clusters.[17] Some bimetallic clusters even show indication of atomic ordering like phase seperation much similar to their bulk counterparts.[15] Brief survey on these properties by theoretical means (e.g.

chemical order parameters)[18,19] has been proven fruitful to answer the long lasting questions on growth and form of the bulk matter itself.

Aluminum, in its cluster state is quite remarkable. Throughout the years, aluminum cluster has provided tons of information about this mysterious state of matter. Starting from the revolutionary concept of superatoms[5–9], unique reactivities, catalytic properties and unusual stabilities[5,8,20–26], family of aluminum clusters is no short of experimental and theoretical outcomes. However, this robust database does not exists for the case of heteroatomic aluminum clusters. Among the notable investigations, effect of lower valence impurities like Li, Na or Mg on the electronic structures and stability of aluminum cluster are well cited.[27–30] Studies with higher valence impurities[31–41] like C, Si, Ge, Sn, Pb including stable binary magic clusters like $Al_{12}C$ or $Al_{13}H$ which are crucial for future designing of cluster assembled material are also investigated by different research groups.[33,42–48] Even, effect of doping of elements of the same group (for example boron) on series of Al cluster is well established.[49,50] However, in comparison, few results are available which include effect of transition metal doping on the properties of aluminum nanoclusters. Even within these rigorous culminations, most of the calculations are based on the magnetic and spectroscopic properties of a limited number of transition metal doped aluminum clusters.[51–56] Studies related with the influence of spin multiplicities on the thermo–chemical properties of these clusters are even more scarce and substantial amount of doubt still exists about the shell structure, chemical reactivity, stabilities and about other associated phenomena[57] of them as reported studies are neither complete nor entirely conclusive. Hence, the urgency of a detailed investigation is obvious and will have tremendous impact in upcoming days.

The current chapter includes a comprehensive analysis of the influence of spin on the properties of transition metal doped aluminum clusters. Density functional theory based investigations have shown that although impure clusters with minimum spin exhibit clear indication of jellium shell structure in terms of odd–even oscillation in various calculated properties, high spin ground state structures show more of regular trends similar to the bulk materials. To further confirm the argument, thermodynamic data of the adsorption of CO_2 on the impure clusters are computed and compared with the experimental results available in the literature.[58] Except few minor deviations observed in specific cases, the overall exothermicity (ΔH) pattern of CO_2 adsorption on impure clusters are found to be consistent with the experimental heat of adsorption trends obtained for bulk transition metals. Even, the structure of the optimized CO_2–cluster conformer is also found to be consistent with the previously calculated results available in the literature.[59]

The chapter is organized as follows. Section 2 includes all the computational details associated with the current work. Section 3 comprises the result and discussion section including a brief description of the account of spin of impure clusters along with the thermochemical investigation based on the heat of adsorption values of CO_2 on the surface of the clusters. Section 4 contains the conclusions and final remarks.

4.2 Computational Details

The starting geometry for the stable ground state conformers of Al_6 and Al_8 clusters are taken from the current literature based on the DFT calculation with generalized gradient approximation (GGA).[60] The initial geometries taken are also found to be same with the global minima obtained for both Al_6 and Al_8 cluster by most recent studies using state of the art Monte Carlo methods and DFT.[61,62] Both the Al_6 and Al_8 clusters are optimized with using Meta-GGA M06–2X Exchange Functional and also with Perdew, Burke and Ernzerhof's PBE–PBE functional with valence triple ζ (VTZ) quality 6-311g basis augmented with 'd' and 'p' polarization

function.[63] As dopant atom, all the elements from first transition metal series starting from Sc to Zn are included. In both Al_6 and Al_8 aluminum clusters, all the chemically nonequivalent sites are properly identified by condensed Fukui functions(f_A)[64] and chosen as the suitable site for doping. The condensed Fukui functions(f_A), with the finite difference approximation are defined as,

$$Electrophilicity : f_A^+ \simeq q_{A,N+1} - q_{A,N} \tag{4.1}$$

$$Nucleophilicity : f_A^- \simeq q_{A,N} - q_{A,N-1} \tag{4.2}$$

where $q_{A,N+1}$, $q_{A,N}$ and $q_{A,N-1}$ are the Hirshfeld population (HP) of a particular atom A for the $(N+1)$, N and $(N-1)$ electronic systems respectively. The three dimensional representations of the Fukui functions are evaluated by subtracting the density volume data at fixed geometry for the respective systems obtained by the given level of theory.

In cluster chemistry, proper identification of lowest energy ground state conformer is usually a complicated process. Unlike molecules, a cluster can have numerous isomers which are often close lying in energy. Therefore, the identification of the proper ground state becomes highly dependent on the level of theory employed. Moreover, the process becomes more complicated as the number of isomers increases exponentially with the increment of the numbers of constituent atoms. Hence, to find the appropriate ground state, use of efficient global optimization codes or genetic algorithm are commonly suggested.[61,62,65] However, as the clusters used in the present chapter are quite small in size (N$\leq$8), a rather simplified approach is followed. The initial guess geometries of all the mono–doped clusters are generated based on the skeleton of optimized Al_6 and Al_8 clusters by replacing the chemically nonequivalent aluminum atoms with first row transition metals as dopant. All these initial structures are distorted along all three coordinates to generate further starting geometries and allowed individually to relax towards nearest local minima at fixed spin multiplicities in accordance to the Berny optimization algorithm using M06–2X functional as implemented in Gaussian09 package.[63]. Other possible conformers are also optimized in the same level of theory and calculated energies are noted. Finally, all of these conformers are further tested in several possible spin multiplicity upto S=15 and only the lowest energy structures obtained in each case with associated multiplicity are used as the probe for CO_2 adsorption. The final selected structures are again optimized with PBE–PBE functional as well. In order to properly understand the role of the dopant atom in CO_2 binding, the CO_2 molecules are adsorbed on the doped cluster in all possible orientation which directly involves the transition metal atom as at least one of the binding sites. In each case, the lowest energy adduct is considered as the final product. For all the first row d block metals Los Alamos ECP basis LANL2DZ is used. Normal modes of all the optimized structures are carefully observed and it is confirmed that all the optimized structures have no imaginary frequency. Aside from the thermochemical data of the CO_2 adsorption, other associated properties like binding energies, HOMO–LUMO gap, Ionization energies etc. are calculated only for the Al_5M(M=Sc–Zn) clusters. Distance of the transition metals are measured from the center of mass (COM) of the Al_5M clusters. The Wigner–Seitz radius(r_{ws}) in bulk transition metals are calculated from the bulk density (ρ) of the material in S.T.P and their molecular weight(M)[66] using the standard formula for a non–interacting system,[67]

$$r_{ws} = \left(\frac{3M}{4\pi\rho N_A}\right)^{\frac{1}{3}} \tag{4.3}$$

Binding energies of the doped cluster are calculated using the following equation

$$E_b = -\frac{E_C - E_M - nE_{Al}}{n+1} \tag{4.4}$$

where E_C is energy of the mono–doped cluster, E_M is the energy of dopant atom and E_{Al} is the energy of Al atom. n is the total number of aluminum atoms within the doped cluster. Similarly, the adiabatic first ionization energies of impure clusters are defined by the following

$$I.E = E_{N-1}^{(v',s')} - E_N^{(v,s)} \tag{4.5}$$

i.e. the difference between the energy of the vibrational ground state of the neutral species (v = 0) with that of the positive ion (v′ = 0) with respective spins s and s′ corresponding to the minimum energy in both the cases. To analyze the stabilization interactions involved within the clusters and in between the clusters and CO_2 molecule, Natural Bond Orbital (NBO) calculations are performed by the NBO 3.0 package implemented in Gaussian 09. The donor–acceptor stabilization energies (ΔE_{ij}) calculated by second order perturbation theory analysis of Fock matrix within the NBO Basis is given by

$$\Delta E_{ij} = q_i \frac{F_{ij}^2}{\Delta\varepsilon_{ji}} \tag{4.6}$$

where q_i is the occupancy number of donor orbital. F_{ij} is off–diagonal elements of Fock matrix in NBO basis. $\Delta\varepsilon_{ji}$=ε_j-ε_i is the difference of orbital energies between acceptor(j) and donor(i) NBO.

In order to access the aromatic character of Al_5M clusters, nucleus independent chemical shift ($NICS_{iso}$) values are calculated using gauge independent atomic orbital method (GIAO) method in Gaussian09.[63,68,69] The ghost atom probe is implemented at the geometric center of each cluster and the negative of the nuclear magnetic shielding tensor (NMST) value at this inert probe is calculated in M06-2X/6-311g(d,p) level of theory. According to the common convention, the clusters with negative NICS values are considered as aromatic, whereas the clusters with positive value are treated as anti–aromatic in nature.

4.3 Results and Discussion

To understand the effect of transition metal doping on the structure and reactivity of aluminum nanoclusters, ground state conformers of Al_6 and Al_8 are taken as the clusters of choice. Optimized structure of Al_6 cluster in its ground state is distorted octahedral with two different bond lengths (2.9Å and 2.6Å in M06–2X functional) On the other hand, ground state Al_8 cluster has a bicapped octahedral structure which can easily be constructed based on the framework of Al_6 cluster by introducing two new atoms on any two triangular faces trans to each other. In spite of the distortion present in Al_6 cluster all the six aluminum atoms are still chemically equivalent as each atom has one pair of short and one pair of long bonds. The chemical equivalency of each atom of Al_6 cluster can further confirmed by the three dimensional grid representation of condensed Fukui function(f_A^+) depicted in Figure 4.1. However, in case of Al_8 cluster there are three sets of chemically equivalent sites (designated by a,b and c in Figure 4.1) rather than two as expected. The reason for this anomaly lies within the fact that the two newly added atoms are not equidistant from all three aluminum atoms on the triangular faces. Calculation in M06–2X functional shows that one bond is approximately 0.4 Å longer than the other two. As a result, this distortion introduces a subtotal of three sets non equivalent sites on Al_8 cluster which can be considered as suitable sites for doping of the ‘d’ block elements. One intriguing question which can be asked at this point is about the rationalization behind the choice of these two clusters among the others. The choice of Al_6 and Al_8 clusters is not random, instead it serves a special purpose. As illustrated in Figure 4.2, both the octahedral and bicapped octahedral structure can be considered as lattice fragments of most commonly occurring bcc, fcc and hcp crystal lattice

structures in bulk solids. Hence, these two clusters are chosen over the others keeping in mind that the calculated results within this chapter may provide a useful resource for comparison of results in between the clusters and of bulk crystalline solids.

4.3.1 Properties of the clusters with minimum spin

In cluster chemistry one major rule regarding the spin of the atomic clusters is the rule of minimum multiplicity.[70] Being a multi–electronic system, in most of the s and p block metal clusters and even in noble metal clusters, inter–system crossing between spin states is assumed to occur so rapidly that clusters in their ground state configuration exist in the lowest possible spin state i.e. the energetically minimized ground state conformer is usually either in singlet or doublet spin states depending on whether it is a odd or a even numbered electronic system. As closed shell clusters achieve additional stability than open shell clusters due to electron pairing or shell closing, the whole series of clusters show periodic odd–even oscillation in all the properties which are directly associated with electronic stability of the clusters. However, exception to the rule of minimum multiplicity is not uncommon and as a matter of fact clusters consisting of transition metals are probably the oldest and finest example of this type.[15] Most of the transition metal clusters shows high spin due to the splitting of the 'd' orbitals similar to the crystal field effect (CFE) observed in transition metal complexes. Even ground state conformer of transition metal clusters with spin state as high as 10 or more are also plentiful and are of frequent choice of investigation to cluster chemists.[71,72] Although the existence of high spin atomic clusters are well documented, influence of the spin upon the thermochemical properties of atomic clusters is of recent interest. Among the most notable investigations from current literature, dependence of spin state of aluminum and alane clusters on their reactivity pattern with oxygen[70,73–77] or the newly introduced unusual concept of no–pair ferromagnetic bonding (NPFM)[78,79] in alkali and noble metal clusters has proven to be highly influential in elucidating the prime role of spin on the properties of clusters.

In order to investigate the role of spin on the properties of transition metal doped aluminum clusters we have chosen mono–doped clusters with minimum multiplicity as the starting point. As expected, all the evaluated properties based on the DFT calculation show adequate indication supporting the presence of jellium shell structure within the clusters. As depicted in Figure 4.3a, binding energies of Al_5M (M=Sc–Zn) clusters in both functionals show periodic oscillations clearly indicating the existence of odd–even effect within the series. The highest binding energy among the listed clusters in Table 4.1 is obtained for Al_5Cr cluster (2.70 and 3.03 eV in M06–2X and PBE–PBE functional respectively) whereas Al_5Fe shows the second highest Binding energy in M06–2X functional. Similar trends of the binding energies are also obtained for all three classes of Al_7M clusters as well. The odd–even effect is also found to be prominent in other calculated properties as well. Evaluated ionization energy (IE) values (Figure 4.3c) for Al_5M series shows oscillatory trends similar to the binding energies including the prominent maximum at Al_5Cr (10.35 eV in M06–2X functional). Also, the clusters with higher binding energies show higher I.E values when compared with other members within the Al_5M family. This correlation between the stability of Al_5M cluster in terms of binding energy and I.E concludes that the key factor which is responsible for the stabilities of the low spin impure aluminum clusters is of electronic origin.The structural or geometrical effects plays minor or insignificant role. The same conclusion can also be drawn by the donor–acceptor stabilization energies obtained through the NBO analysis. In the pristine Al_6 cluster, NBO calculation in M06–2X functional indicates the presence of multiple donor–acceptor stabilizing interaction with resulting stabilization energies within 220-265 kcal mol^{-1}, whereas no intra–cluster stabilizing interaction energy higher than 140 kcal mol^{-1} is observed for Al_5Cr cluster. This is of–course a direct contrast with the evaluated binding energy orders of these two representative clusters as binding energy

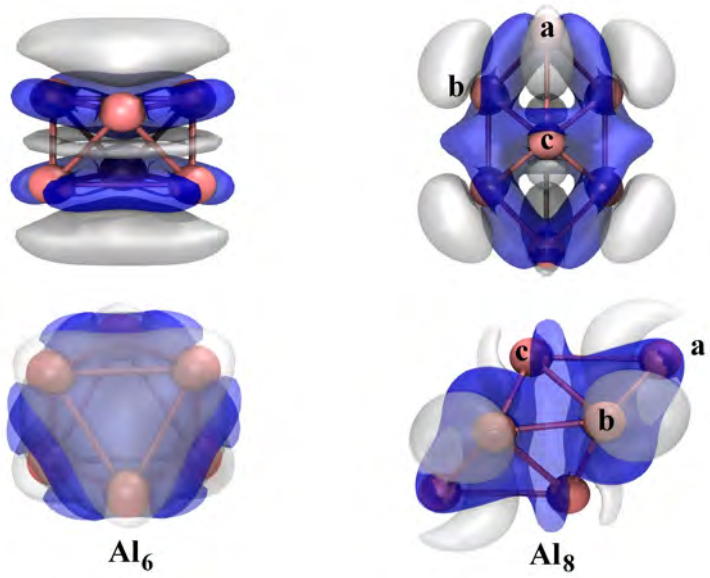

FIGURE 4.1: A pictorial representation of the Fukui function (f_A^+) of Al_6 and Al_8 clusters. The figure indicates presence of three chemically distinct sites (a, b, c) in Al_8 cluster. The top panel represents the frontal view whereas the bottom panel depicted the side view of f_A^+.

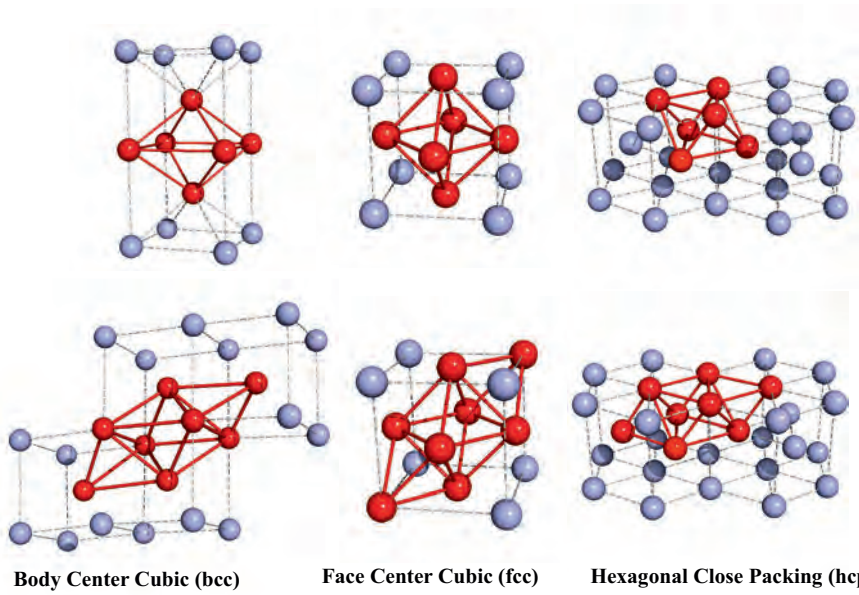

FIGURE 4.2: An illustration of octahedral and bicapped octahedral sites within bcc, fcc and hcp crystal structures showing that both the Al_6 and Al_8 cluster can indeed be considered as lattice fragment of the same.

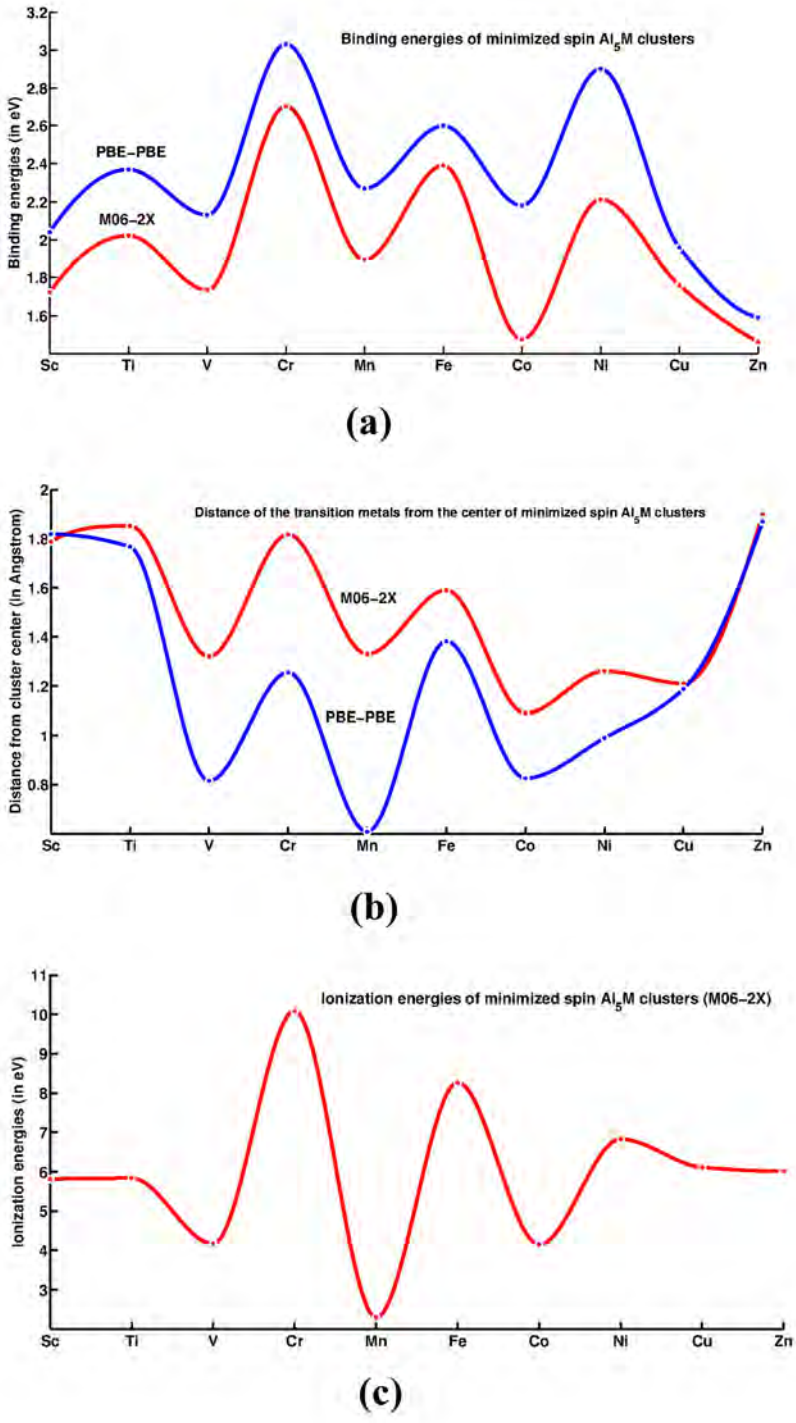

FIGURE 4.3: Plots of calculated properties of minimum spin Al_5M clusters (a) Binding energies (eV) (b) Distance of transition metal atoms from cluster center (in Å) (c) Ionization Energies (eV). The figure shows prominent presence of odd–even effect in all calculated properties. All the data points are fitted with shape preserving interpolant for visualization purpose.

TABLE 4.1: Properties of minimum spin Al_5M clusters

Clusters (Multiplicity)	Binding Energies(eV)		Distance of M from cluster center(Å)		Ionization Energies(eV)
	M06–2X	PBE–PBE	M06–2X	PBE–PBE	M06–2X
$Al_5Sc(1)$	1.72	2.04	1.79	1.82	5.81
$Al_5Ti(2)$	2.02	2.37	1.85	1.77	5.83
$Al_5V(1)$	1.73	2.13	1.32	0.81	4.16
$Al_5Cr(2)$	2.70	3.03	1.82	1.25	10.08
$Al_5Mn(1)$	1.89	2.27	1.33	0.61	2.29
$Al_5Fe(2)$	2.39	2.60	1.59	1.38	8.26
$Al_5Co(1)$	1.47	2.18	1.09	0.83	4.15
$Al_5Ni(2)$	2.21	2.90	1.26	0.99	6.82
$Al_5Cu(1)$	1.76	1.96	1.21	1.19	6.11
$Al_5Zn(2)$	1.46	1.59	1.90	1.87	6.01

TABLE 4.2: Properties of ground state Al_5M clusters

Clusters (Multiplicity)	Distance of M from cluster center(Å)		HOMO–LUMO gap(eV)		Binding energies(eV)	Ionization Energies(eV)	$NICS_{iso}$
	M06–2X	PBE–PBE	M06–2X	PBE–PBE	M06–2X	M06–2X	M06–2X
$Al_5Sc(3)$	1.86	1.87	2.59	0.33	1.76	6.01	188.66
$Al_5Ti(4)$	1.87	1.79	2.75	0.34	2.05	5.93	53.15
$Al_5V(5)$	1.48	1.18	2.81	0.56	2.11	6.02	63.67
$Al_5Cr(6)$	1.54	1.31	2.87	0.66	2.79	6.01	-4.01
$Al_5Mn(7)$	1.74	1.65	2.66	0.45	2.57	5.98	24.82
$Al_5Fe(4)$	1.78	1.54	2.83	0.57	2.45	6.20	-0.11
$Al_5Co(3)$	1.37	0.82	2.91	0.61	1.80	6.13	-156.76
$Al_5Ni(2)$	1.26	0.99	2.79	0.46	2.21	6.13	-15.75
$Al_5Cu(1)$	1.21	1.19	2.92	0.60	1.76	6.11	-4.03
$Al_5Zn(2)$	1.90	1.87	2.71	0.53	1.46	6.01	17.84

of pristine Al_6 cluster (1.85 eV in M06–2X) is found to be nearly $\frac{2}{3}$ rd than that of Al_5Cr cluster. Wiberg bond indices (WBI) calculated in the NAO basis also indicates that in Al_6 cluster there are two types of bonds with WBI 0.89 and 0.48 respectively. The sum total WB indices in Al_6 cluster per atom is found to be 2.8, whereas for the case of Al_5Cr the WB indices are found to be much lower by magnitude and no WBI index higher than 0.2 is observed. The low bond orders and the absence of high energy stabilization interactions further confirms that the higher stability of Al_5Cr cluster is not due to geometrical reason but rather due to presence of filled jellium shell configuration of the impure clusters itself. One important observation about the ionization energies of Al_5M clusters is that except the case for Cr and Mn, the IE values of doped clusters are within the range of 4.1–8.2 eV, relatively closer (within a deviation of $\pm$2.5 eV) to that of pristine Al_6 cluster which shows a I.E value of 6.6 eV in M06–2X functional. The explanation of this phenomenon can be given by recalling the fact that in an atomic cluster the magnitude of ionization energy mostly depends on the composition of the cluster surface as the loosely bound valence electrons are usually associated within the surface of the cluster, which in all these cases are by and large aluminum. Aside from ionization and binding energies the prominent presence of odd–even effect is also observed in the distance of doped transition metal from the center of mass of Al_5M clusters as shown in Figure 4.3b. The principle reason for this periodic oscillation can again be attributed to the 'Jahn–Teller' distortion due to the alternate presence of open jellium shells within the impure clusters. One important observation regarding the odd–even effect which is worth mentioning is that the magnitude of odd even oscillation in each properties is more prominent at the middle portion of the series specifically from Al_5V upto Al_5Ni. Clusters present at both end show somewhat less oscillation by magnitude, even in some specific cases (e.g binding energy and I.E trends of Al_5Cu–Al_5Zn) the oscillation is found to be not present at all.

4.3.2 Properties of high spin clusters

As mentioned in earlier section, most of the transition metal containing atomic clusters usually shows high spin due to loss of degeneracy of jellium orbitals. Aluminum clusters with transition metal impurities, presented in the current study is found to be no exception of the rule. Most of the ground state optimized structures of both Al_5M and Al_7M shows high spin as presented in Figure 4.4 and Figure 4.5 respectively. Although it is observed that clusters with Ni, Cu and Zn usually prefer the lowest possible spin states in their ground state. In all the four series (Al_5M, Al_7M(a–c)), ground state impure clusters with Ni,Cu and Zn are always found to be exist in their minimum spin conformers. Among the listed doped clusters, the lowest energy conformer with highest spin is obtained for Al_5Mn cluster with a spin multiplicity as high as 7. A priori investigation on the spin state of impure clusters confirmed that there exists a well defined trend between the type of dopant atom and the spin of ground state conformer. In both Al_5M and Al_7M clusters the spin multiplicity associated with minimum energy structures follow a 'bell' shaped distribution curve. Starting from scandium the multiplicity of the clusters show a regular increment until it reaches a maximum value for chromium (S=6) (or manganese (S=7) for Al_5M) then following a smooth decrement finally converges to the minimum spin multiplicities obtained for the case of Ni–Zn. The spin multiplicity of ground state optimized structure of Al_5Cr, Al_5Fe, Al_5Ni and Al_7Ni clusters are found to be in agreement with the multiplicity values reported by Li et al.[51] Aside from the aforementioned spin multiplicity trend, another crucial thing to notice is that each transition element shows preference towards a particular spin value. As for example clusters containing scandium show a multiplicity of 3, all chromium doped clusters show spin multiplicity 6, iron doped clusters have a multiplicity value of 4 and so on. This significant observation concludes the spin multiplicities of the ground state mono-doped clusters depends on the type of dopant transition metal atoms and other related factors

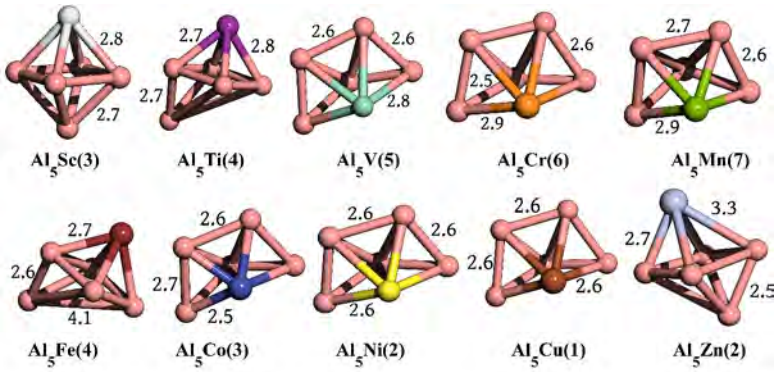

FIGURE 4.4: Optimized structures of ground state Al_5M clusters with spin multiplicity included within the parenthesis. All the clusters except Al_5Ni–Al_5Zn are of high spin in nature.

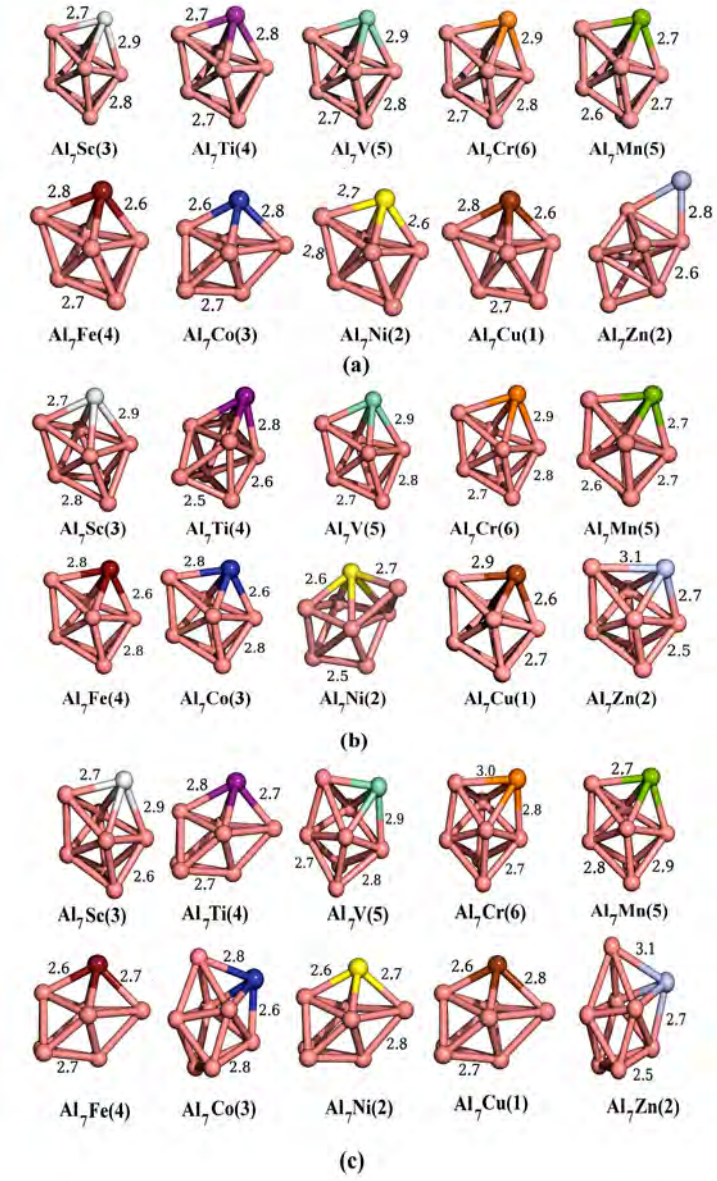

FIGURE 4.5: Optimized structures of ground state Al_7M clusters with spin multiplicity included within the parenthesis. All the clusters except Al_7Ni–Al_7Zn are of high spin in nature.

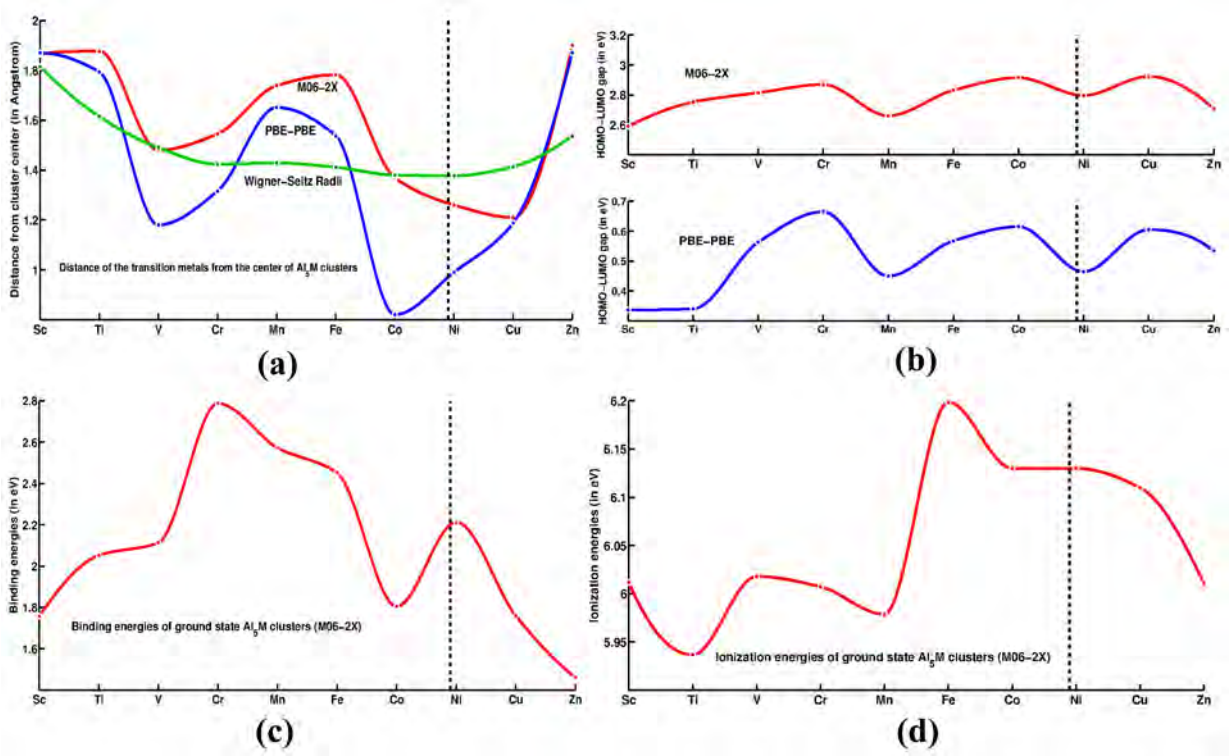

FIGURE 4.6: Calculated properties of ground state Al_5M clusters (a) Distance of transition metal atoms from cluster center (in Å) (b) HOMO-LUMO gap (eV) (c) Binding Energies (eV) and (d) Ionization Energies (eV). All the high spin clusters show smooth trends rather than the periodic oscillation observed in minimum spin clusters. Presence of odd–even oscillation can only be observed in some specific cases (e.g HOMO–LUMO gap) of Al_7Ni–Al_7Zn (separated by a vertical line) clusters as their ground state structures are of minimum spin. All the data points are fitted with shape preserving interpolant for better visualization.

plays insignificant role. However, it is also important to mention that as each aluminum cluster behaves quite differently, it is unlikely that the same spin trends will be conserved for other clusters within the aluminum family as well. In fact it is highly probable that for each different series of impure aluminum clusters there exists a unique spin distribution corresponding to the ground state structures.

To understand the differential behavior of high spin impure clusters with that of low spin ones, several properties are calculated like the previous case as shown in Table 4.2. The calculated properties of high spin ground state clusters show little resemblance with their low spin counterparts described earlier. From Figure 4.6, it is evident that in all the calculated properties of high spin clusters, the odd-even oscillation is completely absent, which was pretty dominant in minimum spin clusters. Instead, in the high spin clusters the periodic oscillations are replaced by rather smooth trends, a remarkable feature which is rarely observed for small sized atomic clusters. Odd–even oscillations are only observed for clusters with Ni,Cu and Zn (separated by dashed vertical lines in Figure 4.6) as their optimized ground state structures are of minimum spin. Although, as stated in the earlier section, oscillation for clusters with lower end transition elements are not found to be very prominent hence except for the HOMO–LUMO gap (Figure 4.6b) the oscillation for Al_5Ni–Al_5Zn is not pronounced for other calculated properties. At this point it will be interesting to compare the given trends of high spin ground state structures to the properties of bulk binary metals, since regular trend in properties is one of the unique characteristics of bulk solids. Unfortunately complete database for bulk binary Al-Tm metals is not available because in bulk phase most of the 'd' block elements show negligible miscibility to aluminum. Except zinc and copper all other transition metals are found to be unsuitable for alloying due to their tendency to form well separated layers as a certain consequence of their lower solubility in aluminum.[80] However, careful observations can still reveal several conclusive similarities in between the properties of bulk phase and impure nanoclusters. As for example, Figure 4.6a collects the comparison in between the distance of the doped transition metals from the center of mass of the Al_5M cluster with the calculated Wigner–Seitz (r_{ws}) radius of the transition metals in bulk state. The Wigner–Seitz radii of bulk transition metals follow roughly a parabolic behavior only deviating at manganese resulting in a 'w' shaped curve. In both the functional the distance of transition metals from the center of mass of Al_5M clusters shows similar distribution like the WS radius of bulk transition metals. The deviation at the place of manganese for its 'd^5' configuration is also well reproduced and much more prominent than the bulk metals. Although the general shape of the curve is well presented, the relative trends are seen to be out of order in both functionals when compared to the bulk WS values. Explanation of this phenomenon can be given by invoking the fact that in binary metal clusters the atomic volume of individual element is not the only factor which controls the inter–atomic distances within the clusters. Several other factors like the bulk state miscibility or the radius ratio of constituent atoms for close packing also play key role in determining the atomic organization within the cluster.[15,17]

Aside from the inter–atomic distances smooth trends are also observed in other properties as well. HOMO–LUMO gap of Al_5M series (Figure 4.6b) shows a steady increase up to Al_5Cr then following a sudden drop at Al_5Mn it again increases upto Al_5Co and finally converges with the plot of HOMO–LUMO gap of low spin clusters (Al_5Ni–Al_5Zn). Odd–even effect is also found to be absent in the binding energy trends of the clusters as shown in Figure 4.6c although Al_5Cr is still found to be most stable cluster followed by Al_5Mn as the second most stable one. However, no correspondence in between the binding energy and the Ionization energy (Figure 4.6d) trend is found this time, signifying that in high spin clusters the prime reason for the stabilities are not of electronic in origin. The I.E values depicted in Figure 4.6d follows

a rhythmic trends similar to other calculated properties. Except the deviation at specific cases the overall trend of I.E of high spin clusters show some similarities with the atomic I.E trend of transition elements. According to the NIST database[81] the I.E trend of transition metal atoms up to cobalt follows the following order Fe>Co>Mn>Ti>Cr>V>Sc. Whereas, for Al_5M clusters the I.E trend is found to be Al_5Fe>Al_5Co>Al_5V>Al_5Sc∼Al_5Cr>Al_5Mn>Al_5Ti i.e. the trend closely follows the elemental order of ionization energies. Another important point is that, the overall range of I.E of high spin clusters (5.9–6.2 eV) is much closer with that of pristine Al_6 cluster (6.6 eV) as compared to low spin cluster and no unusually high or low I.E values are obtained for any member of the series. This signifies the shell effect is indeed less significant for the present case and hence, certainly plays a minor role in determining the properties of high spin clusters.

4.3.3 Adsorption of CO_2 on transition metal doped aluminum clusters

In order to confirm the arguments raised in the previous section it is crucial to investigate additional physiochemical properties of the impure clusters and compare them with the properties of bulk transition metals. One of the well documented features of bulk d block elements is the ability to adsorb gaseous species like O_2, N_2, CO_2, CO, C_2H_4 or even H_2, a phenomenon which is essential to understand and develop new catalyst for heterogeneous chemical reactions. According to the available literature it is well established that in the bulk state the affinity towards the gaseous species reduces along the series.[82] Therefore, although first few transition metals are able to strongly adsorb CO_2 in gas phase, later members of the same series like Cu and Zn shows less affinity towards CO_2. To justify the conclusions drawn earlier, DFT calculations are carried out on both series of impure clusters (Al_5M and Al_7M(a-c)) in M06–2X and PBE–PBE functionals. It is expected that if the impure clusters really have some similarities with bulk transition metals, all the thermochemical parameters(ΔH and ΔG) should show a steady decrement in their absolute values along the series of doped transition metal. Therefore, scandium or titanium doped clusters are expected to show higher exothermicity and spontaneity towards CO_2 whereas copper and zinc doped cluster should show lowest affinity towards CO_2 binding. Careful investigation reveals that there exists two different types of binding mode of CO_2 with doped clusters which directly involves the transition metal as a binding site. First one is the linear or terminal binding, where one of the terminal oxygen atom is directly bonded with the doped transition metal atom in a near perpendicular position. Second one is the parallel binding mode where one oxygen atom of CO_2 is bonded with the transition metal and the second one is with one of the nearest aluminum atom leaving the carbon atom at a central position. DFT calculations show that among both the binding modes the terminal binding is the weaker one, having ΔH values ranging from positive to -20 kcal/mol in both type of clusters and in all the functionals. On the other hand, the parallel mode of binding is found to be highly exothermic and also more favorable in terms of free energy data calculated in both functionals.

Figure 4.7 and 4.8 show the optimized structures of parallel bonding of CO_2 with both Al_5M and Al_7M(a–c) series of clusters in gas phase. It is evident from Tables 4.3–4.6 and from Figure 4.9 that in all the four cases every associated thermodynamic parameters (by absolute magnitude) tends to decrease along the transition metal series as observed in the bulk state. As predicted, high Exothermicity (ΔH) and spontaneity in terms of the calculated free energies(ΔG) are usually observed for first few transition elements like Sc, Ti or V and slowly decreases towards the end of the series. Comparison of the present results with the experimental values for bulk metals immediately establishes the similarities between both type of materials. Article

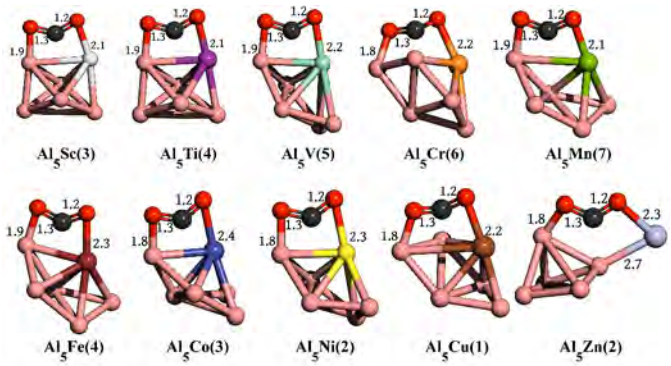

FIGURE 4.7: Structures of optimized ground state $Al_5M....CO_2$ complexes with spin multiplicity included within the parenthesis.

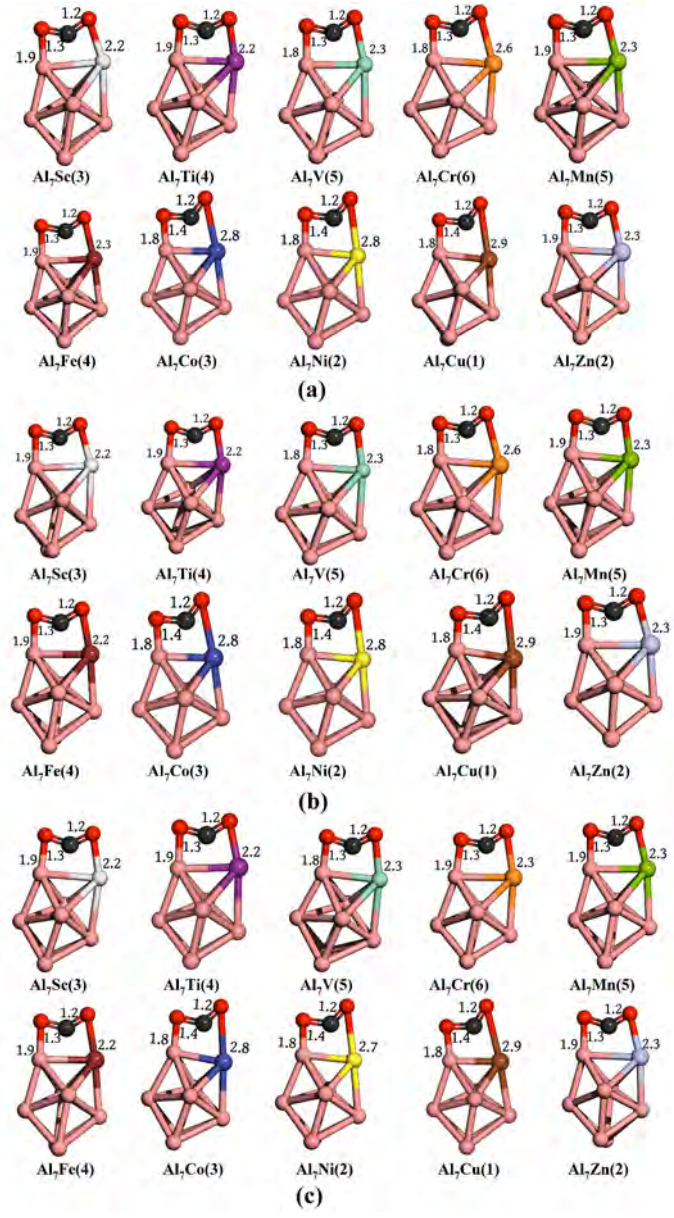

FIGURE 4.8: Structures of optimized ground state of $Al_7M[(a)–(c)]....CO_2$ complexes with spin multiplicity included within the parenthesis.

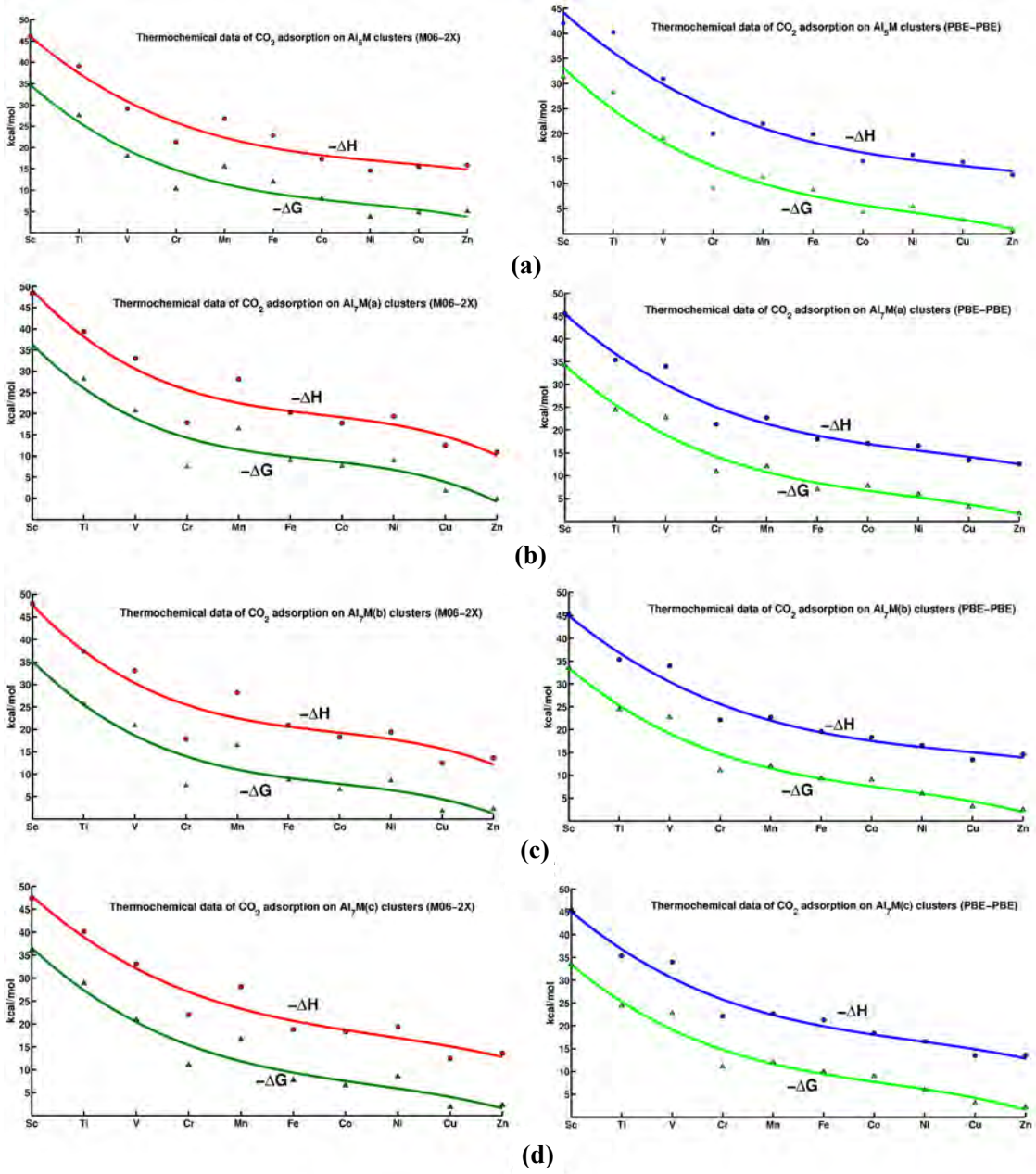

FIGURE 4.9: Plots of thermodynamic parameters (-ΔH and -ΔG) of CO_2 adsorption on transition metal doped aluminum clusters in both M06–2X and PBE–PBE functional (a) $Al_5M....CO_2$ (b)–(d) $Al_7M[(a)–(c)]....CO_2$. Except few deviations, most of the data points are well fitted with the cubic interpolation curve drawn in each case.

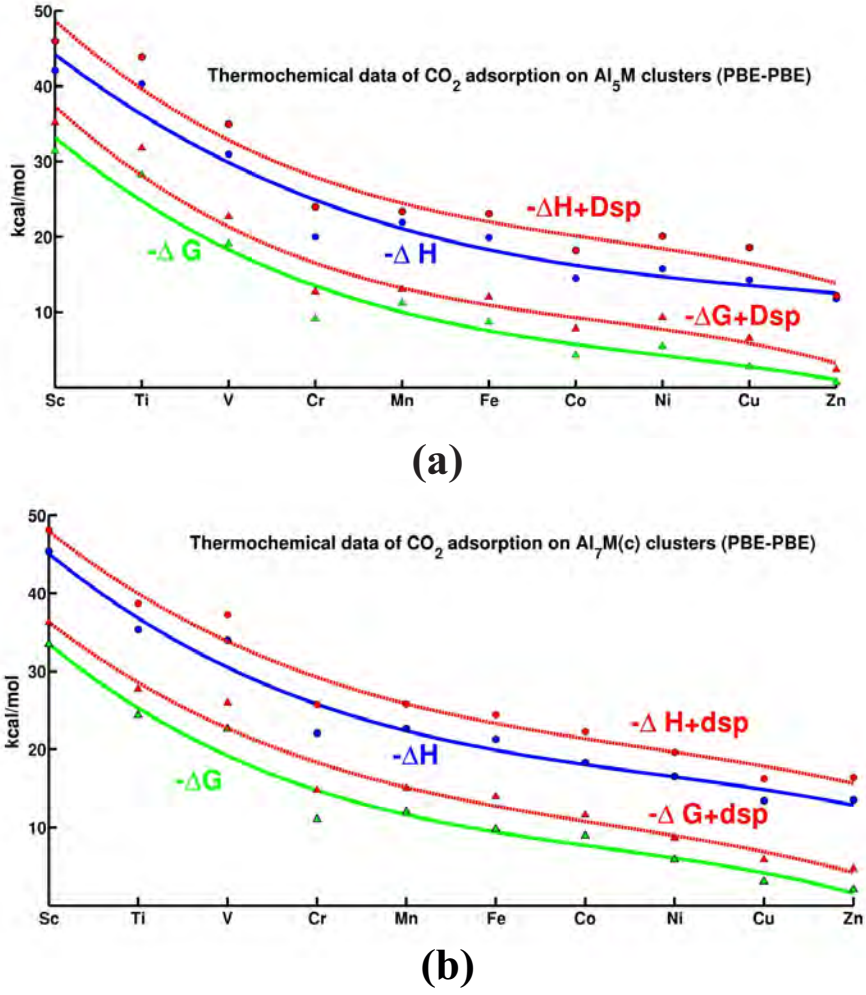

FIGURE 4.10: Plots of thermodynamic properties (-ΔH and -ΔG) of CO_2 adsorption on transition metal doped aluminum clusters in dispersion (DFT-D) corrected PBE–PBE functional (a) $Al_5M....CO_2$ (b) $Al_7M(c)....CO_2$. In both the cases the effect of dispersion is found to be small (within ∼0.3–4.3 kcal/mol)and well within DFT error range.

TABLE 4.3: Thermochemical data of CO_2 adsorption on Al_5M clusters

Clusters (Multiplicity)	ΔE (kcal mol^{-1})		ΔH (kcal mol^{-1})		ΔG (kcal mol^{-1})	
	M06–2X	PBE–PBE	M06–2X	PBE–PBE	M06–2X	PBE–PBE
$Al_5Sc(3)$	-45.70	-41.79	-46.16	-42.06	-34.83	-31.41
$Al_5Ti(4)$	-38.71	-39.75	-39.13	-40.28	-27.50	-28.22
$Al_5V(5)$	-28.73	-30.37	-29.13	-30.95	-17.97	19.05
$Al_5Cr(6)$	-20.94	-19.64	-21.30	-20.01	-10.30	-9.12
$Al_5Mn(7)$	-26.36	-21.71	-26.79	-21.94	-15.52	-11.23
$Al_5Fe(4)$	-22.76	-19.59	-22.84	-19.91	-11.92	-8.73
$Al_5Co(3)$	-17.14	-14.32	-17.28	-14.50	-7.90	-4.32
$Al_5Ni(2)$	-14.32	-15.59	-14.61	-15.78	-3.73	-5.48
$Al_5Cu(1)$	-15.22	-13.85	-15.55	-14.30	-4.70	-2.79
$Al_5Zn(2)$	-15.42	-11.39	-15.91	-11.79	-4.94	-0.68

TABLE 4.4: Thermochemical data of CO_2 adsorption on $Al_7M(a)$ clusters

Clusters (Multiplicity)	ΔE (kcal mol^{-1})		ΔH (kcal mol^{-1})		ΔG (kcal mol^{-1})	
	M06–2X	PBE–PBE	M06–2X	PBE–PBE	M06–2X	PBE–PBE
$Al_7Sc(3)$	-47.33	-45.05	-48.42	-45.54	-35.28	-34.17
$Al_7Ti(4)$	-39.01	-35.01	-39.38	-35.38	-28.10	-24.35
$Al_7V(5)$	-32.18	-33.52	-33.06	-33.98	-20.66	-22.68
$Al_7Cr(6)$	-17.67	-21.02	-17.84	-21.30	-7.44	-10.82
$Al_7Mn(5)$	-27.60	-22.47	-28.13	-22.70	-16.48	-12.00
$Al_7Fe(4)$	-19.87	-17.65	-20.28	-18.00	-8.95	-6.92
$Al_7Co(3)$	-17.69	-17.30	-17.75	-17.06	-7.66	-7.69
$Al_7Ni(2)$	-19.15	-16.35	-19.36	-16.57	-8.90	-5.90
$Al_7Cu(1)$	-12.27	-13.24	-12.52	-13.40	-1.72	-3.11
$Al_7Zn(2)$	-10.90	-12.28	-10.89	-12.57	+0.15	-1.67

TABLE 4.5: Thermochemical data of CO_2 adsorption on Al_7M(b) clusters

Clusters (Multiplicity)	ΔE (kcal mol^{-1})		ΔH (kcal mol^{-1})		ΔG (kcal mol^{-1})	
	M06–2X	PBE–PBE	M06–2X	PBE–PBE	M06–2X	PBE–PBE
$Al_7Sc(3)$	-46.73	-44.74	-47.76	-45.29	-35.07	-33.52
$Al_7Ti(4)$	-36.84	-35.03	-37.42	-35.39	-25.74	-24.40
$Al_7V(5)$	-32.21	-33.54	-33.08	-34.01	-20.82	-22.66
$Al_7Cr(6)$	-17.69	-21.75	-17.87	-22.14	-7.46	-10.98
$Al_7Mn(5)$	-27.63	-22.45	-28.17	-22.68	-16.44	-12.03
$Al_7Fe(4)$	-20.08	-19.40	-20.89	-19.59	-8.67	-9.23
$Al_7Co(3)$	-17.61	-18.54	-18.28	-18.33	-6.56	-8.94
$Al_7Ni(2)$	-19.06	-16.35	-19.35	-16.56	-8.57	-5.89
$Al_7Cu(1)$	-12.27	-13.25	-12.51	-13.41	-1.78	-3.09
$Al_7Zn(2)$	-13.23	-14.03	-13.62	-14.56	-2.29	-2.42

TABLE 4.6: Thermochemical data of CO_2 adsorption on Al_7M(c) clusters

Clusters (Multiplicity)	ΔE (kcal mol^{-1})		ΔH (kcal mol^{-1})		ΔG (kcal mol^{-1})	
	M06–2X	PBE–PBE	M06–2X	PBE–PBE	M06–2X	PBE–PBE
$Al_7Sc(3)$	-47.00	-44.79	-47.41	-45.36	-36.02	-33.47
$Al_7Ti(4)$	-39.68	-35.00	-40.18	-35.35	-28.84	-24.38
$Al_7V(5)$	-32.21	-33.54	-33.07	-34.01	-20.84	-22.66
$Al_7Cr(6)$	-21.71	-21.74	-22.06	-22.10	-10.99	-11.05
$Al_7Mn(5)$	-27.62	-22.45	-28.13	-22.67	-16.52	-12.00
$Al_7Fe(4)$	-18.46	-20.68	-18.80	-21.30	-7.72	-9.79
$Al_7Co(3)$	-17.63	-18.54	-18.29	-18.33	-6.58	-8.94
$Al_7Ni(2)$	-19.04	-16.35	-19.35	-16.57	-8.50	-5.89
$Al_7Cu(1)$	-12.31	-13.27	-12.54	-13.44	-1.83	-3.08
$Al_7Zn(2)$	-13.22	-13.11	-13.63	-13.54	-2.26	-2.09

published by Toyoshima and Somorjai[58] clearly indicates that the heat of adsorption values of CO_2 on different types of transition metal surface follow a systematic declining trend when the experimental data sets are fitted with best fitting polynomial. The Calculated results presented in Figure 4.9 in M06–2X functional for all impure aluminum clusters also shows exactly the similar trend when DFT data points are fitted with best fitting cubic polynomial. In each case maximum heat of adsorption is obtained for the case of Sc and following a systematic decline in the ΔH trend, the minimum value finally corresponds to the elements lowest in the series. The maximum value of heat of adsorption presented in this chapter is obtained for $Al_7Sc(a)$ (-48.4 kcal mol^{-1} in M06–2X) cluster and the minimum value which is -10.9 kcal mol^{-1} in M06–2X is calculated for $Al_7Zn(a)$ cluster. The same trend is also observed in PBE–PBE functional as well. Another important point to note is that the effect of dispersion in the calculated parameters is observed to be small which can be proven from the DFT–D comparison plot presented in Fig 4.10. This observation indeed signifies that the binding of CO_2 with the impure cluster is primarily due to electron sharing between CO_2 and the cluster and the dispersion effect plays minor role. The resemblance with the bulk is also noticed in the optimized structures of Al_nM–CO_2 complexes as presented in Figure 4.7 and 4.8. In all the cases the CO_2 molecule is observed to be deviated from linearity along with substantial increment of both the C=O bond. Both this observation signifies the existence of charge transfer from metal centers to CO_2 moiety. Also as aluminum is more electro–positive than transition metals, the increment of both the C=O bond is found to be asymmetric i.e oxygen atom attached to the aluminum side shows longer C=O bond distance (1.3Å) than the other C=O bond (1.2Å) which is bonded with the doped transition metal. These observations are indeed consistent with the theoretical calculation of CO_2 adsorption on various transition metal surfaces by Cundari and Wilson[59] and henceforth can be considered as conclusive evidence about the similarities of impure clusters with bulk metals.

Although the relative trend obtained by best fitted cubic polynomial curves as shown in Figure 4.9 clearly demonstrates the similarity between impure clusters and bulk solids, some system specific deviations from the systematic trend are observed when individual values are carefully accounted. The deviation from regular declining trend is noticed specifically in two regions as indicated in Figure 4.9. First one is observed for lower end clusters with Co, Ni, Cu and Zn as dopant atom and only prominent in the results obtained in M06–2X functional. Slight oscillation in all the thermochemical parameters are noticed which results alteration of their relative order within themselves. In Table 4.3, Al_5Cu shows higher exothermicity (-15.2 kcal/mol) values than Al_5Ni (-14.3 kcal/mol) cluster in M06–2X functional. Similarly, heat of adsorption of $Al_7Ni(b)$ cluster in M06–2X functional (Table 4.5) is found to be higher than $Al_7Co(b)$ cluster by a magnitude of $\sim$1.1 kcal/mol. None of these deviations are large enough and well within ($\pm$ 1–3 kcal/mol) the error margins of DFT functionals. However, the second deviation is a major one and detected for all the clusters doped with chromium atom. It is evident from the plots included in Figure 4.9 that in all the cases clusters doped with chromium atom show a sudden drop in the exothermicity and free energy trend. In both the functionals and for every impure cluster series, the thermochemical parameters for chromium doped clusters are found to be less than manganese doped clusters considering the absolute magnitude (Table 4.3–4.6). Occurrence of such deviations within the smooth trend leads to the suspicion that some other factors must be responsible for these system specific anomalies. As indicated by earlier studies, aside from structural and electronic reason, the stabilities and properties of metal clusters can also be heavily influenced by aromaticity of the metal clusters itself. To account such influences for the present cases, NICS values are calculated for ground state Al_5M clusters in M06–2X functional as shown in Table 4.4. It is observed that among all the ground state clusters, Al_5Cr, Al_5Fe, Al5Co, Al_5Ni and Al_5Cu are found to be aromatic in nature. Among the listed ones, NICS

value indicate that Al_5Co cluster is of highest aromatic character and Al_5Fe being of negligible aromaticity. Now, as binding process of CO_2 with impure clusters involves charge transfer from metal centers to CO_2 moiety, it is certain that cluster with aromatic character will be reluctant to adsorb CO_2 because that will result loss of aromaticity and thereby affecting the stability of the cluster. The situation is similar with the chemical response of aromatic compounds like benzene towards addition reactions. Thus, all the clusters with aromatic character should show lesser heat of adsorption and lower spontaneity towards CO_2 adsorption resulting a break in the trend at their respective positions. Hence, the sudden deviations in the thermodynamic trend observed at the respective places in Figure 4.9 are certainly due to the aromatic nature of specific clusters. However, it is also important to remember that as the absolute values of all the thermochemical properties for lower end clusters are very low, they are highly sensitive on the theoretical method employed, specifically on the choice of DFT functional. Aside from these, due to the minimum spin nature of Ni, Cu and Zn doped cluster slight presence of odd-even effect can also influence the thermodynamic parameters. Hence, It is difficult to conclude how each of these variables separately affects the binding of CO_2 in each case, but it is certain that all of them cumulatively determines the final outcome.

4.4 Conclusions

The present chapter includes an in depth investigation of the influence of spin on properties of transition metal doped aluminum clusters based on density functional theory calculations. Binary metal clusters are of enormous importance due to their wide range of properties and as a possible motif to synthesize new type of materials. Calculated results presented in this chapter show several dissimilarities between the properties of high spin and low spin doped clusters. It is observed that the series of low spin clusters shows prominent odd–even oscillation in all the calculated properties supporting the presence of jellium shell structure, whereas high spin ground state conformers show more of smooth trends similar to the bulk materials. This observation is indeed consistent with the previous theoretical investigation and supports the fact that the electronic shell effect is less important for the high spin ground state of transition metal doped aluminum clusters.[57] In order to further conclude the argument, thermodynamic data of CO_2 adsorption on these doped aluminum clusters are evaluated using DFT. Comparison of the evaluated results with experimental literature shows a similar declining trend of the thermodynamic parameters when changing the dopant atom from Sc to Zn.[58] The resemblance is also reflected in the adsorbed structure of CO_2 on doped clusters as well.[59] Systematic modulation of properties in small sized nano–clusters are indeed of rare occurrence and such resemblance with the characteristics of bulk metals will certainly be beneficial in the voyage of understanding the development of materials from minuscule unit of atoms.

References

(1) Knight, W. D.; Clemenger, K.; de Heer, W. A.; Saunders, W. A.; Chou, M.; Cohen, M. L. *Phys. Rev. Lett.* **1984**, *52*, 2141–2143.

(2) Knight, W. D.; de Heer, W. A.; Clemenger, K.; Saunders, W. A. *Solid State Commun.* **1985**, *53*, 445–446.

(3) Echt, O; Sattler, K; Recknagel, E *Phys. Rev. Lett.* **1981**, *47*, 1121–1124.

(4) Echt, O.; Kandler, O.; Leisner, T.; Miehle, W.; Recknagel, E. *J. Chem. Soc., Faraday Trans.* **1990**, *86*, 2411–2415.

(5) Bergeron, D. E.; Castleman, A. W.; Morisato, T.; Khanna, S. N. *Science* **2004**, *304*, 84–87.

(6) Castleman Jr, A.; Khanna, S. *J. Phys. Chem. C* **2009**, *113*, 2664–2675.

(7) Bergeron, D.; Roach, P.; Castleman, A.; Jones, N.; Khanna, S. *Science* **2005**, *307*, 231–235.

(8) Bergeron, D. E.; Roach, P. J.; Castleman Jr, A. W.; Jones, N. O.; Reveles, J. U.; Khanna, S. N. *J. Am. Chem. Soc.* **2005**, *127*, 16048–16053.

(9) Reber, A. C.; Khanna, S. N.; Castleman, A. W. *J. Am. Chem. Soc.* **2007**, *129*, 10189–10194.

(10) Jena, P.; Castleman, J.; Welford, A, *Nanoclusters: A Bridge Across Disciplines*; Elsevier, Oxford: 2010, pp 1–589.

(11) Knight, W.; De Heer, W. A.; Saunders, W. A.; Clemenger, K.; Chou, M.; Cohen, M. L. *Chem. Phys. Lett.* **1987**, *134*, 1–5.

(12) Kappes, M.; Schär, M; Yeretzian, C; Heiz, U; Vayloyan, A; Schumacher, E, *Physics and Chemistry of Small Clusters*; Plenum, New York: 1987, pp 1–263.

(13) Yeretzian, C. *J. Phys. Chem.* **1995**, *99*, 123–130.

(14) Baladron, C; Alonso, J. *Phys. B* **1988**, *154*, 73–81.

(15) Alonso, J., *Structure and Properties of Atomic Nanoclusters*; World Scientific, London: 2005, pp 1–427.

(16) Johnston, R. L., *Atomic and Molecular Clusters*; CRC Press, London and New York: 2002, pp 1–250.

(17) Molina, L.; López, M.; Alonso, J.; Stott, M. *Ann. Phys. (Berlin, Ger.)* **1997**, *509*, 35–44.

(18) Varas, A.; Aguilera-Granja, F; Rogan, J.; Kiwi, M. *J. Magn. Magn. Mater.* **2015**, *394*, 325–334.

(19) Ducastelle, F. In, Terakura, K., Akai, H., Eds.; Springer Berlin Heidelberg: Berlin, Heidelberg, 1993; Chapter Order and Phase Stability in Alloys, pp 133–142.

(20) Bergeron, D.; Castleman, A. *Chemical physics letters* **2003**, *371*, 189–193.

(21) Reber, A. C.; Khanna, S. N.; Roach, P. J.; Woodward, W. H.; Castleman Jr, A. *J. Phys. Chem. A* **2010**, *114*, 6071–6081.

(22) Kulkarni, B. S.; Krishnamurty, S.; Pal, S. *J. Phys. Chem. C* **2011**, *115*, 14615–14623.

(23) Das, S.; Pal, S.; Krishnamurty, S. *The Journal of Physical Chemistry C* **2014**, *118*, 19869–19878.

(24) Ashman, C; Khanna, S.; Pederson, M. *Chem. Phys. Lett.* **2000**, *324*, 137–142.

(25) Burgert, R.; Stokes, S. T.; Bowen, K. H.; Schnöckel, H. *Journal of the American Chemical Society* **2006**, *128*, 7904–7908.

(26) Leuchtner, R.; Harms, A.; Castleman Jr, A. *J. Chem. Phys.* **1989**, *91*, 2753–2754.

(27) Cheng, H. P.; Barnett, R.; Landman, U. *Phys. Rev. B* **1993**, *48*, 1820–1824.

(28) Wang, H.; Ko, Y. J.; Zhang, X.; Gantefoer, G.; Schnoeckel, H.; Eichhorn, B. W.; Jena, P.; Kiran, B.; Kandalam, A. K.; Bowen Jr, K. H. *J. Chem. Phys.* **2014**, *140*, 124309.

(29) Wang, H.; Zhang, X.; Ko, Y. J.; Grubisic, A.; Li, X.; Ganteför, G.; Schnöckel, H.; Eichhorn, B. W.; Lee, M. S.; Jena, P. *J. Chem. Phys.* **2014**, *140*, 054301.

(30) Popov, I. A.; Zhang, X.; Eichhorn, B. W.; Boldyrev, A. I.; Bowen, K. H. *Phys. Chem. Chem. Phys* **2015**, *17*, 26079–26083.

(31) Li, X.; Wang, L. S. *Phys. Rev. B* **2002**, *65*, 153404.

(32) Kumar, V.; Bhattacharjee, S.; Kawazoe, Y. *Phys. Rev. B* **2000**, *61*, 8541–8547.

(33) Rao, B.; Jena, P *J. Chem. Phys.* **2001**, *115*, 778–783.

(34) Sun, Z.; Xu, H. G.; Feng, G.; Xu, X. L.; Zheng, W. J. *Chem. Phys. Lett.* **2014**, *615*, 56–61.

(35) Zhang, Z. G.; Xu, H. G.; Feng, Y.; Zheng, W. J. *J. Chem. Phys.* **2010**, *132*, 161103.

(36) Sun, Z.; Zhu, Q.; Gao, Z.; Tang, Z. *Rapid Commun. Mass Spectrom.* **2009**, *23*, 2663–2668.

(37) Zhang, X.; Ganteför, G.; Bowen, K. H.; Alexandrova, A. N. *J. Chem. Phys.* **2014**, *140*, 164316.

(38) Wang, L. M.; Huang, W.; Wang, L. S.; Averkiev, B. B.; Boldyrev, A. I. *J. Chem. Phys.* **2009**, *130*, 134303.

(39) Zhao, J. Y.; Zhao, F. Q.; Xu, S. Y.; Ju, X. H. *J. Mol. Graphics Modell.* **2014**, *48*, 9–17.

(40) Guo, L.; Zhang, X. *J. Phys. Chem. C* **2013**, *118*, 533–543.

(41) Gong, X.; Kumar, V. *Phys. Rev. Lett.* **1993**, *70*, 2078.

(42) Li, S.; Gong, X. *Phys. Rev. B* **2004**, *70*, 075404.

(43) Burkart, S.; Blessing, N.; Klipp, B.; Müller, J.; Ganteför, G.; Seifert, G. *Chem. Phys. Lett.* **1999**, *301*, 546–550.

(44) Han, Y. K.; Jung, J.; Kim, K. H. *J. Chem. Phys.* **2005**, *122*, 124319–124319.

(45) Duque, F; Molina, L.; López, M.; Alonso, J. *Eur. Phys. J. D* **2001**, *16*, 285–288.

(46) Qian, M.; Reber, A. C.; Ugrinov, A.; Chaki, N. K.; Mandal, S.; Saavedra, H. M.; Khanna, S. N.; Sen, A.; Weiss, P. S. *ACS Nano* **2009**, *4*, 235–240.

(47) Gong, X. *Phys. Rev. B* **1997**, *56*, 1091–1094.

(48) Grubisic, A; Li, X; Stokes, S.; Vetter, K; Ganteför, G.; Bowen, K.; Jena, P; Kiran, B; Burgert, R; Schnöckel, H *J. Chem. Phys.* **2009**, *131*, 121103.

(49) Jena, P.; Khanna, S.; Rao, B. K., *Physics and Chemistry of Finite Systems: from Clusters to Crystals*; Kluwer Academic Publishers, Dordrecht Boston and London: 1992; Vol. 1, pp 1–1414.

(50) Wang, H.; Zhang, X.; Ko, Y. J.; Gantefoer, G.; Bowen, K. H.; Li, X.; Kiran, B.; Kandalam, A. K. *J. Chem. Phys.* **2014**, *140*, 164317.

(51) Wang, M.; Huang, X.; Du, Z.; Li, Y. *Chem. Phys. Lett.* **2009**, *480*, 258–264.

(52) Pal, R; Cui, L. F.; Bulusu, S.; Zhai, H. J.; Wang, L. S.; Zeng, X. C. *J. Chem. Phys.* **2008**, *128*, 024305.

(53) Thomas, O. C.; Zheng, W.; Bowen, K. H. *J. Chem. Phys.* **2001**, *114*, 5514–5519.

(54) Ko, Y. J.; Shakya, A.; Wang, H.; Grubisic, A.; Zheng, W.; Gotz, M.; Gantefor, G.; Bowen, K. H.; Jena, P.; Kiran, B. *J. Chem. Phys.* **2010**, *133*, 124308.

(55) Aguilera-Granja, F; Longo, R.; Gallego, L.; Vega, A *J. Chem. Phys.* **2010**, *132*, 184507.

(56) Montejano-Carrizales, J.; Aguilera-Granja, F; Morán-López, J. *Eur. Phys. J. D* **2011**, *64*, 53–62.

(57) Chauhan, V.; Singh, A.; Majumder, C.; Sen, P. *J. Phys.: Condens. Matter* **2014**, *26*, 015006.

(58) Toyoshima, I; Somorjai, G. *Catal. Rev.: Sci. Eng.* **1979**, *19*, 105–159.

(59) Liu, C.; Cundari, T. R.; Wilson, A. K. *J. Phys. Chem. C* **2012**, *116*, 5681–5688.

(60) Rao, B.; Jena, P *J. Chem. Phys.* **1999**, *111*, 1890–1904.

(61) Rondina, G. G.; Da Silva, J. L. *J. Chem. Inf. Model.* **2013**, *53*, 2282–2298.

(62) Candido, L.; Rabelo, J. T.; Da Silva, J. L.; Hai, G. Q. *Phys. Rev. B* **2012**, *85*, 245404.

(63) Frisch, M.; Trucks, G.; Schlegel, H.; Scuseria, G.; Robb, M.; Cheeseman, J.; Scalmani, G; Barone, V; Mennucci, B; Petersson, G. *Gaussian 09 Revision A.01, Wallingford CT*.

(64) Yang, W.; Mortier, W. J. *J. Am. Chem. Soc.* **1986**, *108*, 5708–5711.

(65) Drebov, N.; Ahlrichs, R. *J. Chem. Phys.* **2010**, *132*, 164703.

(66) Dayah, M. Dynamic Periodic Table., (accessed Dec 20, 2015).

(67) Girifalco, L. A., *Statistical Mechanics of Solids*; Oxford University Press USA: 2003; Vol. 58.

(68) Bühl, M.; van Wüllen, C. *Chem. Phys. Lett.* **1995**, *247*, 63–68.

(69) Schleyer, P. v. R.; Maerker, C.; Dransfeld, A.; Jiao, H.; Hommes, N. J. v. E. *J. Am. Chem. Soc.* **1996**, *118*, 6317–6318.

(70) Burgert, R.; Schnöckel, H.; Grubisic, A.; Li, X.; Stokes, S. T.; Bowen, K. H.; Ganteför, G.; Kiran, B.; Jena, P. *Science* **2008**, *319*, 438–442.

(71) Ballone, P; Jones, R. *Chem. Phys. Lett.* **1995**, *233*, 632–638.

(72) Nayak, S. K.; Khanna, S.; Rao, B.; Jena, P *J. Phys. Chem. A* **1997**, *101*, 1072–1080.

(73) Neumaier, M.; Olzmann, M.; Kiran, B.; Bowen, K. H.; Eichhorn, B.; Stokes, S. T.; Buonaugurio, A.; Burgert, R.; Schnokel, H. *Journal of the American Chemical Society* **2014**, *136*, 3607–3616.

(74) Burgert, R.; Schnöckel, H. *Chemical Communications* **2008**, 2075–2089.

(75) Li, X.; Grubisic, A.; Stokes, S. T.; Cordes, J.; Ganteför, G.; Bowen, K. H.; Kiran, B.; Willis, M.; Jena, P.; Burgert, R. *Science* **2007**, *315*, 356–358.

(76) Reber, A. C.; Khanna, S. N.; Roach, P. J.; Woodward, W. H.; Castleman, A. W. *J. Am. Chem. Soc.* **2007**, *129*, 16098–16101.

(77) Grubisic, A.; Li, X.; Stokes, S. T.; Cordes, J.; Ganteför, G.; Bowen, K. H.; Kiran, B.; Jena, P.; Burgert, R.; Schnöckel, H. *J. Am. Chem. Soc.* **2007**, *129*, 5969–5975.

(78) Alikhani, M.; Shaik, S *Theor. Chem. Acc.* **2006**, *116*, 390–397.

(79) Danovich, D.; Shaik, S. *Acc. Chem. Res.* **2013**, *47*, 417–426.

(80) Hatch, J. E., *Aluminum: Properties and Physical Metallurgy*; ASM International, Ohio: 1984, pp 1–424.

(81) Lide, D. R., *CRC Handbook of Chemistry and Physics*; CRC Press, Boca Raton: 1992, pp 10–211.

(82) Atkins, P.; De Paula, J., *Elements of Physical Chemistry*; Oxford University Press, Oxford and New York: 2009, pp 1–1097.

Chapter 5

Radical Attached Aluminum Nanoclusters: An Alternative Way of Cluster Stabilization

5.1 Introduction

In material chemistry and nanotechnology, atomic clusters are of colossal interest since past four decades. Whether considered solo in gas phase or as superatomic assembly for nanofabrication, nanoclusters of main group elements have shown promising outcomes in both theoretical and experimental domain. Current advancements in versatile disciplines also have shown the latent potential of atomic clusters towards the development of novel materials with unique catalytic, optical and magnetic properties.[1–11] Evolution of state–of–the–art experimental techniques, theoretical methodologies and computational resources in recent years also have provided adequate assistance in the conquest of understanding the characteristics and behavior of atomic clusters.[12–15] In spite of all this achievements in the respective research fields, the large scale applications of small sized clusters are still implausible due to their demanding condition for synthesis and substantial instability. Most of the small sized nanoclusters are metastable in nature with extremely short lifetime and highly reactive as well.[16,17]Therefore, they can only be synthesized in near vacuum condition in completely inert atmosphere.[18,19] Also, due to their unstable nature, small clusters have high tendency to coalescence with each other in order to form bigger clusters with enhanced stability.[20] Hence, stabilization of small sized atomic clusters is one of the major challenges in current cluster chemistry.

The stability of nanoclusters usually depends on two major factors, electronic and geometric.[18,19,21,22] The concept of electronic stability can better be understood by invoking the concept of jellium model[23–25], where the existences of loosely bound valence electrons are considered against a uniform positive charged background. Based on an approximate potential which is predominantly determined by the structure and composition of the cluster itself, the solution of Schrödinger equation yields discrete energy shells much similar to an atom. Thus, clusters with filled jellium shell achieve additional stability due to higher HOMO–LUMO gap when compared with their open shell counterparts. If the potential is approximated as spherical and uniform, then the corresponding shell ordering with incremental energy is found to be as 1S, 1P, 1D, 2S, 1F, 2P, 1G.[23,24,26] Hence, the number of electrons (n_e) needed to obtain a filled shell configuration follows a series like 2, 8, 18, 20, 34, 40, 58 etc. Clusters with 'n_e' number of valence electrons are considered as 'magical' in nature due to their enhanced stability when compared with rest of the members of the family. Except few limitations[19] observed in specific cases, the jellium model is found to be work exceptionally well in determining the properties of simple metal clusters. On the other hand, the geometric stability is mostly important to weakly bonded clusters (e.g inert gases or molecular clusters) where the stability of the clusters is determined by short–range intermolecular forces and electronic effects plays insignificant role.[27,28]

Due to the weak nature of the force, clusters with closed packed icosahedral structures with high atomic density show additional stability then the rest of the members. Such magic clusters, therefore follow Mackay icosahedra series (n_g) based on the number of constituent atoms within the cluster[29] :

$$n_g = 1 + \sum_{k=1}^{n} (10k^2 + 2) \tag{5.1}$$

First few geometric magic numbers are 13, 55, 147, 309 and 561 for n=1, 2, 3, 4 and 5 respectively. Although in majority of clusters, the stability of the species is primarily determined by any one of the aforesaid factors, in rare cases both geometric and electronic factors can indeed play major role.[30–32] One classic example is the case of Al_{13}^- cluster, which can be considered as double magic cluster with a 13 atom icosahedral structure along with 40 valence electrons, corresponds to a closed jellium configuration. To add further complexity in the scenario, other associated factor like aromaticity can also influence the overall stability and reactivity of nanoclusters.[33–35]

Although the Jellium shell model is primarily designed in order to explain the properties of simple pristine metal clusters, studies have justified the validation of the model in some other scenarios as well.[36–38] In present days, the most common way to stabilize a metallic cluster is to use suitable ligands to produce a organometallic complex with the cluster. In such entities the sensitive metal core is protected by the attached organic group via complex formation, thus preventing the cluster either from coalescence with each other or from reacting with unwanted impurities.[39] Theoretical calculation have shown that such complexes also follows a modified electron counting stability rule where the shell closing magic numbers (n_e) is observed to be dependent on the numbers of ligands attached with the metallic core. For a complex with chemical formula $[M_N L_X]^z$ this new electron counting equation can be presented as,[40–42]

$$n_e = N_M v_M - X_L w_L - z \tag{5.2}$$

where, N_M represents the number of metal atoms within the core each with atomic valence number v_M. X_L is the number of ligands attached with the core. w_L is the number of electrons withdrawn by each of the ligands and z is the overall charge of the complex. Thus, if the number of electrons in the metallic core(n_e) of the cluster complex corresponds to an electronic shell closure number (n_e) as mentioned earlier, the respective species is found to be stable and can be considered as a superatomic complex. Like the jellium model for pristine clusters, the superatomic complex theory is also found to be able to explain the properties of cluster complexes extensively well. Successful implementation is observed for ligand protected gold and silver clusters. As for example, the gold–thio complex $Au_{25}(SR)_{18}^-$ [SR= Thiolate group] has eight valence electrons.[43] Similarly, the core of $Au_{102}(SR)_{44}$ superatomic complex is found to be consists of a 58 electronic closed shell configuration.[44–46] Even, structure of gold superatomic complex with minimum possible shell closing number of 2 is also predicted theoretically.[47] Very recently Häkkinen and coauthors[40–42] have found that the superatomic complex theory is also equally applicable to mono–layer protected small and medium sized aluminum and gallium clusters as well. Calculated results reveals that complex like $Al_8(Cp)_4$, [Cp=C_5H_5] has a 20 electronic closed shell configuration,where $Al_4(Si^tBu)_4$ complex can be considered as a 8 electronic closed shell superatomic complex.

Although the process of ligand attachment to stabilize bare clusters becomes routine for experimental investigations, such implementations are certainly not beyond limitations. As most of the ligand attached clusters can only be synthesized via wet chemistry or in inert matrices,[48–51] therefore, it is difficult to utilize the procedure for the stabilization of small size metastable clusters which are usually synthesized in gas phase and in near vacuum condition via supersonic expansion or related techniques. Thus, throughout the years, experimental and

theoretical investigations of superatomic complexes has been mostly limited to relatively stable large scale clusters like silver and gold[52–61] and only an inadequate numbers of ligand stabilized very small sized (n≤20) clusters have been reported by state–of–the–art experimental techniques.[62–64] According to the modern definition, a free radical is a neutral, electron deficient, species with partially filled orbital. Due to the presence of vacant electronic shell, radicals are extremely reactive and have high tendency to accept electron(s) in order to complete the octet. Hence, based on the chemical intuition it is expected that like ligated clusters, equation 2 will be equally valid for radical attached clusters as well. On the other hand, radicals can easily be produced either in solvents or in gas phase by various means like photolysis, electrolysis or thermolysis.[65–68] Although most of the radicals are metastable due to their high reactivity, there are enough varieties of them which are stable enough for experimental manifestation with ease. Moreover, their enriched existence in galaxies and nebulas also proves that radicals are able to sustain long enough in cold vacuum inert atmosphere much similar to the clusters.[69,70] Based on all these observations, one can argue that if synthesized, radical attached clusters can serve as an alternative of ligand protected clusters with similar thermodynamic stability and with equivalent or larger set of choices. Aside from this, computational studies on radical attached clusters may be proven fruitful in understanding the stability and reactivity of small scale metal clusters. In depth analysis and direct comparison of the properties with ligated clusters may also be able to provide new insights and may yield answers to unresolved questions. Hence, from theoretical standpoint, case study on radical attached clusters are definitely intriguing like the ligated clusters complexes. The current chapter presents such a theoretical account of thermodynamic and electronic stabilities of radical attached aluminum clusters. Direct comparison of the calculated results with small sized experimentally synthesized ligated aluminum cluster is also included. The effect of different substituents on the thermodynamic stabilization of radical attached clusters are also discussed in detail. The chapter is organized as follows, section 2 includes the computational information for all the calculations presented in this chapter. Section 3 contains the detailed discussion and comparison of thermodynamic and electronic stability of radical attached clusters and Section 4 concludes the chapter.

5.2 Computational Details

The initial starting geometries of aluminum clusters are taken from previously reported studies as available in current literature.[71–73] All the clusters are optimized with both M06–2X and B3LYP functional using triple zeta quality basis (TZVP) without any symmetry constraints. The energies of pristine aluminum clusters in different spin multiplicities are further calculated in M06–2X functional and it is observed that clusters with lowest possible spin multiplicities are minimum in energy. This observation is found to be valid for radical attached clusters as well. Therefore, throughout the present chapter all the pristine as well as radical or ligand attached clusters are considered to be of minimum spin *i.e.* the value of $2S+1$ is either 1 or 2 depending whether the species is a closed shell or an open shell system. In all the calculations, Berny optimization algorithm is used as implemented in Gaussian 09 package.[74] As organic radicals, 12 commonly known radicals with variable composition and properties are chosen. To determine the global minimum for radical attached clusters, Fukui indices are evaluated (see **ESI**†) for all the possible sites of each cluster and separate optimizations are performed by attaching selected radicals at all of the chemically non equivalent sites. Only the lowest energy conformer in each case are considered for the present chapter. All the radical attached as well as ligand attached complexes are optimized using the same level of theory as mentioned above. The normal modes of vibration of each optimized structure are carefully observed and it is made sure that all the optimized structures belong to local minimum and not saddle points. The reported

thermodynamic parameters are calculated at 1 atm pressure and 298.15K temperature and zero-point energy corrections are added accordingly. Although the calculations are performed in two different functional as mentioned earlier, the optimized structures presented in all the figures are obtained in M062X/TZVP level of theory if not mentioned otherwise. The charge transfer analysis and Kohn–Sham orbital correlation diagram is calculated using Charge Decomposition Analysis (CDA)[75,76] in open source Multiwfn[77,78]package, using the output file obtained from Gaussian09 calculation. The Natural Bond Orbital (NBO) analysis is performed for specific cases using the NBO 3.0 suite as implemented in Gaussian 09. The Density of States (DOS) plots included in this chapter are also generated by Multiwfn using C–squared population analysis (SCPA) method[79] fitted with normalized gaussian broadening function,

$$G(x) = \frac{1}{c\sqrt{2\pi}} e^{-\frac{x^2}{2c^2}} \tag{5.3}$$

where $c = \frac{FWHM}{2\sqrt{2ln2}}$.

The full width at half maximum (FWHM) value is set to 0.3 eV for all the DOS plots included in this chapter. The steric regions present within the radical attached complexes is evaluated by Reduced Density Gradient(RDG) calculation in Multiwfn.[80] The RDG function is defined as,

$$RDG(r) = \frac{1}{2(3\pi^2)^{1/3}} \frac{|\nabla\rho(r)|}{\rho(r)^{4/3}} \tag{5.4}$$

The RDG calculations are performed with a isovalue of 0.5 using high quality grids each containing more than 1.7 million points. The RDG isosurfaces are colormapped in accordance with the sign of the real space function $\lambda_2(r) \cdot \rho(r)$, where $\rho(r)$ is the electron density at point 'r' and $\lambda_2(r)$ is the second largest eigenvalue of calculated Hessian matrix of electron density. The van der Waals (vdW) volume of specific clusters and radicals are calculated by Monte Carlo (MC) method as implemented in Multiwfn package using a isovalue of 0.001 for all the cases. In the MC method 'N' numbers of particles are distributed randomly within a rectangular box of volume 'V'. If 'n' numbers of particles are found to be present within the vdW region, then the vdW volume of the species is calculated as,

$$V_{vdW} = \frac{n \cdot V}{N} \tag{5.5}$$

The total number of particles N is defined by $100 \cdot 2^i$.For each species, the value of 'i' is increased gradually by unit intervals until the variation in between two consecutive vdW volume is found to be small enough to consider as converged. The converged values are taken as the vdW volume of the respective species in each case.

5.3 Results and Discussion

In order to understand the effect of radical attachment on the thermodynamic stability of small sized aluminum clusters, it is essential to account for all the stabilization effects originating from different contributing factors. As mentioned in the introduction section, the stability of pristine metal clusters are solely depends on two major factors, geometric and electronic, commonly abbreviated as Cluster Size Effects (CSE).[19] Figure 5.1 shows the influence of both these effects on the thermodynamic stability of double magic Al_{13}^- cluster. Based on the thermodynamic parameters calculated by M06–2X functional, it is evident that both the effects play crucial role in determining the overall thermodynamic stability of Al_{13}^- cluster. However, as geometric stability can only be achieved for a limited number of clusters which satisfy the

icosahedral close–packing condition (Equation 1), therefore, for the most part, stabilization of pristine metal clusters is usually achieved by electronic means. On the other hand, the situation for radical attached metal clusters is expected to be somewhat different. Although the geometric and electronic effects within the central metal core would certainly be crucial for the stabilization, the thermodynamic stability of individual radicals, geometrical and electronic effects within them may also play dominant role in the overall stabilization of the cluster–complexes. Hence, keeping that in mind, in the present chapter 12 common organic radicals are chosen with variable chemical properties. Based on the electronic effects which determine the reactivities and stabilities,[81] these radicals can further be distributed into four separate categories as illustrated in Figure 5.2. Radicals belong to Group I consist of common alkyl radicals with dominant inductive effect. As the central carbon atom is electron deficient due to incomplete octet, hence, The stability of these series increase with the increment of the number of electron pushing group attached with it. Therefore, the stability order of Group I radicals is found to be
Tertiary(3°) > Secondary(2°)>Primary(1°)>Methyl
which is the left to right sequence as depicted in the top panel of Figure 5.2 .

Two common radicals with unsaturation namely ethenyl ($C_2H_3\cdot$) and ethynyl ($C_2H\cdot$) are considered within Group II. The stability of these radicals depends on the hybridization state of the central carbon atom bearing the lone electron.[81] Thus ($C_2H_3\cdot$) is more stable than ($C_2H\cdot$) radical as the carbon atom bearing the unpaired electron is sp^2 hybridized in the former whereas for the later it is 'sp' hybridized. Due to higher 's' character of the ethynyl carbon the open shell electron is held more firmly near the nucleus thus reducing the stability of the radical. Radicals included in Group III are stabilized by the delocalization of electrons. Thus radical with maximum number of C_6H_5 group (triphenylmethyl radical ($(C_6H_5)_3C\cdot$)) attached with the central carbon shows highest stability due to resonance. Thus, the stability of these series decrease from left to right with the decrement of the number of phenyl group. The last group (Group IV) consists of two radicals $(CF_3)_3C\cdot$ and $Cl\cdot$ with high group electronegativity. Being highly electronegative, these radicals are usually unstable and highly reactive and associated with high charge transfer when attached with any substrate.

Similar to the radicals, five small sized aluminum clusters Al_3, Al_6, Al_7, Al_{13} and Al_{20} with both closed and open shell structure are chosen for radical attachment. Among the selected clusters only Al_3 cluster is planar, whereas, ground state structures of the other clusters are three dimensional in nature. Considering the jellium shell structure, both Al_3 and Al_7 clusters are just one electron higher than their respective closed magic shell configuration. On the other hand, Al_6 cluster is a magic cluster with 18 valence electron and Al_{13} cluster is one electron short from achieving 40 electron shell closure. In order to account for the electronic stability and comparison, optimized ground state conformer of Al_4 cluster is used. The result and discussion section is segmented into two separate sections. First part includes a brief description, analysis and comparison of thermodynamic stabilities of radical attached clusters whereas the second part is solely focused on the electronic shell structures of cluster–complexes.

5.3.1 Account of Thermodynamic Stability of Radical Attached Clusters

The calculated thermodynamic parameters of mono radical and ligand attached aluminum clusters calculated in M06–2X and B3LYP functional are included in Table 5.1 and 5.2 respectively. The optimized ground state structures of selected mono–radical attached clusters in M06–2X clusters are included in Figure 5.3 as well. As expected, the result shows wide variations in terms of exothermicities (ΔH) and free energies (ΔG) due to the broad range of radical types and clusters chosen for the present chapter. However, careful observation reveals some systematic trend within the parameters when individual classes of radicals are considered separately. As for example, the thermodynamic stability order of Group I radical attached clusters decreases

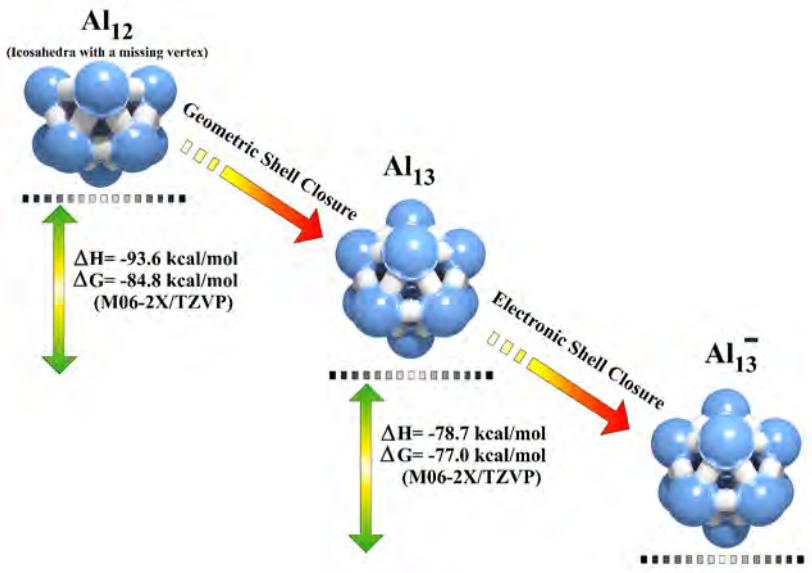

FIGURE 5.1: The stability stairs for Al_{13}^- clusters showing the importance of both the electronic and geometric shell effect on the overall thermodynamic stability of the cluster anion.

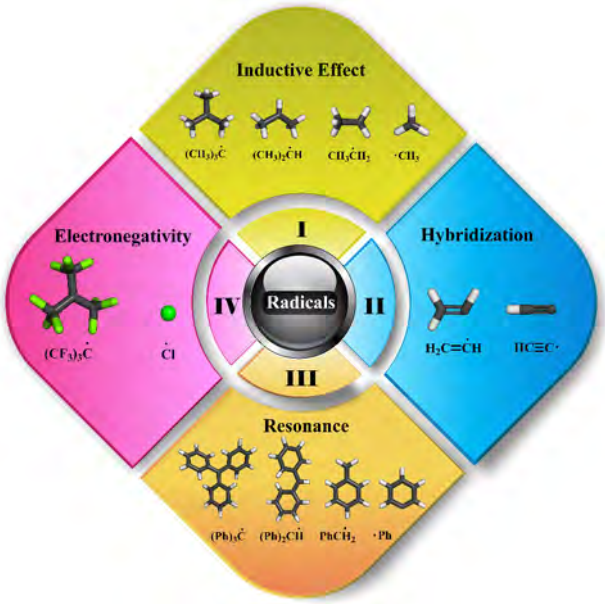

FIGURE 5.2: The list of radicals included in the present chapter. Based on the type of the dominant electronic effects the radicals are divided into four separate categories.

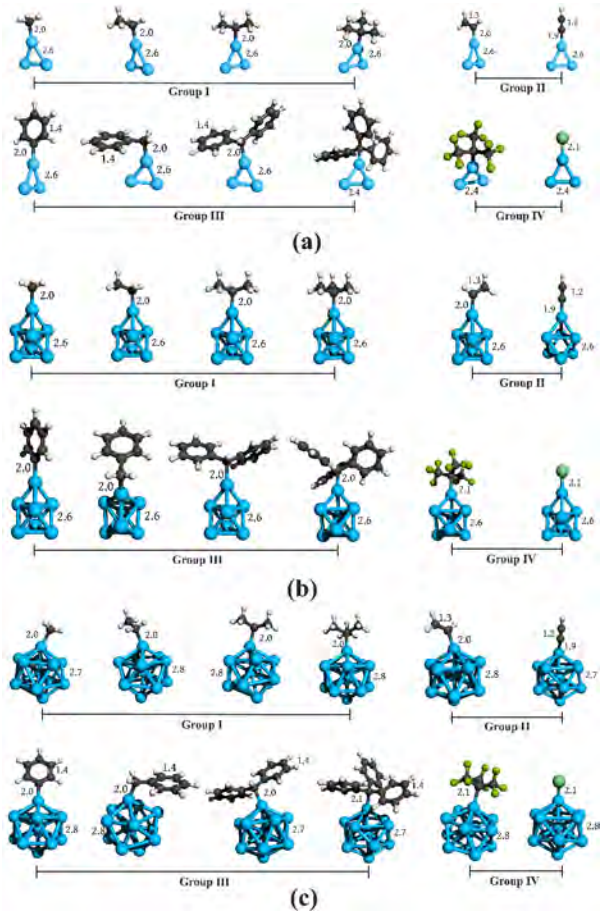

FIGURE 5.3: Optimized structures of mono–radical attached cluster complexes for (a) Al_3, (b) Al_7 and (c) Al_{13} cluster.

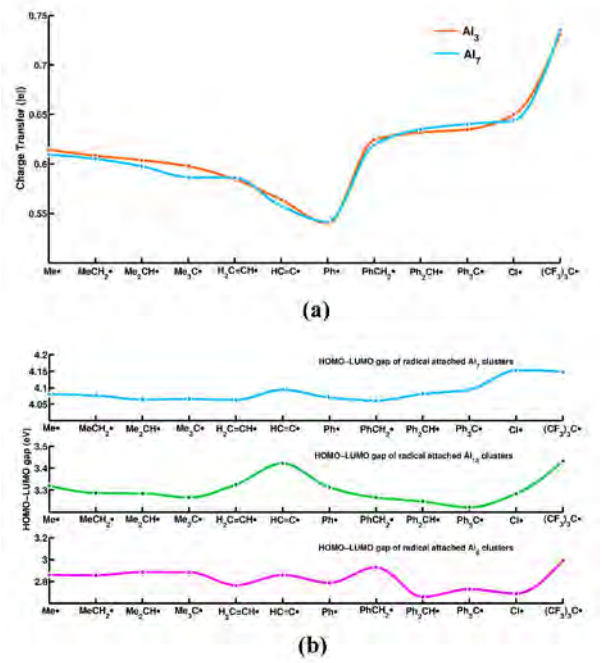

FIGURE 5.4: Plot of charge transfer from cluster core to radicals for Al_3 and Al_7 clusters. (b) Trends in HOMO–LUMO gap for Al_7, Al_{13} and Al_6 radical–cluster complexes.

TABLE 5.1: Thermodynamic data (in kcal/mol) of radical stabilized aluminum clusters calculated in M06–2X/TZVP level of theory. B3LYP calculated results are given in parenthesis.

Radicals	Thermodynamic Parameters	Aluminum Nanoclusters Al_3	Al_6	Al_7	Al_{13}	Al_{20}
CH_3·	ΔH	-63.37(-57.66)	-52.32(-51.22)	-69.92(-63.97)	-56.21(-58.52)	-46.79(-48.96)
	ΔG	-54.33(-47.98)	-43.32(-42.00)	-59.10(-56.50)	-44.42(-49.78)	-37.24(-39.53)
CH_3CH_2·	ΔH	-57.28(-50.41)	-47.12(-44.80)	-63.81(-56.58)	-51.46(-51.77)	-41.04(-42.07)
	ΔG	-45.67(-38.44)	-35.31(-31.76)	-50.35(-46.51)	-36.75(-41.12)	-28.23(-30.19)
$(CH_3)_2CH$·	ΔH	-53.09(-44.92)	-43.93(-38.62)	-60.57(-50.64)	-48.05(-45.97)	-39.84(-36.77)
	ΔG	-41.96(-30.30)	-32.75(-27.24)	-45.47(-41.08)	-32.27(-34.12)	-24.63(-21.77)
$(CH_3)_3C$·	ΔH	-51.37(-40.62)	-42.22(-34.41)	-58.40(-46.28)	-45.44(-41.15)	-37.62(-31.49)
	ΔG	-37.48(-25.75)	-30.53(-22.04)	-42.60(-35.32)	-31.28(-30.03)	-23.92(-17.68)
H_2C=CH·	ΔH	-70.80(-64.46)	-62.77(-56.06)	-76.76(-70.90)	-62.54(-64.97)	-53.71(-55.38)
	ΔG	-58.89(-53.74)	-51.24(-44.42)	-63.24(-60.24)	-50.40(-54.86)	-40.52(-44.20)
HC≡C·	ΔH	-105.78(-104.18)	-94.27(-97.51)	-111.70(-110.25)	-96.86(-104.32)	-86.38(-94.43)
	ΔG	-96.13(-93.14)	-84.77(-87.40)	-100.48(-101.48)	-85.71(-94.64)	-76.32(-83.54)
Ph·	ΔH	-71.68(-65.48)	-64.54(-55.72)	-77.53(-71.14)	-64.46(-66.15)	-62.16(-56.11)
	ΔG	-61.04(-53.82)	-52.72(-43.79)	-65.35(-62.35)	-52.20(-53.64)	-50.38(-44.35)
$PhCH_2$·	ΔH	-52.54(-41.93)	-41.82(-35.59)	-58.13(-47.73)	-46.91(-42.48)	-45.20(-33.02)
	ΔG	-42.50(-31.03)	-31.08(-25.96)	-47.40(-38.84)	-32.00(-32.43)	-30.59(-21.85)
Ph_2CH·	ΔH	-45.92(-32.46)	-36.35(-25.29)	-51.18(-37.46)	-38.48(-31.16)	-29.73(-21.73)
	ΔG	-35.27(-21.53)	-25.29(-14.98)	-39.23(-29.00)	-25.43(-20.81)	-17.59(-9.73)
Ph_3C·	ΔH	-39.93(-24.25)	-30.50(-14.38)	-46.24(-28.70)	-29.24(-16.38)	-27.98(-7.75)
	ΔG	-29.46(-12.72)	-19.56(-3.51)	-31.65(-19.14)	-13.49(-6.01)	-14.69(+4.71)
Cl·	ΔH	-99.96(-94.84)	-85.91(-85.60)	-105.34(-100.70)	-86.87(-91.71)	-86.77(-84.05)
	ΔG	-92.55(-86.45)	-79.40(-79.24)	-96.38(-94.63)	-78.20(-84.77)	-76.58(-75.89)
$(CF_3)_3C$·	ΔH	-71.06(-56.81)	-62.42(-51.19)	-77.09(-63.65)	-62.31(-56.12)	-60.95(-46.28)
	ΔG	-56.76(-44.67)	-48.99(-38.14)	-62.83(-52.72)	-47.11(-43.01)	-45.85(-32.37)

TABLE 5.2: Thermodynamic data (in kcal/mol) of mono–ligand stabilized aluminum clusters calculated in M06–2X/TZVP level of theory. B3LYP calculated results are given in parenthesis.

Ligands	Thermodynamic Parameters	Aluminum Nanoclusters Al_3	Al_6	Al_7	Al_{13}	Al_{20}
Cp [= C_5H_5]	ΔH	-73.49(-54.20)	-60.96(-45.36)	-75.61(-55.59)	-51.44(-38.61)	-48.28(-34.36)
	ΔG	-59.86(-42.61)	-49.54(-35.19)	-60.33(-43.86)	-37.63(-28.67)	-35.65(-23.34)
Cp^* [= $C_5(Me)_5$]	ΔH	-71.49(-49.61)	-61.33(-40.89)	-76.38(-50.92)	-51.97(-33.20)	-52.18(-31.44)
	ΔG	-57.79(-37.80)	-48.83(-29.81)	-59.34(-40.21)	-35.19(-20.80)	-36.41(-17.78)

with the increment in the number of methyl group attached with the central carbon of the respective radical. This observation is also found to be consistent for all the listed clusters given in Table 5.1. In order to understand this trend, CDA analysis is performed and it is observed that the amount of charge transfer (in terms of $|e|$) also follows a similar trend. Figure 5.4a shows plot of charge transfer for Al_3 and Al_7 cluster complexes in M06–2X functional. It is evident from Figure 5.4a that for both the clusters, amount of charge transfer follows a smooth declining trend from methyl ($CH_3\cdot$) to tertiary butyl ($(CH_3)_3C\cdot$) radical. The evaluated charge transfer trend of group I radical attached clusters can easily be explained by invoking the concept of inductive effect.[81] As the +I effect goes on increasing from methyl to tertiary butyl radical, hence, it is expected that the $(CH_3)_3C\cdot$ radical will be most reluctant to accept additional charges due to the presence of three electron pushing methyl groups. On the other hand, $CH_3\cdot$ radical is anticipated to have maximum electron affinity and expected to show high charge transfer among all this radicals of group I. However, rationalization of the observed thermodynamic trend of group I radical attached clusters based on inductive effect alone is definitely not recommended as two major factors can contribute simultaneously. Firstly, as the thermodynamic stability trend is found to be the same with the magnitude of charge transfer for group I radicals, it is not unusual to suspect that the jellium shell structure of the metal cluster core within the complex playing a major role here. Moreover, from Table 5.1 it is evident that both the Al_3 and Al_7 cluster complexes show higher exothermicity and spontaneity (in terms of ΔG) than the rest of the members of the series. As both of these clusters are the closest one to achieve filled jellium shell configuration than the rest by just losing one electron, it is conclusive that jellium configuration of the cluster core is certainly important for the present case. As each cluster differs drastically in terms of the jellium structure, both ΔH and ΔG values follow unpredictable pattern with incremental cluster size as can be seen from Table 5.1. By qualitative observation and considering all the radicals, it is found that Al_7 complexes shows highest exothermicity and spontaneity followed by Al_3 complexes. The lowest absolute values of ΔH and ΔG is observed for Al_{20} cluster complexes in most cases, although there are scenarios where the values are too close with other radical attached clusters, hence can not be said with certainty (e.g. $Cl\cdot$ attached complexes in Table 5.1). However, It is also important to remember that unlike the stability order trend of Group I radicals, their anions follows exactly an opposite trend. Thus upon electron attachment the CH_3^- anion is found to be most stable whereas $(CH_3)_3C^-$ anion is least stable due to the presence of high +I effect. As the radical attached clusters follows the same thermodynamic stability trend it is certain that both the shell effect and the thermodynamic stability of the attached radical anions play dominant role in determining the overall thermodynamic stability of the cluster–radical complexes.

Similar to the case of Group I radicals, the thermodynamic stability of radical attached clusters of other categories also follows the anionic stability order of the respective radicals in most cases. As can be seen from Table 5.1, that for all the clusters with group II attached radical, ethynyl ($C_2H\cdot$) attached clusters shows higher stability than ethenyl ($C_2H_3\cdot$) radical attached clusters. In radical chemistry it is well known that due to higher 's' character of 'sp' hybridized ethynyl carbon, the anionic electron density lies closer to the nucleus and gets highly stabilized via coulombic interaction. The conclusion can further be clarified from Figure 5.5 which represents the partial density of states (PDOS) diagram in M06–2X functional for both the radicals. It can be seen that the SOMO of ethynyl ($C_2H\cdot$) radical is energetically lower(~ 3 eV), with a high SOMO–LUMO gap and also has higher 's' character than $C_2H_3\cdot$ radical (Figure 5.5). Hence, ethynyl anion (C_2H^-) is observed to be more stable than ethenyl anion ($C_2H_3{}^-$). As a matter of fact, clusters attached with ethynyl ($C_2H\cdot$) radical shows maximum thermodynamic stability among all the radical attached clusters included in the present study. The calculated exothermicity and ΔG values (Table 5.1) are found to be much higher for $C_2H\cdot$ attached clusters than the results obtained for mono–ligated clusters presented in Table 5.2. However, according to CDA

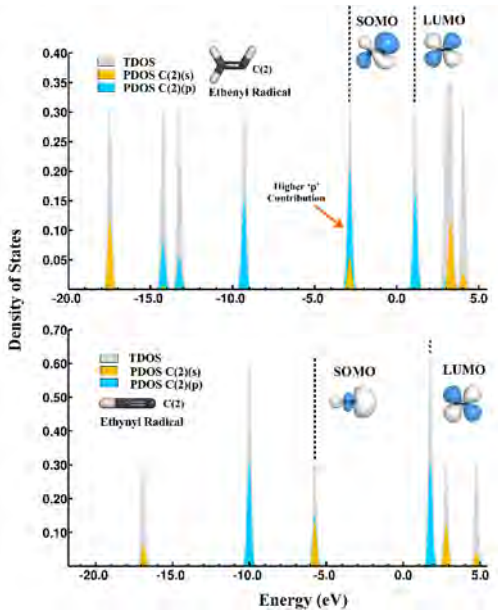

FIGURE 5.5: DOS plot of vinyl and ethynyl radicals. The higher 's' character of SOMO of ethynyl radical due to 'sp' hybridization is the sole reason of the high thermodynamic stability of C_2H_4 radical attached clusters.

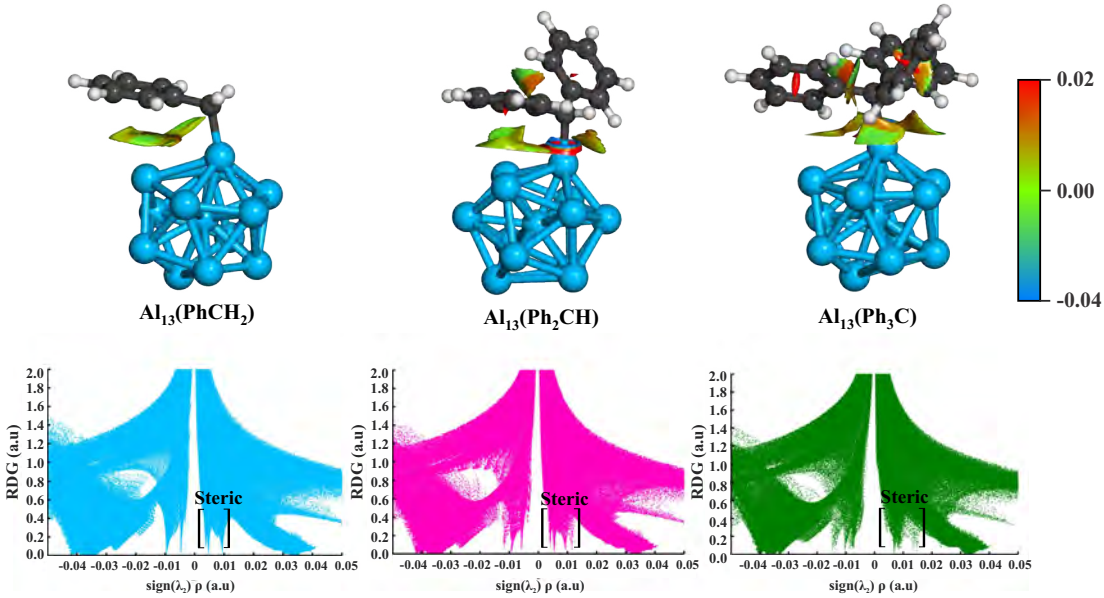

FIGURE 5.6: Reduced density gradient (RDG) isosurface (top panel) and scatter plot (bottom panel) for Group III radical attached Al_{13} clusters. The figures shows systematic amplification of steric effect with the increment of the number of attached Ph group.

analysis, an opposite trend is noticed in terms of charge transfer as can be seen from Figure 5.4a . In both the Al_3 and Al_7 clusters ethenyl ($C_2H_3\cdot$) radical shows higher charge transfer than $C_2H\cdot$ radical. This particular trend seems to be doubtful as from chemical intuition it is expected that $C_2H\cdot$ radical, having more 's' character should show higher charge transfer than ethenyl radical. Therefore, for the present case it is not unusual to doubt the accuracy of the charge transfer trend as obtained by CDA analysis. NBO calculation confirms this suspicion (see **ESI**[†]) and according to the calculated result in M062X functional $C_2H\cdot$ radical indeed shows higher charge transfer than $C_2H_3\cdot$ radical and thereby follows the observed thermodynamic stability trend as well. The charge transfer trend is also found to be driven by the same principle for Group III radicals as well. The amount of charge transfer from cluster to radical is found to be proportional with the number of contributing resonating structures of the radical anion. Thus phenyl radical shows least amount of charge transfer whereas, triphenylmethyl ($Ph_3C\cdot$) radical shows highest amount of charge transfer due to enhanced delocalization of the electron density within the three phenyl moiety. However, in terms of exothermicity viz. thermodynamic stability, Group III attached radicals is the only series which follows an inverse stability order than the anionic stability trend of the respective radicals. Thus, although triphenylmethyl (Ph_3C^-) anion is the most stable anion and shows highest charge transfer among all four, $Ph_3C\cdot$ attached clusters are found to be least thermodynamically stable for all the clusters included in the chapter. In order to account for the inverse trend as observed for Group III radical attached clusters, reduced density gradient (RDG) calculation is performed on $PhCH_2\cdot$, $Ph_2CH\cdot$ and $Ph_3C\cdot$ radical attached Al_{13} clusters in M06–2X functional (Figure 5.6). RDG calculation is considered one of the most efficient way to identify non–covalent interactions (NCI) acting within a molecule.[80,82,83] The upper panel of Figure 5.6 clearly indicates the presence of steric regions in all three radical attached clusters. The number of steric regions also found to increase rapidly while moving from $PhCH_2\cdot$ to $Ph_3C\cdot$ radical. As depicted in Figure 5.6, the $Al_{13}PhCH_2$ complex consists of only one such NCI region. However in $Al_{13}(Ph_2CH)$, presence of three such regions is observed, two NCI region is detected in between the radical and the cluster and the third one is found to occur due the mutual repulsion of the Ph groups. In terms of the numbers of non–covalent interactions, $Al_{13}(Ph_3C)$ cluster complexes shows a maximum of six steric regions, three in between the Ph groups and the Al_{13} core and another three are observed to be within the Ph groups themselves. Furthermore, not only the number of interactions increases with the increment of the Ph groups present in the attached radical, the steric interactions also gets stronger proceeding from $PhCH_2\cdot$ to $Ph_3C\cdot$. The lower panel of Figure 5.6 includes the scatter plots of RDG for all three clusters and it is evident from the plots that the steric region has gradually expanded towards more positive value of $\text{sign}(\lambda_2)\rho$, signifying stronger steric repulsion while moving from benzyl to triphenylmethyl radical. At this point, it is important to mention that although the RDG calculations are performed specifically for Al_{13} cluster–complexes, it is expected that steric interactions will be of equally dominating in other clusters as well. The certainty of this argument lies on the fact that, Al_3, the smallest clusters included within the study is also 21% larger by van der Waals' volume than phenyl (C_6H_5) group. Calculation of vdW volumes by Monte Carlo Method indicates that the vdW volume for a single phenyl group is 114 $Å^3$ whereas, Al_3 cluster has a volume of 138.1 $Å^3$, which is certainly lower than vdW volume of Al_{13} (424.3 $Å^3$) but still expected to be high enough to introduce significant amount of steric strain within the complex. Therefore, the inverse thermodynamic stability trend as observed for Group III radical attached cluster can be considered entirely due to the presence of steric effect. Although the addition of Ph groups in the radical stabilizes the incoming charge density more efficiently via enhanced resonance, but on the other hand, that also destabilize the whole complex due the increment in the number of steric interactions present within the system.

As expected, among all the selected radicals highest amount charge transfer is obtained for $(CF_3)_3C\cdot$ of group IV (Figure 5.4a) due to the presence of sheer number of electronegative

fluorine atom. However, according to the thermodynamic stability of group IV radical attached clusters it is observed that $Cl\cdot$ radical attached clusters shows more exothermicity than $(CF_3)_3C\cdot$ radical attached clusters. In all the selected clusters attached with chlorine radical shows second highest (after ethynyl ($C_2H\cdot$) radical) thermodynamic stability in terms of calculated parameters in both functionals. This particular thermodynamic trend can again be explained by invoking the concept of relative stability of both the radicals anions. As chlorine atom is better in stabilizing the incoming negative charge via dispersion due to the larger size of its anion, therefore, the stability order of the radical attached clusters follows the same trend. The connection between the thermodynamic stability order of radical anions and the stability trends of radical attached clusters is certainly crucial, since, it may grant *a priori* perception about the stability of final complex even before synthesis. At this point it will be interesting to look into the HOMO–LUMO gap of mono–radical attached aluminum clusters. Figure 5.4b illustrates the plot of HOMO–LUMO gap for selected cluster complexes included within this chapter. As can be seen from the plots, except Group III radicals, the HOMO–LUMO gap closely follows the same trend as of charge transfer. The highest HOMO–LUMO gap is also observed for Group IV radical attached clusters, similar to the observed charge transfer trend discussed earlier. This observation is expected as higher charge transfer from cluster core to radical also ensures enhanced electronic stabilization of the complex as a whole. The principle reason which lies behind this argument is, the higher the charge transfer, the attached radical comes closure to achieve a filled octet structure. Secondly, for clusters like Al_3 and Al_7, high charge transfer to the attached radical also ensures that the cluster core becomes inert due to electronic shell closure by donating one excess electron. Among the three cluster–complex series presented in Figure 5.4b, the HOMO–LUMO gap is found to be minimum for Al_6 cluster-complexes. Since, Al_6 is a 18 electronic closed shell magic numbered cluster, it is certain that upon charge transfer, the cluster core would certainly become more reactive because of the adjacency to an open shell configuration. As mentioned earlier, Group III radicals are the only group of radicals which does not follow any regular trend of HOMO–LUMO gap like the others. It can be seen from Figure 5.4b, for each cluster the HOMO–LUMO gap of Group III radicals follows a random trend and hence cannot be generalized. The explanation of this erratic behavior can again be attributed to the additional electronic effects (like steric) which affects each species individually depending on the geometric and electronic structures of the complexes.

5.3.2 The Electronic Structure of Radical Attached Aluminum Clusters

As mentioned in earlier section, according to the superatomic complex theory (SACT) the electronic structure of the cluster–complexes plays major role determining the stabilities and reactivities of the species. Hence, in order to have an in depth perception about the properties of radical attached complexes, it is essential to investigate the electronic structure of the radical–cluster complexes and compare the calculated results with the ligated cluster complexes already available in the literature. Among the experimentally synthesized stable superatomic complexes of aluminum, the cyclopentadienyl (Cp= C_5H_5) or pentamethylcyclopentadienyl (Cp*= C_5Me_5) ligand protected clusters by Schnöckel and co-workers are found to be of profound interest since their first discovery.[62,84–86] Numerous studies on these cluster–complexes in both theoretical and experimental domain has been performed in the last two decades. Starting from structural characterization, bonding and physical properties, detailed molecular dynamics simulations of ligated clusters including the oxidation reactions are added to recent literature.[87–89] Very recently Häkkinen and coworkers[40–42] have proven the existence of superatomic shell structures within small and medium sized cyclopentadienyl and related ligated clusters. Their calculation on Al_4L_4(L=ligands) and related series of clusters have established the validity of superatomic complex theory in small sized ligated–clusters as well. Furthermore, the enhanced stability of

Al_4L_4 type of cluster–complex is also attributed to the closed jellium shell configuration consisting of 8 valence electrons. Therefore, In order to compare the electronic structure of radical attached clusters with that of ligated ones, three different radical attached clusters with tetrahedral Al_4 core are optimized and several properties are calculated. The radicals which are selected for this purpose are respectively ethynyl ($C_2H\cdot$), phenyl($C_6H_5\cdot$) and chlorine ($Cl\cdot$) as they have shown high thermodynamic stability based on the assessment described in the thermodynamics section (Table 5.1 and 5.2) of the present chapter. The optimized structures of these radical attached clusters along with $Al_4(Cp)_4$ clusters are included in Figure 5.7. Table 5.3 enlists all the calculated thermodynamic parameters including charge transfer and HOMO–LUMO gap for these cluster complexes. It is evident from Table 5.3 that all three radical attached clusters shows equivalent or higher thermodynamic stability with the well known $Al_4(Cp)_4$ clusters. Specifically speaking, both the $Al_4(C_2H)_4$ and Al_4Cl_4 clusters show significantly high exothermicity and spontaneity(ΔG) values ($\gtrsim$ 140 kcal/mol) in both functional when compared with $Al_4(Cp)_4$ ligated–complex. The relative ordering of both the exothermicity as well as the ΔG for Al_4X_4(X=Radicals) complexes is found to be consistent with the results obtained for the mono–radical attached clusters described earlier. Thus $Al_4(C_2H)_4$ complex is found most exothermic then Al_4Cl_4 and Al_4Ph_4 complex is observed to be least stable among all three. In terms of tetramerization energies (T.E) as included in Table 5.3, all three radical attached complex are found to be more thermodynamically stable than $Al_4(Cp)_4$ complex. The calculated T.E for $Al_4(Cp)_4$ complex is found to be moderately exothermic ($\sim$ -28 kcal/mol in m06–2X) with slightly positive value of ΔG, which is expected since $Al_4(Cp)_4$ superatom is known to decompose at temperature higher than 243K.[86] Whereas, all the radical attached Al_4 clusters show high negative value of ΔH and ΔG even at room temperature signifying their high thermodynamic stability than $Al_4(Cp)_4$. The calculated charge transfer data from cluster core to radical by CDA analysis also show an expected trend. Thus, being highly electronegative, highest amount of charge transfer ($\sim$ 1.1 |e|) is observed for chlorine radical in Al_4Cl_4. The Al_4Ph_4 cluster complex shows the lowest amount of charge transfer (0.45 |e|) and $Al_4(C_2H)_4$ complex having an intermediate value of 0.49 |e|. On the other hand, the amount of charge transfer from cluster to ligand in the $Al_4(Cp)_4$ligated cluster is found to be 0.79|e| as indicated by CDA analysis. This value is much higher than both $C_2H\cdot$) and $C_6H_5\cdot$ radical but certainly lower than the chlorine one. Also to mention, the CT value obtained for $Al_4(Cp)_4$ complex is indeed an exact match with the Bader charge analysis value obtained in the original paper by Clayborne and coworkers,[40]thus validating the reliability of our results.

Aside from the thermodynamic and CT data, Table 5.3 also includes the calculated HOMO–LUMO gaps for these three radical attached clusters along with $Al_4(Cp)_4$. DFT calculation indicates the presence of very high HOMO–LUMO gap in $Al_4(Cp)_4$ complex (4.58 eV in B3LYP functional) indicating the enhanced stability of $Al_4(Cp)_4$. The HOMO–LUMO gap is found to be $\sim$ 3.2 eV higher than the pristine Al_4 cluster which shows a H–L gap of 1.35 eV in the same level of theory. Similar to the ligated cluster high HOMO–LUMO gap is also obtained for all three radical attached clusters as well. The Al_4Cl_4 complex shows nearly the same HOMO–LUMO gap as $Al_4(Cp)_4$ in both DFT functionals (Table 5.3). In comparison, the $Al_4(C_2H)_4$ and Al_4Ph_4 show slightly less HOMO–LUMO gap by magnitude. However, in comparison with pristine Al_4 cluster the H–L gaps are still found to be very high. The calculated values are found to be even higher than the well known double magic Al_{13}^- cluster which has a HOMO–LUMO gap of 2.61 eV in the same level of theory.

To understand the core structure of radical attached clusters CDA analysis is performed in M06–2X functional and orbital correlation diagrams for both $Al_4(C_2H)_4$ and Al_4Cl_4 complexes are constructed (Figure 5.8). Now, according to the superatomic complex theory, the jellium configuration of Al_4 cluster core in a Al_4L_4 complex should be $1S^2\ 1P^6\ 1D^0$ considering three valence electrons per aluminum atom and also if each attached ligand or radical takes away

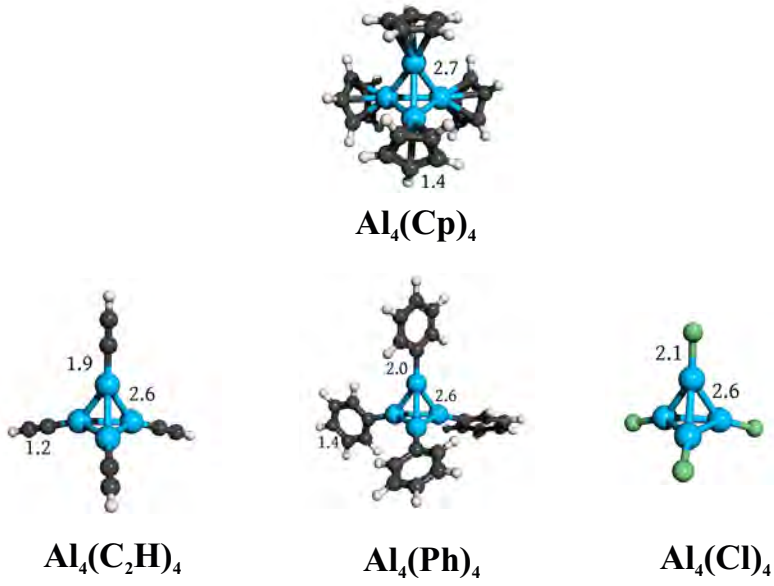

FIGURE 5.7: Optimized structures of Al_4 complexes. The top panel shows the structure of Al_4Cp_4 ligand–cluster complex whereas the bottom panel consists of $Al_4(C_2H)_4$, Al_4Ph_4 and Al_4Cl_4 radical–cluster complexes

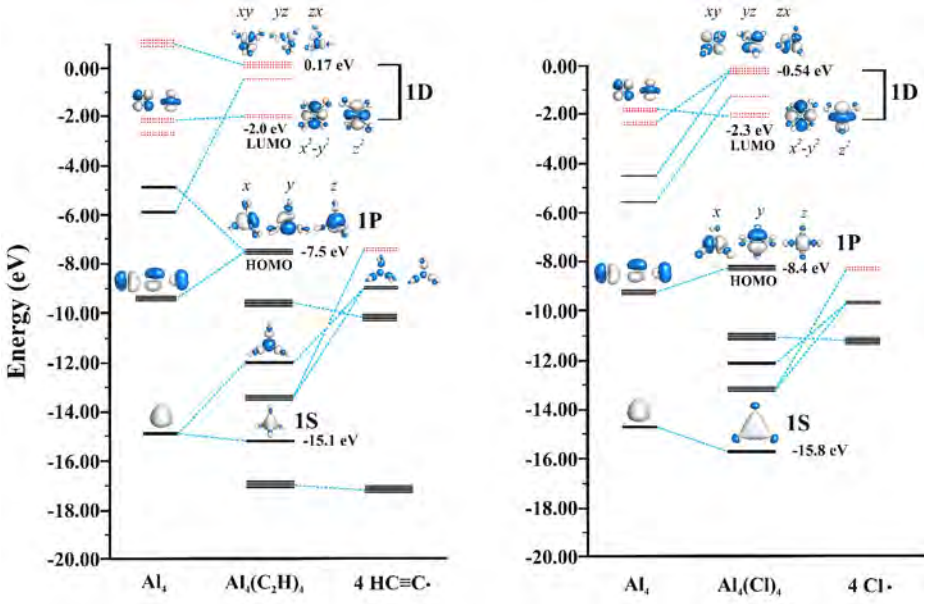

FIGURE 5.8: The Kohn-Sham orbital correlation diagram for $Al_4(C_2H)_4$ (left) and Al_4Cl_4 (right) cluster complexes. The orbital order clearly indicates the presence of jellium shell structures within the radical–cluster complexes. In both the complexes the 'D' orbital has split into two subsets due to the tetrahedral (T_d) crystal field effect.

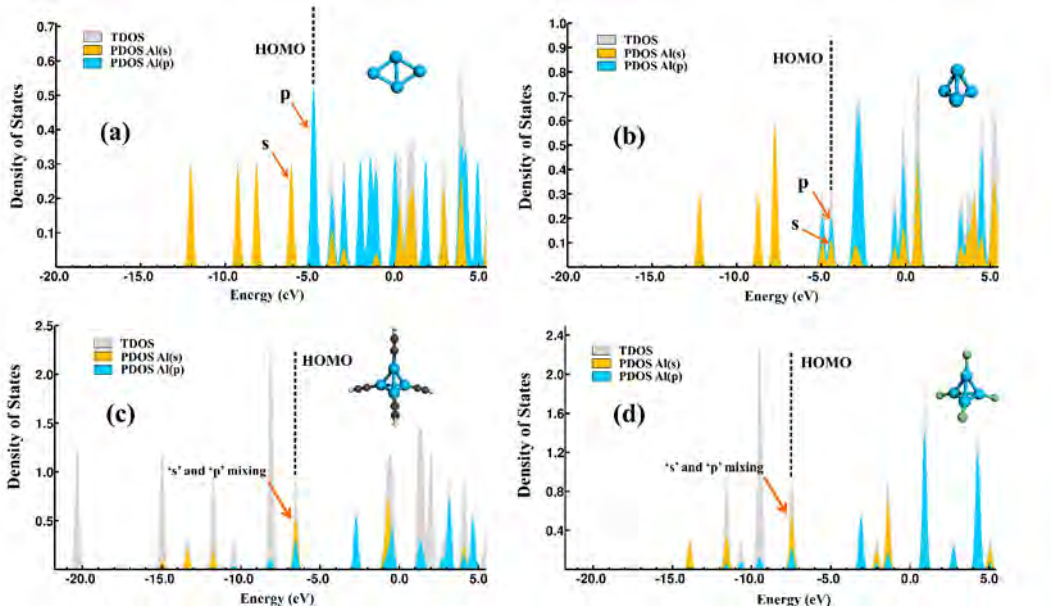

FIGURE 5.9: The Partial Density of States (PDOS) diagram of **(a)** Planar Al_4 cluster. **(b)** Tetrahedral Al_4cluster **(c)** $Al_4(C_2H)_4$ cluster complex and **(d)** Al_4Cl_4 cluster complex. Significant amount of 's' and 'p' mixing is observed in later two cases which explains the observed trivalent nature of aluminum in small superatomic complexes.

TABLE 5.3: Calculated data for ligand and radical attached Al_4 clusters in M06–2X/TZVP level of theory. B3LYP calculated results are given in parenthesis.

Al_4 Cluster Complexes	Thermodynamic Parameters (kcal mol^{-1})		Tetramerization Energy (kcal mol^{-1})		Charge Transfer (|e| in M062X)	HOMO–LUMO gap (eV)	AIE (eV)	VDE (eV)
	ΔH	ΔG	ΔH	ΔG				
Al_4Cp_4	-297.76(-228.20)	-242.96(-180.51)	-27.63(-11.70)	+6.33(+18.83)	0.79	6.16(4.58)	5.64(5.61)	1.17(1.56)
$Al_4(C_2H)_4$	-443.20(-438.88)	-398.90(-395.02)	-94.04(-82.80)	-75.17(-66.65)	0.49	5.51(3.80)	7.64(7.43)	1.85(1.94)
Al_4Ph_4	-304.65 (-282.09)	-256.39(-236.49)	-105.97(-92.49)	-71.70(-60.04)	0.45	5.19(3.52)	6.89(6.63)	1.78(1.71)
Al_4Cl_4	-420.36(-403.40)	-385.55(-370.36)	-61.67(-50.52)	-32.56(-21.79)	1.08	6.10(4.37)	8.63(8.41)	2.45(2.44)

one electron. It is evident from Figure 5.8 , that both the radical complexes has a 8 electronic closed shell jellium core structure. The HOMO of both complexes are found to be three fold degenerate 'P' state as predicted. The low lying 'S' state is also clearly visible in the diagram ensuring the core orbital of the complexes is in accordance with the prediction of jellium model. In the specific case of $Al_4(C_2H)_4$ complex, slight mixing of the 'S' state with the HOMO state of the ethynyl ligands is observed, thus producing one bonding and one antibonding type of orbital. On the other hand, in both the complexes 'P' shell is found nearly pure in nature with $\sim$ 70% contribution from the orbitals of aluminum. The LUMO state in both the radical–attached complexes is also found to be of 'D' type in nature. As the complexes are consists of a core with tetrahedral (T_d) symmetry, 'D' orbital has split into two subsets according to the rule of Crystal Field Theory (CFT). Figure 5.8 shows the relative positions of the two subsets of 'D' shell for $Al_4(C_2H)_4$ and Al_4Cl_4 complex. The Splitting energy (Δ_t) in M06–2X functional is found to be 1.8 eV (1.7 eV in B3LYP) for Al_4Cl_4 complex and of 2.17 eV (2.03 eV in B3LYP) in $Al_4(C_2H)_4$ complex. Both the values are way higher than the Δ_t values obtained for $Al_4(Cp)_4$ ligated clusters(0.33 eV and 0.43 eV in M062X and B3LYP functional respectively) implying higher field strength of both radicals in comparison of C_p ligands. The included diagrams for radical attached clusters are in very well agreement with the correlation diagram as obtained previously for small sized ligated aluminum cluster.[40] All these observations further confirm the presence of superatomic shell in small sized radical attached cluster and henceforth it can be expected that the superatomic complex theory i.e equation 2 will be equally valid for radical attached clusters as well.

Although the presence of jellium core in radical attached Al_4 cluster is already well established by now, one intriguing question regarding the valence electron count of Al_4X_4 complexes should be asked at this point. Based on earlier investigations it is already established that in small sized aluminum clusters Al_n($n\leq6$) aluminum behaves as monovalent metal due to wide separation of 's' and 'p' orbitals. This is the sole reason that the ground state optimized structures of aluminum clusters up to n=5 is two dimensional in nature.[18,71] Starting from Al_6, clusters beginning to become three dimensional as the hybridization between 's' and 'p' states start to build up and aluminum metal behaves as trivalent from this point onwards. This foundation is in direct contradiction with the conclusion drawn for the jellium core structures of Al_4X_4 clusters explained earlier. It is already established (Figure 5.8) that Al_4X_4 complexes have a jellium core structure with valence electron count n_e=8 which is only possible if the attached radicals somehow enhanced the 'sp' hybridization to make the aluminum atoms trivalent in Al_4 core. In order to resolve this arguments partial density of states (PDOS) calculation is performed in B3LYP functional on planar Al_4, tetrahedral Al_4 clusters including $C_2H\cdot$ and $Cl\cdot$ attached Al_4X_4 cluster complexes as depicted in Figure 5.9. It can be clearly seen from Figure 5.9a that the HOMO in planar Al_4 cluster is entirely of 'p' type and as expected, there is a well separated gap of 1.4 eV in B3LYP functional between 's' and 'p' states. In tetrahedral Al_4 isomer (Figure 5.9b) which is about 3 eV (B3LYP) higher in energy than the planar one, marginal mixing of 's' and 'p' state is observed but the HOMO state seems to be negligibly perturbed (lowered by $\sim$ 0.3 eV in B3LYP). On the other hand, in both the $Al_4(C_2H)_4$ and Al_4Cl_4 complexes high amount of 's' and 'p' mixing is observed in the HOMO state as can be seen from Figure 5.9c and 5.9d. This observation indeed indicates the facilitation of 'sp' hybridization of aluminum atom upon radical attachment as predicted earlier. These radical induced 'sp' hybridization is the sole reason of the trivalent nature of aluminum in this size scale as indicated by the orbital correlation diagram (Figure 5.8). The enhanced hybridization of cluster complexes is also observed in ligated clusters as reported in earlier literature.[40] The major reason behind the induced hybridization is due to the stabilization of the HOMO states of the complexes upon radical attachment. As can be seen from the Figure 5.9, that in both the radical attached cluster the HOMO state has shifted significantly to lower energy when compared with planar ($E_{HOMO(B3LYP)}$=-4.7

eV) or tetrahedral ($E_{HOMO(B3LYP)}$=-4.4 eV) pristine Al_4 clusters. This stabilization is found to be higher in Al_4Cl_4 complex ($E_{HOMO(B3LYP)}$=-7.5 eV) compared to $Al_4(C_2H)_4$ ($E_{HOMO(B3LYP)}$=-6.5eV) cluster complex. The enhanced electronic stability of the radical attached clusters are also reflected in the ionization energy (I.E) values of these complexes as shown in Table 5.3. All the radical attached Al_4 clusters shows high I.E values compared to the $Al_4(Cp)_4$. The highest I.E is observed for Al_4Cl_4 (8.6 eV in M06–2X and 8.4 in B3LYP functional) followed by $Al_4(C_2H)_4$. Especially the I.E values for both the $Al_4(C_2H)_4$ and Al_4Cl_4 complexes are $\sim$ 2-3 eV higher than the $Al_4(Cp)_4$ superatomic complexes. In terms of the calculated vertical detachment energies (VDE) of the respective anions(Table 5.3), the radical attached clusters usually have shown close proximity with the VDE value calculated for $Al_4(Cp)_4$ anion. The values of VDE of radical attached clusters are found to be higher than $Al_4(Cp)_4$ anion by 0.61–1.28 eV in M06–2X functional(0.15–0.88 eV in B3LYP), the highest being observed for Al_4Cl_4 anion. The high value of I.E of neutral complexes and similar VDE of respective anions with $Al_4(Cp)_4^-$ of radical attached clusters further concludes the presence of filled jellium shell in radical attached complexes also their enhanced stability compared to the ligated clusters.

5.4 Conclusions

The present chapter includes a brief analysis of the thermodynamic stabilities and electronic structure of few selected radical attached clusters using DFT as a tool of choice. The calculated results has shown that the thermodynamic stabilities of radical attached clusters are highly dependent on the stabilities of the attached radical anions as well as other electronic effects within the complexes including the electronic shell effect. The dependency of the thermodynamic stability of radical attached complexes on the radical anion is certainly important as it can provide the concept of stability of the radical attached complex prior to synthesis. Calculation of other related properties like HOMO–LUMO gap, charge transfer etc are also found to be consistent with the calculated thermodynamic stability trends and also with the type of attached radicals. Construction of Kohn–Sham orbital correlation diagram obtained via CDA analysis also proves the presence of jellium shell structures within the complex which also justifies the validity of superatomic complex thoery (SACT) for radical attached clusters as well. Inclusion of the Density of States (DOS) diagram further confirms the presence of enhanced 'sp' hybridization in small sized radical attached clusters. Comparison with the experimental and theoretical results of ligated clusters also shows the resemblance between both type of clusters. The enhance stability of radical attached clusters are of crucial importance since it can bestow new opportunities and alternatives for synthesizing stable superatomic complexes craved by cluster chemists for decades.

References

(1) Castleman, A. W.; Khanna, S. N.; Sen, A.; Reber, A. C.; Qian, M.; Davis, K. M.; Peppernick, S. J.; Ugrinov, A.; Merritt, M. D. *Nano Lett.* **2007**, *7*, 2734–2741.

(2) Castleman Jr, A.; Khanna, S. *J. Phys. Chem. C* **2009**, *113*, 2664–2675.

(3) Claridge, S. A.; Castleman Jr, A.; Khanna, S. N.; Murray, C. B.; Sen, A.; Weiss, P. S. *Acs Nano* **2009**, *3*, 244–255.

(4) Castleman Jr, A.; Wei, S *Annu. Rev. Phys. Chem.* **1994**, *45*, 685–719.

(5) Reveles, J. U.; Clayborne, P. A.; Reber, A. C.; Khanna, S. N.; Pradhan, K.; Sen, P.; Pederson, M. R. *Nat. Chem.* **2009**, *1*, 310–315.

(6) Moseler, M.; Häkkinen, H.; Landman, U. *Phys. Rev. Lett.* **2002**, *89*, 176103.

(7) Moseler, M; Häkkinen, H; Barnett, R.; Landman, U. *Phys. Rev. Lett.* **2001**, *86*, 2545.

(8) Lindgren, J.; Clayborne, A.; Lehtovaara, L. *J. Phys. Chem. C* **2015**, *119*, 19539–19547.

(9) Grubisic, A.; Ko, Y. J.; Wang, H.; Bowen, K. H. *J. Am. Chem. Soc.* **2009**, *131*, 10783–10790.

(10) Leuchtner, R.; Harms, A.; Castleman Jr, A. *J. Chem. Phys.* **1989**, *91*, 2753–2754.

(11) Li, X.; Wu, H.; Wang, X. B.; Wang, L. S. *Phys. Rev. Lett.* **1998**, *81*, 1909.

(12) Burgert, R.; Stokes, S. T.; Bowen, K. H.; Schnöckel, H. *Journal of the American Chemical Society* **2006**, *128*, 7904–7908.

(13) Neumaier, M.; Olzmann, M.; Kiran, B.; Bowen, K. H.; Eichhorn, B.; Stokes, S. T.; Buonaugurio, A.; Burgert, R.; Schnokel, H. *Journal of the American Chemical Society* **2014**, *136*, 3607–3616.

(14) Bergeron, D. E.; Castleman, A. W.; Morisato, T.; Khanna, S. N. *Science* **2004**, *304*, 84–87.

(15) Bergeron, D.; Roach, P.; Castleman, A.; Jones, N.; Khanna, S. *Science* **2005**, *307*, 231–235.

(16) Castleman Jr, A.; Keesee, R. *Annu. Rev. Phys. Chem.* **1986**, *37*, 525–550.

(17) Kappes, M.; Schär, M; Yeretzian, C; Heiz, U; Vayloyan, A; Schumacher, E, *Physics and Chemistry of Small Clusters*; Plenum, New York: 1987, pp 1–263.

(18) Alonso, J., *Structure and Properties of Atomic Nanoclusters*; World Scientific, London: 2005, pp 1–427.

(19) Johnston, R. L., *Atomic and Molecular Clusters*; CRC Press, London and New York: 2002, pp 1–250.

(20) Jena, P.; Castleman, J.; Welford, A, *Nanoclusters: A Bridge Across Disciplines*; Elsevier, Oxford: 2010, pp 1–589.

(21) Khanna, S.; Jena, P *Phys. Rev. Lett.* **1992**, *69*, 1664.

(22) Khanna, S.; Jena, P *Phys. Rev. B* **1995**, *51*, 13705.

(23) Knight, W. D.; Clemenger, K.; de Heer, W. A.; Saunders, W. A.; Chou, M.; Cohen, M. L. *Phys. Rev. Lett.* **1984**, *52*, 2141–2143.

(24) Knight, W. D.; de Heer, W. A.; Clemenger, K.; Saunders, W. A. *Solid State Commun.* **1985**, *53*, 445–446.

(25) Ekardt, W *Phys. Rev. B* **1984**, *29*, 1558.

(26) Knight, W.; De Heer, W. A.; Saunders, W. A.; Clemenger, K.; Chou, M.; Cohen, M. L. *Chem. Phys. Lett.* **1987**, *134*, 1–5.

(27) Echt, O; Sattler, K; Recknagel, E *Phys. Rev. Lett.* **1981**, *47*, 1121–1124.

(28) Miehle, W; Kandler, O; Leisner, T; Echt, O *J. Chem. Phys.* **1989**, *91*, 5940–5952.

(29) Mackay, A. *Acta Crystallogr.* **1962**, *15*, 916–918.

(30) Ahlrichs, R.; Elliott, S. D. *Phys. Chem. Chem. Phys.* **1999**, *1*, 13–21.

(31) Rao, B.; Khanna, S.; Jena, P *Phys. Rev. B* **2000**, *62*, 4666.

(32) Chuang, F.; Wang, C.; Ho, K. *Phys. Rev. B* **2006**, *73*, 125431.

(33) Chattaraj, P. K., *Aromaticity and Metal Clusters*; CRC Press: 2010.

(34) Alexandrova, A. N.; Boldyrev, A. I. *J. Phys. Chem. A* **2003**, *107*, 554–560.

(35) Boldyrev, A. I.; Wang, L. *Chem. Rev.* **2005**, *105*, 3716–3757.

(36) Walter, M.; Akola, J.; Lopez-Acevedo, O.; Jadzinsky, P. D.; Calero, G.; Ackerson, C. J.; Whetten, R. L.; Grönbeck, H.; Häkkinen, H. *Proc. Natl. Acad. Sci. U. S. A.* **2008**, *105*, 9157–9162.

(37) Walter, M.; Moseler, M.; Whetten, R. L.; Häkkinen, H. *Chem. Sci.* **2011**, *2*, 1583–1587.

(38) Akola, J.; Kacprzak, K. A.; Lopez-Acevedo, O.; Walter, M.; Gr$^{'}$onbeck, H.; Häkkinen, H. *J. Phys. Chem. C* **2010**, *114*, 15986–15994.

(39) Luo, Z.; Reber, A. C.; Jia, M.; Blades, W. H.; Khanna, S. N.; Castleman, A. *Chem. Sci.* **2016**.

(40) Clayborne, P. A.; Lopez-Acevedo, O.; Whetten, R. L.; Grönbeck, H.; Häkkinen, H. *J. Chem. Phys.* **2011**, *135*, 094701.

(41) Clayborne, P. A.; Lopez-Acevedo, O.; Whetten, R. L.; Grönbeck, H.; Häkkinen, H. *Eur. J. Inorg. Chem.* **2011**, *2011*, 2649–2652.

(42) Lopez-Acevedo, O; Clayborne, P.; Häkkinen, H *Phys. Rev. B* **2011**, *84*, 035434.

(43) Akola, J.; Walter, M.; Whetten, R. L.; Häkkinen, H.; Grönbeck, H. *J. Am. Chem. Soc.* **2008**, *130*, 3756–3757.

(44) Jung, J.; Kang, S.; Han, Y.-K. *Nanoscale* **2012**, *4*, 4206–4210.

(45) Hulkko, E.; Lopez-Acevedo, O.; Koivisto, J.; Levi-Kalisman, Y.; Kornberg, R. D.; Pettersson, M.; Häkkinen, H. *J. Am. Chem. Soc.* **2011**, *133*, 3752–3755.

(46) Schnöckel, H.; Schnepf, A.; Whetten, R. L.; Schenk, C.; Henke, P. *Z. Anorg. Allg. Chem.* **2011**, *637*, 15–23.

(47) Jiang, D.; Whetten, R. L.; Luo, W.; Dai, S. *J. Phys. Chem. C* **2009**, *113*, 17291–17295.

(48) Olivares, A.; Laskin, J.; Johnson, G. E. *J. Phys. Chem. A* **2014**, *118*, 8464–8470.

(49) Boyen, H.-G.; Kästle, G; Weigl, F; Koslowski, B; Dietrich, C; Ziemann, P; Spatz, J.; Riethmüller, S; Hartmann, C; Möller, M, et al. *Science* **2002**, *297*, 1533–1536.

(50) Maity, P.; Xie, S.; Yamauchi, M.; Tsukuda, T. *Nanoscale* **2012**, *4*, 4027–4037.

(51) Carotenuto, G.; Martorana, B.; Perlo, P.; Nicolais, L. *J. Mater. Chem.* **2003**, *13*, 2927–2930.

(52) Wu, Z.; Lanni, E.; Chen, W.; Bier, M. E.; Ly, D.; Jin, R. *J. Am. Chem. Soc.* **2009**, *131*, 16672–16674.

(53) Kumar, S.; Bolan, M. D.; Bigioni, T. P. *J. Am. Chem. Soc.* **2010**, *132*, 13141–13143.

(54) Levi-Kalisman, Y.; Jadzinsky, P. D.; Kalisman, N.; Tsunoyama, H.; Tsukuda, T.; Bushnell, D. A.; Kornberg, R. D. *J. Am. Chem. Soc.* **2011**, *133*, 2976–2982.

(55) Jin, R. *Nanoscale* **2010**, *2*, 343–362.

(56) Negishi, Y.; Nobusada, K.; Tsukuda, T. *J. Am. Chem. Soc.* **2005**, *127*, 5261–5270.

(57) Pei, Y.; Zeng, X. C. *Nanoscale* **2012**, *4*, 4054–4072.

(58) Pei, Y.; Gao, Y.; Zeng, X. C. *J. Am. Chem. Soc.* **2008**, *130*, 7830–7832.

(59) Pei, Y.; Gao, Y.; Shao, N.; Zeng, X. C. *J. Am. Chem. Soc.* **2009**, *131*, 13619–13621.

(60) Gao, Y.; Shao, N.; Zeng, X. C. *ACS nano* **2008**, *2*, 1497–1503.

(61) Shao, N.; Pei, Y.; Gao, Y.; Zeng, X. C. *J. Phys. Chem. A* **2009**, *113*, 629–632.

(62) Purath, A.; Dohmeier, C.; Ecker, A.; Schnöckel, H.; Amelunxen, K.; Passler, T.; Wiberg, N. *Organometallics* **1998**, *17*, 1894–1896.

(63) Huber, M.; Schnöckel, H. *Inorg. Chim. Acta* **2008**, *361*, 457–461.

(64) Henke, P.; Huber, M.; Steiner, J.; Bowen, K.; Eichhorn, B.; Schnöckel, H. *J. Am. Chem. Soc.* **2009**, *131*, 5698–5704.

(65) Driscoll, D. J.; Martir, W.; Wang, J. X.; Lunsford, J. H. *J. Am. Chem. Soc.* **1985**, *107*, 58–63.

(66) Smith, R. L.; Kenttaemaa, H. I. *J. Am. Chem. Soc.* **1995**, *117*, 1393–1396.

(67) Giese, B.; Baldwin, J., *Radicals in Organic Synthesis: Formation of Carbon–Carbon Bonds*; Pergamon Press,Oxford: 1986.

(68) Forrester, A. R.; Hay, J. M.; Thomson, R. H., *Organic Chemistry of Stable Free Radicals*; Academic Press, New York: 1968.

(69) Tucker, K.; Kutner, M.; Thaddeus, P *Astrophys. J.* **1974**, *193*, L115–L119.

(70) Robinson, B. J. *Sci. Am.* **1965**, *213*, 26–33.

(71) Rao, B.; Jena, P *J. Chem. Phys.* **1999**, *111*, 1890–1904.

(72) Rondina, G. G.; Da Silva, J. L. *J. Chem. Inf. Model.* **2013**, *53*, 2282–2298.

(73) Candido, L.; Rabelo, J. T.; Da Silva, J. L.; Hai, G. Q. *Phys. Rev. B* **2012**, *85*, 245404.

(74) Frisch, M.; Trucks, G.; Schlegel, H.; Scuseria, G.; Robb, M.; Cheeseman, J.; Scalmani, G; Barone, V; Mennucci, B; Petersson, G. *Gaussian 09 Revision A.01, Wallingford CT*.

(75) Dapprich, S.; Frenking, G. *J. Phys. Chem.* **1995**, *99*, 9352–9362.

(76) Frenking, G.; Fröhlich, N. *Chem. Rev.* **2000**, *100*, 717–774.

(77) Lu, T.; Chen, F. *J. Comput. Chem.* **2012**, *33*, 580–592.

(78) Xiao, M.; Lu, T. *J. Adv. Phys. Chem.* **2015**, *4*, 111–124.

(79) Ros, P.; Schuit, G. *Theor. Chim. Acta* **1966**, *4*, 1–12.

(80) Johnson, E. R.; Keinan, S.; Mori-Sanchez, P.; Contreras-Garcia, J.; Cohen, A. J.; Yang, W. *J. Am. Chem. Soc.* **2010**, *132*, 6498–6506.

(81) Sykes, P., *A Guidebook to Mechanism in Organic Chemistry*; Pearson Education,India: 1986.

(82) Wang, T.; Liu, J.; Sun, H.; Chen, L.; Dong, J.; Sun, L.; Bi, Y. *RSC Adv.* **2014**, *4*, 1864–1873.

(83) Barbosa, T. M.; Viesser, R. V.; Abraham, R. J.; Rittner, R.; Tormena, C. F. *RSC Adv.* **2015**, *5*, 35412–35420.

(84) Vollet, J.; Hartig, J. R.; Schnöckel, H. *Angew. Chem., Int. Ed.* **2004**, *43*, 3186–3189.

(85) Purath, A.; Köppe, R.; Schnöckel, H. *Chem. Commun.* **1999**, 1933–1934.

(86) Huber, M.; Henke, P.; Schnöckel, H. *Chem.Eur.J.* **2009**, *15*, 12180–12183.

(87) Alnemrat, S.; Hooper, J. P. *J. Chem. Phys.* **2014**, *140*, 104313.

(88) Alnemrat, S.; Hooper, J. P. *J. Chem. Phys.* **2014**, *141*, 144304.

(89) Ahlrichs, R.; Ehrig, M.; Horn, H. *Chem. Phys. Lett.* **1991**, *183*, 227–233.

Chapter 6

Investigation of Carbon–Iodine Bond Activation on Niobium Metcar (Nb_8C_{12})

6.1 Introduction

In the realm of material chemistry, atomic clusters are small sized multiatomic particles with variable composition and unique properties. Being the only link between atoms and the bulk materials known to mankind till date, atomic clusters have been the prime motif of material investigation since past four or five decades. Throughout all these years, both theoretical and experimental investigations have not only enriched the respective research fields with interesting outcomes but also have introduced the scientific community to a vast new domain of material chemistry which was never explored before. Starting from the concept of the third dimension of the periodic table as an alternate building blocks[1–3] to novel motifs with fascinating magnetic, optic and catalytic properties,[4–19] the research field of clusters is of no short of captivating outcomes for practical manifestation in near future. In spite of these promises, there lies a major complication in order to incorporate these marvelous ideas into reality. Most atomic clusters are usually metastable and highly reactive in nature and therefore can only be synthesized in vacuum or inert atmosphere. Hence, past few years have seen a substantial increment in the number of experimental or theoretical research focused on the stabilization of nanoclusters.[8,20–22] Beginning with the concept of jellium shell closure[23,24] in either pristine or impure clusters, rigid matrix based stabilization to the implementation of superatomic complex theory,[8,20–22,25,26] it is fortuitous that cluster chemists now have an entire set of arsenal for stabilizing metastable clusters to some extent just enough to make them suitable for small scale experimental manifestation. In addition to that, the added insight by the latest theoretical developments further enhances the in depth understanding of the stabilization process of nanoclusters resulting in new types of artificial stable motifs. However, besides the new developments, at this point it is also important to recollect the fact that, although somewhat rare,there are a few class of clusters which are naturally stable. One of the most well known examples of these type are the family of fullerenes, the first prototype (i.e. C_{60}) of which was invented in 1985 at Rice University.[27,28] The legacy of fullerenes which followed soon after the innovation and their impact on modern material science is certainly a familiar topic to every material chemists by heart. However, fullerenes are not the only species that can be classified as stable clusters. The second example of similar carbon containing stable clusters is the metalcarbohedrenes, discovered by Castleman and coworkers[29–31] nearly seven years after the innovation of C_{60}. Metalcarbohedrenes, commonly abbreviated as 'metcar' is a class of stable metal carbide clusters with chemical stoichiometry M_8C_{12}, where 'M' is usually an early d block element. The presence of first metcar ($Ti_8C_{12}^+$) was detected as a dominant *'supermagic'* peak much similar to that of C_{60} in the mass

spectrum during an attempt to dehydrogenate hydrocarbons by titanium metal.[29] Related experiments soon established the fact that the term 'metcar' indicates an entire class of clusters including binary ones, rather than a single entity.[30,32–35] This captivating innovation paved the ground for new studies including physical and chemical properties, reactivities and structural characterization including bonding and stability of individual metcars.[36–49] The most remarkable among these is definitely the structural characterization of titanium metcar (Ti_8C_{12}). Based on the stoichiometry of the cluster as obtained from the mass spectrometry, the initial structural prediction of Ti_8C_{12} was a regular dodecahedron with T_h symmetry, similar to the C_{20} fullerene.[29–31] This speculated structure was definitely a logical choice, primarily because of two separate reasons. Firstly, as the total atom count of both Ti_8C_{12} and C_{20} is the same hence the Ti_8C_{12} cluster can be considered a derivative of C_{20} simply by replacing two carbon atom from each pentagonal ring by titanium keeping the skeleton intact. As for second reason, reaction of polar molecules with Ti_8C_{12} and V_8C_{12} results in the adsorption of upto 8 molecules, which signifies all the eight metal sites are equivalent by coordination. Also to mention that the regular dodecahedron structure is among the five platonic solids, all of which are very well known abundant stable structures often preferred by nature. However, theoretical calculations showed the possibility of two different structures which are of D_{2d} and T_d symmetry respectively, and are expected to be lower in energy than the T_h structure proposed earlier.[50–56] Detailed investigations in this regard soon established the fact that the theoretical calculations are indeed correct and the distorted T_d structure is confirmed to be the ground state, later verified by experiments.[57]

Aside from the structural characterization of metcars, the chemical response of the clusters also attracts considerable attention of chemists since their first discovery. Small scale reaction with polar (e.g H_2O, CH_3OH, NH_3 and $(CH_3)_2CO$) as well as non–polar molecules like benzene, methane and ethylene are studied in depth and also supported by theoretical calculations.[36,42,45,58–60] The studies with non–polar molecules are of special importance since it is observed that only a maximum of four non–polar molecules can be attached with a single metcar. This observation indirectly proves the existence of two separate set of metal sites in the cluster, thus confirming the tetrahedral shaped ground state consisting of a smaller inner tetrahedron surrounded by a larger outer tetrahedron each consisting with four metal atoms around each vertices. These investigations further elucidate the reactivity trend of different metcars and it is observed that titanium metcar cation is more chemically stable compared to Vanadium or Niobium metcar cations which are found to be more reactive in comparison. The difference in reactivity in between different metcars is also observed in the dissociation reaction of carbon halogen bond using metcar as catalyst.[57,61] Upon using methyl iodide as the reactant, experimental observation reveals that while $Ti_8C_{12}^+$ is only able to abstract single halogen atom from CH_3I, vanadium and niobium metcar cations are able to form bonds with multiple number of iodine atoms. Even both these metcars are able to dissociate much stronger halocarbon bonds like C–Br and C–Cl and also form bonds with multiple numbers of chlorine and bromine atoms. The oxidative dissociation of carbon halogen bond is one of pivotal reaction steps in common chemistry. Especially, because C–I bond dissociation is one of the major intermediate steps of coupling reactions which are among the few techniques available to organic chemist which results direct formation of C–C bond.[62] Due to this reason, a significant portion of recent researches has solely been focused on the understanding of detailed mechanism including thermodynamic and kinetic data of carbon halogen bond dissociation. Aside from the most commonly used catalyst[63,64] like palladium, platinum on nickel in depth theoretical and experimental studies on more unconventional materials like gold[65,66] and even aluminum clusters[5] are also available. However, to the extent of our knowledge no such theoretical investigation encompassing the reaction mechanism and other related aspects of C–I activation on metcar is studied earlier. The present chapter includes such a theoretical investigation of C–I dissociation on niobium metcar using Density functional theory as a computational tool of choice. The calculated results are

analyzed and compared with the earlier experimental results available in the literature. The rest of the chapter is organized as follows, The next section (section 2) contains the computational details of the calculations presented in the chapter. Section 3 includes the thermodynamic and kinetic data of C–I dissociation on both neutral and cationic niobium metcar in addition to other associated calculations. Section 4 concludes the chapter.

6.2 Computational Details

The initial guess structure of tetrahedral Nb_8C_{12} is taken from previous studies reported in earlier literature.[50–56] The neutral as well as the cationic structure of Nb–metcar are optimized assigning different spin multiplicities in both M06–2X as well as B3LYP functional using TZVP basis for 'C' atoms and LANL2DZ–ECP basis for Niobium. It is observed that in both the functional the Nb_8C_{12} cluster with minimum spin multiplicity (S=1) is lowest in energy. As organic molecules containing C–I bond,we have chosen three common molecules similar to our earlier works.[67,68] The pre–reaction complexes are derived by attaching the R–I molecule in all possible sites within the cluster, and only the lowest energy conformer is considered in each case. Similar to the metcar, all the pre–reaction complexes are further optimized incorporating different spin multiplicities to identify the lowest energy conformer, which is found to be of minimum spin as earlier. The Binding energies of RI molecule with Nb_8C_{12} and $Nb_8C_{12}^+$ metcars are calculated by the following formula,

$$\Delta E_b = E_{Metcar...I-R} - E_{R-I} - E_{Metcar} \tag{6.1}$$

All the optimizations included in the present chapter are performed using Berny optimization method in Gaussian09.[69] The normal modes of vibration in all the optimized structures are scrutinized and it is made sure that all normal modes of vibration are real for global minimum whereas only one significant imaginary frequency corresponds to the C-I bond is present in case of first order saddle points (Transition States). Intrinsic reaction coordinate (IRC) calculations are further performed for the transition states and it is verified that the IRC path properly connects to the complexes on both side of the saddle point. The condensed Fukui indices (f_A^+) on each optimum point of the overall reaction coordinate are calculated using Hirshfeld population analysis(HPA). The condensed Fukui indices for nucleophilic attack of an atom 'A' within a molecule containing a subtotal of 'N' electron is expressed as,

$$f_A^+ \simeq q_{A,N+1} - q_{A,N} \tag{6.2}$$

where $q_{A,N+1}$ and $q_{A,N}$ are the Hirshfeld population of atom A in the $(N+1)$ and N electronic molecular systems respectively, both having the same equilibrium geometry. All the thermodynamic parameters and related data presented in the chapter are calculated in 298.15 K temperature and 1 atm pressure. The two types of the rate constants (i.e. TST and TSTW) and other associated kinetic data are calculated using the open source Kinetic and Statistical Thermodynamical Package (KiSThelP).[70] The classical rate constant i.e. k_TST is defined as,

$$k_{TST} = \sigma . \frac{k_b T}{h} . \left(\frac{RT}{P^0}\right)^{\Delta n} . e^{-\frac{\Delta G^{\ddagger,0}}{k_b T}} \tag{6.3}$$

and the expression for the Wigner tunneling corrected rate constant (k_TSTW) is,

$$k_{TSTW} = \chi(T) . k_{TST} \tag{6.4}$$

whereas,all the included terms have their usual significance. $\chi(T)$ is the transmission coefficient which is calculated by the imaginary frequency of the unbound mode at the respective saddle point,

$$\chi(T) = 1 + \frac{1}{24}\left(\frac{h\, Im(\nu^{\ddagger})}{k_b T}\right)^2 \tag{6.5}$$

The three parametric Arrhenius equation is defined as,[71]

$$k = AT^n exp\left[-\frac{\Delta E_a}{RT}\right] \tag{6.6}$$

whereas, A is the pre–exponential factor and 'n' is a constant. The other used terms have their usual significance. The deformation density plot is constructed by subtracting the respective three dimensional density data of the complex from its individual components. The bond polarity index (BPI) and the atoms in molecules (AIM) analysis is performed in open source Multiwfn package[72] utilizing the output file of Gaussian09. The common definition of BPI of a bond between atom 'A' and 'B' within a molecule is given as,[73,74]

$$BPI_{A-B} = (EI_A - EI_A^{ref}) - (EI_B - EI_B^{ref}) \tag{6.7}$$

The EI_A and EI_B terms denote the energy index (EI) of respective atoms within the molecule and EI^{ref} terms are the energy index obtained from homonuclear reference molecules of atom A and B. The definition of EI of an atom 'A' within a molecule is presented as,

$$EI_A = \frac{\sum_i^{val} \varepsilon_i \eta_i \Theta_{i,A}}{\sum_i^{val} \eta_i \Theta_{i,A}} \tag{6.8}$$

where $\Theta_{i,A}$ signifies the composition of atom A in the i^{th} MO. η_i and ε_i are respectively the occupation number and energy of the i^{th} MO. The summation of equation (6.8) only runs over all the valence MOs. The Wiberg bond indices are calculated for individual geometries as well as geometries along the IRC path as required using the NBO 3.0 package as implemented in Gaussian09.

6.3 Results and Discussion

In order to acquire a brief understanding of C–I bond dissociation process on neutral and cationic Nb_8C_{12} cluster, both the structures were first optimized using a reasonable initial guess as a starting point. The global minima for both neutral and cationic Nb_8C_{12} are found to be slightly distorted from the ideal tetrahedral structure. This observation is indeed consistent and can be confirmed from the earlier studies on other metcars as well.[75] Comparing the optimized (M06–2X) structures of both Nb_8C_{12} and $Nb_8C_{12}^+$ metcar with a standard T_d symmetric reference structure reveals that the root mean square deviations are respectively 0.139 Å and 0.146 Å. The RMSD value within the neutral and cationic Nb_8C_{12} cluster is found to be much smaller about 0.0246 Å, signifying small structural deviation in between neutral and the cationic Nb metcar. As for molecules with C–I bond we have chosen three very common organic compounds with variable C–I bond strength namely methyl($-CH_3$), vinyl ($-C_2H_3$) and phenyl ($-C_6H_5$) iodides. Except CH_3I, which is the only one with experimental validation, the choice of other two iodides are completely arbitrary and included only to ensures enough variation in the calculated results

due to their uneven bond strength. The bond dissociation enthalpy (ΔH^0_{298K} in kcal mol^{-1}) order of these three iodides are observed to be,[76]

C_6H_5-I (65.0±1.0) >$H_2C=CH-I$ (61.9±1.0) >H_3C-I (57.1±0.5)

Thus the C–I bond in phenyl iodide is the strongest and methyl iodide can be considered as the weakest among the three. These variations in the bond dissociation energies among the iodides are expected to influence the computed reaction parameters which in turn may provide more insight of the C-I dissociation process on both the metcars. All the necessary thermodynamic and kinetic data presented in this chapter are evaluated for all three iodides by using three different DFT functional. However, for specific mechanistic related discussions we have solely restricted ourselves with the results obtained for CH_3I in M06–2X functional. The major reason of this choice is twofold. Firstly, as already mentioned methyl iodide is the only organo–iodide with available experimental results. Secondly, Minnesota functionals like M06-2X are very well known for its superior performance in determining accurate molecular structures, activation barrier and even can take care of small to medium range dispersion effect.[77–79] Hence, the structure and thermochemical parameters included in the figures also consists solely of results obtained from M06–2X functional if not stated otherwise.

The overall energy landscape of C–I bond dissociation of all three iodides on Nb_8C_{12} and $Nb_8C_{12}^+$ metcar is depicted in Figure 6.1 and Figure 6.2 respectively. The thermodynamic parameters, calculated in three different functionals are enlisted in Table 6.1 and Table 6.2 as well. The first step of the reaction is the formation of pre–reaction complex (P.R.C) via the adsorption of R–I molecule on the surface of metcar. Due to the dual tetrahedral structure of metcar, the incoming R–I molecule can attach itself with Nb atoms located in either inner(Nb^i) or outer(Nb^o) tetrahedra. DFT investigations indicate that the pre–reaction complex with R–I molecules attached with Nb^o is more thermodynamically stable than the other structures. The electronic energy difference between the two structures in M06–2X functional is found to be about 6 kcal/mol for the attachment of CH_3I on neutral Nb_8C_{12}. The binding energies (Table 6.1 and 6.2) of the R–I molecules on both neutral and cationic metcar are also found to be quite significant, possibly due to better orbital matching resulting in higher stability as both Nb and I shares the same row in the periodic table. Comparing with other results available in the current literature, the binding energies are found to be much higher than that of small sized neutral aluminum cluster[67] and also than most of the neutral and cationic gold clusters[66] of similar size range ($3\leq$ n ≤ 20). It is interesting to observe that binding energies of R–I molecules with $Nb_8C_{12}^+$ is relatively higher (about $\sim$6 kcal/mol) than the neutral metcar. To understand these discrepancies, we have decided to take a brief look on the formation process and the characteristic of the newly formed Nb–I bond in both the clusters. The top panels of figure 6.3a and 6.3b depicts the snapshots of deformation density plots of the initial approach of CH_3I molecule towards the neutral and cationic cluster respectively. From the plots it is pretty evident that there exists slight differences in the bond formation process of CH_3I with Nb metcar and its cation. For the case of neutral Nb_8C_{12} (Fig 6.3a) it is observed that a significant amount of charge density is accomodated around the R–I molecule. As a result the formation of Nb–I bond results from major contribution of iodine atom and the Nb^o atom of the metcar provides minor contribution as a donor. However, when the system is cationic (Fig 6.3b), it can be seen that the electron density around the incoming iodine atom is widely depleted and in this case the Nb^o atom acts as the major donor to form the bond with the iodine atom. These variation in the bond formation process creates a difference in the ionic charecter of both bonds and the resulting bond in the cationic metcar becomes stronger due to high ionic character resulting in the observed high binding energy. This conclusion is further confirmed via the calculation of bond polarity index (BPI) in M06–2X functional. The BPI is a direct representation of the polarity of a chemical bond in terms of numerics rather than simple visualization, allowing

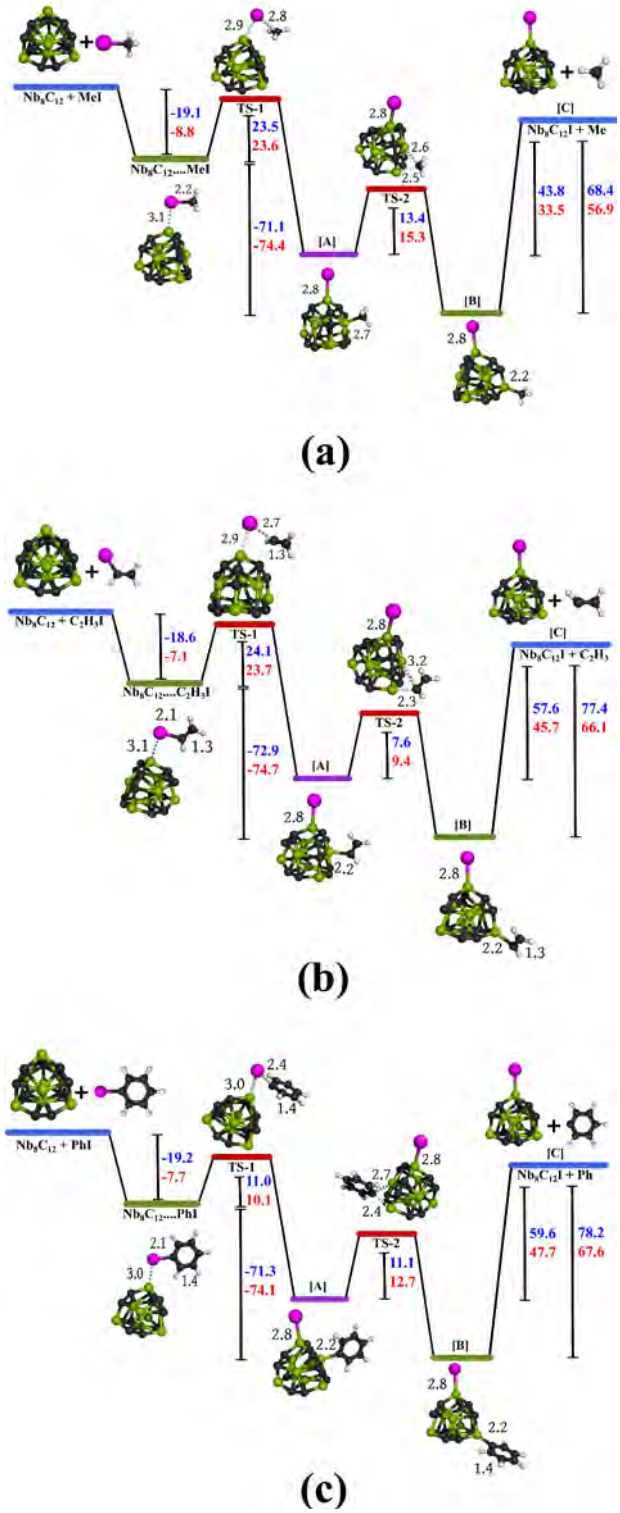

FIGURE 6.1: Reaction coordinate (M06–2X) diagrams of the reaction of neutral Nb_8C_{12} with (a) H_3C-I (b) $H_2C=CH-I$ and (c)$Ph-I$. The ΔH (Blue) and ΔG (Red) values of each step are also included.

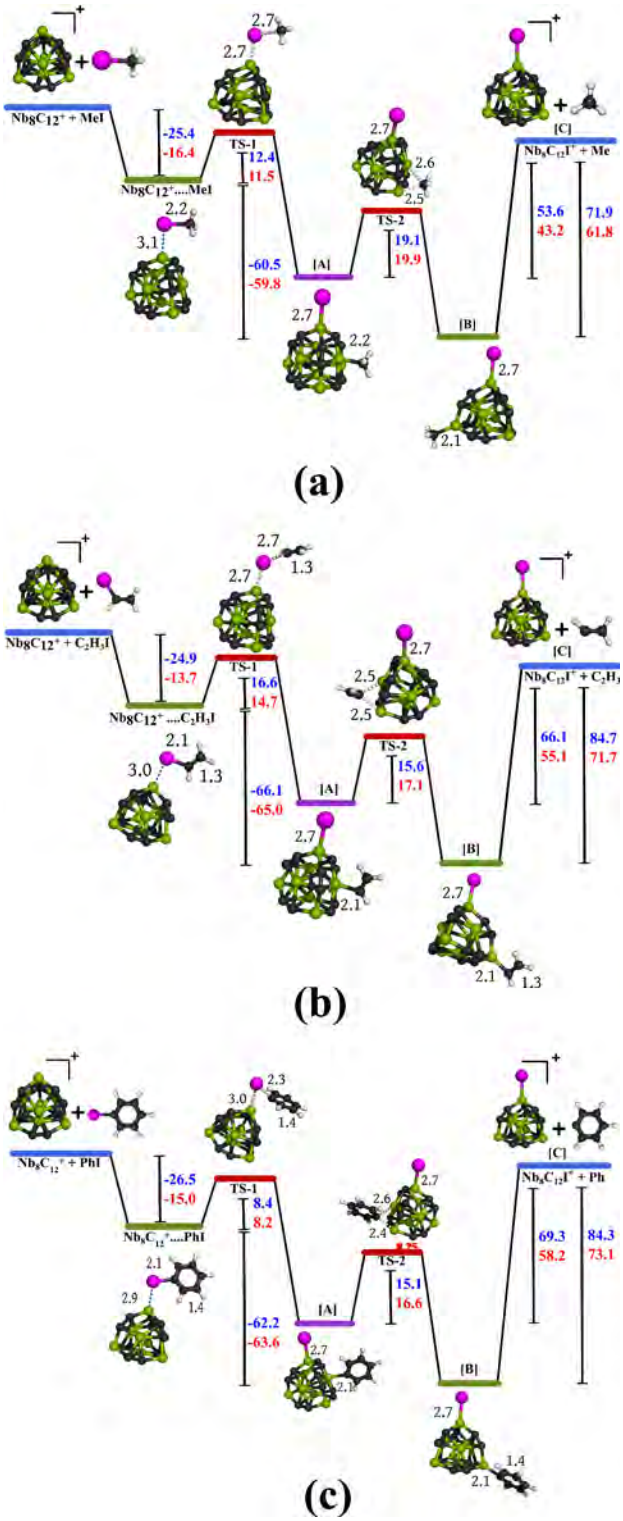

FIGURE 6.2: Reaction coordinate diagrams of the reaction of cationic Nb_8C_{12} with (a) H_3C-I (b) $H_2C=CH-I$ and (c)$Ph-I$. The ΔH (Blue) and ΔG (Red) values of each step are also included.

quantitative characterization of the type of that particular bond in the process. Calculation of BPI of Nb–I bond for both metcar reveals that the BPI_{Nb-I} of $[Nb_8C_{12}\cdot..ICH_3]$ is higher (-0.118 a.u) than the BPI_{Nb-I} obtained for $[Nb_8C_{12}\cdot..ICH_3]^+$ complex (-0.154 a.u). The lower (more negative) value of BPI_{Nb-I} bond in $[Nb_8C_{12}\cdot..ICH_3]^+$ complex indicate that the Nb–I bond in cationic complex is more ionic in nature than than its neutral counterpart resulting in higher binding energy. The direct influence of this ionic nature is also reflected in the bond order of Nb–I in in both the pre–reaction complexes. Thus, while the Wiberg bond indices (WBI) of Nb–I bond in $[Nb_8C_{12}\cdot..ICH_3]$ complex is found to be 0.59, the WBI $_{Nb-I}$ for the same in the cationic complex is observed to be slightly higher (0.70). As expected, the calculated Wiberg bon indices of the newly formed Nb–I bonds indicate that they are indeed partial in nature in both neutral and cationic pre–reaction complexes (P.R.C) signifying the bond formation process is not yet complete. At this point it is also important to mention that although the binding energies of R–I molecule differs due to the nature of the newly formed Nb^o–I bond on Nb_8C_{12} and $Nb_8C_{12}{}^+$ metcar, the binding energy values seems nearly invariant on the type of the 'R' group attached with the iodine. Thus, for both the neutral and cationic Nb metcar, the binding energies for all three R–I molecule are observed to be very close in value as evident from the rightmost column of Table 6.1 and 6.2.

From the reaction coordinates as depicted in Figure 6.1 and 6.2, it is observed that the overall reaction pathway towards the most thermodynamically stable product is not as simple as expected from the first glance. Although the dissociation of C-I bond is found to be a one step process goes via a single transition state (TS–1), DFT investigation indicates that the resulting C–I dissociated complex([A]) is not the most thermodynamically stable one. There exists another post reaction complex [B] along the reaction coordinate which is the most stable one and connected with complex [A] via a second transition state (TS–2). Thus the overall reaction pathway for each individual R–I molecule must be characterized by two separate activation barrier ΔE_a1 and ΔE_a2 respectively, as included in the Table 6.1 and 6.2. The existence of two separate post–reaction complexes along the reaction coordinate may seems baffling at first look but the explanation of this observation is rather simple and can be provided by recollecting the structure of the cluster itself. As mentioned earlier, due to the tetrahedral structure of metcars, the metal atoms present on the surface can be classified into two separate categories (inner (Nb^i) and outer (Nb^o) for our present case) based on the coordination of the metal atoms. Attaching the dissociated '–R' functional group with each types of Nb atoms yields two separate post reaction complexes with different thermodynamic stabilities. Hence, for each iodides, the first transition state (TS–1) leads to the cleavage of C–I bond from the pre–reaction complex resulting simultaneous attachment of the dissociated R group to nearest Nb^i atom (Structure [A] in Fig 6.1 and 6.2). The second reaction step starts from the resulting complex [A] and directs towards the most thermodynamically stable post reaction complex. This proceeds via a second transition state (TS–2) which involves a direct intra–cluster transfer of the R group from the Nb^i atom to a Nb^o atom via a three membered transition state. The final structure (Structure [B] in Fig 6.1 and 6.2) where the 'R' functional group is attached to the Nb^o atom is observed to be most thermodynamically stable post–reaction complex within the whole reaction coordinate as indicated by the DFT investigation. Thus Structure [A] serves as an intermediate between the first (TS–1) and the second transition state (TS–2), which connects with the stable post reaction complex [B]. The enthalpy difference(Δ H) between [A] and [B] is observed to be 24.6 and 18.3 kcal/mol for the reaction of MeI on neutral and cationic Nb_8C_{12} respectively. Structure [C] shown in both Figure 6.1 and 6.2 is the dissociated post reaction complex as included in the corresponding experimental paper.[57] The dissociated complex([C]) is observed to be energetically closure with [A] than [B] for each iodides. Also from Figure 6.1 and 6.2, it is observed that the gaps (both Δ H and Δ G) with either [A] or [B] complex with [C] is found to be higher in the $Nb_8C_{12}{}^+$ than the neutral Nb_8C_{12}. The increment are usually found to be $\sim$ 10 kcal/mol

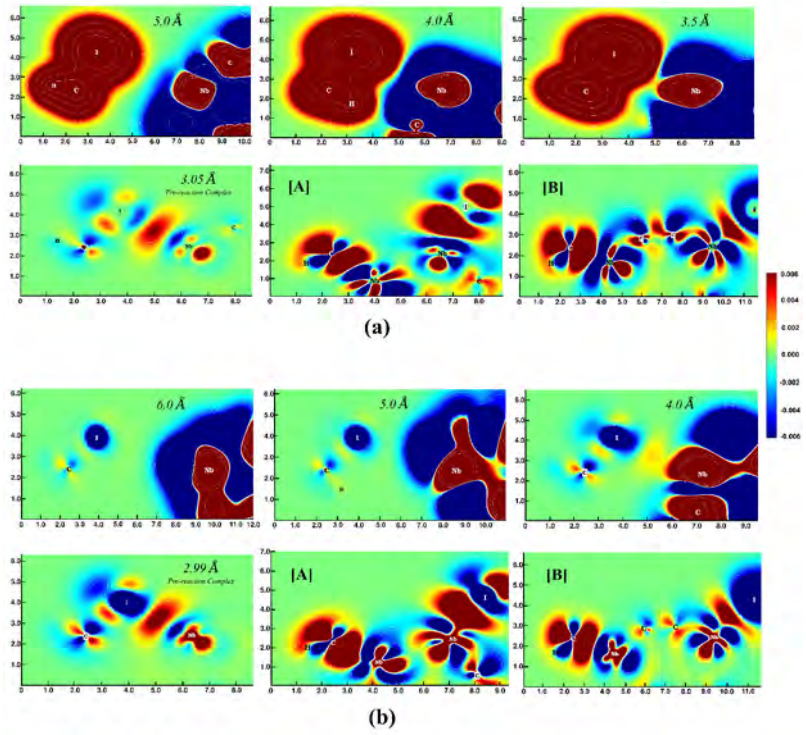

FIGURE 6.3: Deformation density plot of the initial approach of H_3C-I towards (a) neutral Nb_8C_{12} and (b) cationic Nb_8C_{12} cluster. The lower panels of (a) and (b) shows the deformation density plots of pre–reaction complex, structure [A] and structure [B] respectively.

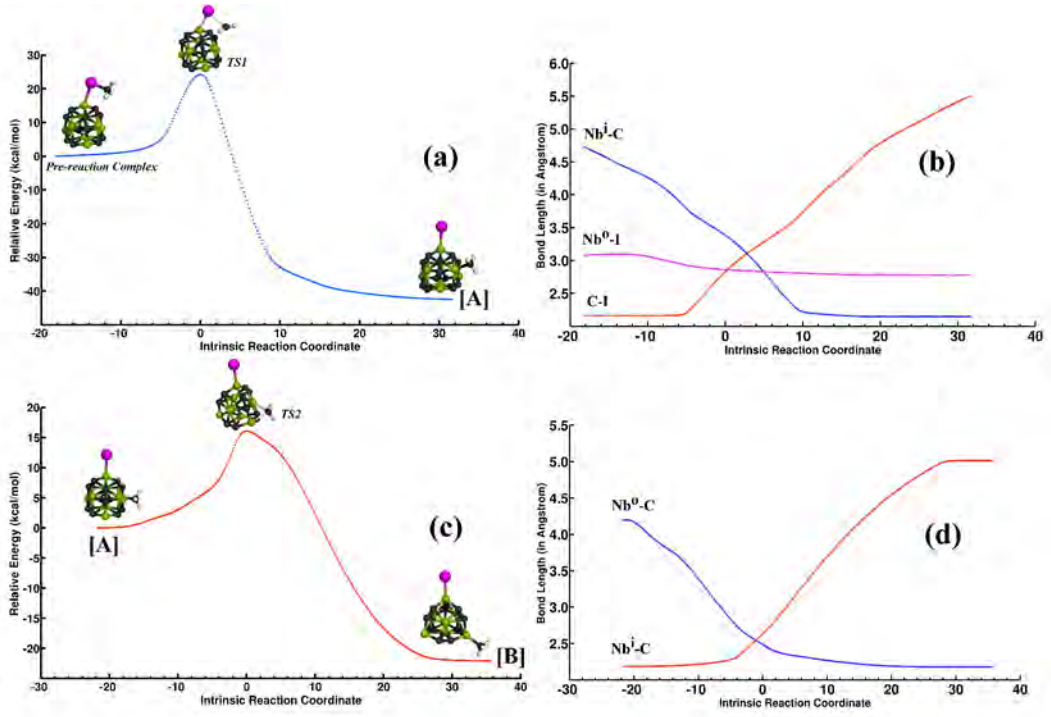

FIGURE 6.4: Sample IRC plots of the two reaction steps of the reaction between Nb_8C_{12} and H_3C-I. Figure (b) and (d) show the changes in the length of selected bonds along the IRC.

for the Δ H and Δ G separation between [A] and [C] and ∼ 4–7 kcal/mol between [B] and [C] respectively. This whole reaction coordinate is further confirmed by IRC calculations. Figure 6.3 collects two sample IRC plots for both step of the reaction between CH_3I and Nb_8C_{12} cluster in M06–2X functional. The resulting changes in the bond lengths of specific pre–selected bonds within the IRC are also included in the right hand side of the figure(Fig 6.4b and 6.4d). As can be seen from Figure 6.4a and 6.4c, both the transition states properly connects with the predicted chemical species on both positive and negative side of their respective intrinsic reaction coordinate. Thus the first transition state (TS–1) connects to the pre–reaction complex on the negative direction of IRC and smoothly converges to complex [A] on the positive direction of IRC (Fig 6.4a). The next reaction step is confirmed by a second IRC calculation included in Figure 6.4c. As depicted, similar to the TS–1, the second transition state (TS–2) also connects with complex [A] on the left hand side and converges to the thermodynamically stable complex [B] on the positive direction of the IRC. Similar conclusion can be drawn from the other calculated IRCs on both neutral and cationic Nb–metcar, thus validating the reliability of our result.

As mentioned earlier, the thermodynamic parameters regarding TS–1 and TS–2 and also the exothermicity values in M06–2X, B3LYP and BHandHLYP functional are enlisted in Table 6.1 and 6.2. The overall range of both the activation barriers in all three DFT functional is found to be varied from low to medium range (∼ 2-26 kcal/mol), ensuring decent catalytic activity of the metcar on the C–I bond. A close look of the first activation barriers (ΔE_a1) reveals that for all three iodides and in all three functionals, the cationic Nb_8C_{12} shows lower activation barrier than the neutral one, which signifies the higher catalytic activity of $Nb_8C_{12}^+$ compared to the Nb_8C_{12} towards the oxidative addition of C–I bond. The ΔE_a1 values calculated for $Nb_8C_{12}^+$ are observed to be often comparable with the activation barrier obtained for the case of small sized aluminum clusters[67]. The lowest first activation barrier is calculated to be $\Delta G^{\ddagger}$ = 4.6 kcal/mol which is obtained in BhandHLYP functional for the oxidative addition of C_6H_5I on $Nb_8C_{12}^+$. As a matter of fact, the ΔE_a1 obtained for C_6H_5I in all three functional is observed to be the lowest among all the iodides. Whereas, the activation barriers calculated for CH_3I and $H_2C{=}CHI$ are usually either in close proximity with each other or one is higher than the other without any predictable pattern. The result is interesting, since the C–I bond in C_6H_5I has the maximum dissociation energy among the three iodides. The observed low activation barrier of $Nb_8C_{12}^+$ compared to the neutral metcar can be justified by the calculated HOMO/SOMO–LUMO gaps of the respective metcar. The SOMO–LUMO gap of $Nb_8C_{12}^+$ is found to be 2.47 eV (1.03 eV in B3LYP) which is lower by 0.3 eV compared to the HOMO–LUMO gap obtained for the neutral metcar (2.77 eV in M06–2X and 1.25 in B3LYP functional). The lower energy gap signifies slightly high reactivity of the cationic metcar over the neutral one and thus explains the trend obtained in the calculated activation barrier. The variation of the activation barriers can be viewed in a more prominent way by looking the respective rate constants for Nb_8C_{12} and $Nb_8C_{12}^+$ presented in Table 6.3 and 6.4. As already mentioned in the computational details, the rate constants included in the present chapter are calculated using two different methods, the classic transition state theory (TST) and the Wigner tunneling corrected version of classic transition state theory (TSTW) respectively. The calculated rate constants are also associated with pre exponential factor (A) and the constant(n) in accordance with the three parameter Arrhenius equation. As can be seen from Table 6.3 and 6.4, the value of temperature dependent constant (n) of the three parametric Arrhenius equation is found to be usually higher (> 1) for the first reaction barrier, whereas for the second reaction barrier the values of 'n' lies below 1 as well as small negative value close to zero. The higher value of 'n' for the first reaction barrier signifies that the first reaction barrier of C–I dissociation on both Nb_8C_{12} and $Nb_8C_{12}^+$ is more sensitive on the temperature than the second barrier. The exothermicity values(which is the enthalpy difference between the complex [B] and the pre–reaction complex) listed in Table 6.1 and 6.2 is observed to be really high, ranging within ∼ -70 to -81 kcal/mol for neutral Nb_8C_{12}

TABLE 6.1: Thermodynamic data of C–I bond activation on neutral Nb_8C_{12} metcar

R-I	Activation Barrier												Exothermicity						Binding Energy
	M06-2X				B3LYP				BHandHLYP				M062X		B3LYP		BHandHLYP		M06-2X
	ΔE_a1		ΔE_a2		ΔE_a1		ΔE_a2		ΔE_a1		ΔE_a2								
	$\Delta H^{\ddagger}$	$\Delta G^{\ddagger}$	$\Delta H^{\ddagger}$	$\Delta G^{\ddagger}$	$\Delta H^{\ddagger}$	$\Delta G^{\ddagger}$	$\Delta H^{\ddagger}$	$\Delta G^{\ddagger}$	$\Delta H^{\ddagger}$	$\Delta G^{\ddagger}$	$\Delta H^{\ddagger}$	$\Delta G^{\ddagger}$	ΔH	ΔG	ΔH	ΔG	ΔH	ΔG	
CH_3I	23.50	23.67	13.39	15.28	13.97	13.11	19.34	20.64	22.63	22.42	19.02	20.22	-71.14	-71.47	-71.64	-72.16	-78.63	-79.44	-18.57
$H_2C{=}CHI$	24.14	23.75	7.59	9.38	9.81	9.18	11.51	13.72	24.10	25.46	7.95	10.02	-72.94	-74.77	-72.93	-74.48	-81.22	-81.01	-18.04
PhI	11.03	10.14	11.16	12.69	8.16	12.55	17.00	19.06	13.73	17.75	6.52	9.31	-71.37	-74.11	-73.85	-71.25	-80.88	-81.39	-18.58

TABLE 6.2: Thermodynamic data of C–I bond activation on $Nb_8C_{12}{}^+$ metcar

R-I	Activation Barrier												Exothermicity						Binding Energy
	M06-2X				B3LYP				BHandHLYP				M062X		B3LYP		BHandHLYP		M06-2X
	ΔE_a1		ΔE_a2		ΔE_a1		ΔE_a2		ΔE_a1		ΔE_a2								
	$\Delta H^{\ddagger}$	$\Delta G^{\ddagger}$	$\Delta H^{\ddagger}$	$\Delta G^{\ddagger}$	$\Delta H^{\ddagger}$	$\Delta G^{\ddagger}$	$\Delta H^{\ddagger}$	$\Delta G^{\ddagger}$	$\Delta H^{\ddagger}$	$\Delta G^{\ddagger}$	$\Delta H^{\ddagger}$	$\Delta G^{\ddagger}$	ΔH	ΔG	ΔH	ΔG	ΔH	ΔG	
CH_3I	12.39	11.53	19.13	19.97	6.37	4.66	22.28	23.91	6.57	4.96	24.49	24.63	-60.49	-59.84	-59.70	-60.27	-68.11	-68.12	-24.83
$H_2C{=}CHI$	16.67	14.68	15.63	17.10	8.97	8.45	14.91	15.35	8.81	7.86	19.61	21.11	-66.12	-65.05	-63.00	-62.22	-74.77	-73.00	-24.30
PhI	8.39	8.25	15.09	16.60	6.29	8.82	19.00	20.90	1.92	4.65	21.87	23.51	-62.20	-63.58	-62.37	-63.59	-72.10	-71.89	-25.96

TABLE 6.3: Kinetic Data of first reaction barrier (ΔE_a1) of C-I bond activation on neutral and cationic Nb_8C_{12} metcar in M06–2X functional

R-I	CH_3I						$H_2C{=}CHI$						PhI					
	TST			TSTW			TST			TSTW			TST			TSTW		
	k	A	n	k	A	n	k	A	n	k	A	n	k	A	n	k	A	n
Neutral	$2.76x10^{-05}$	$3.92x10^{07}$	1.89	$3.23x10^{-05}$	$8.49x10^{06}$	2.10	$2.43x10^{-05}$	$2.88x10^{07}$	2.08	$3.11x10^{-05}$	$4.62x10^{06}$	2.33	$2.30x10^{05}$	$1.93x10^{10}$	1.23	$2.59x10^{05}$	$5.22x10^{09}$	1.41
Cation	$2.18x10^{04}$	$4.63x10^{09}$	1.44	$2.52x10^{04}$	$1.08x10^{09}$	1.64	$1.07x10^{02}$	$6.30x10^{07}$	2.36	$1.19x10^{02}$	$1.86x10^{07}$	2.53	$5.59x10^{06}$	$1.57x10^{10}$	1.08	$8.05x10^{06}$	$2.66x10^{09}$	1.31

TABLE 6.4: Kinetic Data of second reaction barrier (ΔE_a2) of C-I bond activation on neutral and cationic Nb_8C_{12} metcar in M06–2X functional

R-I	CH_3I						$H_2C{=}CHI$						PhI					
	TST			TSTW			TST			TSTW			TST			TSTW		
	k	A	n	k	A	n	k	A	n	k	A	n	k	A	n	k	A	n
Neutral	$3.83x10^{01}$	$8.98x10^{11}$	-0.04	$4.03x10^{01}$	$4.60x10^{11}$	0.05	$8.21x10^{05}$	$3.96x10^{11}$	0.11	$8.29x10^{05}$	$3.44x10^{11}$	0.13	$3.06x10^{03}$	$2.93x10^{11}$	0.22	$3.08x10^{03}$	$2.72x10^{11}$	0.23
Cation	$1.40x10^{-02}$	$1.07x10^{11}$	0.54	$1.5x10^{-02}$	$4.34x10^{10}$	0.67	$1.79x10^{00}$	$1.67x10^{11}$	0.32	$1.90x10^{00}$	$7.63x10^{10}$	0.43	$4.16x10^{00}$	$1.13x10^{11}$	0.37	$4.19x10^{00}$	$1.01x10^{11}$	0.38

and within $\sim$ -60 – -75 kcal/mol for Nb_8C_{12} cation as calculated for all three iodides and in three different functional.

In order to gain further insight of the overall reaction mechanism, we have included few additional calculations within the chapter. One of such included in Figure 6.5(a and b) represents the change of Wiberg bond index (WBI) of C–I bond in the NAO basis along the IRC of the first transition state(TS–1) of both neutral and cationic Nb_8C_{12}. The WBI of both the dissociated C–I bond as well as newly forming Nb^o–I bond are included in the figure. The crossover point, i.e. where the bond indices of both the breaking and newly forming bonds are become equal to each other are also clearly shown in Figure 6.5a and 6.5b. Figure 6.5a shows that for neutral Nb_8C_{12} the WBI promptly converges from $\sim$ 1 in the pre–reaction complex to nearly zero at the end of the corresponding IRC. At the same time the Nb^o–I bond index start to increase from 0.6 in the P.R.C and finally proceed towards a WBI value of 1.23 in the complex [A]. In a similar fashion, in accordance to Figure 6.5b, on the cationic Nb_8C_{12} the WBI of the C–I bond decreases from $\sim$ 1 and converges towards zero. Whereas, for the case of the newly formed Nb^o–I bond, the WBI starts to increase from a value of 0.7 in the P.R.C and finally converges towards the value of 1.46 as calculated in [A]. The observed higher bond order of Nb^o–I as obtained in the complex [A] of cationic Nb_8C_{12} can again be attributed to the ionic character of the respective bond as described earlier. In Figure 6.6, we have included the change of the Fukui function (f^+) (Fig 6.6a and 6.6b) and the HOMO–LUMO or SOMO–LUMO gap (Fig 6.6c and 6.6d) along the reaction pathway for the reaction of CH_3I with Nb_8C_{12} and $Nb_8C_{12}{}^+$. The major differences of the C–I dissociation process on both neutral and cationic Nb–metcar are evident from all the four plots (6a–6d). The dissimilarities are especially prominent at the position of TS–1 in comparison to other portions of the plots. Focusing first on the change of f^+ along the reaction pathway, it can be seen that at the position of TS–1, the trend of f^+ values of Nb^o and the attached I atom follows an opposite pattern in the neutral Nb–metcar compared to the cation. Thus, in neutral Nb_8C_{12} metcar, the f^+ value of I atom shows a large increment and the respective f^+ value of Nb^o atom is significantly lowered compared to the value obtained in the P.R.C. However, in $Nb_8C_{12}{}^+$ an opposite trend is noticed. In which, the f^+ value of the attached iodine in TS–1 is found to be lower than that in P.R.C and the f^+ value of Nb^o atom seems to have higher value in TS–1 than in the P.R.C. The explanation of this unusual trends can be provided by reciting the charge transfer trend in between Nb^o and iodine atom as observed in the P.R.C. As explained earlier, in the neutral Nb–metcar, as iodine is electron rich, a major portion of the electron desity needed to form the Nb^o–I bond is contributed by the iodine atom. Since the Nb^o–I bond is still partial in the pre–reaction complexes, it is therefore expected that the flow of electron density will continue until the WBI of Nb^o–I bond reaches a value of $\sim$ 1 and therefore provide a stronger coordination. Thus, in the neutral metcar, the f^+ value of iodine shows a gradual increase due to the loss of electron density. On the other hand, the f^+ value of Nb^o atom shows a slight decrement as the incoming electron density from iodine is much greater than the contribution provided by the Nb^o atom for the bond formation. An opposite situation is happening for cationic system, where Nb^o atom provides major contribution towards the bond formation and iodine atom plays minor part. WBI calculation indeed confirms this explanation and the Nb^o–I bond formation process is observed to be near complete in the first transition state itself. For neutral system the WBI of Nb^o–I bond is found to be 0.98 and for the cationic system which is observed to be about 1.21, i.e, higher than the neutral one. The C–I bond is also found to be mostly cleaved at TS–1 as expected, having a WBI of 0.38 and 0.34 in neutral and cationic system respectively. After TS–1, f^+ values of both the atoms follow a near parallel path upto complex [B] in both neutral and cationic Nb–metcar. The value of the nucleophilic Fukui index for Nb^i atom in both neutral and cationic Nb–metcar is observed to be nearly constant till TS–1, then after a sudden drop at the intermediate [A], it again steadily increases to complex B. The f^+ value of the 'C' atom is observed to be the least perturbed

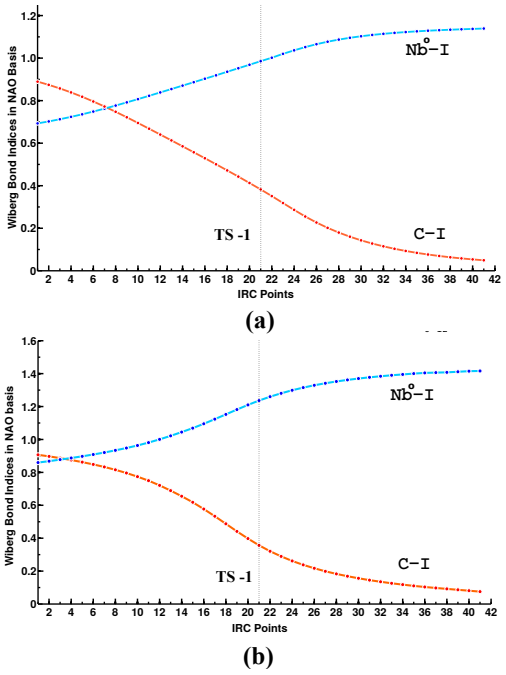

FIGURE 6.5: Variation of Wiberg bond indices of Nb^o–I and C–I bonds along the Intrinsic Reaction Coordinate(IRC) points of TS–1 for (a) Nb_8C_{12} +H_3C-I and (b) $Nb_8C_{12}{}^+$ +H_3C-I reaction.

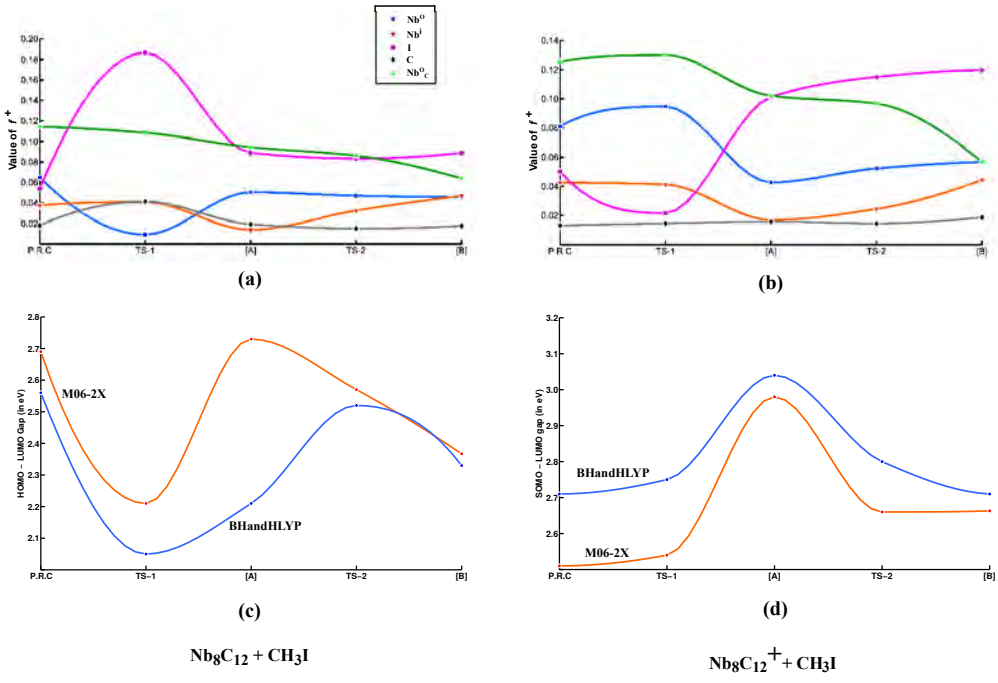

FIGURE 6.6: The alteration of fukui function (f^+) of selected atoms along the reaction coordinate of the dissociation of H_3C-I on (a) Neutral Nb_8C_{12} and (b) Cationic Nb_8C_{12}.

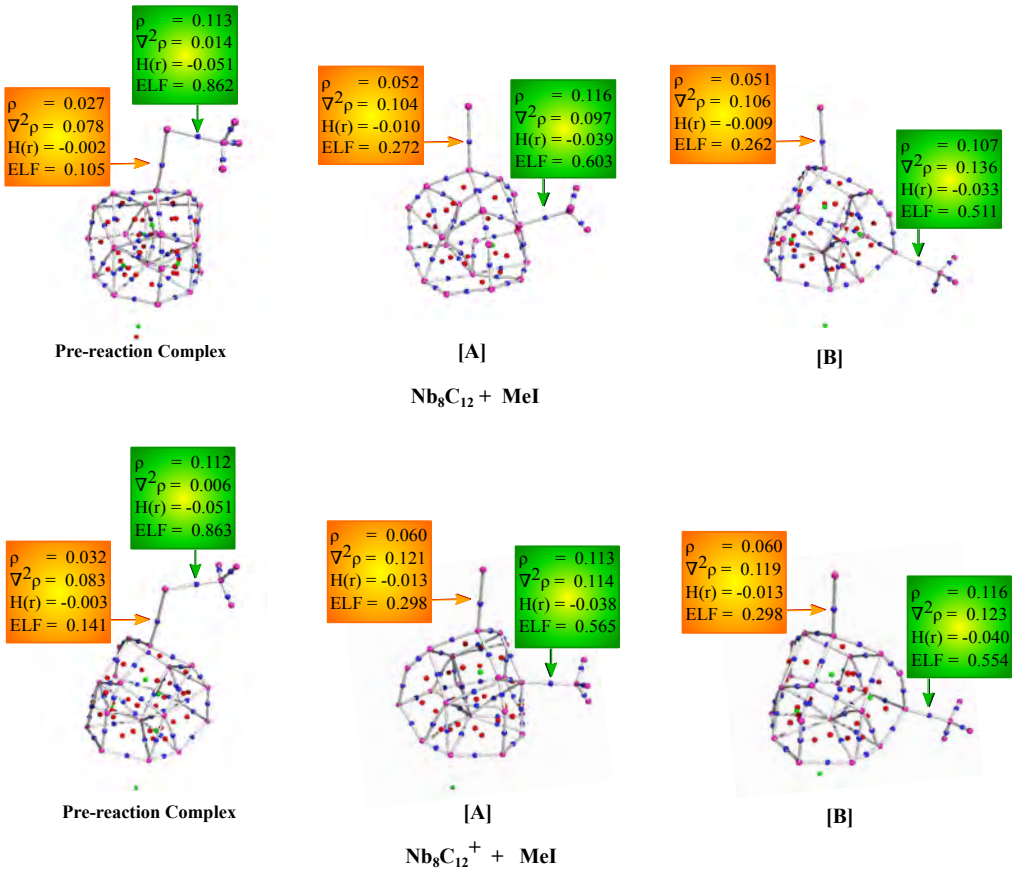

FIGURE 6.7: Molecular graphs of pre–reaction complexes, structure [A] and structure [B] of the dissociation of CH_3I molecule on Nb_8C_{12} (top panel) and $Nb_8C_{12}{}^+$ (bottom panel).

throughout the reaction coordinate and only a single minor increment is noticed at TS–1 on neutral Nb_8C_{12}. The unperturbed nature of f^+ of carbon atom throughout the reaction coordinate may be due to the simultaneous bond breaking and formation process as observed in both the transition states. In both Fig 6.6a and 6.6b, the Nb^o atom in which the CH_3 group finally gets migrated to form complex [B](denoted as Nb^o_C in Fig 6.6a–6.6b), shows a continuous decrease in the respective Fukui function value from TS–1 till complex [B]. Similar to the Fukui index the trend in the HOMO/SOMO–LUMO gaps (Fig 6.6c and 6.6d) along the reaction coordinate are also found to be unique for the neutral and the cationic cluster. The overall range of the HOMO–LUMO gap calculated in both M06–2X and BHandHLYP functional is found to be within 2–3 eV. The prime differences in between Fig 6.6c and 6.6d is again found to be located at the position of first transition state. In Fig 6.6a, the HOMO–LUMO gap shows a sudden drop at TS–1, signifying low HOMO–LUMO gap of the first transition state compared to the P.R.C. In contrary, the SOMO–LUMO gap for the case of cationic metcar shows a steady increase till reaching maximum at complex [A] followed by a steady decrease and finally reaching a value of 2.66 (2.7 in BHandHLYP) at complex [B]. Except the BHandHLYP calculated results in Fig 6.6c, the intermediate complex [A] is usually indicated to have high HOMO/SOMO–LUMO gap, ensuring it's high thermodynamic stability as an intermediate. In order to have further clarification we have performed AIM analysis on the optimized structures of key complexes as obtained along the reaction pathway of the dissociation of CH_3I on both neutral and cationic Nb-Metcar. The molecular graphs of such kind is assembled into two groups(a and b) of Figure 6.7. The position of four different types of critical points along with the bond paths are clearly visible. The values of four important parameters e.g, electron density(ρ), laplacian of electron density ($\nabla^2\rho$),local energy density (H(r)) and the electron localization function (ELF) at two of the most important bond critical points are also included in Figure 6.7.

6.4 Conclusions

The present chapter presents a concise theoretical accounts of the reaction mechanism along with the kinetic and thermodynamic detail of carbon–iodine dissociation reaction on Niobium metcar and it's cation. The C-I dissociation reaction is the only abstraction reaction observed on metcars and process is of enormous significance to synthetic chemists. In depth DFT investigation have shown that although the dissociation process is single step, the 'R' group migration is completed within an overall of two reaction steps consisting of two transition states separated by an intermediate complex. The investigation also signifies that there exists few fundamental differences of the C–I dissociation process on neutral and cationic metcar which are responsible for significantly altering the calculated reaction parameters. Considering the overall range of calculated activation barriers, $Nb_8C_{12}{}^+$ is found to be more reactive towards C–I dissociation. The first activation barrier is observed to be of low to medium range signifying decent catalytic activity of Nb-metcar towards mono–halogen abstraction compared to the commonly used catalysts. Aside from the mechanistic details, few other useful reaction parameters like the rate constants, pre–exponential factor and the temperature dependent constant in accordance to three parametric Arrhenius equation are also included. Further insight is gathered from the Fukui indices,HOMO/SOMO–LUMO gap and via the AIM analysis. The detail mechanism of C–I dissociation on metcar is still mostly unexplored and hence the current study may be able to provide a decent contribution to enlighten some of the riddles encompassing metcars till this days.

References

(1) Bergeron, D. E.; Castleman, A. W.; Morisato, T.; Khanna, S. N. *Science* **2004**, *304*, 84–87.

(2) Castleman Jr, A.; Khanna, S. *J. Phys. Chem. C* **2009**, *113*, 2664–2675.

(3) Bergeron, D.; Roach, P.; Castleman, A.; Jones, N.; Khanna, S. *Science* **2005**, *307*, 231–235.

(4) Bergeron, D. E.; Roach, P. J.; Castleman Jr, A. W.; Jones, N. O.; Reveles, J. U.; Khanna, S. N. *J. Am. Chem. Soc.* **2005**, *127*, 16048–16053.

(5) Bergeron, D.; Castleman, A. *Chemical physics letters* **2003**, *371*, 189–193.

(6) Jena, P.; Khanna, S.; Rao, B. K., *Physics and Chemistry of Finite Systems: from Clusters to Crystals*; Kluwer Academic Publishers, Dordrecht Boston and London: 1992; Vol. 1, pp 1–1414.

(7) Reber, A. C.; Khanna, S. N.; Roach, P. J.; Woodward, W. H.; Castleman Jr, A. *J. Phys. Chem. A* **2010**, *114*, 6071–6081.

(8) Luo, Z.; Reber, A. C.; Jia, M.; Blades, W. H.; Khanna, S. N.; Castleman, A. *Chem. Sci.* **2016**.

(9) Burgert, R.; Schnöckel, H.; Grubisic, A.; Li, X.; Stokes, S. T.; Bowen, K. H.; Ganteför, G.; Kiran, B.; Jena, P. *Science* **2008**, *319*, 438–442.

(10) Neumaier, M.; Olzmann, M.; Kiran, B.; Bowen, K. H.; Eichhorn, B.; Stokes, S. T.; Buonaugurio, A.; Burgert, R.; Schnokel, H. *Journal of the American Chemical Society* **2014**, *136*, 3607–3616.

(11) Burgert, R.; Stokes, S. T.; Bowen, K. H.; Schnöckel, H. *Journal of the American Chemical Society* **2006**, *128*, 7904–7908.

(12) Reveles, J. U.; Clayborne, P. A.; Reber, A. C.; Khanna, S. N.; Pradhan, K.; Sen, P.; Pederson, M. R. *Nat. Chem.* **2009**, *1*, 310–315.

(13) Robles, R; Khanna, S. N.; Castleman Jr, A. *Phys. Rev. B* **2008**, *77*, 235441.

(14) Grubisic, A.; Ko, Y. J.; Wang, H.; Bowen, K. H. *J. Am. Chem. Soc.* **2009**, *131*, 10783–10790.

(15) Wang, M.; Huang, X.; Du, Z.; Li, Y. *Chem. Phys. Lett.* **2009**, *480*, 258–264.

(16) Alikhani, M.; Shaik, S *Theor. Chem. Acc.* **2006**, *116*, 390–397.

(17) Aguilera-Granja, F; Longo, R.; Gallego, L.; Vega, A *J. Chem. Phys.* **2010**, *132*, 184507.

(18) Montejano-Carrizales, J.; Aguilera-Granja, F; Morán-López, J. *Eur. Phys. J. D* **2011**, *64*, 53–62.

(19) Varas, A.; Aguilera-Granja, F; Rogan, J.; Kiwi, M. *J. Magn. Magn. Mater.* **2015**, *394*, 325–334.

(20) Clayborne, P. A.; Lopez-Acevedo, O.; Whetten, R. L.; Grönbeck, H.; Häkkinen, H. *J. Chem. Phys.* **2011**, *135*, 094701.

(21) Walter, M.; Akola, J.; Lopez-Acevedo, O.; Jadzinsky, P. D.; Calero, G.; Ackerson, C. J.; Whetten, R. L.; Grönbeck, H.; Häkkinen, H. *Proc. Natl. Acad. Sci. U. S. A.* **2008**, *105*, 9157–9162.

(22) Jung, J.; Kang, S.; Han, Y.-K. *Nanoscale* **2012**, *4*, 4206–4210.

(23) Knight, W. D.; Clemenger, K.; de Heer, W. A.; Saunders, W. A.; Chou, M.; Cohen, M. L. *Phys. Rev. Lett.* **1984**, *52*, 2141–2143.

(24) Knight, W. D.; de Heer, W. A.; Clemenger, K.; Saunders, W. A. *Solid State Commun.* **1985**, *53*, 445–446.

(25) Kacprzak, K. A.; Lehtovaara, L.; Akola, J.; Lopez-Acevedo, O.; Häkkinen, H. *Phys. Chem. Chem. Phys.* **2009**, *11*, 7123–7129.

(26) Harkness, K. M.; Tang, Y.; Dass, A.; Pan, J.; Kothalawala, N.; Reddy, V. J.; Cliffel, D. E.; Demeler, B.; Stellacci, F.; Bakr, O. M., et al. *Nanoscale* **2012**, *4*, 4269–4274.

(27) Kroto, H. W.; Heath, J. R.; O'Brien, S. C.; Curl, R. F.; Smalley, R. E., et al. *Nature* **1985**, *318*, 162–163.

(28) Krätschmer, W; Lamb, L. D.; Fostiropoulos, K; Huffman, D. R. *Nature* **1990**, *347*, 27.

(29) Guo, B.; Kerns, K.; Castleman Jr, A. *Science* **1992**, *255*, 1411.

(30) Wei, S; Guo, B.; Purnell, J; Buzza, S; Castleman Jr, A. *The Journal of Physical Chemistry* **1992**, *96*, 4166–4168.

(31) Wei, S.; Guo, B. C.; Purnell, J.; Buzza, S.; Castleman, A. W. *Science* **1992**, *256*, 818–820.

(32) Cartier, S.; May, B.; Castleman Jr, A. *The Journal of chemical physics* **1994**, *100*, 5384–5386.

(33) Purnell, J; Wei, S; Castleman, A. *Chemical physics letters* **1994**, *229*, 105–110.

(34) Cartier, S.; Chen, Z.; Walder, G.; Sleppy, C.; Castleman Jr, A. *Science* **1993**, *260*, 195–197.

(35) Deng, H.; Guo, B.; Kerns, K.; Castleman, A. *International Journal of Mass Spectrometry and Ion Processes* **1994**, *138*, 275–281.

(36) Deng, H.; Kerns, K.; Castleman, A. *Journal of the American Chemical Society* **1996**, *118*, 446–450.

(37) Liu, P.; Rodriguez, J. A.; Hou, H.; Muckerman, J. T. *The Journal of chemical physics* **2003**, *118*, 7737–7740.

(38) Liu, P.; Rodriguez, J. A.; Muckerman, J. T. *The Journal of Physical Chemistry B* **2004**, *108*, 18796–18798.

(39) Wang, L. S.; Li, S.; Wu, H. *The Journal of Physical Chemistry* **1996**, *100*, 19211–19214.

(40) Lee, S.; Gotts, N. G.; Von Helden, G.; Bowers, M. T. *Science* **1995**, *267*, 999.

(41) Liu, P.; Lightstone, J. M.; Patterson, M. J.; Rodriguez, J. A.; Muckerman, J. T.; White, M. G. *The Journal of Physical Chemistry B* **2006**, *110*, 7449–7455.

(42) Kerns, K.; Guo, B.; Deng, H.; Castleman Jr, A. *Journal of the American Chemical Society* **1995**, *117*, 4026–4029.

(43) Lightstone, J. M.; Patterson, M. J.; Liu, P.; White, M. G. *The Journal of Physical Chemistry A* **2006**, *110*, 3505–3513.

(44) Kerns, K.; Guo, B.; Deng, H.; Castleman Jr, A. *The Journal of chemical physics* **1994**, *101*, 8529–8534.

(45) Poblet, J.-M.; Bo, C.; Rohmer, M.-M.; Bénard, M. *Chemical physics letters* **1996**, *260*, 577–581.

(46) Benard, M.; Rohmer, M.-M.; Poblet, J.-M.; Bo, C. *The Journal of Physical Chemistry* **1995**, *99*, 16913–16924.

(47) Li, S.; Wu, H.; Wang, L.-S. *Journal of the American Chemical Society* **1997**, *119*, 7417–7422.

(48) Muñoz, J.; Pujol, C.; Bo, C.; Poblet, J.-M.; Rohmer, M.-M.; Benard, M. *The Journal of Physical Chemistry A* **1997**, *101*, 8345–8350.

(49) Selvan, R; Pradeep, T *Chemical physics letters* **1999**, *309*, 149–156.

(50) Dance, I. *Journal of the Chemical Society, Chemical Communications* **1992**, 1779–1780.

(51) Dance, I. *Journal of the American Chemical Society* **1996**, *118*, 6309–6310.

(52) Gueorguiev, G.; Pacheco, J. *Physical review letters* **2002**, *88*, 115504.

(53) Chen, H; Feyereisen, M; Long, X.; Fitzgerald, G *Physical review letters* **1993**, *71*, 1732.

(54) Lou, L; Nordlander, P *Chemical physics letters* **1994**, *224*, 439–444.

(55) Gueorguiev, G.; Pacheco, J. *Physical Review B* **2003**, *68*, 241401.

(56) Byun, Y.; Freiser, B. S. *Journal of the American Chemical Society* **1996**, *118*, 3681–3686.

(57) Deng, H.; Guo, B.; Kerns, K.; Castleman Jr, A. *The Journal of Physical Chemistry* **1994**, *98*, 13373–13378.

(58) Guo, B.; Kerns, K.; Castleman Jr, A. *Journal of the American Chemical Society* **1993**, *115*, 7415–7418.

(59) Sakurai, H; Castleman Jr, A. *The Journal of chemical physics* **1999**, *111*, 1462–1466.

(60) Byun, Y.; Lee, S.; Kan, S.; Freiser, B. S. *The Journal of Physical Chemistry* **1996**, *100*, 14281–14288.

(61) Oro, L. A.; Braunstein, P.; Raithby, P. R., *Metal Clusters in Chemistry*; Wiley-vch Weinheim, Germany: 1999; Vol. 3.

(62) Johansson Seechurn, C. C.; Kitching, M. O.; Colacot, T. J.; Snieckus, V. *Angewandte Chemie International Edition* **2012**, *51*, 5062–5085.

(63) Yin, L.; Liebscher, J. *Chemical Reviews* **2007**, *107*, 133–173.

(64) Jana, R.; Pathak, T. P.; Sigman, M. S. *Chemical reviews* **2011**, *111*, 1417–1492.

(65) González-Arellano, C.; Abad, A.; Corma, A.; García, H.; Iglesias, M.; Sanchez, F. *Angewandte Chemie* **2007**, *119*, 1558–1560.

(66) Nijamudheen, A; Datta, A. *The Journal of Physical Chemistry C* **2013**, *117*, 21433–21440.

(67) Sengupta, T.; Das, S.; Pal, S. *Nanoscale* **2015**, *7*, 12109–12125.

(68) Sadhukhan, T.; Samanta, B.; Ansari, S. A.; Pal, S. *Theoretical Chemistry Accounts* **2016**, *135*, 234.

(69) Frisch, M.; Trucks, G.; Schlegel, H.; Scuseria, G.; Robb, M.; Cheeseman, J.; Scalmani, G; Barone, V; Mennucci, B; Petersson, G. *Gaussian 09 Revision A.01, Wallingford CT*.

(70) Canneaux, S.; Bohr, F.; Henon, E. *Journal of computational chemistry* **2014**, *35*, 82–93.

(71) McNaught, A. D.; McNaught, A. D., *Compendium of chemical terminology*; Blackwell Science Oxford: 1997; Vol. 1669.

(72) Lu, T.; Chen, F. *Journal of computational chemistry* **2012**, *33*, 580–592.

(73) Allen, L. C.; Egolf, D. A.; Knight, E. T.; Liang, C. *Journal of physical chemistry* **1990**, *94*, 5602–5607.

(74) Reed, L. H.; Allen, L. C. *The Journal of Physical Chemistry* **1992**, *96*, 157–164.

(75) Baruah, T.; Pederson, M. R.; Lyn, M.; Castleman Jr, A. *Physical Review A* **2002**, *66*, 053201.

(76) Luo, Y.-R., *Handbook of bond dissociation energies in organic compounds*; CRC press: 2002.

(77) Hohenstein, E. G.; Chill, S. T.; Sherrill, C. D. *Journal of Chemical Theory and Computation* **2008**, *4*, 1996–2000.

(78) Walker, M.; Harvey, A. J.; Sen, A.; Dessent, C. E. *The Journal of Physical Chemistry A* **2013**, *117*, 12590–12600.

(79) Zhao, Y.; Truhlar, D. G. *Theoretical Chemistry Accounts: Theory, Computation, and Modeling (Theoretica Chimica Acta)* **2008**, *120*, 215–241.

Chapter 7

Summary and Outlook

The present thesis includes a selected accounts of stability and catalytic activity of different class of atomic clusters. The major scope of the thesis is to understand the influence of different stabilization factors on the various properties and reactivities of atomic clusters. The first chapter provides an introduction to the basic concept of cluster chemistry. Aside from the defination, classification, historical accounts and methods of synthesis, an in depth discussion on electronic and geometric stabilities are included as well. Few widely used theoretical models are also explained in short. Chapter 2 contains the fundamentals of Density functional Theory (DFT) which is the theoretical method used throughout all the works included within the thesis. This chapter is mostly focuced on the earlier fundamental developments and encompassing the ideas like the Thomas–Fermi model to the Kohn–Sham equation. A short account of conceptual DFT is also added. Chapter 3 is the first working chapter. In chapter 3, the influence of the electronic shell effect upon the catalytic activity of small sized aluminum clusters towards C–I activation is investigated. It is observed that the jellium shell configuration of the cluster is the major contributing factor behind the reactivity of aluminum cluster towards C–I dissociation. Thus although in bulk state aluminum is totally inert, the electronic shell effect in nanoscale can make them extremely reactive and provide comparable reaction barriers with the conventional catalysts available. Chapter 4 shows how the electronic shell structure can alter various properties of metal clusters. Thus, whereas the transition metal doped metal cluster with low spin shows prominent presence of odd–even effect in every calculate properties and therefore, behaves like a cluster. However, their high spin counterparts shows more resemblance to the bulk solids rather than the cluster and which get reflected in the smooth trends observed in the evaluated properties. Chapter 5 consists of a proposal, that small sized metastable clusters can effectively be stabilized via attaching radicals in place of commonly used ligands. The thermodynamic stabilities with few model radicals is reported along with the comparison with standard stable complexes. The superatomic complex theory is also verified via the construction of the Kohn–Sham correlation diagram. Chapter 6 is focused on the details reaction mechanism along with thermodynamic and kinetic details of C–I activation on Niobium Metcar (Nb_8C_{12}) and its cation. The family of metcar is considered as stable and the individual members mostly behave like molecules rather than the clusters. Despite the experimental results, the reaction mechanism of C–I activation on metcar is still unknown and Chapter 6 may be able to shed some light in that context. The beautifully odd structure of metcar has also provides some interesting tweaks in the reaction mechanism which would otherwise be much simplistic in nature.

Despite the efforts to rationalize the properties of selected class of atomic clusters in terms of their stabilities and reactivities presented in this thesis, few questions still remain unanswered. It is needless to say that, such occasions are potent enough to provide ample opportunities for new investigations in both the theoretical and experimental domain. As for example, the investigation included in Chapter 3 shows that selected aluminum nanoclusters with specific electronic configurations can be act as an alternative catalyst for C–I bond dissociation. However, small

sized aluminum clusters are infamous due to their metastable nature as well as for high reactivity and hence stabilizing them is absolutely essential before even approaching for large scale practical applications. The real problem in this specific case is not only the stabilization, but how to stabilize them without altering the catalytic activity. Theoretical investigation with experimental collaboration is certainly essential for this type of problems and such studies will definitely aid the research field and may even whole material chemistry if positive outcomes are achieved. New problems based on the influence of other factors on activation barrier can also be designed and may be extended further with experimental collaborations. Similarly, in the context of Chapter 4, we can argue, can the resemblance with the bulk be generalized? Is there any prescribed rules which can be derived to explain in which cases such resemblance can be expected and where such similarities will be absent? In the context of radical based stabilization, experimental confirmation is certainly necessary along with the synthesis of suitable radicals apart from the model systems presented within Chapter 5. New experimental set-ups and methodologies may also have to developed, since, it is expected radical attachment process will not be as similar as ligand attachment due to the subtle differences hidden within their chemical nature. Aside from the conventional stabilization procedure, one may also think of any possible out of the box solutions for cluster stabilization. In this aspect, computational study will certainly be come in handy, since it is usually cheaper than experiments where a trial and error scenario in concerned. The study on Niobium metcar presented in Chapter 6 is mostly partial, since there exists a series of different metcars as well as a plethora of interesting problem for which no theoretical results are published in spite of the availability of experimental results. The reason behind this void is due to the unavailability of sufficient computational resources or efficient algorithm in the early 90's which could handle the calculations for such big systems. Therefore, a fresh revisit to the old problems with new computational tools may be proven worthwhile for the sake of cluster as well as material chemistry.

Appendix A

List of Publications

1. Achintya Kumar Dutta, **Turbasu Sengupta**, Nayana Vaval, Sourav Pal: Electron attachment to DNA and RNA nucleobases: An EOMCC investigation. International Journal of Quantum Chemistry 09/2014; 115(12):753–764., DOI:10.1002/qua.24892

2. Kamalika Ghatak, **Turbasu Sengupta**, Sailaja Krishnamurty, Sourav Pal, *Computational investigation on the catalytic activity of Rh6 and Rh4Ru2 clusters towards methanol activation*. Theoretical Chemistry Accounts 12/2014; 134(1):1597., DOI:10.1007/s00214-014-1597-z

3. Himadri Pathak, B. K. Sahoo, **Turbasu Sengupta**, B. P. Das, Nayana Vaval, Sourav Pal, *A Relativistic Equation-of-motion Coupled-Cluster Investigation of the Trends of Single and Double Ionization Potentials in the He and Be Isoelectronic Systems*. Journal of Physics B Atomic Molecular and Optical Physics 05/2015; 48:111009., DOI:10.1088/0953-4075/48/11/115009

4. **Turbasu Sengupta**, Susanta Das, Sourav Pal, *Oxidative addition of C-I bond on aluminum nanoclusters*. Nanoscale 06/2015; 7(28):12109–12125., DOI:10.1039/C5NR02278A

5. Susanta Das, **Turbasu Sengupta**, Achintya Kumar Dutta, Sourav Pal, *Electron Detachment and Subsequent Structural Changes of Water Clusters*. The Journal of Physical Chemistry A 02/2016; 120(7):1065–1073., DOI:10.1021/acs.jpca.5b09389

6. **Turbasu Sengupta**, Susanta Das, Sourav Pal, *Transition Metal Doped Aluminum Clusters: An Account of Spin*. The Journal of Physical Chemistry C 04/2016; 120(18):10027–10040., DOI:10.1021/acs.jpcc.6b00510

7. **Turbasu Sengupta**, Sourav Pal, *Radical Attached Aluminum Nanoclusters: An Alternative Way for Cluster Stabilization*. Physical Chemistry Chemical Physics 07/2016; 18(31):21746-21759., DOI:10.1039/C6CP03601E

8. **Turbasu Sengupta**, Muntazir S. Khan, Sourav Pal, *Investigation of Carbon–Iodine bond activation on Niobium Metcar (Nb_8C_{12})*. (To be Submitted)